The University Of Sheffield.

Academic unit of Radiology

Imaging in pulmonary hypertension: the role of MR and CT

A thesis by

Smitha Rajaram

Submitted for the degree of

Doctorate of medicine

September 2013

Registration Number: 100261194

Acknowledgment

Foremost, I would like to express my sincere thanks to my supervisors Prof Wild and Dr Kiely for their continuous support throughout the research. Their motivation, patience, enthusiasm and immense knowledge have been an invaluable support and encouragement for this work.

I would also like to thank the PH clinicians Robin Condliffe and Charlie Elliot for their assistance with statistical analysis and ethical approval and Judith Hurdman for her exhaustive right heart catheter data. I would also like to acknowledge radiologists Christine Davies and Catherine Hill for providing clinical radiological input. I would like to thank Helen Marshall and Dave Capener for providing insight into MR physics and experimental techniques. A special thanks to Andy Swift, clinical lecturer and former fellow research radiologist. He was greatly helpful and took time for adding new ideas to my work.

Finally, a special mention goes to my family for their support and patience in completing this work and my husband for keeping the long days of thesis writing eventful.

Support

The work described in this thesis has been funded by Pfizer through an unrestricted educational grant and I thank them for their generous financial support.

Summary

Pulmonary hypertension (PH) is a debilitating disease with many causes that has a significant impact on quality of life and results in premature death. Until recently imaging has only played an adjunctive role to primary diagnostic modalities such as echocardiography and right heart catheterization in identifying these patients.

The advent of newer imaging techniques and developments in hardware has opened up a new scope for imaging. CT offers excellent structural detail while MRI provides superb functional information without the risk of radiation. These modalities now offer a robust and in-depth diagnostic approach for the investigation of patients with suspected pulmonary hypertension.

This document explores the role of MR and CT imaging methods in investigating patients with pulmonary vascular disease and different aspect of lung disease. In particular, subgroups of pulmonary hypertension associated with unique morphological changes have been closely scrutinized. In this work the value of MR angiography in patients suspected with chronic thromboembolic pulmonary hypertension or unexplained PH has been explored and in the same subgroup of patients, the role of 3D MR lung perfusion as a diagnostic tool has also been demonstrated. This research has also shown that the thoracic CT offers valuable prognostic information and imaging characteristics in patients with each of the major subcategories of pulmonary arterial hypertension. Furthermore, the diagnostic accuracy and prognostic significance of MR and CT indices for the detection of PH in patients with connective tissue disease associated with PH has been highlighted. Finally, the feasibility and diagnostic quality of MRI to identify structural parenchymal lung changes have also been analysed and this study demonstrates the potential clinical utility of imaging high risk patients with MRI in longitudinal studies thereby avoiding the hazards of radiation exposure.

Table of Contents

List of figures

List of Tables

1 Introduction

1.1 Imaging of the Lung and Pulmonary Vasculature

Imaging of the thorax has played a vital role in medicine and has been used widely in the diagnosis, management and follow-up of patients with varied pathologies. The techniques that are commonly used in clinical practice include the plain chest radiograph (X-ray), computed tomography (CT), ventilation-perfusion scintigraphy and Positron emission tomography. The role of Magnetic resonance imaging (MRI) has predominantly been restricted to that of a complementary imaging tool largely in a research setting. This section of the introduction gives an overview of the imaging techniques routinely used for thoracic imaging.

1.1.1 Chest Radiograph

The chest radiograph continues to be the first line imaging technique for assessment of patients with known or suspected lung disease and provides a general overview of the lung and pulmonary vasculature. The two dimensional nature of a chest radiograph means there is super position of imaged structures over the lungs and it has been estimated that up to 40% of the lungs are obscured on a conventional chest radiograph [1]. In the last decade, the digital chest radiograph has replaced analog film imaging and several perceptual limitations of the conventional chest radiograph have been overcome through newer applications, detectors and image processing and display techniques.

Three of the applications useful for chest imaging are dual-energy radiography, temporal subtraction radiography and digital tomosynthesis. With *dual-energy radiography* (figure 2) two images of different tissue types can be generated and this results in improved differentiation of superimposed structures. *Temporal subtraction radiography* selectively highlights the new changes on the radiograph by subtracting the previous radiograph of the patient from the current one. *Digital tomosynthesis* is sectional imaging in which multiple radiographs of one region are taken at discrete angles and an image is reconstructed. These

applications coupled with image processing and display techniques has improved conspicuity of abnormalities [2].

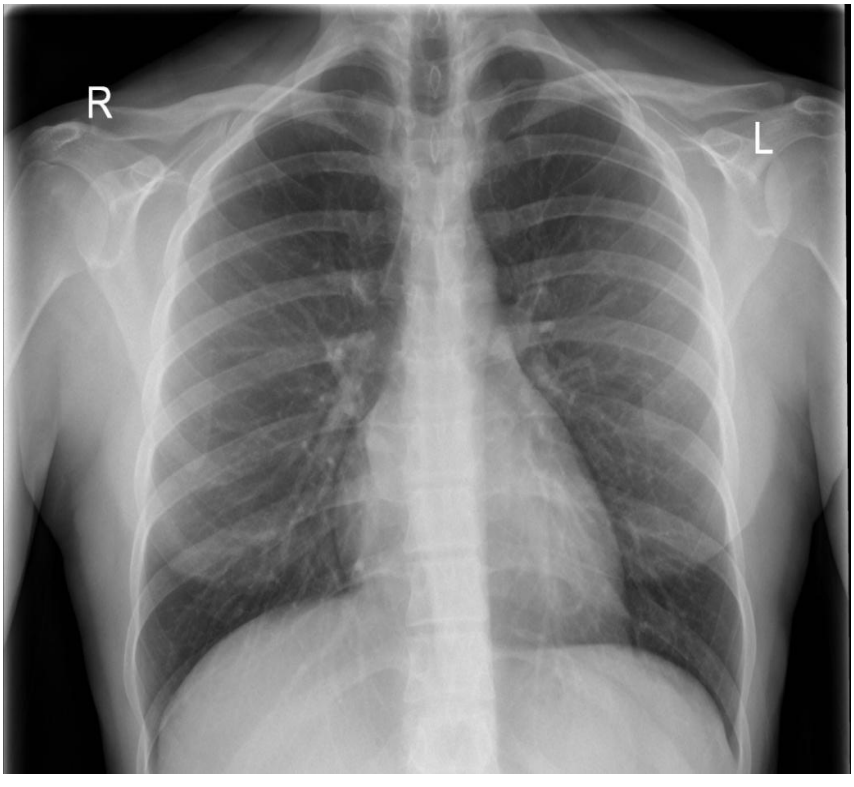

Figure 1: Normal plain chest Radiograph

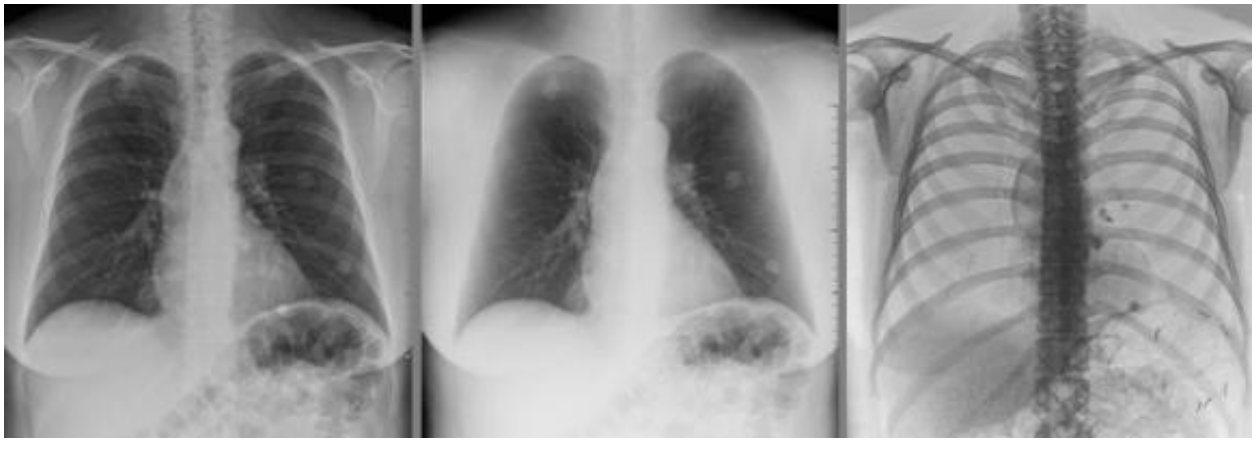

Figure 2: Dual energy radiography shows a chest radiograph with soft tissue (middle) and bone density (right)

1.1.2 Radionuclide imaging

Ventilation-perfusion (V/Q) scintigraphy involves simultaneous imaging of the distribution of pulmonary blood flow and ventilation. Ventilation studies are performed after inhalation of Krypton or Technetium-labelled aerosol of Diethylene Triamine Pentaacetic acid (DTPA) or Technegas and perfusion studies are performed after intravenous injection of radioactive technetium macro aggregated albumin (Tc99m-MAA). The main clinical application for this technique is in the evaluation of patients suspected with pulmonary embolism (PE). However since the introduction of multidetector CT scanners there has been a dramatic decline in the use of this technique for investigating PE. This is also compounded by the fact that the results of V/Q scintigraphy are probabilistic reports rather than definite and there are also a high number of “indeterminate” scans requiring further investigations to confirm the diagnosis [3-5]. Superior to planar V/Q scintigraphy is the single-photon emission computed tomography (SPECT) that provides 3D data representation and a better contrast resolution (figure 4). Unlike planar imaging, there is no overlap of structure in SPECT and hence it offers higher specificity and the “indeterminate” scans are greatly reduced [6]. The documented radiation dose for a V/Q scintigraphy is 0.5 to 1mSv and for a SPECT scan is 1.2–2 mSv [7].

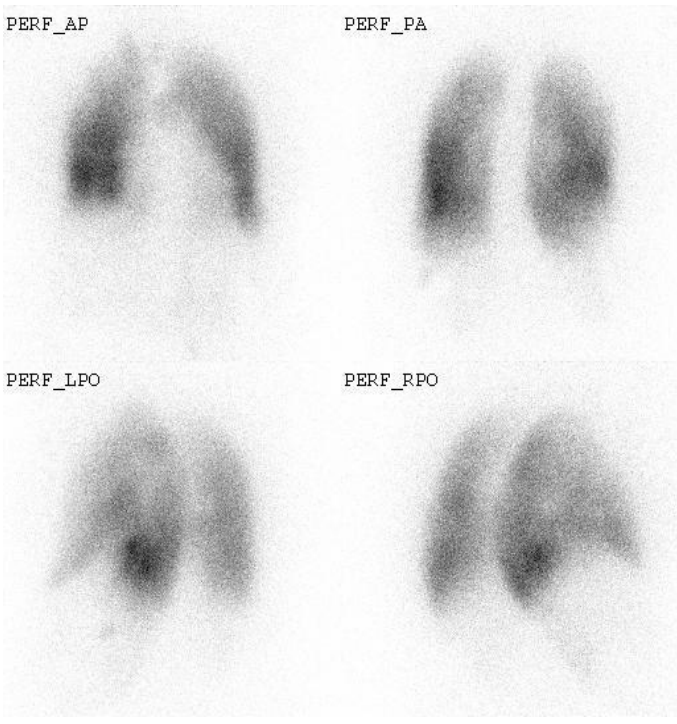

Figure 3: Normal perfusion scintigraphy

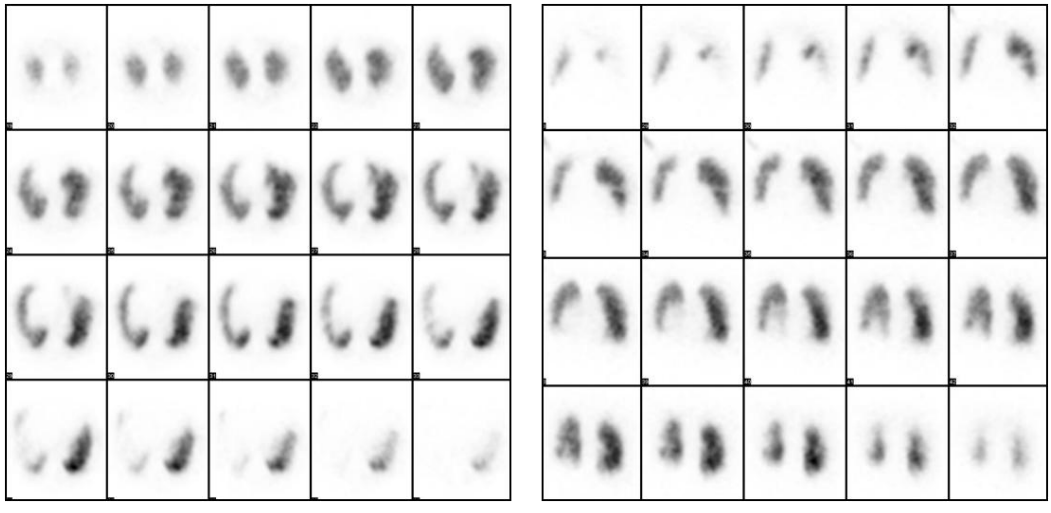

Figure 4: Axial and coronal SPECT lung perfusion images

Radionuclide myocardial perfusion scintigraphy offers a method of visualizing blood flow to the heart and is well established as a functional cardiac imaging technique. It is performed with single photon emission computed tomography (SPECT) or positron emission tomography (PET) using radioactive material such as thallium or technetium. Hybrid imaging methods that combine SPECT with CT or PET with CT are also now available. Studies show that the combined scanning techniques such as SPECT with CT or PET with CT improve specificity for diagnosing coronary artery disease and also lessen the radiation doses [8-9].

A recent study showed ^{18}FDG-PET imaging to quantify increased cellular metabolism in patients with pulmonary arterial hypertension. They found N-Terminal Probrain natriuteric peptide (NT-ProBNP) to correlate with 18-FDG uptake in the right ventricle (RV) in those with PH. They also found increased 18-FDG uptake in the lung parenchyma and RV of subjects with idiopathic pulmonary arterial hypertension [10].

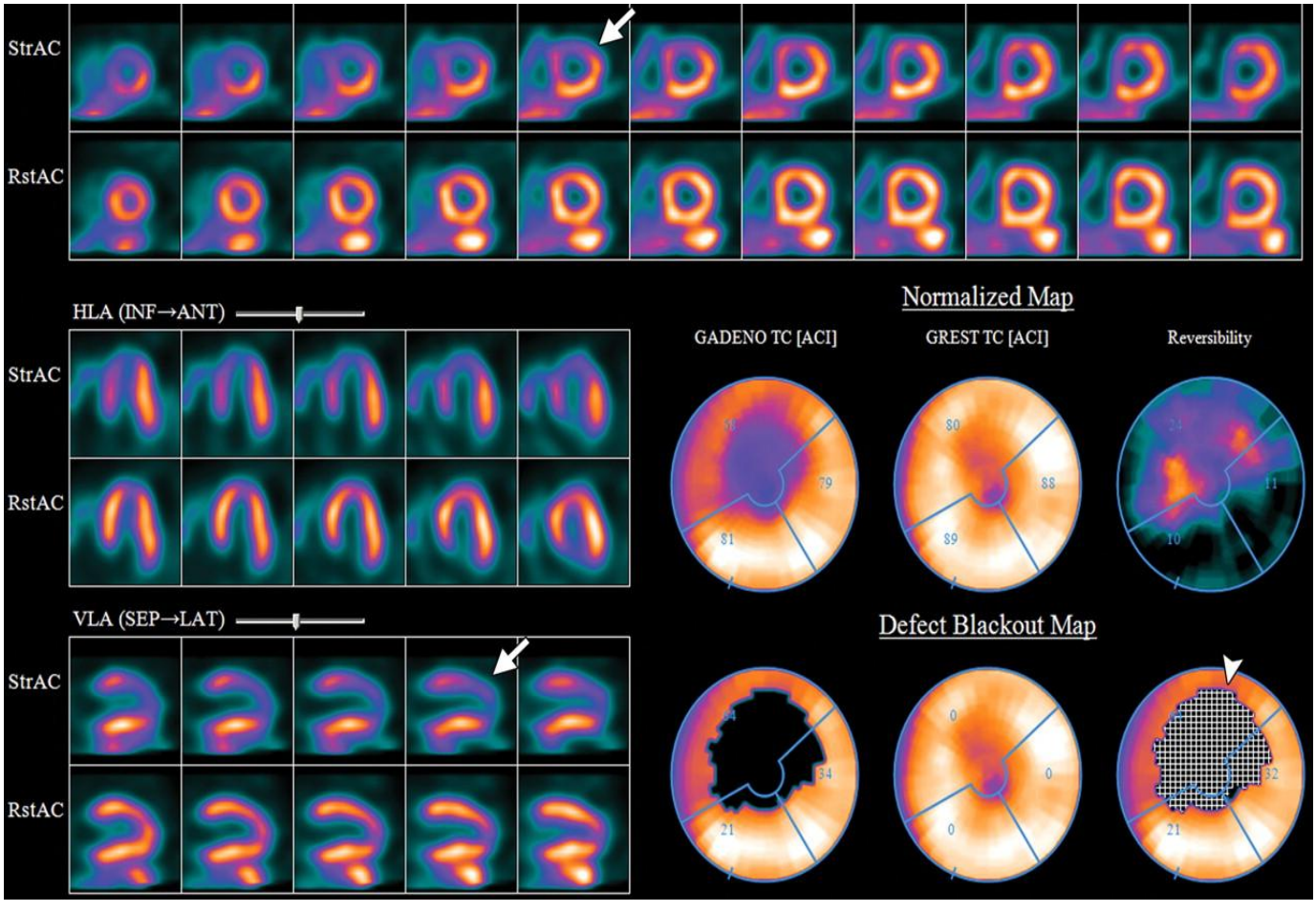

Figure 5: Myocardial perfusion imaging examination performed with SPECT/CT, stress and rest images [9]

1.1.3 Computed Tomography (CT)

The idea of imaging a cross section of the human body on a radiographic film was first proposed by an Italian scientist Alessandro Vallebona in the early 1900s. Radon later came up with the mathematical basis for tomographic imaging. The first CT prototype was built in 1961 by William Oldendorf. In this prototype an X-ray source and a detector that was mechanically coupled together rotated around the body to be imaged. The first commercial CT scanner was invented by Sir Godfrey Hounsfield in 1967 at EMI Central Research Laboratories, UK and Allan Cormack developed the mathematical theory behind the currently used CT scanners.

CT has been the 'workhorse' of thoracic imaging for over three decades and has had a major impact on the evaluation of disease of the lung and cardiovascular system.

Multidetector spiral CT has more or less replaced axial single-slice CT and these scanners have the ability to cover the entire chest in less than 5s breathhold with slice thickness of sub-millimetre or less [11]. With narrow collimations detailed display of the pulmonary arteries down to the subsegmental level is now possible [12]. These features make CTPA useful for assessment of various thoracic and pulmonary vascular abnormalities. Hounsfield unit (HU), a quantitative scale for describing radiodensity, differs for different tissue, for example HU for air is around −1000 HU and for lung is −500HU.

The continuous data from spiral CT scanners allow several methods of 2D and 3D image processing. With *multiplanar reconstruction* or MPR a stack of axial images are aligned to form a contiguous image and this can be reconstructed into any arbitrary 2D image plane. 3D image display techniques such as *maximum intensity projection* (MIP) or *minimum intensity projection* (MINIP) display structures of interest that has the highest or lowest intensity than adjacent structures. MINIP is a data visualization method that uses all the data in a volume of interest to generate a single two dimensional image with the lowest attenuation value on every view and hence enables detection of low-density structures in a given volume. Similarly MIP consists of projecting the voxel with the highest attenuation value on every view. These techniques are ideal for depiction of

pulmonary vessels (MIP) and subtle emphysema (MINIP). Finally, *Volume Rendering Technique* (VRT) allows reconstruction of a 3D model from a 2D image stack.

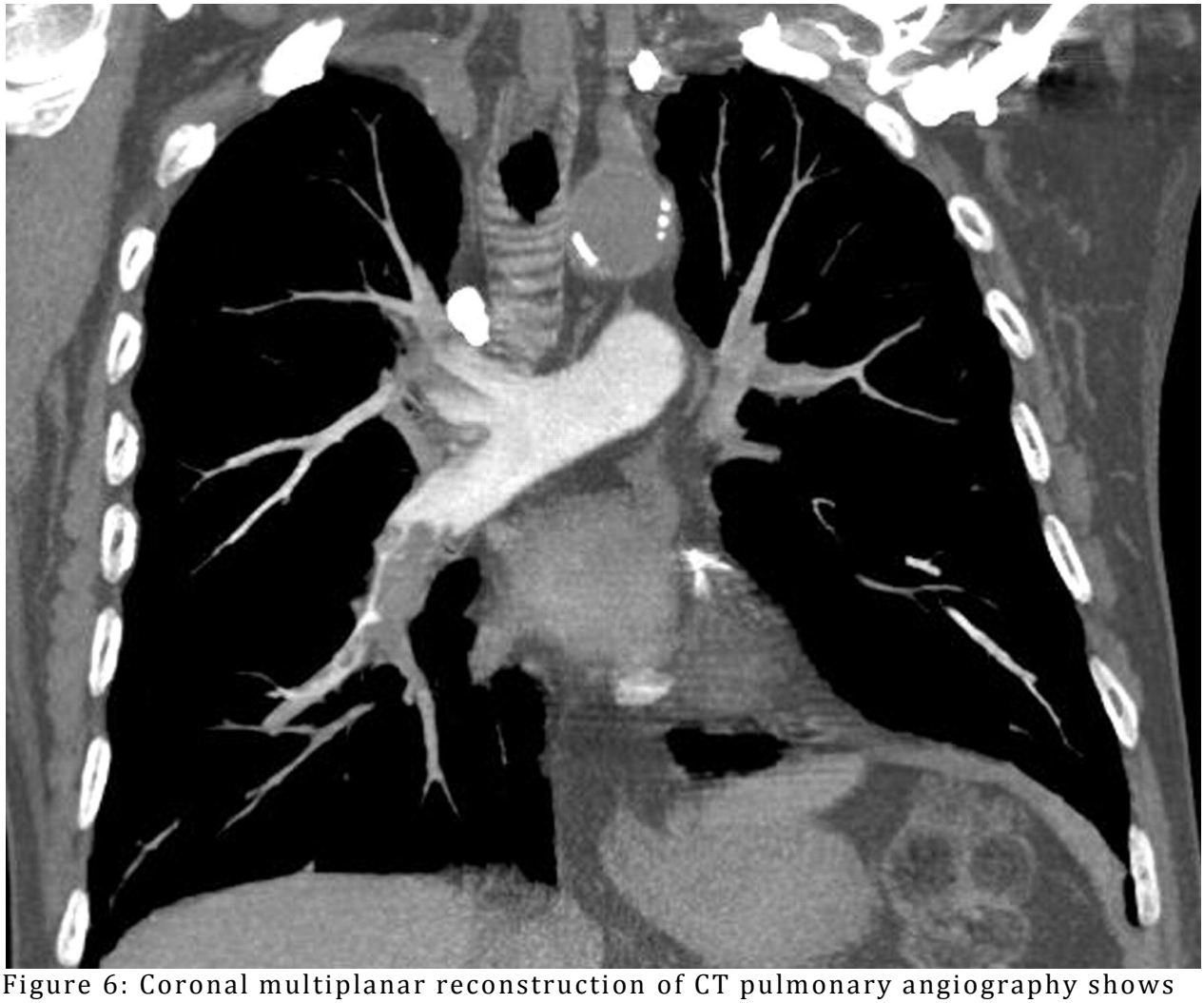

Figure 6: Coronal multiplanar reconstruction of CT pulmonary angiography shows bilateral intravascular filling defects

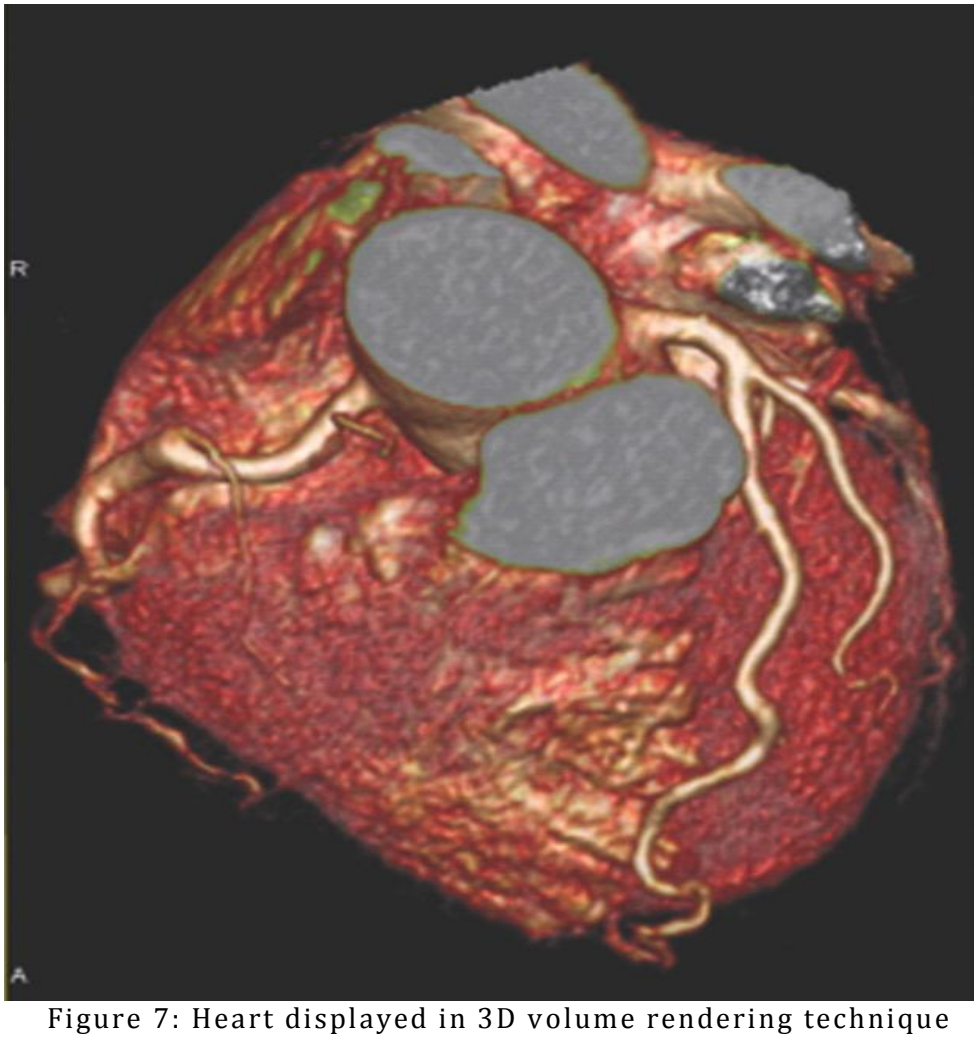

Figure 7: Heart displayed in 3D volume rendering technique

Dual-energy CT is a relatively new technique in which datasets from two x-ray tubes operating at different energy potentials (80 KV and 120 or 140 KV) are simultaneous captured [13]. Using this technique lung ventilation or perfusion images can be acquired by using either intravenous iodine (perfusion) or inhaled gas xenon (ventilation) as contrast agents respectively. This method provides additional clinically relevant perfusion or ventilation information in the same examination. Thoracic applications of this technique include perfusion imaging in patients with suspected pulmonary embolism and xenon ventilation-perfusion imaging for patients with lung diseases. Cardiac applications include cardiac viability, cardiac perfusion and myocardial iron detection [14]. The approximate dose for dual energy CT is 2.70 mSv [15].

True pulmonary perfusion imaging is based on quantification of tissue enhancement at serial time points after IV administration of contrast medium. In dual-energy CT the datas are acquired at a single time point and hence the CT assesses the pulmonary blood volume and provides a map of lung microcirculation at a given time point only[16]. In healthy people, collateral supply from bronchial arteries and other systemic vessels is negligible, however in patients with pulmonary hypertension there is considerable increase in collateral supply from dilated bronchial arteries and this is a significant limitation of dual energy CT is the assessment of patients with PH especially CTEPH.

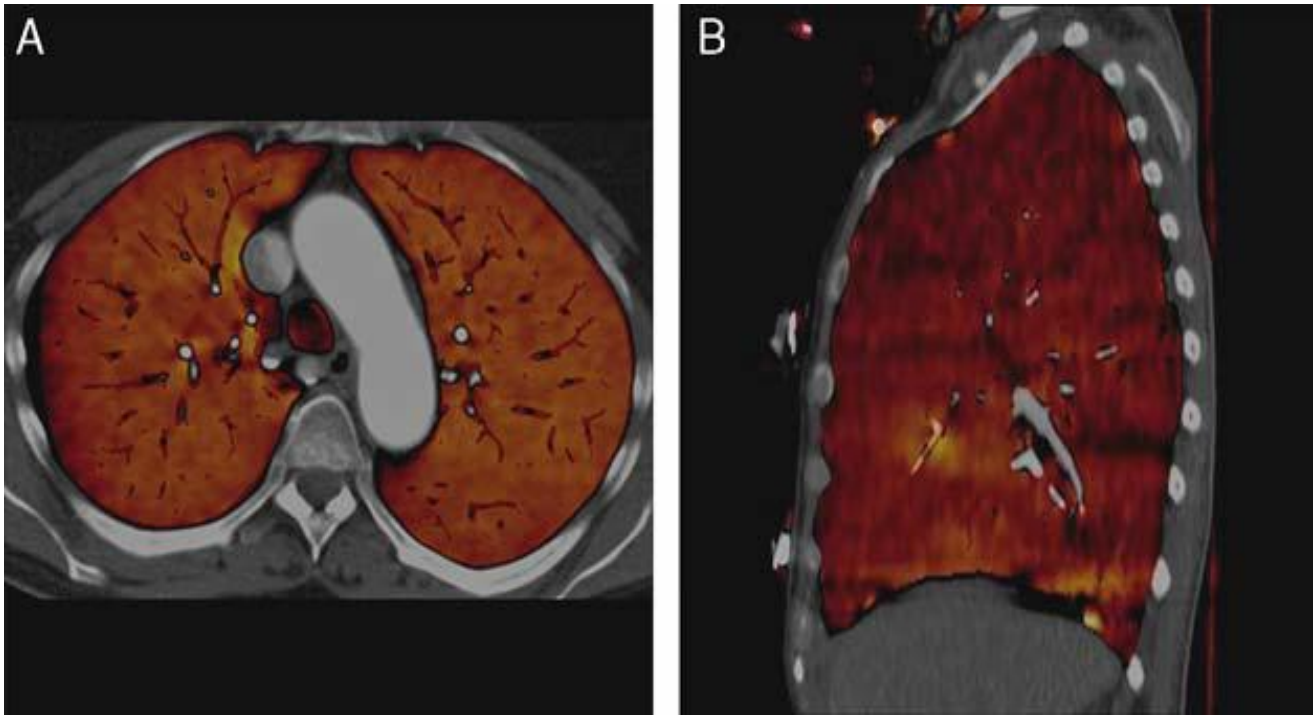

Figure 8: Axial (A) and sagittal (B) dual energy CT. Iodine map shows homogenous perfusion signal intensity in keeping with no pulmonary embolism (attenuation range of −960 HU and −600 HU)[17]

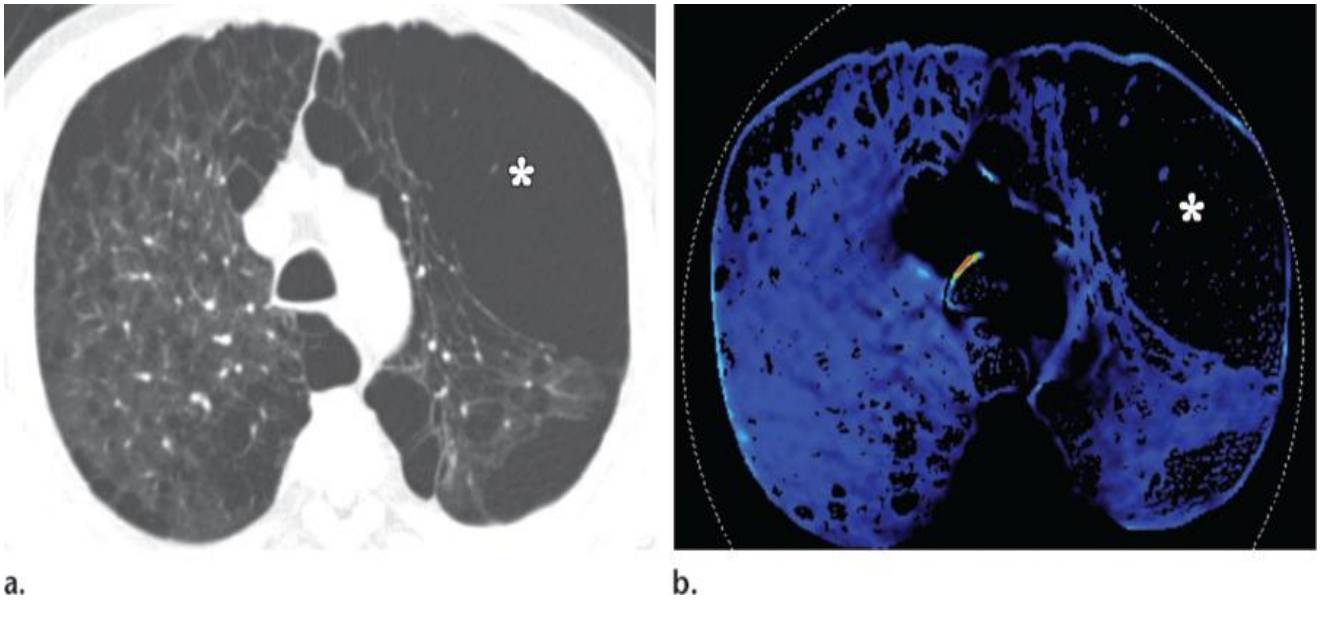

Figure 9: (a) CT (lung window) shows severe bullous emphysema especially in the left upper lobe (*) (b) Image from xenon ventilation CT shows a ventilation defect in the area of emphysema (*)[13]

Cardiac gated CT techniques minimises imaging artifacts caused by cardiac motion and improve temporal resolution of the images. The imaging data from the same point in the cardiac cycle at every heart beat are then combined together to create a 3D volume for each desired cardiac phase.

High Resolution Computed Tomography (HRCT) is commonly used to evaluate diffuse infiltrative lung disease. By using a thin-section CT with narrow collimation, smaller field of view and a higher spatial resolution (edge-enhancing) algorithm, HRCT provides very fine architectural details of the lung morphology up to the level of pulmonary lobules.

Lastly, computer-aided diagnostic or CAD tools provide a computer output to assist in CT image interpretation by improving the accuracy and consistency of radiological diagnosis and also by reducing the image reading time.

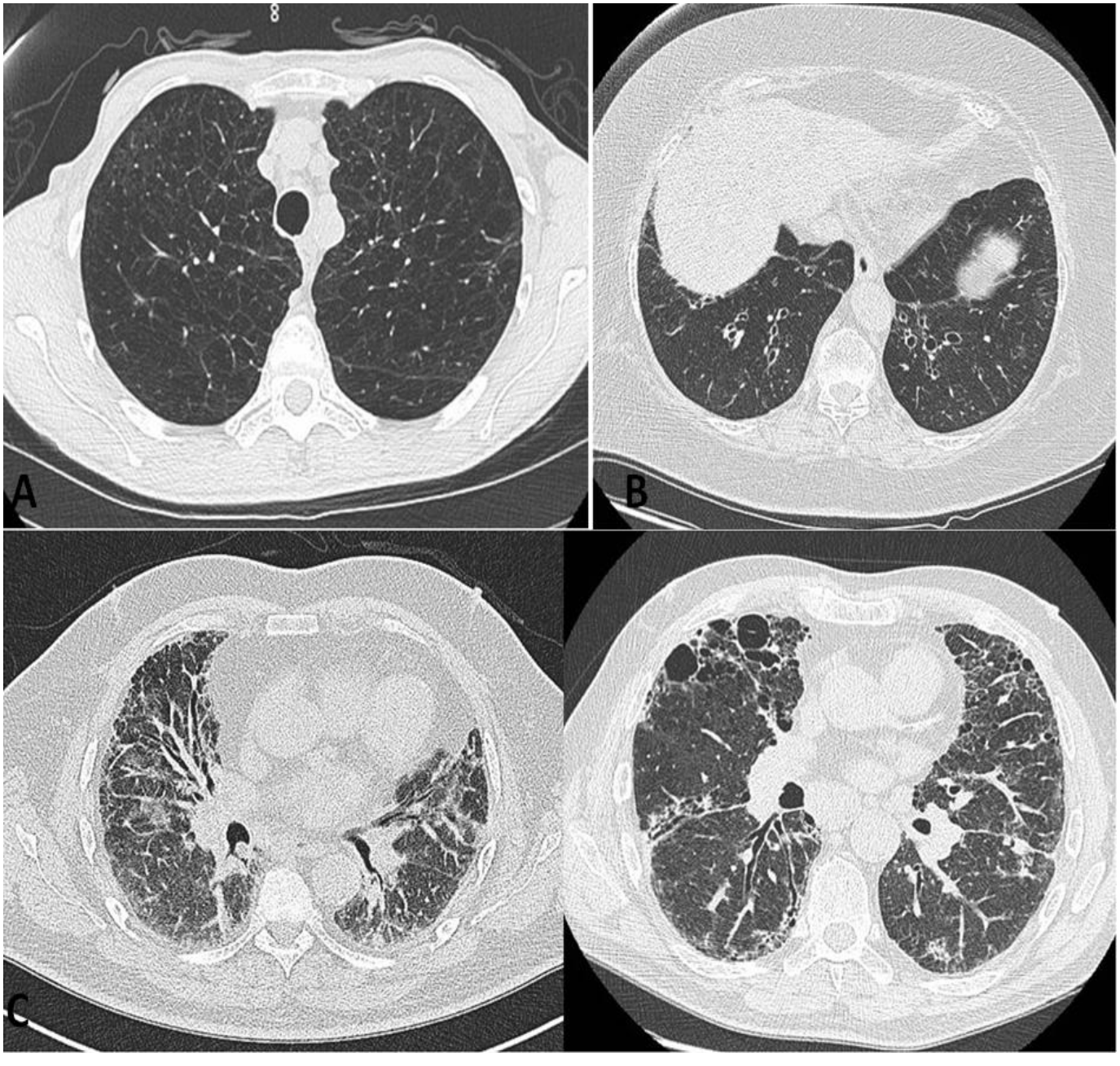

Figure 10: (A) Bilateral panlobular emphysema, (B) bronchiectasis **and (C)**fibrosis

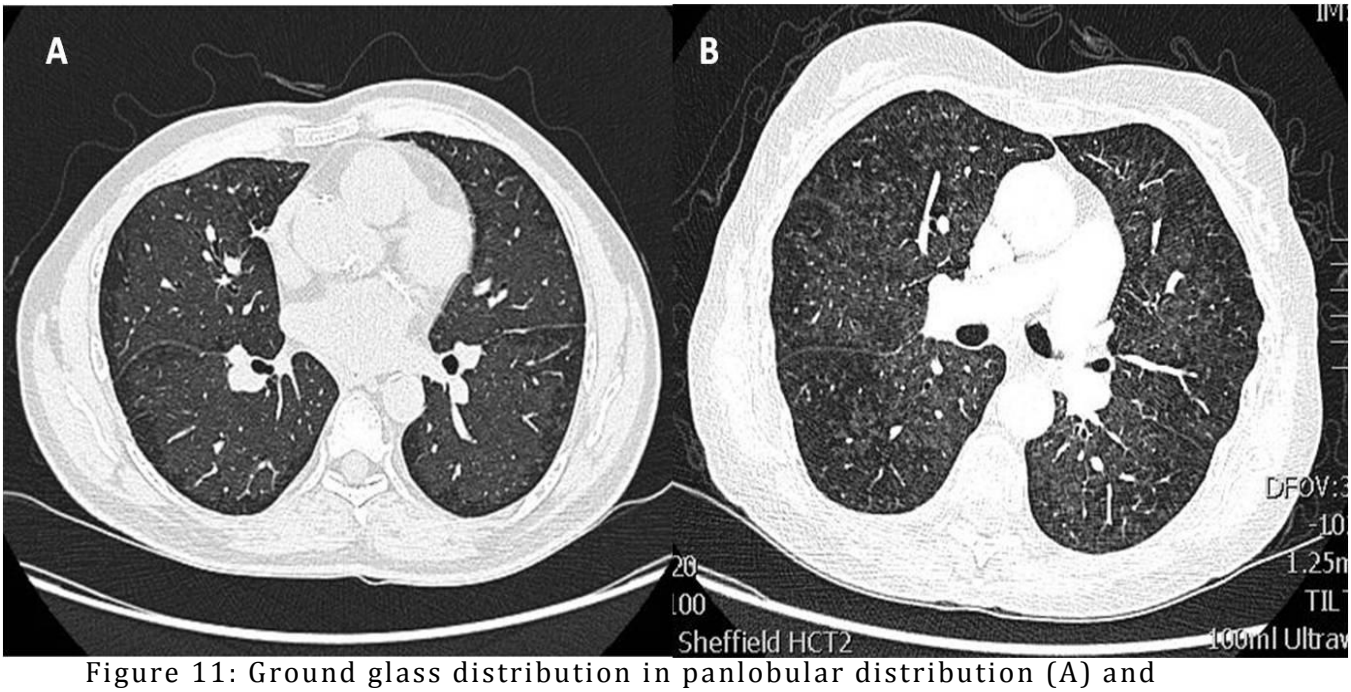

Figure 11: Ground glass distribution in panlobular distribution (A) and centrilobular distribution (B)

1.1.4 Invasive pulmonary angiography

In recent years digital subtraction angiography (DSA) has replaced conventional X-ray angiography. This modality was previously considered to be the definitive diagnostic test for imaging the pulmonary vasculature and some centres consider it to be the 'gold standard' in the diagnosis of pulmonary vasculature disorders such as chronic thromboembolic disease and pulmonary arteriovenous malformations [18]. With the advent of non-invasive modalities such as CT and MR pulmonary angiography which provide complementary structural and function information, DSA is increasingly being confined to image guided interventions and specialist pulmonary vascular centres. It is performed following injection of iodinated contrast agent usually using a 7-French catheter usually via internal jugular approach. The radiation dose with this technique is approximately 6 mSv compared to 4 mSv for a CTPA [19].

The main disadvantage of this technique is that the acquisition of high-quality images and the interpretation of angiograms can be challenging. In addition, this

is an invasive catheter examination associated with local complications and a quoted mortality of 0.5% [20].

Figure 12: Digital subtraction angiography

1.1.5 Magnetic Resonance Imaging

This section gives a brief outline of the qualitative and functional information that are possible with cardiac and pulmonary MR imaging, details of which are elaborated in **section 1.2.5** of Introduction (under MRI) and in **section 2.7** of Methodology.

The diagnostic potential of MRI was first suggested by Damadian in 1977 with reports that cancerous tissue can be differentiated from normal tissue using MRI [21]. This motivated the development of MRI for medical use.

The inherent excellent soft-tissue contrast with superior temporal and spatial resolution has led cardiac MRI to occupy a valuable niche in the diagnosis of various congenital and acquired cardiovascular disorders. These include imaging of the pericardium in constrictive cardiac syndromes, defining the anatomy in congenital heart disease and characterisation of cardiac tumors.

Cardiac MRI offers global and regional analysis of ventricular morphology and function such as the ventricular volume, ejection fraction and ventricular wall motion. Flow velocities and volume of blood passing through vessels or cardiac valves can be quantified by encoding the MRI signal phase for velocity and this technique (phase contrast MRI) allows quantification of cardiac output and intra-cardiac shunts. Using contrast enhancement techniques assessment of myocardial perfusion and myocardial viability is made feasible. In MRI, the blood can be made to appear both darker and lighter compared to surrounding tissue which assists in structural analysis of the heart and pulmonary vasculature.

3D contrast enhanced MR angiography is most commonly applied for imaging the pulmonary vasculature. This technique utilises the T1 shortening effect of gadolinium chelate contrast agents and by combining with parallel imaging technique and high gradient strength system the pulmonary vasculature can be imaged in a short breath-hold time. A high spatial resolution can be achieved by following a monophasic single breath-hold protocols or by using time resolved multiphase sequence to study regional haemodynamics and perfusion.

MRI is also used as a problem solving tool in the assessment of mediastinal and chest wall abnormalities particularly to evaluate tumours or lesions for mediastinal or chest wall extension [22].

MR imaging for the assessment of the lung parenchyma is challenging. This is principally because of the poor inherent proton density of normal lung tissue resulting in low signal to noise ratio (SNR). Secondly, there is degradation of the signal from the lung parenchyma due to T2* dephasing from magnetic susceptibility gradients at the air-soft tissue interfaces [23]. Finally suboptimal image quality also results from cardiac pulsation and breathing motion.

1.1.6 Radiation concerns

There are several ways to quantify radiation exposure and the most commonly used measurement is the *Effective dose*. Effective dose is an estimation of the whole-body dose that would be required to produce the same risk as the partial-body dose that was actually delivered in a localized radiologic procedure [24]. The below table gives the estimated effective doses for various imaging investigations related to the thorax.

Table 1: Comparison of effective doses

Procedure	Effective Dose(mSV)
Chest radiograph	0.05 – 0.1
V/Q scan	1.2 – 2.0
Q scan	0.8 - 1
High resolution CT with 10mm intersection gap	0.7
Chest CT low dose	1.5
SPECT lung perfusion imaging	2- 3
Digital pulmonary angiography	6.0
Conventional chest CT/ CTPA	7.0- 12
Annual background radiation dose	2.5

[24-26]

Advances in imaging techniques have revolutionised medical imaging and in the last 20 to 30 years there has been a considerable increase in the number of imaging investigations performed. Since the turn of the century there has been a two-fold increase in the number of CT examinations [24] and CT alone accounts for around 68% of the total radiation dose from diagnostic imaging [27].

This level of increase in radiation exposure from diagnostic radiology is of a growing concern particularly in children, pregnant mothers and patients needing frequent imaging for therapy follow up for example. It is well established through epidemiological and experimental evidence that exposure to ionizing radiation,

even at low doses, is linked with the development of leukaemia and solid cancers [28]. According to a *risk-model* developed by the Biological Effects of Ionizing Radiation (BEIR) VII 'one individual in 1000 would develop cancer from an exposure to effective dose of 10 mSv and one individual in 100 persons would be expected to develop cancer from 100 mSv' [29]. USA based studies have also estimated that 1%–2% of all cancers in the future will be caused by CT examination [30-31]. Although no prospective epidemiologic study that has quantified adverse effects of low dose radiation exists up-to-date, the above reports show the extent of radiation concern. Radiation exposure has also been associated with increased risk of cardiovascular disorders and benign tumors [29].

A commonly encountered scenario in clinical practice is analysed below from the radiation dose point of view. A pregnant woman may present with a suspected Pulmonary Embolism (PE) and V/Q scintigraphy and CTPA are among the investigations to rule out PE. The fetal radiation exposure for CTPA varies from 0.003-0.13 mSV with the additional dose to maternal breast tissue [32]. With V/Q scan the whole-body dose is lower than CT (1.2–2.0 mSv), however the estimated dose to the fetus from a V/Q scanning is three times higher than for CTPA (0.1-0.37 mSV) [33-34]. The risk for maternal cancer is and the risk to the fetus is. This example gives an idea of the radiation exposure and highlights the need for alternative radiation free modality for high risk population. This is the motivation for much of the work presented in this thesis.

As the growth in CT utilization increase and the concern about the population dose from CT began to be expressed and subsequently newer dose reduction strategies have emerged. Filtered back projection, iterative reconstruction algorithm and adjusting KV based on patient size are few such techniques. Of these dose reduction methods the most noted is the iterative reconstruction which allows dramatic improvements in image quality [35].

1.2 Overview of Pulmonary hypertension

1.2.1 Introduction

Pulmonary hypertension (PH) is a debilitating condition of the pulmonary vasculature and was first described in 1891 by a German physician E. Romberg when he noticed the thickening of the pulmonary artery in the absence of heart or lung disease at autopsy. It is now a collective term used for a group of disorders that result in elevation of the pulmonary artery pressure eventually leading to right ventricular dysfunction. According to the current internationally agreed guidelines, PH is defined as an increase in mean pulmonary arterial pressure (PAP) of at least 25 mmHg measured at right heart catheterization [36].

The pathogenesis of pulmonary arterial hypertension (PAH) is complex and has been attributed to several factors. Three basic mechanisms; vasoconstriction, remodelling of the pulmonary vessel wall and thrombosis [37] contribute to dysfunction of the pulmonary vascular endothelium, with an in balance of pulmonary vasoconstrictors and vasodilators resulting in an increase the pulmonary vascular resistance (PVR).

According to a USA National Institutes of Health registry and published in 1987, the annual incidence of primary PH now known as idiopathic pulmonary arterial hypertension (IPAH) was 1–2 cases per million population [38]. The French national registry recorded data from 17 French centres between 2002 and 2003 quoted an annual incidence of pulmonary arterial hypertension (PAH) as 2.4 cases per million population [39]. More recently the incidence of PAH in Europe was estimated at 7.6 cases per million population and this is based on the data from Scotland and other European countries [40].

1.2.2 Classification

A variety of disorders with diverse aetiology can result in PH and the classification of pulmonary hypertension has undergone a series of changes over the years [41]. Initially it was classified into two simple categories, primary PH and secondary PH depending on whether a cause was identified. The most recent classification was proposed during the 4th world symposium in Dana point in 2008 to group together different conditions with similar clinical features, pathobiological process and therapeutic approaches. This classification is shown in table 2 [42].

Table 2: Updated Clinical Classification of Pulmonary Hypertension from 4th World symposium (Dana Point, 2008)

1 Pulmonary arterial hypertension (PAH)
1.1 Idiopathic PAH
1.2 Heritable
1.2.1 BMPR2
1.2.2 ALK1, endoglin (with or without hereditary hemorrhagic telangiectasia)
1.2.3 Unknown
1.3 Drug- and toxin-induced
1.4 Associated with
1.4.1 Connective tissue diseases
1.4.2 HIV infection
1.4.3 Portal hypertension
1.4.4 Congenital heart diseases
1.4.5 Schistosomiasis
1.4.6 Chronic hemolytic anemia
1.5 Persistent pulmonary hypertension of the newborn

1' Pulmonary veno-occlusive disease (PVOD) and/or pulmonary capillary hemangiomatosis (PCH)

2 Pulmonary hypertension owing to left heart disease
2.1 Systolic dysfunction
2.2 Diastolic dysfunction
2.3 Valvular disease

3 Pulmonary hypertension owing to lung diseases and/or hypoxia
3.1 Chronic obstructive pulmonary disease
3.2 Interstitial lung disease
3.3 Other pulmonary diseases with mixed restrictive and obstructive pattern
3.4 Sleep-disordered breathing
3.5 Alveolar hypoventilation disorders
3.6 Chronic exposure to high altitude
3.7 Developmental abnormalities

4 Chronic thromboembolic pulmonary hypertension (CTEPH)

5 Pulmonary hypertension with unclear multifactorial mechanisms
5.1 Hematologic disorders: myeloproliferative disorders, splenectomy
5.2 Systemic disorders: sarcoidosis, pulmonary Langerhans cell histiocytosis: lymphangioleiomyomatosis, neurofibromatosis, vasculitis
5.3 Metabolic disorders: glycogen storage disease, Gaucher disease, thyroid disorders
5.4 Others: tumoral obstruction, fibrosing mediastinitis, chronic renal failure on dialysis

[42]

1.2.3 Pathophysiological imaging characteristics

The right ventricular function and mechanics play a central role in PH and determine the patients' capability to cope with the disease. The normal pulmonary vascular bed is a low pressure system with low vascular resistance. In patients with PH pressure is chronically raised and increases the afterload to the right ventricle (RV). At this stage the RV undergoes remodelling with adaptive hypertrophy of its wall and attempts to counteract the increased afterload by increasing systolic RV contraction.

This process, however, cannot be sustained and eventually the RV decompensates. The RV begins to dilate and the normal thin walled 'crescent' shape cavity is replaced by a dilated 'spherical' RV. The RV contractility falls and there is an increase in RV volume. Dilatation of the RV chamber leads to dilatation of the tricuspid annulus causing functional tricuspid regurgitation, further exacerbating dilatation. This also shifts the inter-ventricular septum, initially causing flattening and eventually shifting it towards the left ventricle. The normal synchronous interaction of the LV and RV is lost. This process affects the filling of the LV and further compromises the ventricular perfusion. The impairment in RV perfusion further affects the RV function and the vicious cycle eventually ends in RV failure and eventually death.

In patients with pulmonary arterial hypertension remodelling of small pulmonary arteries with proliferation of endothelial cells and smooth muscles play a major role in the pathogenesis of the disease [43]. This abnormal proliferation of endothelial cells results in plexiform lesions [44].

The exact pathophysiology of chronic thromboembolic pulmonary hypertension (CTEPH) still remains unclear. Initially it was thought to be associated with obstruction in larger pulmonary vessels from pulmonary embolism. More recently it has been suggested that CTEPH may be the result of primary arteriopathy and endothelial dysfunction that causes in-situ thrombosis in the lung [45-47]. This theory explains why majority of patients with CTEPH have no history of acute PE [48].

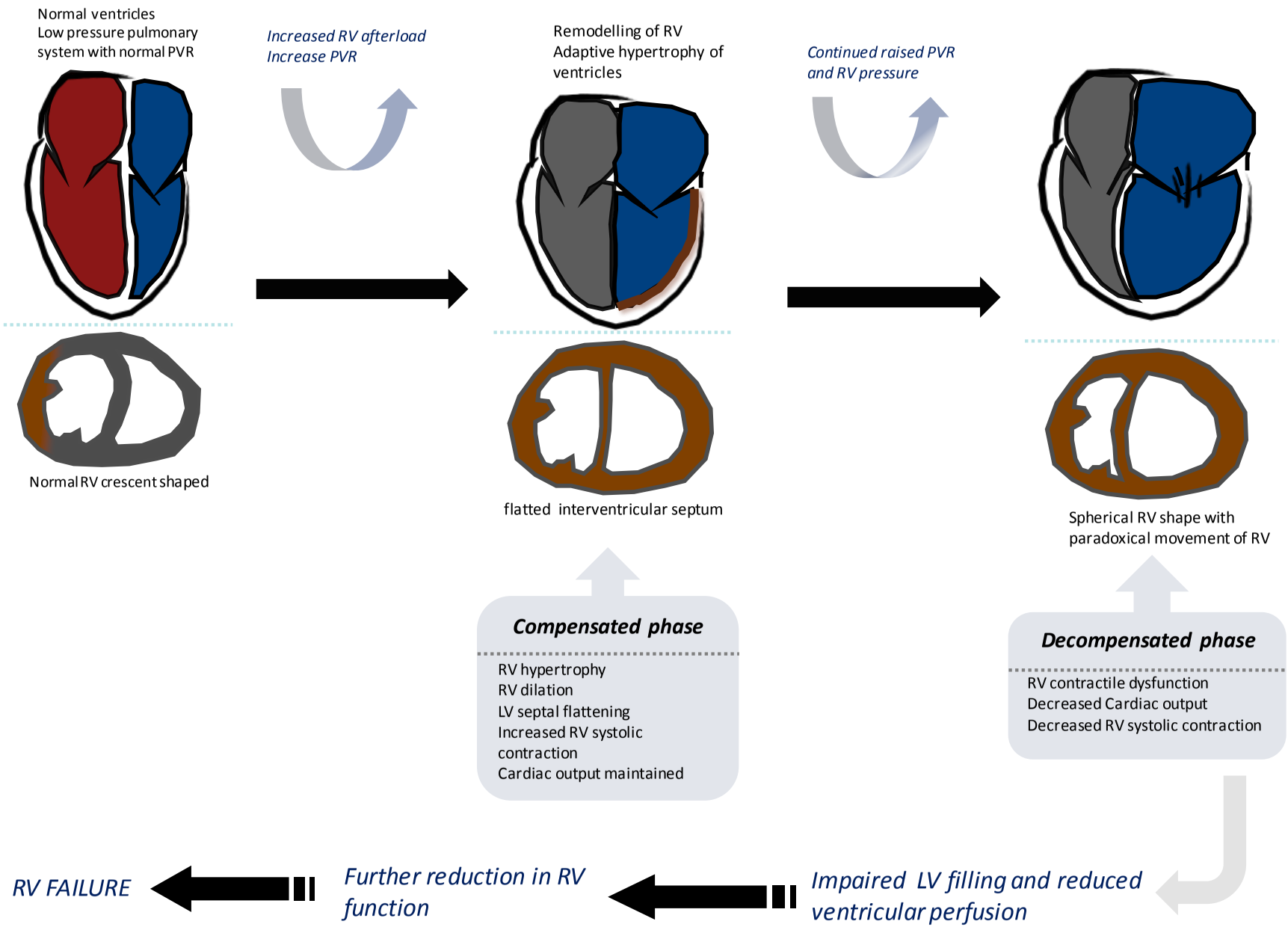
Normal ventricles
Low pressure pulmonary system with normal PVR
Increased RV afterload
Increase PVR
Remodelling of RV
Adaptive hypertrophy of ventricles
Continued raised PVR and RV pressure
Normal RV crescent shaped
flatted interventricular septum
Spherical RV shape with paradoxical movement of RV
Compensated phase
RV hypertrophy
RV dilation
LV septal flattening
Increased RV systolic contraction
Cardiac output maintained
Decompensated phase
RV contractile dysfunction
Decreased Cardiac output
Decreased RV systolic contraction
Impaired LV filling and reduced ventricular perfusion
Further reduction in RV function
RV FAILURE

1.2.4 Clinical work-up of patients with suspected pulmonary hypertension

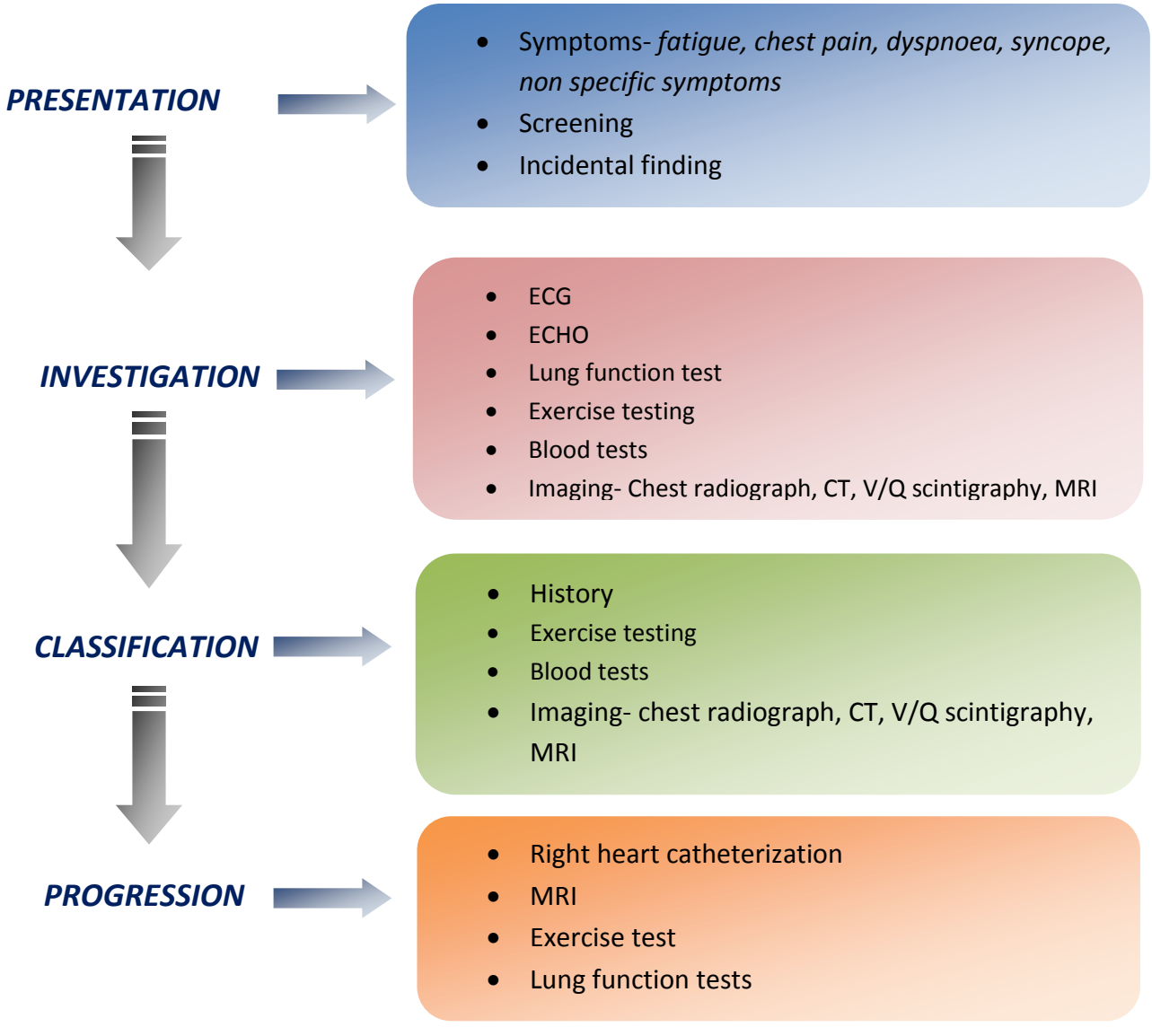

1.2.5 Imaging techniques

Imaging plays a central role in the assessment of patients with PH as it helps to confirm diagnosis, clarify clinical subgroup and determine the underlying cause for PH. More importantly, it also evaluates degree of ventricular dysfunction and extent of haemodynamic impairment, thereby providing valuable information on severity of the disease and aids in non-invasive follow up that is reproducible. This section gives an outline of imaging findings seen in patients with PH.

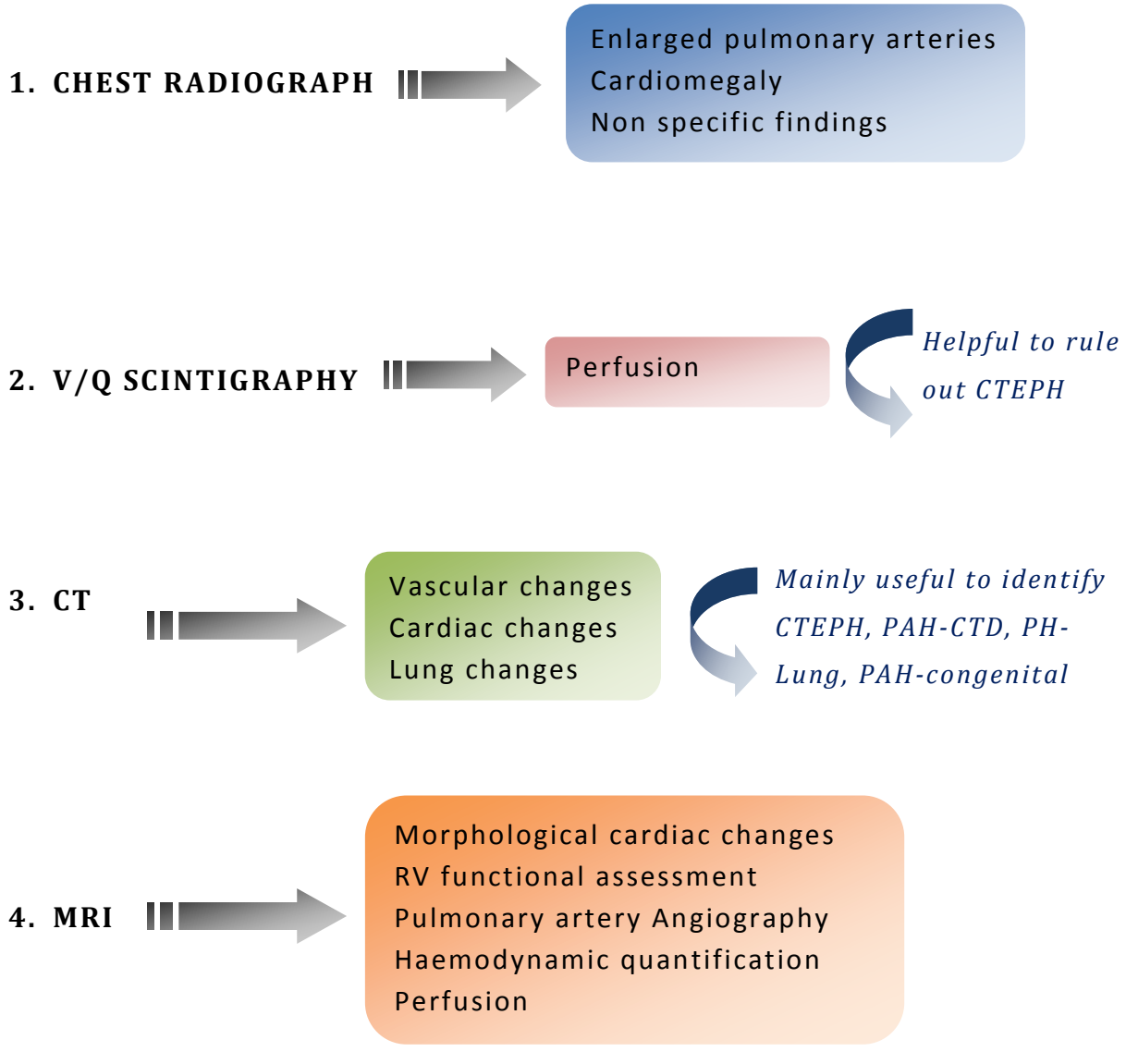

Right heart catheterization:

The current 'gold standard' method for assessing PH is right heart catheterization (RHC) and based on RHC measurement PH is defined as mean pulmonary artery pressure (mPAP) greater than or equal to 25 mmHg [42]. RHC is performed using a Swan-Ganz catheter guided into the right side of the heart either via the internal jugular vein or femoral vein approach. Pressure measurements are made at the level of the right atrium, right ventricle and pulmonary artery.

Pulmonary capillary wedge pressure (PCWP) is measured by occluding the distal branch of the pulmonary artery with the catheter tip which is then assumed to be reflective of left atrial pressure.

Fick and thermo-dilution are two methods of measuring cardiac output. Thermo-dilution is an indicator dilution method and is based on the principle that when an indicator dye is added to circulating blood, the rate of blood flow is inversely proportional to the change in concentration of the indicator dye over time. The Fick method is based on principle that the rate of oxygen consumption is a function of rate of blood flow and the rate of oxygen picked up by the red blood cells. In this method the oxygen concentration of the venous blood and the arterial blood is used to calculate the oxygen consumed over a given period of time. Pulmonary vascular resistance (PVR) is calculated as follows using measurements made at RHC.

$$\text{PVR} = \frac{\text{mPAP}-\text{PCWP}}{\text{CO}}$$

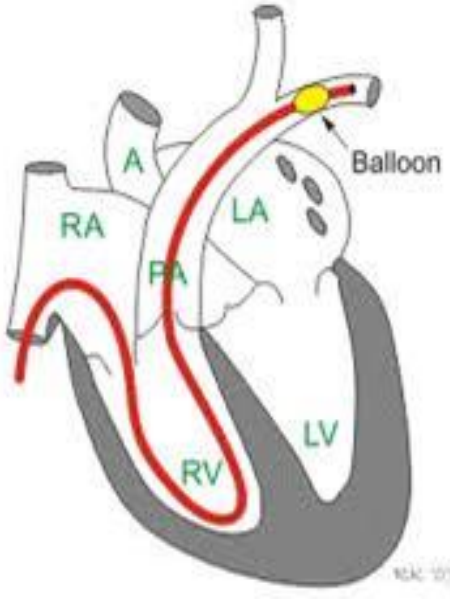

Vasoreactive testing determines how much the pulmonary blood vessel relax over a brief period of time and its main purpose is to identify patients who might respond favourably to calcium channel blockers. It also has prognostic value as patients who have significant acute vasodilator responses have a better prognosis than non-responders. Medications used to perform acute vasodilator testing include inhaled nitric oxide and intravenous epoprostenol. A drop in mean pulmonary artery pressure of at least 10 mm Hg (or 20%) to below 40 mm Hg is considered significant as suggested by the American College of Chest Physician Guidelines.

During RHC a left-to-right shunt may be also be detected and localized if there is a significant step-up in blood oxygen saturation. This is performed by measuring the oxygen saturation in blood samples drawn sequentially from the pulmonary artery, right ventricle, and right atrium, superior and inferior vena cava.

Biomarkers:

Blood biomarkers have proven to be strong non-invasive tools in the assessment of patients with PH. The most important biomarker is brain natriuretic peptides (BNP) and has been widely evaluated for its usefulness in the assessment of RV function. NT-proBNP is the preferred molecule for analysis as it has a longer half-life and superior stability. It has been shown to correlate with the RV systolic dysfunction in patients with PAH and has proven to be a strong predictor of adverse outcome [49]. Other markers with potential diagnostic and prognostic sensitivity include Troponin T, endothelin, inteleukins, osteoprotoglycin and uric acid [50].

Chest radiograph:

Chest radiography is routinely performed in all patients presenting with cardio-respiratory symptoms. However it is usually at a later stage of the disease process that typical radiographic changes of pulmonary hypertension become apparent. These include dilated central pulmonary arteries with pruning of peripheral branches and cardiomegaly specifically, right-sided chamber dilatation [51]. Several non-specific features such as lung disease are also evident on a chest radiograph and is helpful in pointing towards a particular subtype of pulmonary hypertension.

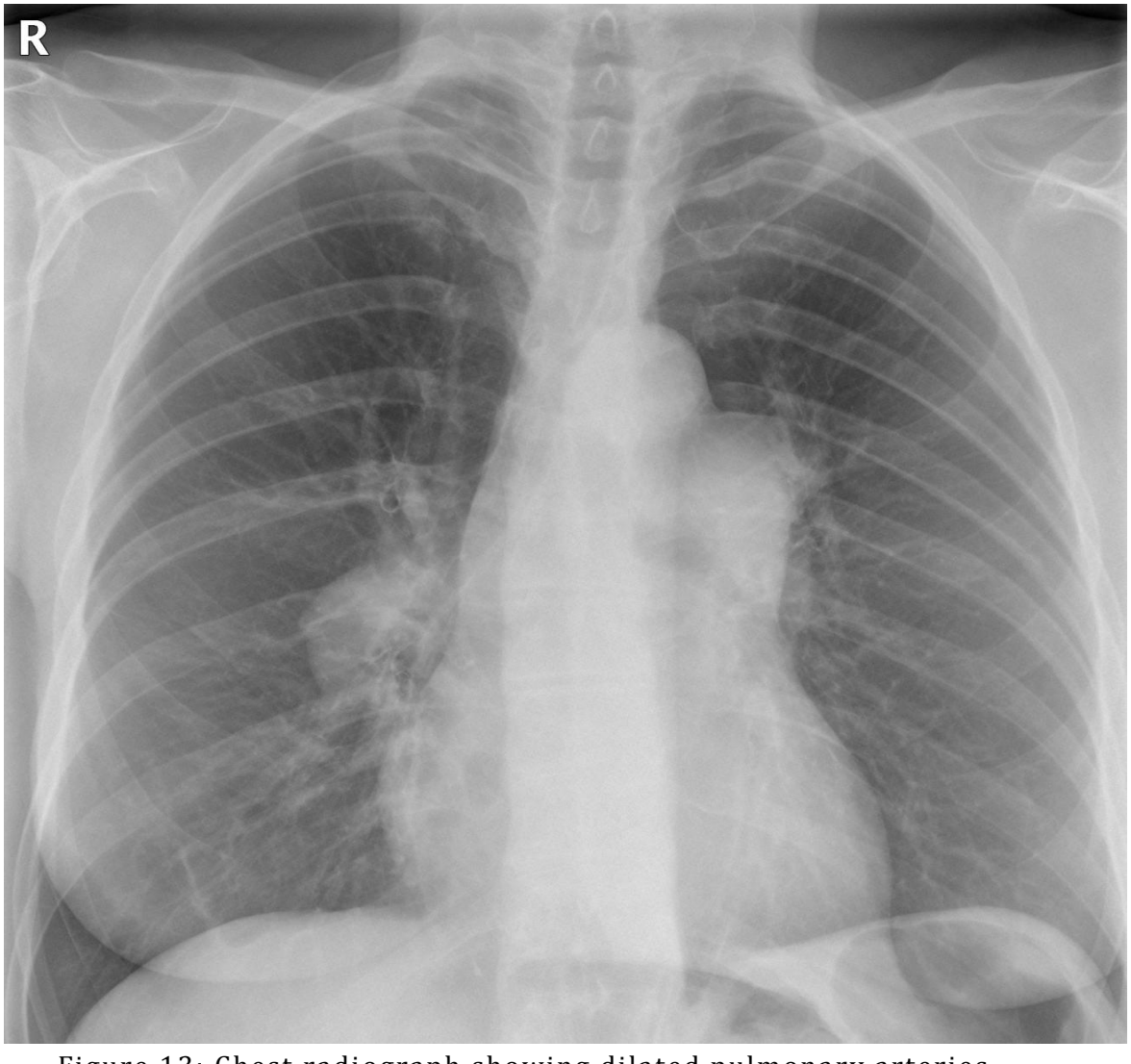

Figure 13: Chest radiograph showing dilated pulmonary arteries

Ventilation perfusion scintigraphy:

Ventilation perfusion (V/Q) scintigraphy has traditionally been used to rule out CTEPH in patients suspected with pulmonary hypertension. Mismatched 'wedge shaped' or segmental perfusion defects diagnosed using modified PIOPED criteria is classically seen in CTEPH [52-53]. Studies have shown that as a simple screening tool perfusion scintigraphy has a very high negative predictive value (98%) [54], but a large proportion of the scans are indeterminate and the

examination becomes inconclusive. V/Q scintigraphy also understates the extent and severity of hemodynamic dysfunction in CTEPH [55].

Patients with idiopathic pulmonary arterial hypertension (IPAH) sometimes demonstrate 'mottled' patchy subsegmental areas of reduced perfusion that are non-segmental in distribution [56]. These findings however are non-specific to IPAH as they also occur with connective tissue disease, pulmonary veno-occulsive disease and pulmonary vasculitis [57]. V/Q scintigraphy is of limited value in patients with lung disease as the distorted lung architecture obscures the pattern of perfusion defects.

Computed Tomography:

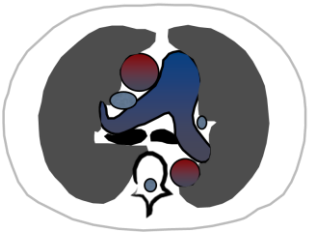

VASCULAR SIGN
Pulmonary artery size
Pulmonary artery aorta ratio
Dilated bronchial and non-bronchial collaterals
Pulmonary artery distensibility (ECG gated)

CARDIAC SIGN
Right to left ventricle ratio
Right ventricle wall thickness
Dilated right atrium and ventricle
Configuration of the interventricular septum

PARENCHYMAL SIGN
Ground glass lung nodules
Mosaic pattern of lung perfusion
Pulmonary infarction
Pulmonary haemorrhage
Features of lung disease Eg emphysema

Vascular signs:

A well established sign of pulmonary hypertension is the size of pulmonary artery (PA). This sign has been exhaustively studied and a transverse PA diameter of greater than 29 mm on axial CT has a very high positive predictive value (97%) for identifying PH [58]. Similarly a larger pulmonary artery diameter compared to the adjacent ascending aorta (pulmonary artery-aorta ratio of greater than 1) is also a sign of PH. This measurement has been shown to correlate, to a varying degree, with mean pulmonary artery pressure and pulmonary vascular resistance (mPAP r=0.626, p=0<.0001) [59]. Revel et al analysed ECG gated-cardiac CT and showed decrease in the distensibility of the main pulmonary artery was not only a marker of PH but also strongly correlated with the severity of the disease [60]. In PH, there is increased blood flow in the bronchial and non-bronchial arteries and this shunting cause vessel dilatation. Dilated bronchial, perihilar and mediastinal collaterals are commonly seen in patients with CTEPH, IPAH and PAH associated with congenital heart disease. The classical CTPA findings of CTEPH are mural thrombosis, stenosis, occlusion, post stenotic dilatation, webs and bands and calcification in the pulmonary arteries. In CTEPH, patients with dilated bronchial arteries show significantly better outcome and lower pulmonary vascular resistance following pulmonary endarterectomy compared to patients without dilated bronchial vessels [61]. Another distinctive CT vascular sign in patients with Eisenmenger syndrome is presence of neovascularity which are tiny, serpiginous intrapulmonary vessels [62].

Figure 14: Dilated pulmonary arterial trunk - a typical feature of Pulmonary hypertension

Cardiac signs:

PH related effects on the heart, which are readily appreciated on a standard CT, are rarely seen in the early stages of the disease. Features of right ventricular compromise that are evident on CT include dilatation of the right sided cardiac chambers, hypertrophy of right ventricle (defined as wall thickness of more than 4 mm) [63], and paradoxical bulging of the interventricular septum towards the left ventricle [64-65]. Reflux of contrast into the inferior vena cava and hepatic veins on contrast enhanced CT is considered to be a marker of tricuspid regurgitation. A semiquantitative system to grade tricuspid regurgitation on CT, devised by Groves et al, showed good correlation with RHC derived systolic pulmonary artery pressure ($r=0.69$, $p<0.001$) [66]. Finally, features of left

ventricular failure such as pleural and pericardial effusions and interstitial oedema and of right ventricular failure such as ascites and hepatic congestion are also evident on CT.

The use of ECG gated-cardiac CT allows more accurate quantification of ventricular function. Revel et al analysed RV outflow tract and quantified RV shortening and myocardial thickness on a cardiac-gated CT and showed significant difference between patients with and without PH [60]. Simon et al quantified regional RV wall hypertrophy and concluded that there are significant phenotypic abnormalities in the right ventricle in patients with PH even in the absence of overt hemodynamic RV decompensation [67].

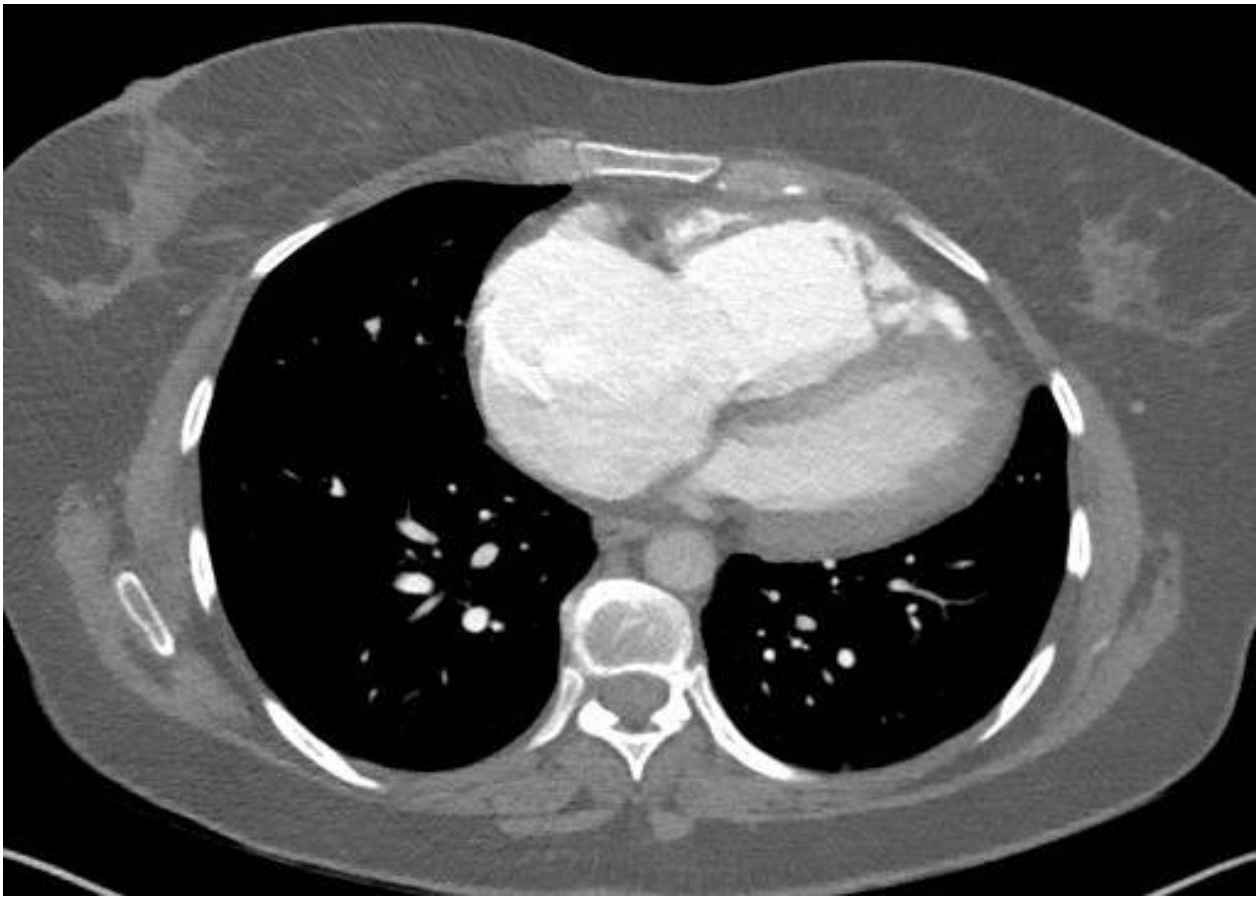

Figure 15: Dilated right atrium and ventricle with posterior displacement of interventricular septum and hypertrophy of the RV free wall

Parenchymal signs:

Ground glass nodules, defined as areas of increased attenuation that does not obscure vessels, is a documented finding in patients with PH [68-69]. The histology of these ground glass changes is poorly understood; one study in patients with Eisenmenger's syndrome demonstrated centrilobular ground glass opacities (GGO) to correlate with dilated capillary networks in alveolar spaces [62] while another isolated study showed them to represent cholesterol granulomas [70]. The distribution of GGO varies in PH. The GGO are seen in patients with IPAH and also been described in patients with pulmonary veno-occulsive disease and pulmonary capillary haemangiomatosis. Interesting, in these group of patients centrilobular GGO have been also shown to correlate with poor therapeutic outcome [71].

Other lung parenchymal changes such as pulmonary infarction, intrapulmonary haemorrhage and segmental mosaic pattern of lung attenuation are seen in high proportion of patients with CTEPH and congenital heart disease associated PAH than in other forms of PH [72].

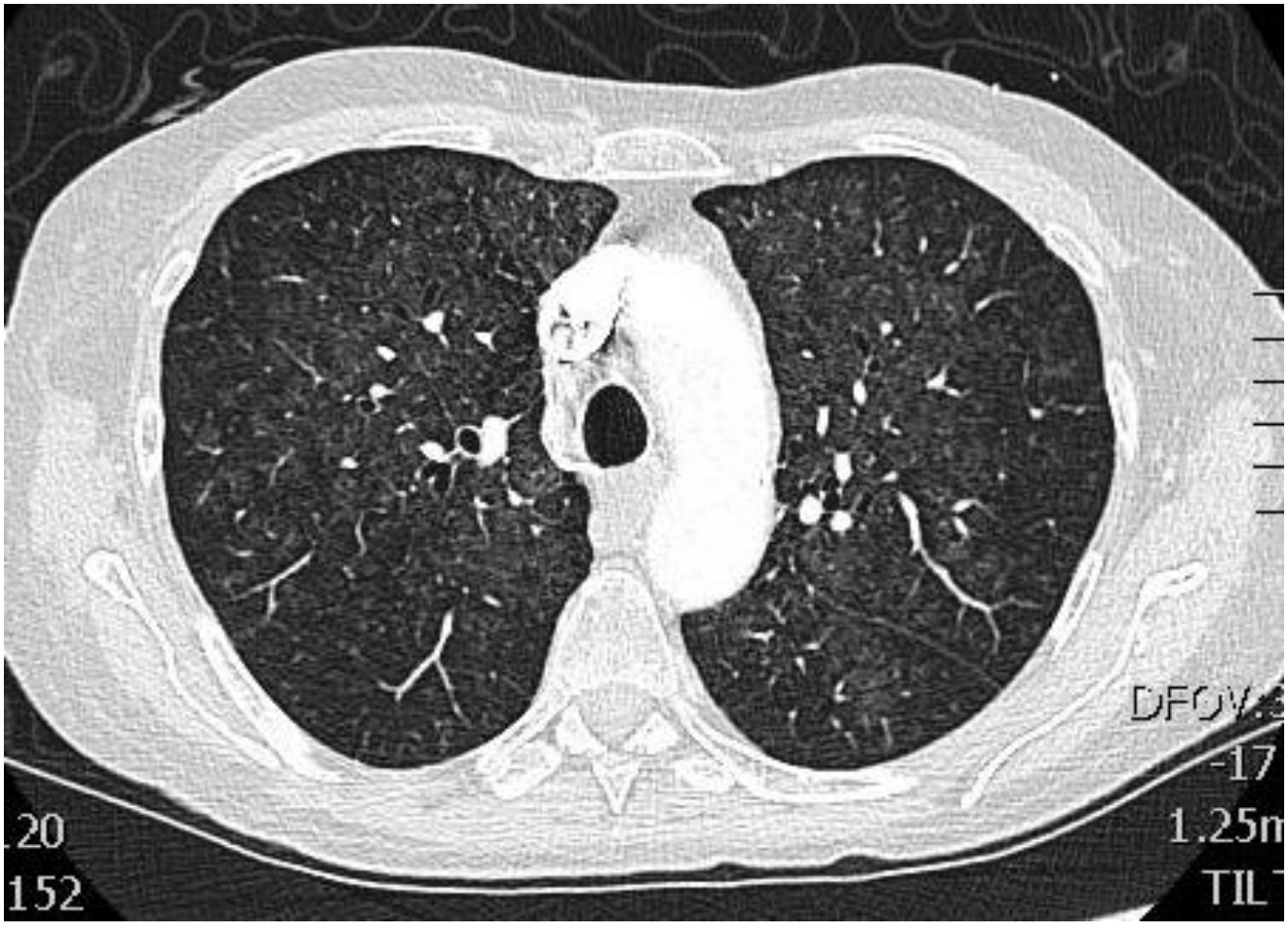

Figure 16: Centrilobular pattern of ground glass nodules

MRI:

MRI is considered as the gold standard for functional and morphological assessment of the heart. The strength of cardiac MRI includes superior spatial, temporal and contrast resolution. The unlimited spatial orientation and 3D data information of MR is similar CT which has high spatial resolution and MPR image reconstruction. Moreover it is non-invasive, does not involve ionizing radiation and is easily reproducible. So it is not surprising that there has been a growing interest in its utility as a diagnostic and prognostic tool in PH [73]. There are several sequences involved in imaging patients suspected with PH and each of these can provide haemodynamic and structural insight into the disease process.

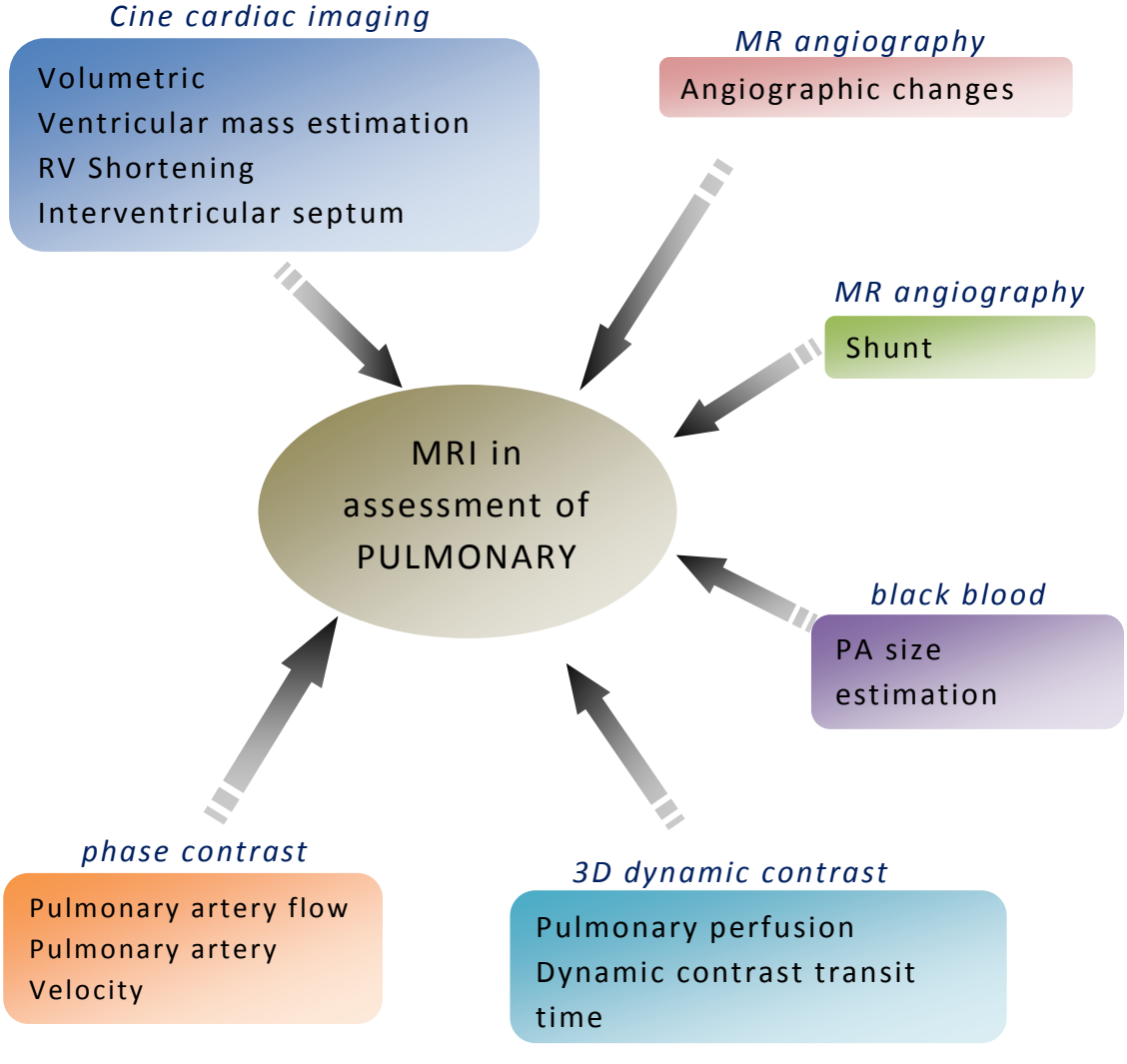

Ventricular volumes and *ejection fraction* can be accurately calculated with cine cardiac imaging and these MR measurements reflect RV function in patients with PH [74-75]. The prognostic importance of these measurements was demonstrated in one study which showed large RV volume (RV end-diastolic volume index ≥84 ml/m2) and low stroke volume (stroke volume index ≤25ml/m2) independently predicted mortality [76] and in another which proved stable or increase in RV ejection fraction (RVEF) (Hazard ratio of 0.929; $p<0.014$) to be associated with survival [77].

Right ventricular mass is routinely measured in patients with PH and ventricular mass index (VMI), which is the ratio of right and left ventricular end diastolic mass, has been correlated with pulmonary vascular resistance and mean pulmonary artery pressure [78-79]. A study by Hagger et al also suggested prognostic significance of high VMI in subset of patients with pulmonary arterial hypertension associated Systemic Sclerosis [78].

Simple semi-quantitative assessment of RV function can be made by measuring the longitudinal and transverse shortening of the RV. Kind et al concluded that compared to longitudinal motion (TAPSE-tricuspid annular systolic excursion), transverse motion of the mid RV show a stronger relationship with RVEF ($R^2=0.70$, $p<0.001$) [80]. A more recent study on the other hand showed improvement in the RV function following vasodilator therapy occurred solely with improvement of the longitudinal RV motion [81].

As a result of reduction in the transeptal pressure gradient in patients with PH there is flattening or paradoxical motion of the interventricular septum and several groups have qualitatively and quantitatively examined this finding. The paradoxical shift of the interventricular septum during diastole was shown to have a higher sensitivity (100%) for diagnosing PH compared to systole (sensitivity of 86%) when the mean pulmonary artery pressure was ≥30 mmHg [74]. Groups who quantified the configuration of interventricular septum concluded that MR–derived curvature ratio (inverse of the radius) reflects RV systolic pressure [82] and the curvature of the interventricular septum strongly correlate with systolic pulmonary artery pressure [75].

Imaging of the myocardium 10-20 minutes after gadolinium administration allows assessment of the myocardium for delayed enhancement. *Delayed myocardial*

enhancement (DME) occurs at the RV insertion points and is a frequent finding in patients with PH from varied etiologies [83]. It is postulated that in PH there is exaggerated disarray of myocardial fibres at the RV insertion points and DME occurs as a result of pooling of blood at these sites [84]. The extent of DME has been shown to correlate with MR derived RV indices such as VMI, mean pulmonary artery pressure, RVEF [85-86]. Sanz et al developed and validated a simple visual score for the extent of DME and showed results that were in agreement with previous studies [83]. The presence of DME at the RV insertion points in patients with PH is also a marker for more advanced disease and poor prognosis according to a recent study in 58 patients with PH [84].

Valuable quantitative data can be derived through *phase contrast imaging* of the pulmonary artery. These include pulmonary artery blood flow, velocity and areas and also evaluation of cardiac function such as the stroke volume. A study by Sanz et al demonstrated that both PA average velocity (of 11.7 cm/s) and minimum PA area (≥6.6 cm2) had a high sensitivity (93%) for detecting PH and also found excellent correlations between PA average velocity and mean PA pressure, systolic PA pressure and pulmonary vascular resistance (r of −0.73, −0.76, and −0.86) [87]. Blood flow pattern in the main PA differs in patients with PH compared to healthy people and early onset of retrograde flow in the PA is thought to be characteristic of PAH [88]. Abnormal stiffness in the PA is well recognised in PH and has been suggested to be a sensitive indictor of early PH [87]. These studies also suggest that pulmonary artery stiffness (defined by relative area change) relates to severity of disease [87] and might be useful prognostically [89].

Pulmonary flow artefacts occur as a result of slow flowing blood in the PA and are appreciated on a double inversion recovery black blood MR sequence. Our group has demonstrated this to be a valuable diagnostic as well as a prognostic tool in the assessment of patients suspected with PH [90].

3D contrast enhanced MR angiography is a well established technique for imaging the pulmonary arteries. The usefulness of contrast-enhanced MRA in the diagnostic work-up of CTEPH has been studied and the typical findings of CTEPH such as the presence of intraluminal webs and bands, vessel occlusions, and organized central thromboembolic material can be readily appreciated on MRA

[91-92]. In one study there was 86% agreement between MR angiography and DSA and/or CT angiography [93]. However MRA is not reliable for the diagnosing CTEPH at the subsegmental level as shown by the results of a small number of studies [91-92]. *Dynamic contrast enhanced 3D MR perfusion imaging* tracks the dynamic passage of contrast through the pulmonary circulation and has been quantitatively used to assess the severity of PH [94-97]. A recent study by Swift et al demonstrated its prognostic significance in patients with PAH [98]. Example of the MR images can be found in chapter 2.

1.2.6 Imaging characteristics

A systematic approach is required to evaluate patients presenting with features of pulmonary hypertension. Besides the typical features of PH described in the above section, there are certain characteristic features on imaging that point towards a certain clinical subgroups of the disease.

1.2.6.1 Group 1: Pulmonary Arterial Hypertension

Idiopathic Pulmonary arterial hypertension (IPAH): Patients with IPAH typically present with enlarged central pulmonary trunk often accompanied by dilated right and left main branches. The pulmonary vessels are usually diffusely tortuous with abrupt tapering (pruning) of segmental and sub-segmental arteries. Calcification and occasionally wall adherent thrombotic material are seen in patients with severe longstanding disease [99]. Lung neovascularity due to dilated bronchial and non-bronchial collaterals are less commonly seen in IPAH when compared to CTEPH [100].

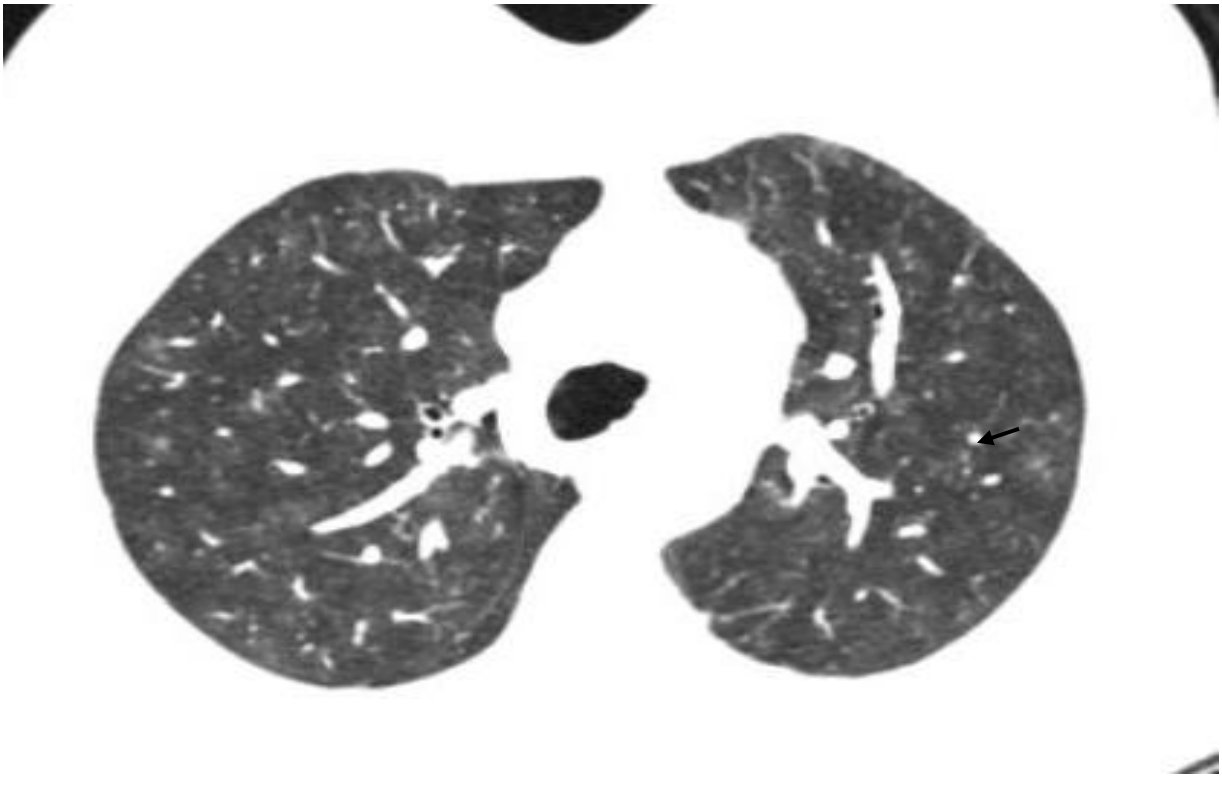

Figure 17: Bilateral centrilobular nodules due to focal perivascular areas of hyper attenuation in IPAH

PAH associated with congenital heart disease: PH may develop from a persistent left-to-right shunt and shunt reversal (Eisenmenger syndrome) in patients with congenital heart defects. Transthoracic echocardiography is usually used to define the anatomy of the cardiac defects; however when transthoracic views are limited transoesophageal echocardiography or TOE can accurately characterize simple and complex congenital malformations.

A large NIH study showed that the structural change secondary to PH was solely related to severity of the pulmonary artery pressure and not to the type or size of the congenital heart defect [101]. Mural calcification in the proximal pulmonary artery and neovascularity are occasional finding in these patients [102]. Centrilobular ground glass nodules are a nonspecific finding commonly appreciated in this subgroup [72]. In patients with left-right shunt, V/Q scintigraphy can reveal early tracer activity in the kidneys. Phase contrast MRI can on the other hand accurately quantifies the extent of intracardiac shunting.

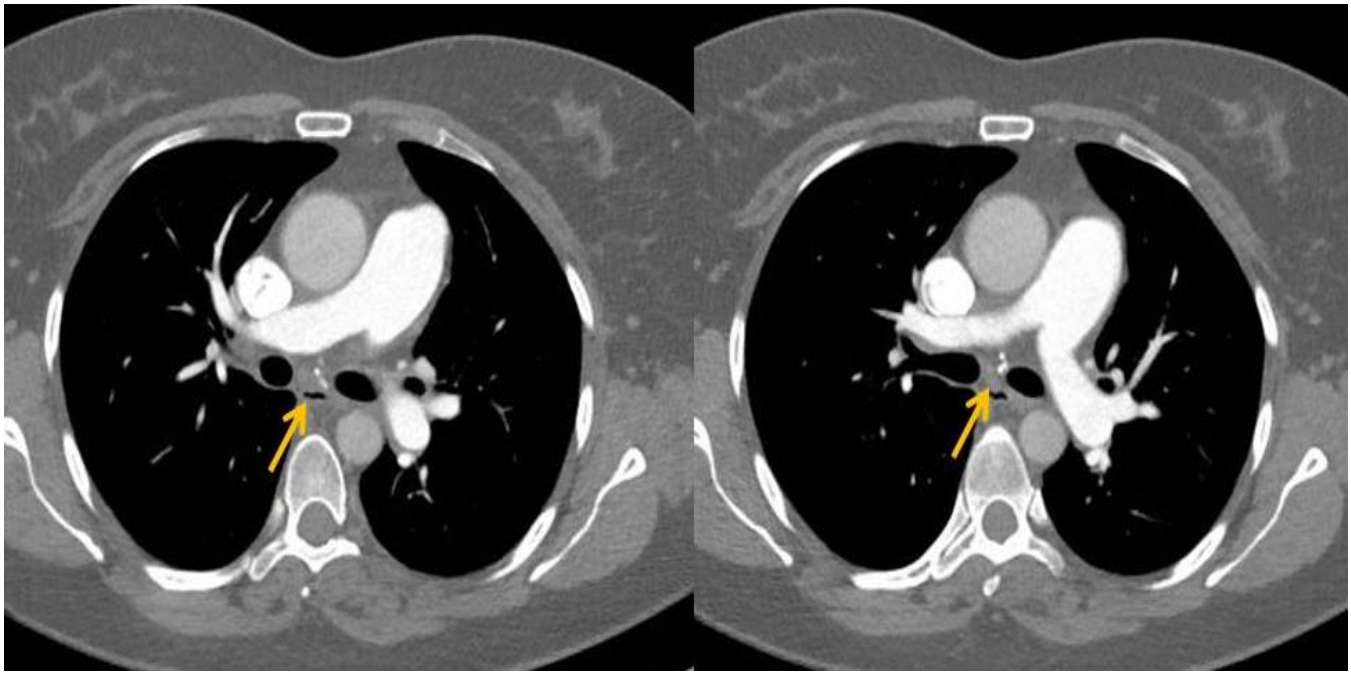

Figure 18: Axial CT images shows presence of dilated bronchial collateral arteries (arrows) in a patient with IPAH.

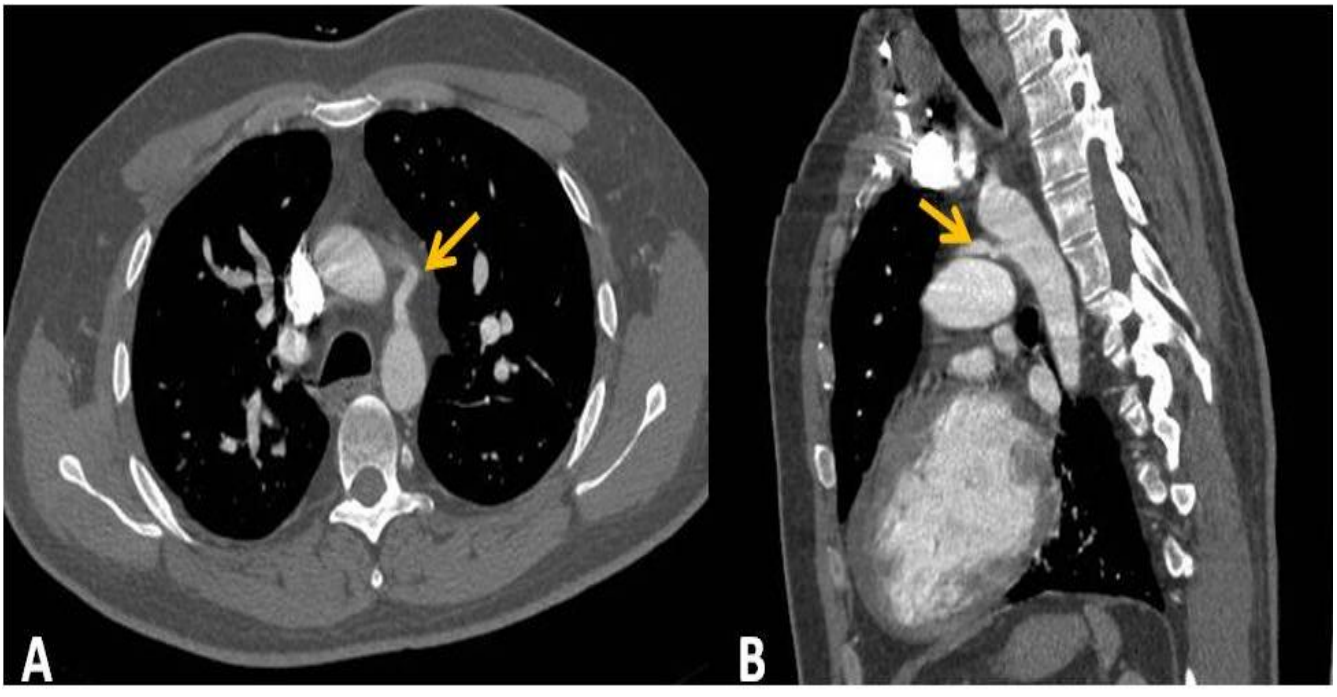

Figure 19: Axial (A) and sagittal CT (B) images shows a patient with PAH secondary to congenital heart disease- patent Ductus Arterious communicating between the aorta and pulmonary trunk (A)

Table 3: Clinical classification of PAH-Congenital heart disease

A	Eisenmenger's syndrome
B	Pulmonary arterial hypertension associated with systemic-to-pulmonary shunts
C	Pulmonary arterial hypertension with small defects
D	Pulmonary arterial hypertension after corrective cardiac surgery

[36]

Pulmonary Hypertension Associated with Connective Tissue Disease (PAH-CTD): Patients with CTD are at increased risk of developing pulmonary arterial hypertension. Amongst the patients with CTD, PAH is most commonly seen in patients with systemic sclerosis particularly those with the limited cutaneous variant [103]. In patients with CTD, PH can develop secondary to lung fibrosis, pulmonary arteriopathy or from a combination of both. The extent or degree of lung fibrosis however does not relate to the severity of PH. In patients with systemic sclerosis, non-specific interstitial pneumonia (NSIP) is the commonest pattern of interstitial lung disease and this is readily recognized on HRCT. Dilatation of the oesophagus is another common finding in this group of patients and is secondary to the connective tissue abnormality.

1.2.6.2 Group 2: PH owing to left heart disease

PH owing to left heart disease is the most common cause of pulmonary hypertension seen in a clinical setting. This is frequently identified at screening through echocardiography and these patients distinctly have enlarged left atrium on imaging. Classical left heart disease findings such as mitral or aortic valve disease or signs of previous ventricular ischemia or infarction are evident. These changes are best appreciated on cardiac MRI where the extent of the left ventricular dysfunction can be accurately quantified. Rarer cardiac causes of PH such as cardiac neoplasm and atrial thrombus can also be identified on CT and MR.

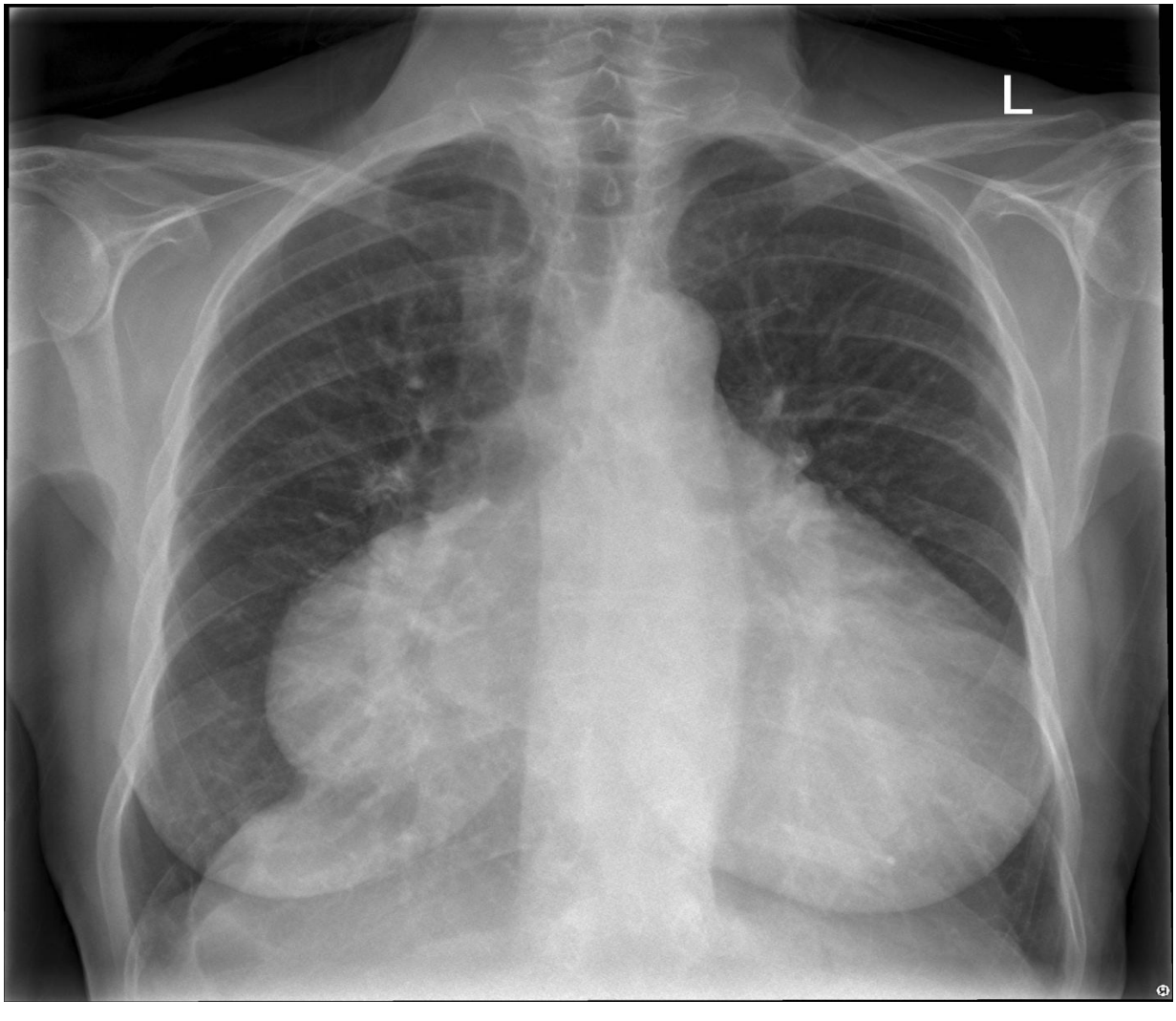

Figure 20: Chest radiograph- massive cardiomegaly with marked enlargement of both atrium and right ventricle

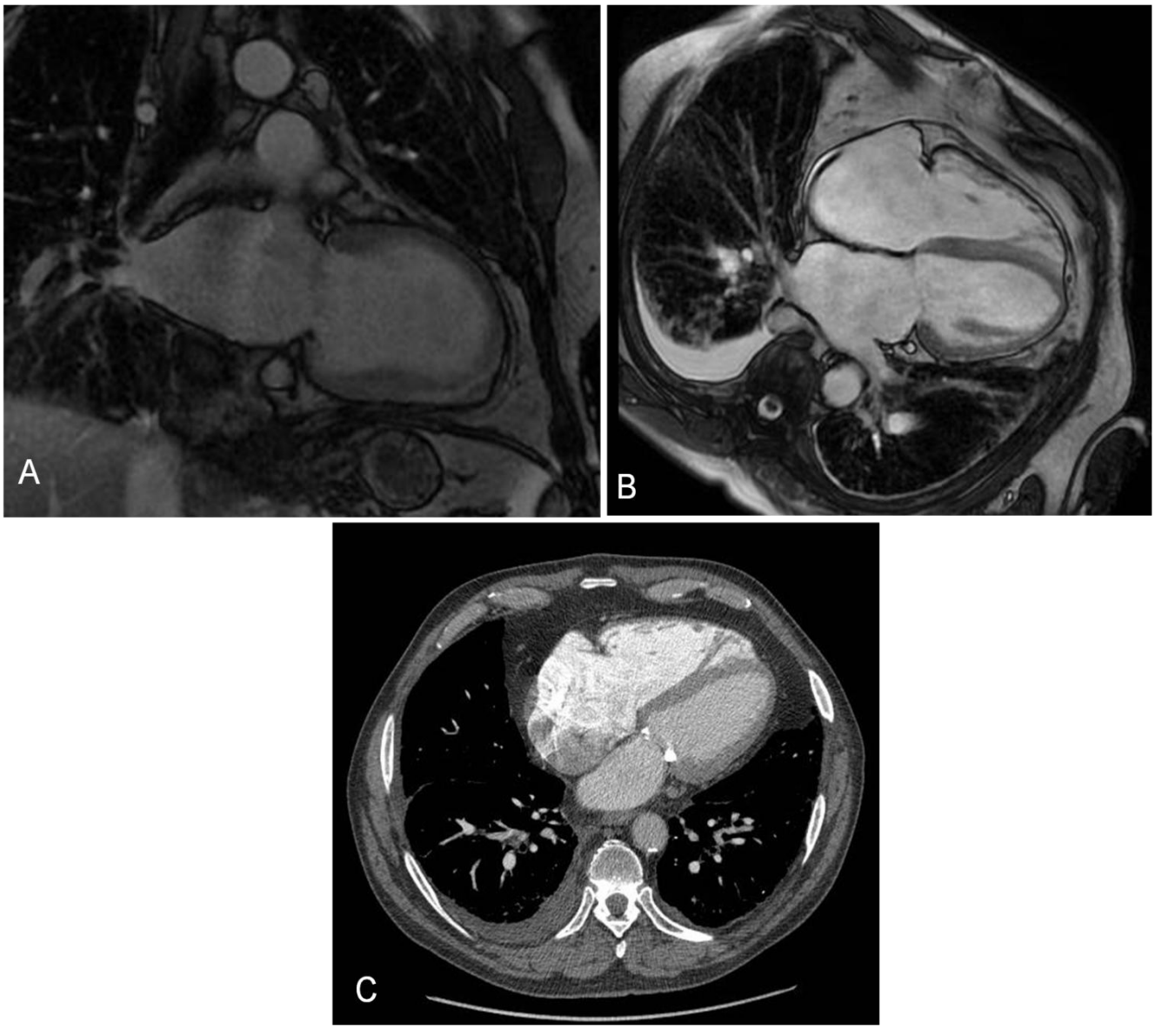

Figure 21: Dilatation of the LV on the LVLA view (A) and 4 chamber view. CT show mitral valve calcification and pleural effusion

1.2.6.3 Group 3: PH owing to lung disease and or hypoxia

PH is observed in patients with both restrictive and obstructive lung diseases and the commonest of them are chronic obstructive pulmonary disease (COPD) and interstitial lung disease (ILD). Features of PH in combination with lung changes on imaging often point towards a diagnosis of PH secondary to lung disease. High resolution CT can further characterise the lung changes and can clarify the underlying lung cause of PH. In patients with pulmonary fibrosis and emphysema, pulmonary artery dilatation can occur in the absence of PH; hence pulmonary artery size or pulmonary artery to aorta ratio is an unreliable sign to predict PH in this subgroup of patients (Devaraj, Wells et al. 2008).

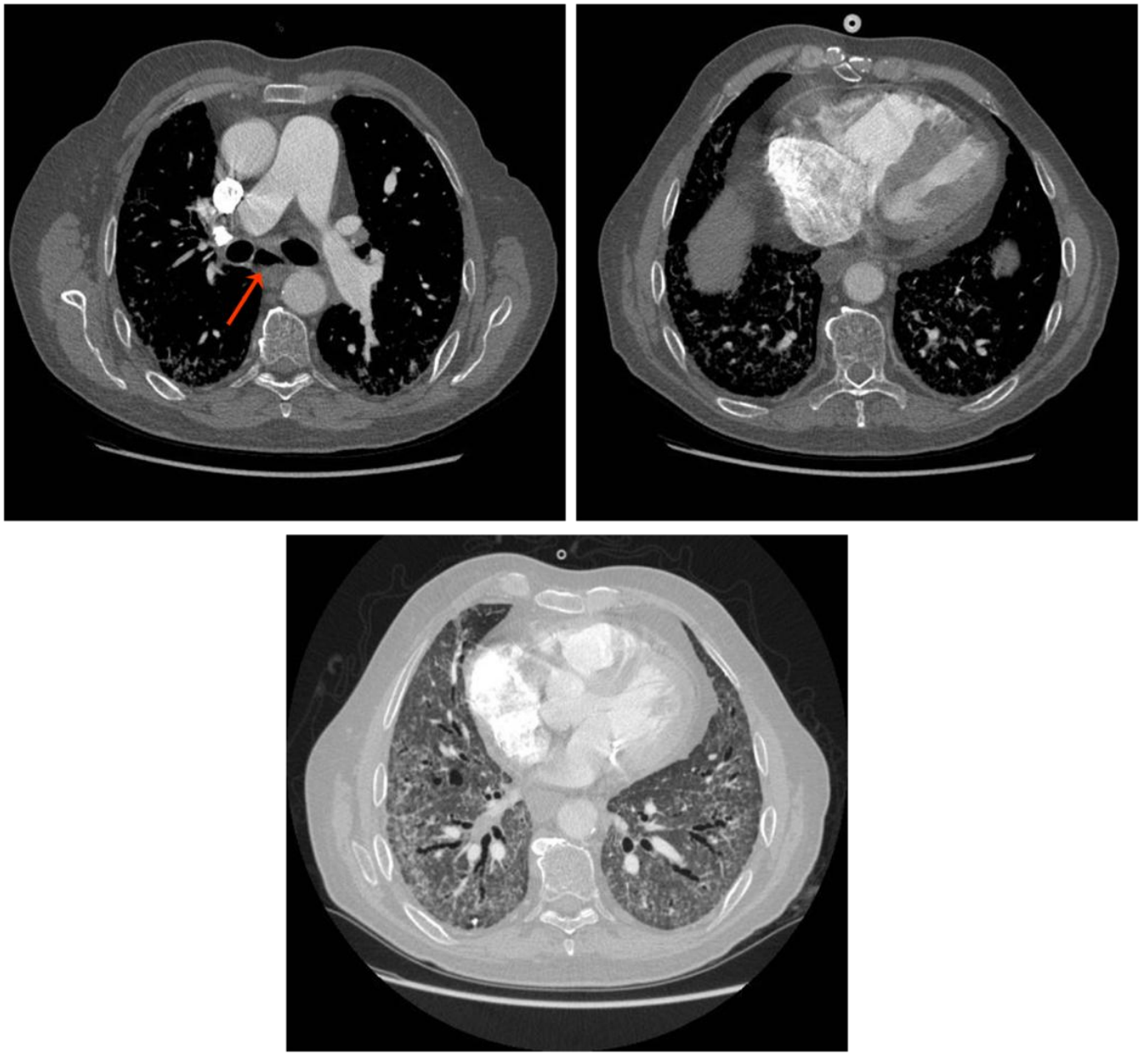

Figure 22: CT-classical features of PAH-SSc-dilated PA and right sided chambers with dilated oesophagus (red arrow) and NSIP pattern of pulmonary fibrosis

1.2.6.4 Group 4: Chronic Thromboembolic Pulmonary Hypertension

The diagnosis of CTEPH is made principally through imaging. The classical CTPA findings of CTEPH are mural thrombosis, stenosis, occlusion, post stenotic dilatation, webs and bands and calcification in the pulmonary arteries. Mosaic pattern of lung perfusion, in the absence of underlying lung disease, is a key feature of CTEPH and is characterized by sharply demarcated regions of hypoattenuation interspersed with areas of normal attenuation. The hypoattenuation is the result of hypoperfusion distal to occlusion with hyperperfusion from compensatory increased blood flow [61, 68]. Dilated bronchial (diameter ≥ 1.5 mm) and non-bronchial collaterals and changes consistent with lung infarcts are frequent CT findings in CTEPH [104-105].

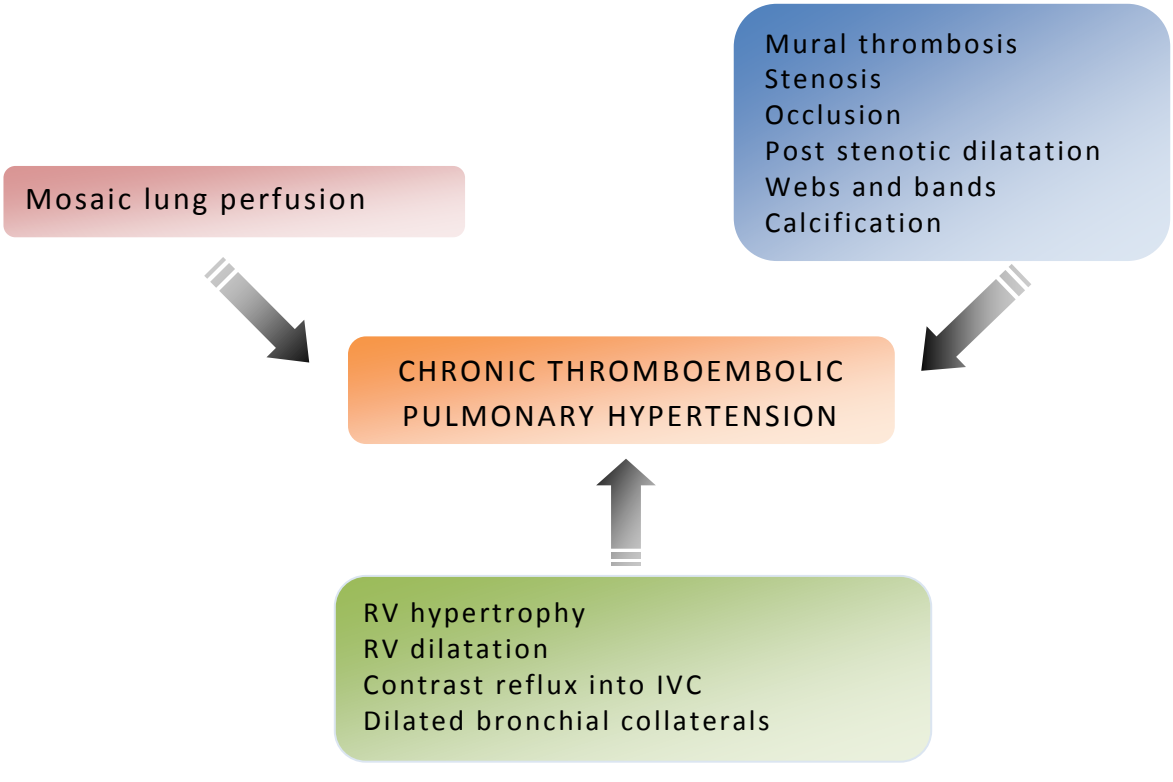

MR pulmonary angiography can clearly portray the changes in the pulmonary vasculature associated with CTEPH without the overlap of venous circulation [92]. Haemodynamic sensitive MR techniques have the potential to quantify the pulmonary blood flow and regional pulmonary vascular resistance and predict the surgical outcome [94, 106].

On perfusion scintigraphy there is typically one or more segmental or larger perfusion defect which is a well recognised feature of CTEPH and pattern of defects can help differentiate large-vessel thromboembolic PH from IPAH [107].

Invasive pulmonary angiography shows presence of "pouching" defects, webs or bands, intimal irregularities, abrupt vascular narrowing and or complete vascular obstruction [18], however in the recent era it is not routinely performed in most centres. Dual energy pulmonary CT angiography performed by simultaneous acquisition of data sets at two different kv can generate images of regional lung perfusion [108]. A study using this technique in CTEPH showed promising results with strong correlation between dual-energy CT derived perfusion and mosaic lung attenuation when lobar ($r > 0.6$; $n = 20$; $p < 0.006$) and whole-lung scores were assessed ($r = 0.77$; $n = 20$; $p < 0.001$) [109].

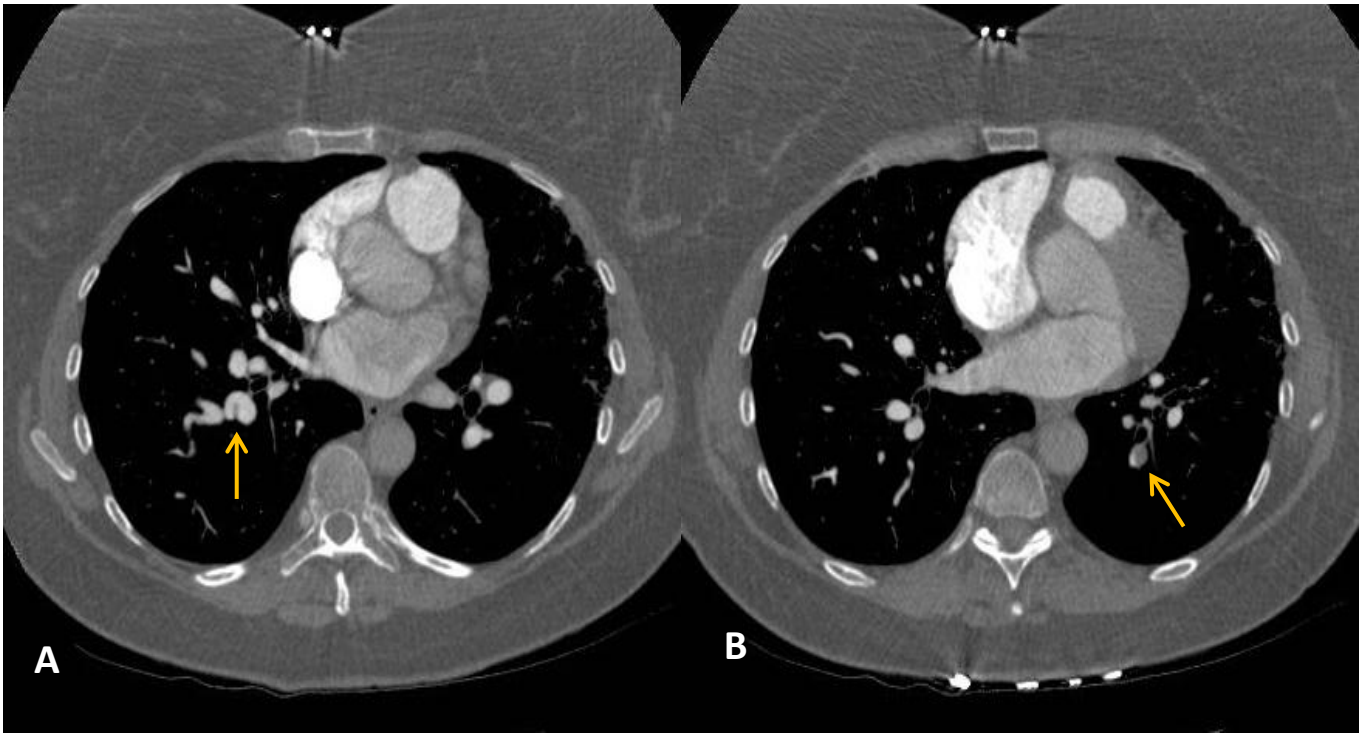

Figure 23: Axial CT- webs in the right lower lobar artery (A) and occlusion of the left lower branch in a patient with CTEPH (B)

Figure 24: Coronal reconstructed CT image shows complete occlusion of the left lower lobe pulmonary artery in the patient with CTEPH

Figure 25: SPECT Perfusion scintigraphy- bilateral segmental perfusion defect consistent with diagnosis of CTEPH

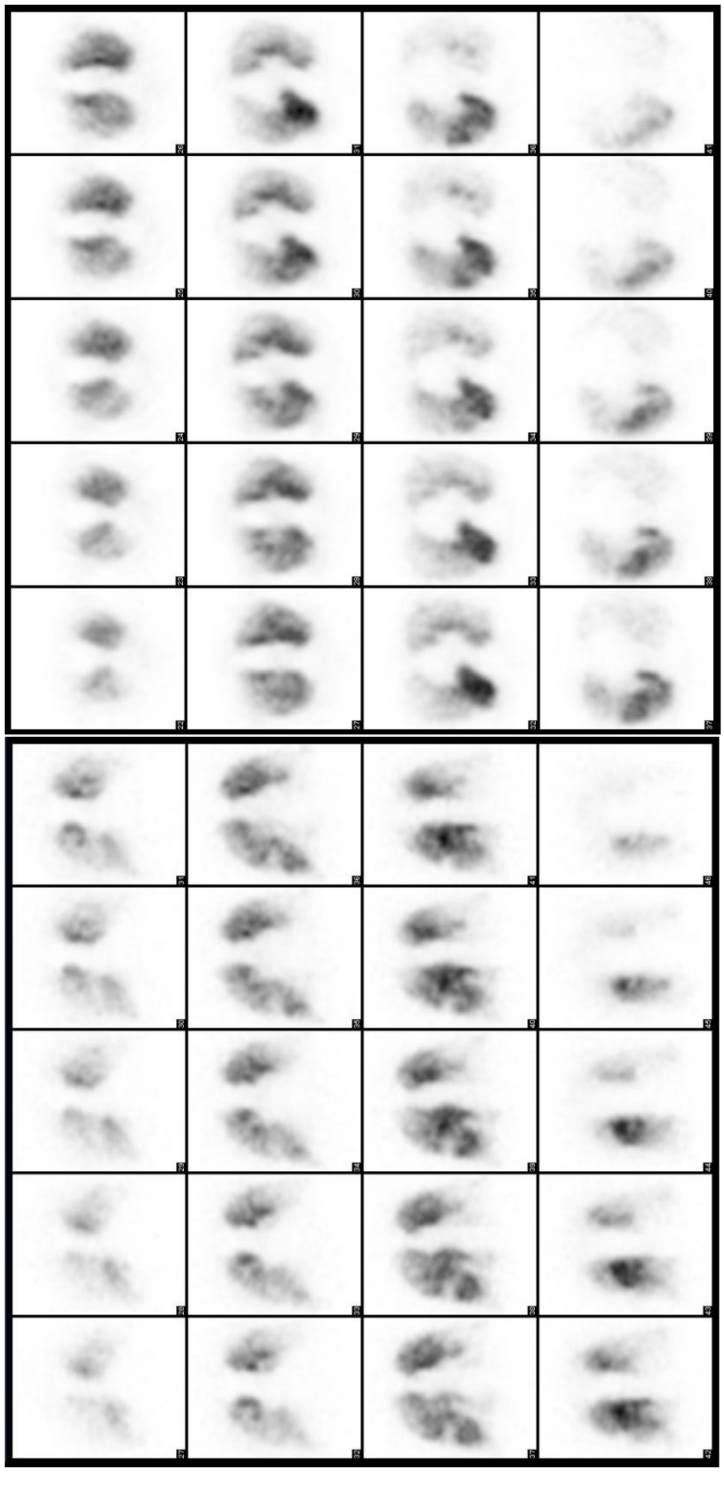

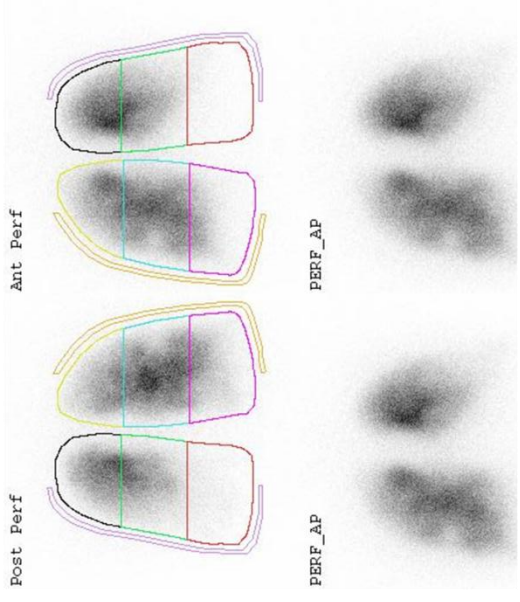

Figure 26: MIP MR angiography-stenosis in both the lower lobe branches and right upper lobe and occlusion of the right upper lobar artery in a patient with CTEPH

Figure 27: Pulmonary angiograph shows stenosis (red arrows) with posstenotic dilatation in a patient with CTEPH

Figure 28: Ground glass pattern of lung attenuation in the perihilar region corresponding to the areas of hyperperfusion with surrounding peripheral perfusion defects

1.2.7 Survival in pulmonary hypertension

It is well recognized that outcome of PH varies widely depending on multiple factors. Age, sex, World Health Organization functional class, etiology, and echocardiography and catheter-derived measures of right ventricular haemodynamics have been shown to predict outcome [39, 110-112]. Study groups have also attempted to derive *mortality risk scores* using the above parameters [113-114].

MR is increasingly being used as a prognostic tool as it is easily reproducible and non-invasive. Direct determinant of RV function from cardiac MR have been scrutinised for prognostic significance and factors such as RV mass, end diastolic volume, RV shortening and stroke volume have emerged to predict prognosis [76-77]. More recently functional MR parameters such as transit time of contrast through the pulmonary arteries was shown to be a strong predictor of adverse outcome and MR derived pulmonary arterial stiffness in patients with PAH predict mortality [89, 115] .

Uncomplicated CT features such as pericardial effusion, mediastinal lymphadenopathy, septal lines and ground glass opacities have also been shown to correlate with the risk of treatment failure [71].

1.2.8 Sheffield Pulmonary Vascular Disease Unit

All patients whose data was used in the research were seen at the Sheffield Pulmonary Vascular Diseases Unit. This unit is one of the largest PH centres in Europe and is one of the 5 dedicated PH investigation and treatment centres in the UK. It serves a referral population of 15 million and in the 12 months up to March 2012 received over 500 referrals and as of 31 March 2012 had 1454 patients with PH under its care. All referred patients undergo a thorough diagnostic evaluation including CT pulmonary angiography, high resolution CT, and cardiac and pulmonary vascular MRI and perfusion scintigraphy and recorded through a database, the *ASPIRE registry [116]*. Ethical approval for analysis of routinely collected clinical data was granted by the North Sheffield Research Ethics Committee (Sheffield, UK)(Ref 06/Q2308/8). Sheffield Pulmonary Vascular Disease Unit is lead by three specialist PH clinicians (Drs Kiely, Elliot and Condliffe) and has experienced radiologists (Drs Davies and Hill) as a part of the multi-disciplinary team.

Table 4: Number of patients seen at each designated centres

Table 2
Number of patients seen during the audit by each designated centre during 2009 - 2012

Designated Pulmonary Hypertension Centre	Number of Patients 2010	Number of Patients 2011	Number of Patients 2012
Freeman Hospital	375	377	408
Golden Jubilee Hospital	409	475	526
Great Ormond Street Hospital for Children	376	376	268
Hammersmith Hospital	851	938	1162
Royal Brompton Hospital	567	736	899
Papworth Hospital	857	859	941
Royal Free Hospital	811	1005	1207
Royal Hallamshire Hospital	1292	1466	1639
Total Patients Seen at Designated Centres	**5538**	**6232**	**7050**
Duplicate Patients	60	36	50
Total Patients Seen in the UK, Channel Islands, Gibraltar and Isle of Man	**5478**	**6196**	**7000**

[117]

2 Methodology

The methods used throughout the thesis are described in this chapter. Some methods are repeated to allow for chapters to could be read in isolation.

2.1 Study population

The study population for this thesis were identified from the ASPIRE registry [116]. Ethical approval for analysis of routinely collected clinical data was granted by the North Sheffield Research Ethics Committee (Sheffield, UK) (Ref 06/Q2308/8). Patient consent was not required to retrospectively include patients into this data. In this registry all consecutive treatment naive patients undergoing assessment of suspected PH using an approach based on right heart catheterisation are included. These patients underwent a standardized diagnostic assessment including blood tests, exercise testing, lung function testing, echocardiography, pulse oximetry and right heart catheterization (RHC). They also undergo a thorough diagnostic evaluation in the including perfusion scintigraphy, CTPA, HRCT and MRI. The ASPIRE registry has very high levels of data completeness at greater than 90% for the vast majority of variables [116].

2.2 Ethics approval

Local research ethics committee approval (Ref 06/Q2308/8) was granted for retrospective analysis of imaging techniques and written informed consent was waived for retrospective studies.

2.3 Patient classification

The form of PH was classified according to standard diagnostic criteria [42] at a joint multidisciplinary meeting by experienced pulmonary vascular physicians and specialist PH radiologists. For patients with CTEPH, suitability for pulmonary endarterectomy was decided following assessment of clinical and radiological data at the UK national pulmonary endarterectomy centre at Papworth Hospital. A mean pulmonary artery pressure ≥ 25 mmHg at right heart catheterization was required to establish a diagnosis of PH. To be classified as pulmonary arterial

hypertension (Group 1) the pulmonary capillary wedge pressure at RHC was required to be ≤15 mmHg.

2.4 Right heart catheterization

Right heart catheterization was performed via the internal jugular vein using a 7 French Swan-Ganz catheter by one of 3 experienced PH consultants. Quantified variables that were recorded are as follows: pulmonary capillary wedge pressure, mean and systolic pulmonary artery pressures, RV end-diastolic pressure, cardiac index (measured by thermodilution technique), pulmonary vascular resistance and mixed venous oxygen saturation.

2.5 Echocardiography

Echocardiography was performed using a Power vision 8000 machine (Toshiba, Japan). Right ventricle size and the tricuspid gradient (TG) were measured using the maximum velocity of tricuspid regurgitation and the simplified Bernoulli equation.

2.6 CT Imaging

2.6.1 Image acquisition

The CT was performed on a 64 slice MDCT scanner (Light-Speed General Electric Medical Systems, Milwaukee, WI).

CT pulmonary angiography: CTPA was performed during a single breath-hold following and standard acquisition parameters were used: 100 mA with automated dose reduction, 120 kV, pitch 1, rotation time 0.5 s and 0.625mm collimation. The field of view was 400x400 mm with an acquisition matrix of 512 x 512. 100ml of intravenous contrast agent (Ultravist 300; Bayer Schering, Berlin, Germany) was administered at a rate of 5ml/sec. The CTPA images were reconstructed using a soft filter to provide contiguous 0.625 mm axial slices from the apex of the lung to the diaphragm for review.

HRCT: 1.25mm HRCT slices were also reconstructed every 10mm from the contrast enhanced acquisition using a high spatial resolution filter.

2.6.2 Image analysis

Pulmonary artery-aorta ratio: The widest short axis diameter of the main pulmonary artery and the corresponding transverse diameter of the ascending aorta on the same image slice were measured and pulmonary artery aorta ratio was derived.

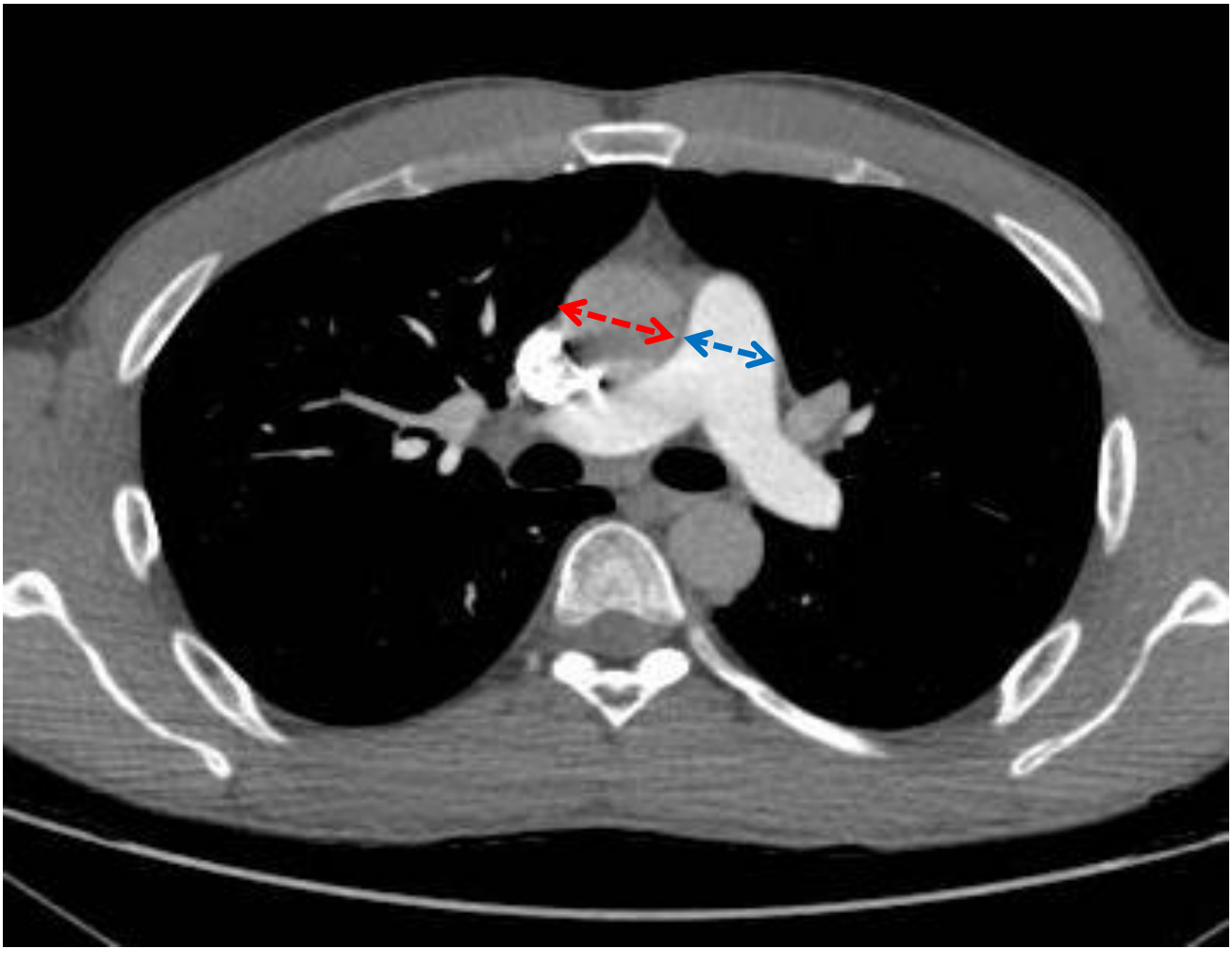

Figure 29: The pulmonary artery (PA) aorta ratio was obtained by measuring the widest transverse diameter of the PA (blue) and the corresponding transverse diameter of aorta (red).

Right ventricle size: The maximum mid-transverse diameters of the right and left ventricular cavities were measured in the axial plane at their widest points between the inner surfaces of the free wall and the interventricular septum. This may lie at different image levels. Using these measurements the ratio of right to left ventricle was obtained [118]

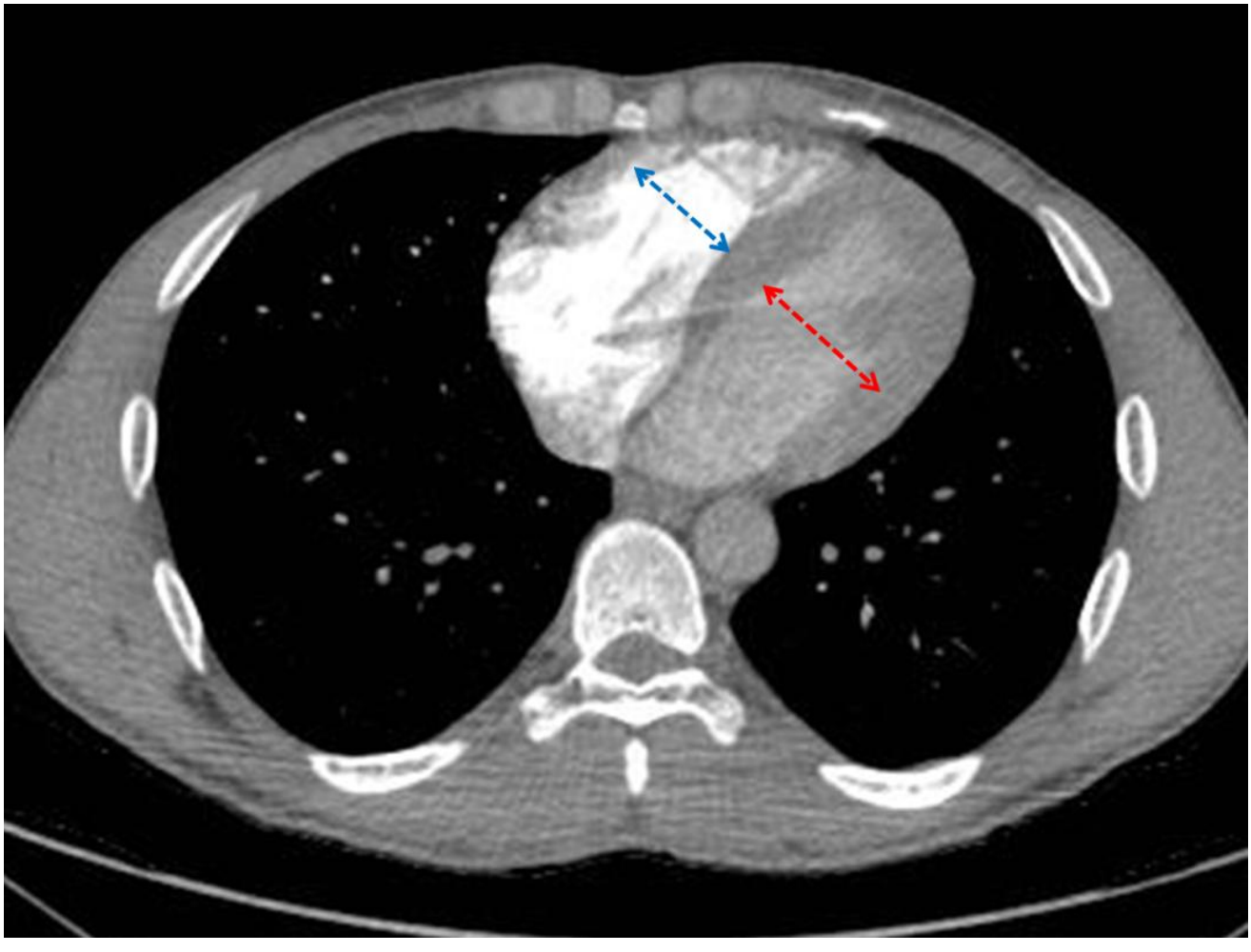

Figure 30: The maximum mid-transverse diameters of the RV (blue arrow) and LV (left arrow) cavities were measured in the axial plane at their widest points between the inner surfaces of the free wall and the interventricular septum

Tricuspid regurgitation: The severity of reflux of intravenous contrast into the inferior vena cava (IVC) or hepatic veins was graded by a semi-quantitative system proposed by Groves et al [66].

0 = there is no reflux into IVC; 1= there is trace of reflux into IVC only 2= reflux into IVC but not hepatic veins; 3= reflux into IVC and proximal hepatic veins

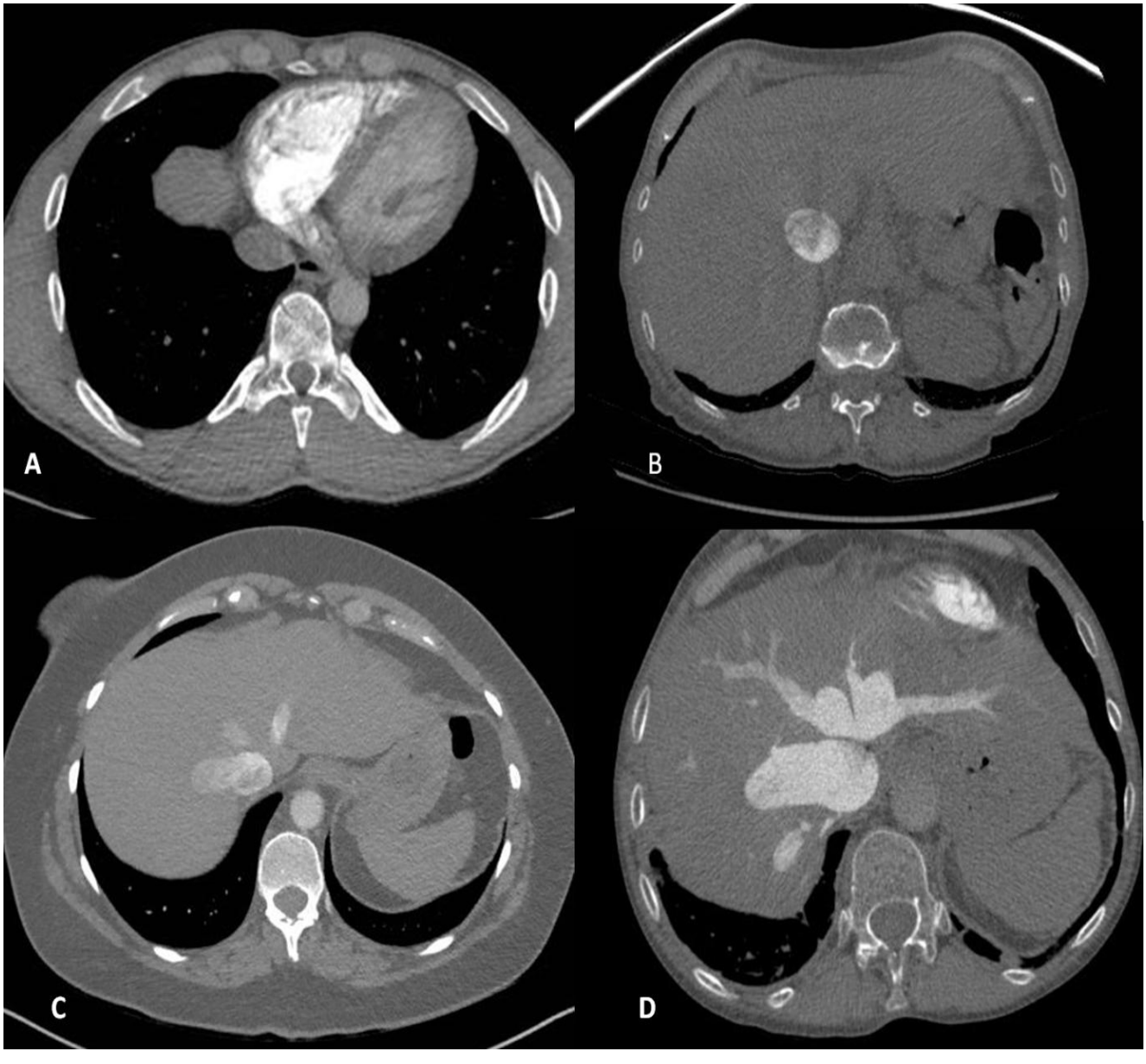

Figure 31: Grading of tricuspid regurgitation (A) 0 = there is no reflux into IVC, (B) 2 = reflux into IVC but not hepatic veins, (C) 3 = reflux into IVC and proximal hepatic veins (D) 4 = reflux into IVC and distal hepatic veins

Interventricular septal configuration: The configuration of the interventricular septum was evaluated on a three-point scale as follows: 'normal' when the interventricular septum is convex toward the right ventricle, 'flattened' when the interventricular septum is straight and 'deviated' when the interventricular septum is convex toward the left ventricle [64].

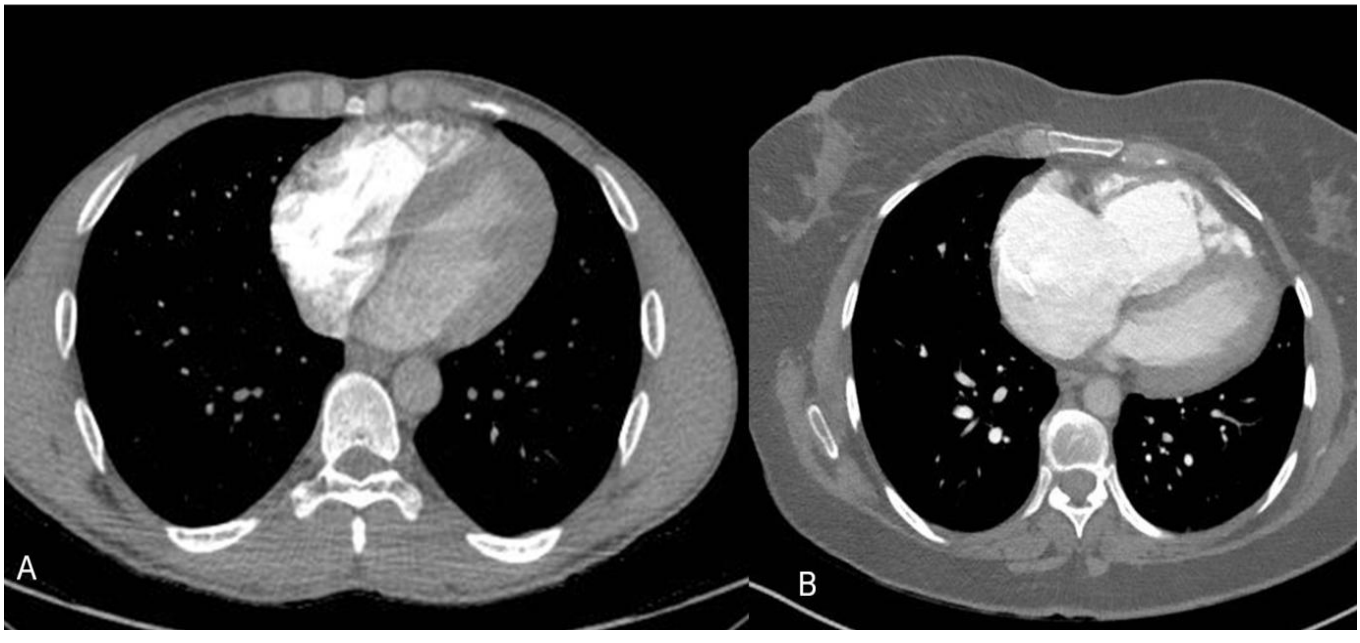

Figure 32: Axial CT images show 'normal' interventricular septum (A) and 'deviated' interventricular septum with convexity towards the left ventricle (B)

Right Atrial size: For assessing the right atrial size on CT, right atrial length was measured from the centre of tricuspid annulus to the superior right atrial wall on the axial mid-chamber view. The size of the right atrium was also qualitatively scored using a simple 3-point visual scale as mild, moderate and severe.

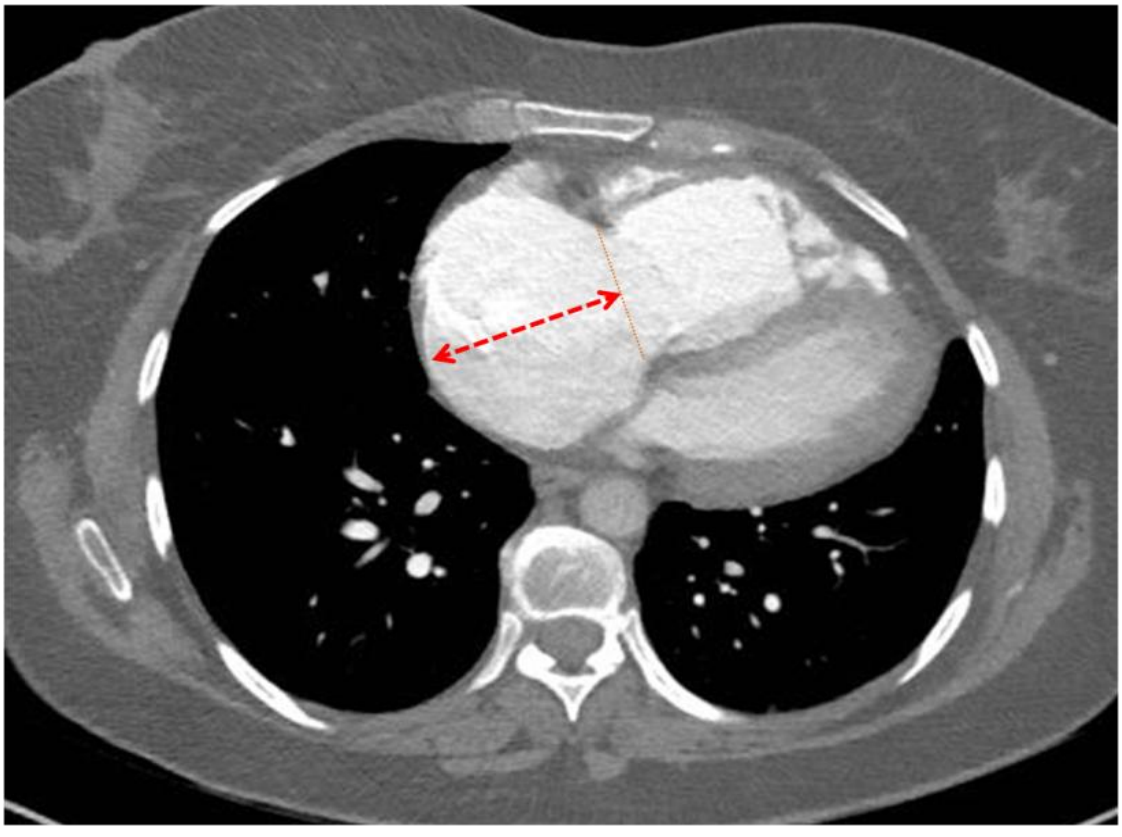

Figure 33: For assessing the right atrial size on CT, right atrial length was measured from the centre of tricuspid annulus to the superior right atrial

RV wall thickness: The transverse thickness of the right ventricular free wall was measured at the mid-chamber view from the axial images [119].

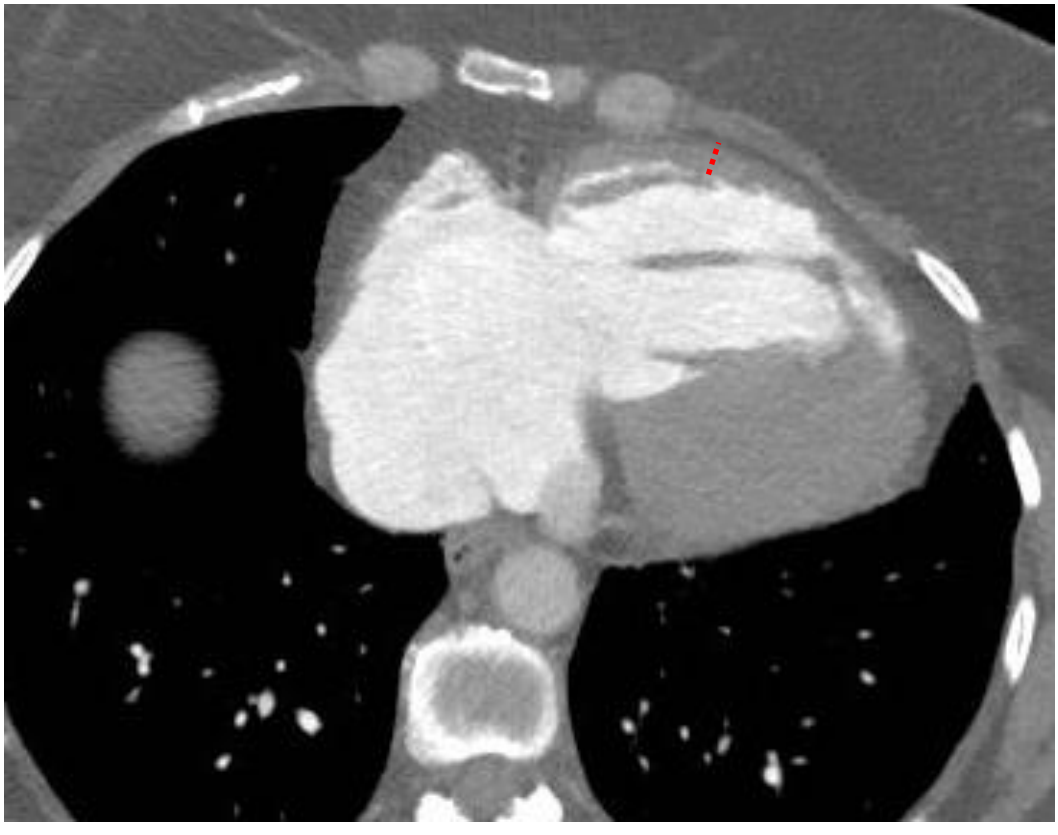

Figure 34: Axial CT image shows thickening of the right ventricular free wall (dotted line) in a patient with IPAH.

Lung and mediastinal changes: Ground glass opacity (GGO) is defined as increased opacity of the lung parenchyma without obscuring the pulmonary vessels. When GGO was present the pattern of change was noted as centrilobular, panlobular homogenous, panlobular heterogenous according to the classification of Engeler et al [120]. The craniocaudal distribution of the GGO was recorded as upper, lower or random and the anterioposterior distribution noted as subpleural, central or random. [71].

Figure 35: Ground glass opacity in the central pattern of distribution

Fibrosis: The criteria for positive interpretation of fibrosis included one or more of the following: interlobular septal thickening, intra-lobular interstitial thickening, honeycombing and traction bronchiectasis or ground-glass opacity [121-122]. Interstitial lung changes were graded based on a grading system used by Gay et al [123] and is outlined in table 1. Each lung was divided into three zones defined as follows: upper zone was defined as above the aortic arch, the middle zone was defined as between the aortic arch and pulmonary veins, and the lower zone was defined as below the pulmonary veins [124]. The sum of the scores for all zones for each patient was obtained (a minimum score was 0 and the maximum score was 30.

Table 5: scoring system for grading interstitial changes on HRCT

Score	Characteristics
0	No interstitial disease
1	Interlobular septal thickening (no discrete honeycombing)
2	Honeycombing involving up to 25% of the zone
3	Honeycombing involving 25 to 49% of the zone
4	Honeycombing involving 50 to 75% of the zone
5	Honeycombing involving > 75% of the zone

*Adapted from Gay et al [123] based upon the relative quantity of honeycombing

For the purpose of this thesis mediastinal lymphadenopathy was considered when the short axis transverse lymph node diameter greater than 10mm and dilated bronchial collaterals was defined as transverse vessel diameter greater than 2 mm[61].

2.7 MR Imaging

2.7.1 Image acquisition

MR imaging was performed on a 1.5 Tesla GE HDx Scanner (GE Healthcare, Milwaukee, USA) with peak gradient strength40 mT/m and slew rate 120 mT/m/ms. An 8 channel cardiac receive array RF coil (GE, Aurora, Ohio, USA) was used throughout.

Steady-state free precession imaging (SSFP):

Proton imaging is performed in the coronal plane as a stack of 2D SSFP images (GE FIESTA sequence). This sequence was performed in full inspiration with a breath hold time of 12 seconds. The imaging parameters are as follows: TR 2.8 ms, TE 1.0ms, Flip angle of 50°, FOV=48 cm x 43.2 cm, 256 x 256 Matrix, 125 kHz bandwidth and slice thickness of 10mm. This sequence is also used for scout images for planning the geometry of the cine cardiac scans.

CINE cardiac imaging:

Four chamber view and contiguous cine short-axis views are acquired using cardiac gated SSFP imaging at end-expiratory breath-holds. The following parameters are used: 20 frames per cardiac cycle, slice thickness 8-10mm, FOV 48, matrix 256 x 256, BW 125 KHz/pixel, TR/TE 3.7/1.6 ms).

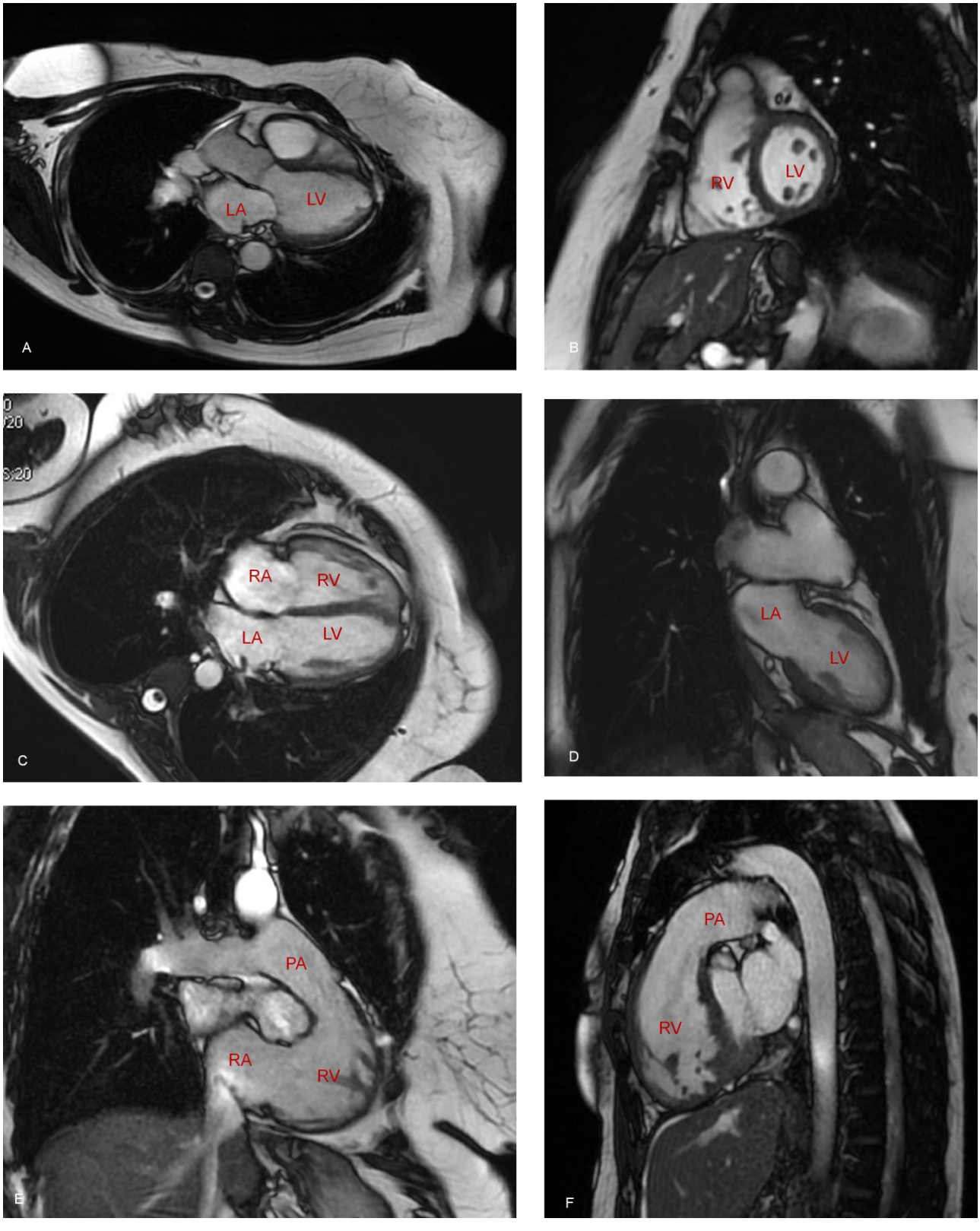

Figure 36: Left ventricle inflow outflow view-LIFOF (A); mid chamber short axis view (B); 4 chamber view (C); Left ventricle left atrium view-LVLA (D); right atrium right ventricle inflow outflow view (E); right ventricle outflow tract view-RVOT (F)

Phase contrast imaging:

Phase-contrast imaging was performed in a plane orthogonally positioned to the PA trunk and through plane encoding is used. This was also performed across the aorta. The sequence parameters were as follows: TR 5.6ms, TE 2.7ms, slice thickness 10mm, FOV 48x28.8, band-width 62.5kHz, matrix = 256x128, 20 reconstructed cardiac phases and velocity encoding 150cm/s.

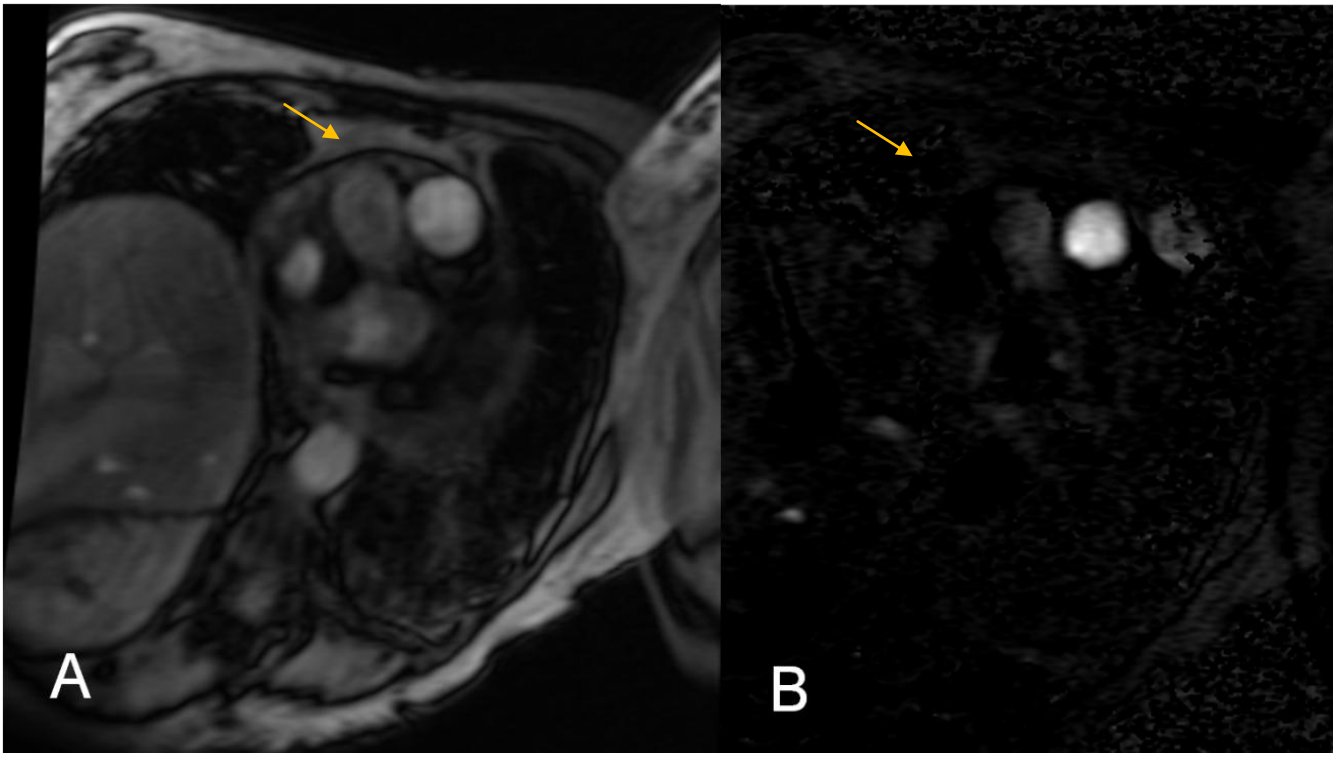

Figure 37: Magnitude (A) and velocity (B) encoded images from phase contrast MRI of the pulmonary artery (yellow arrow).

Delayed myocardial enhancement imaging:

Delayed myocardial enhancement imaging is performed 10-20 minutes following gadolinium injection (0.2 mmol/kg of gadolinium-DTPA; Magnevist, Bayer, Germany). The sequence parameters are as follows: 3D-gradient spoiled turbo-fast field-echo sequence, TR 7.7ms, echo time 3.6ms, slice thickness 8mm, FOV 45x40.5, matrix 256x224.

Black blood imaging:

Black blood imaging is a double inversion recovery sequence and the images are acquired at the level of the pulmonary arteries. It was performed in an axial plane and is a cardiac gated sequence performed during breath hold. The imaging parameters are as follows: 8mm slice thickness, spacing 2mm, TI1 50 ms, TI2 551 ms, ETL (Echo train length) 32, BW 31.2KHz, ASSET 2, FOV 4s (0.9 Phase), TE 42ms, 256x256 matrix.

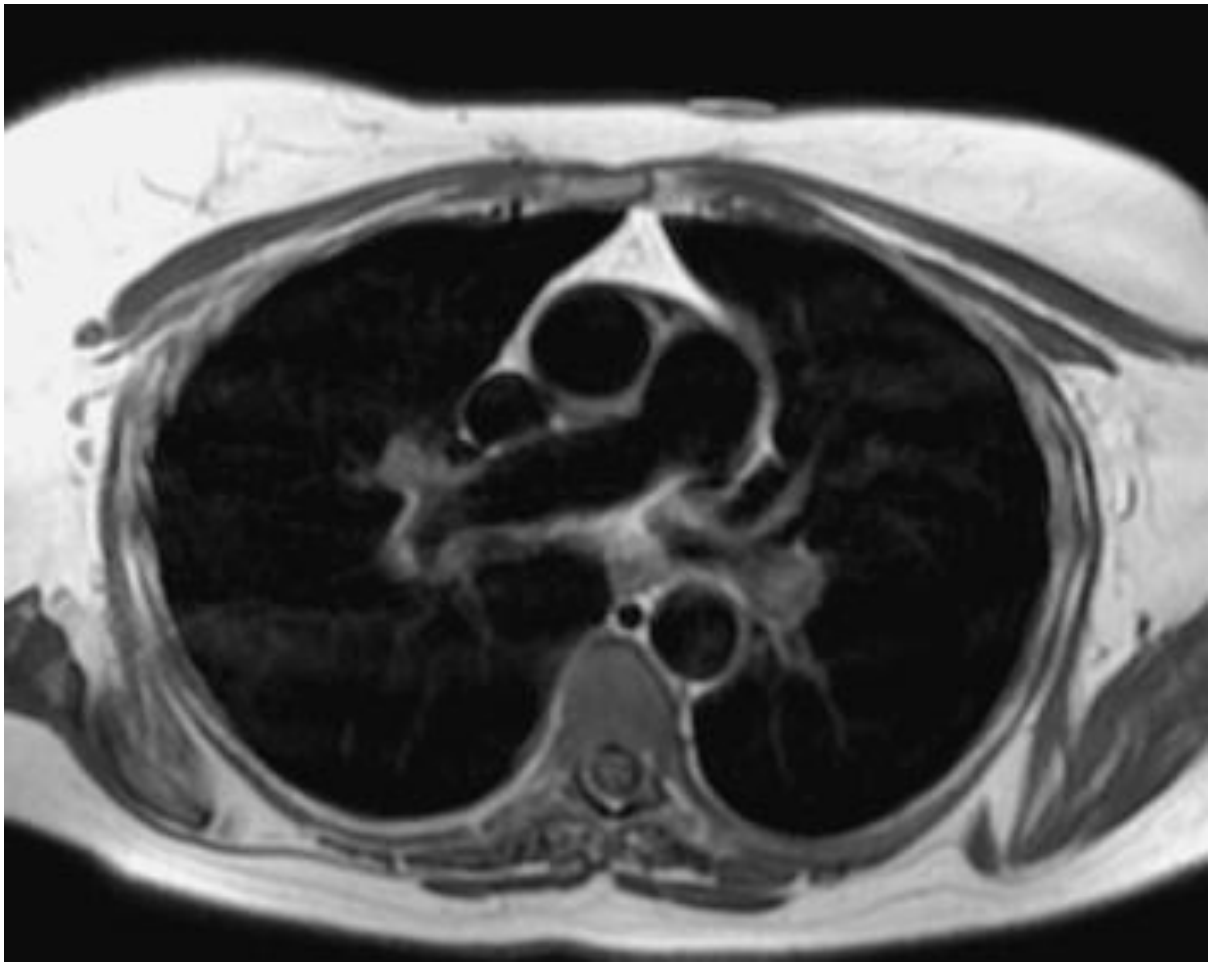

Figure 38: double inversion recovery black blood MRI through the pulmonary artery in a patient without PH.

Dynamic contrast enhanced MR angiography:

MR angiography: MR angiography was performed following an injection of 15ml contrast agent ensuring the total dose of contrast doesn't exceed 0.3ml/kg. This scan was preceded by a timing bolus of contrast agent (0.05ml/kg). The sequence parameters used were: 3D Coronal Spoiled Gradient Echo, TE 1.0ms, TR 2.8 ms, flip angle of 30°, FOV=48 cm2, 2x Asset, 300 x 200 Matrix, 125 kHz bandwidth, slice thickness of 3 mm and average of 60 slices. This was a breath-hold sequence acquired during inspiration.

MR perfusion: Contrast enhanced 3D MR lung perfusion images were acquired using a time resolved 3D spoiled gradient echo sequence with view sharing (TRICKS) [125]. The sequence parameters were: coronal orientation, TE 1.1ms, TR 2.5 ms, flip angle of 30°, FOV=48x48cm, matrix 200 x 80, ASSET R=2, 250 kHz bandwidth, slice thickness of 10mm. This sequence was acquired during full inspiratory breathhold after intravenous administration of 0.05 ml/kg of Gadovist (Schering, Berlin) injected at 4 ml/s followed by a 20ml saline flush.

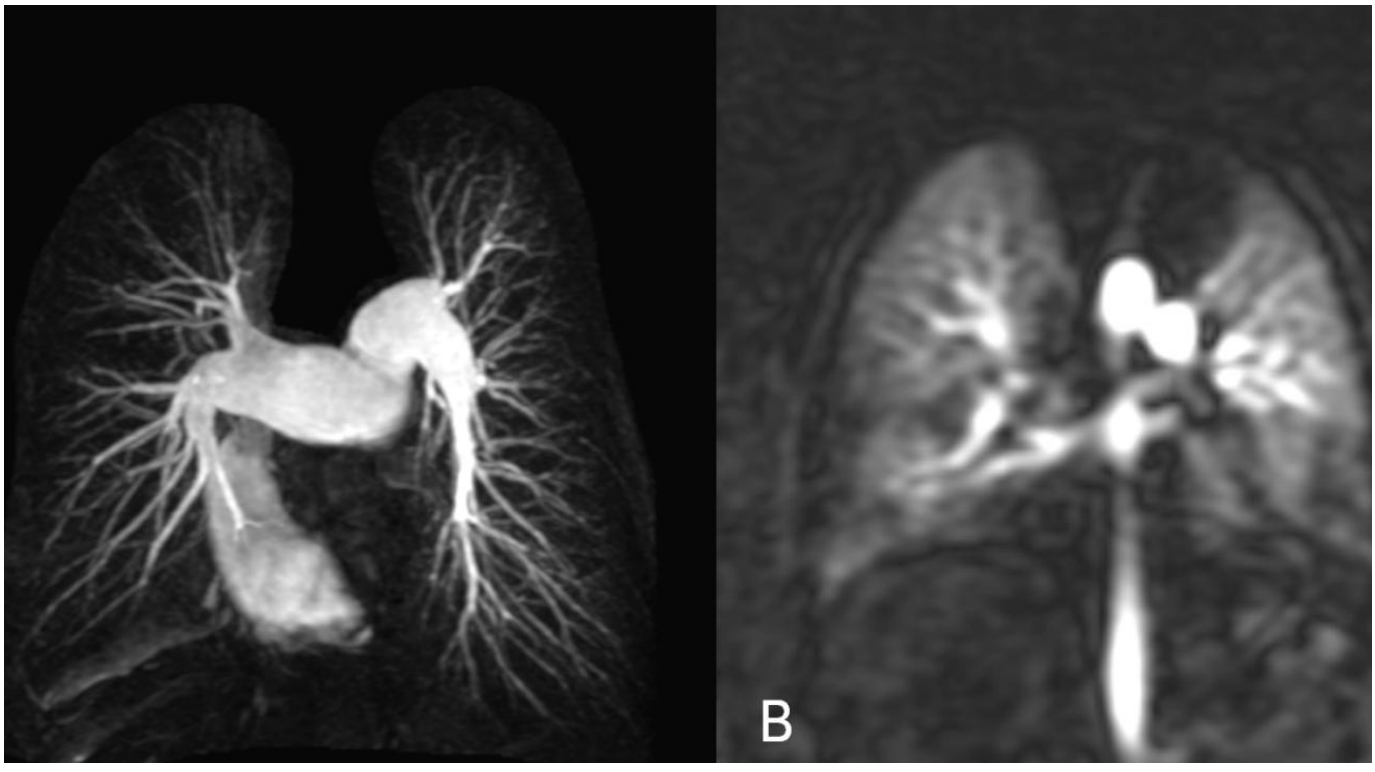

Figure 39: MIP MR angiographic (A) and coronal 3D contrast enhanced perfusion images

2.7.2 Image analysis

The MR images were analysed on a MR GE Advantage Workstation 4.1. At the time of the analysis the observers (SR and AJS) were blinded to the patient clinical information, other imaging findings and right heart catheter haemodynamics.

Volumetric measurements:

The contours of the right ventricle (RV) and left ventricle (LV) were delineated manually on the cine short axis stack images and processed using GE software to obtain RV end diastolic and end systolic volume. The RV ejection fraction and stroke volume were subsequently derived.

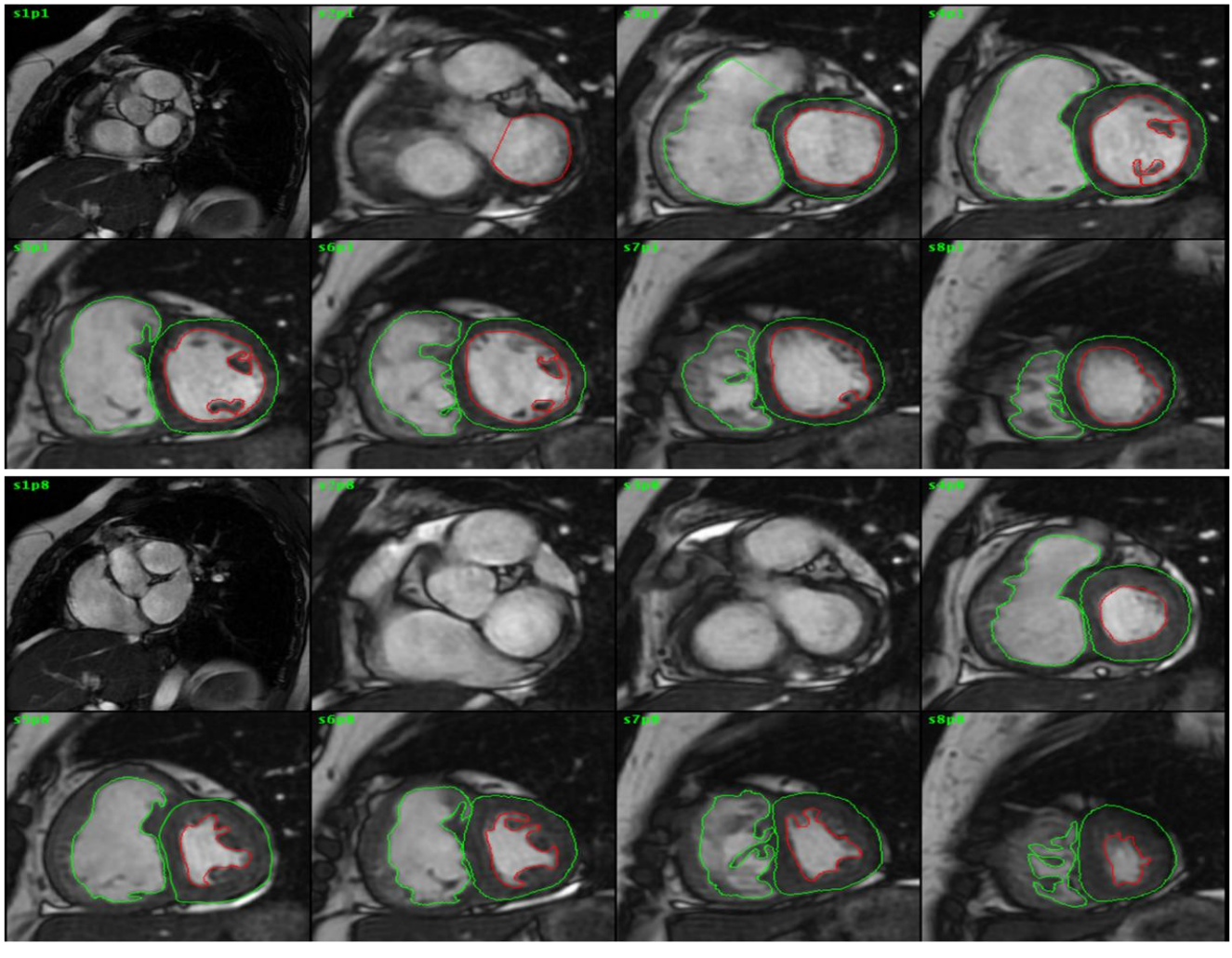

Figure 40: Short axis cine diastolic (above) and systolic (below) images used for deriving volume measurements and ejection fraction (see ROI traced images)

Ventricular mass index (VMI):

The RV epicardial and endocardial borders on each end-diastolic short axis slice image were outlined. The inter-ventricular septum was considered as part of the LV. The myocardial volume for each slice was calculated by multiplying the area of the RV wall by the slice thickness. The product of the sum total of the myocardial slice volumes for each ventricle and the density of myocardium (1.05 g/cm3) gave an estimate of RV mass. RV mass index= RV mass/body surface area (BSA) g/m2. The LV epicardial and endocardial borders on each end-diastolic short axis slice were outlined, LV end diastolic mass was thus derived. VMI was defined as RV mass divided by LV mass [79].

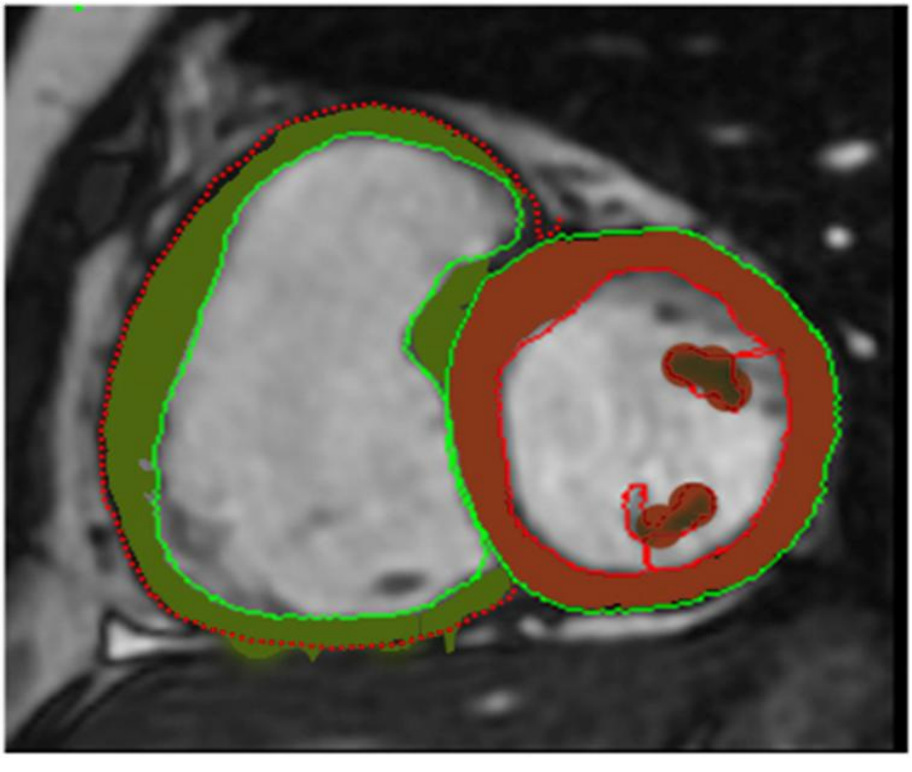

Figure 41: Representative image showing how the epi and endocardial borders of the ventricles are traced for measuring VMI

Longitudinal and transverse RV wall motion:

The RV longitudinal and transverse motion are quantified by means of the tricuspid annular systolic excursion (TAPSE) and septum-free-wall distance (SFD) respectively by this method described by Kind et al [80]. These measurements are

obtained at end diastole and end systole images on the 4-chamber view. TAPSE is the change in the distance between the tricuspid annulus and RV apex. SFD is the change in the perpendicular distance between interventricular septum and RV free wall at the mid-point between the apex and the base.

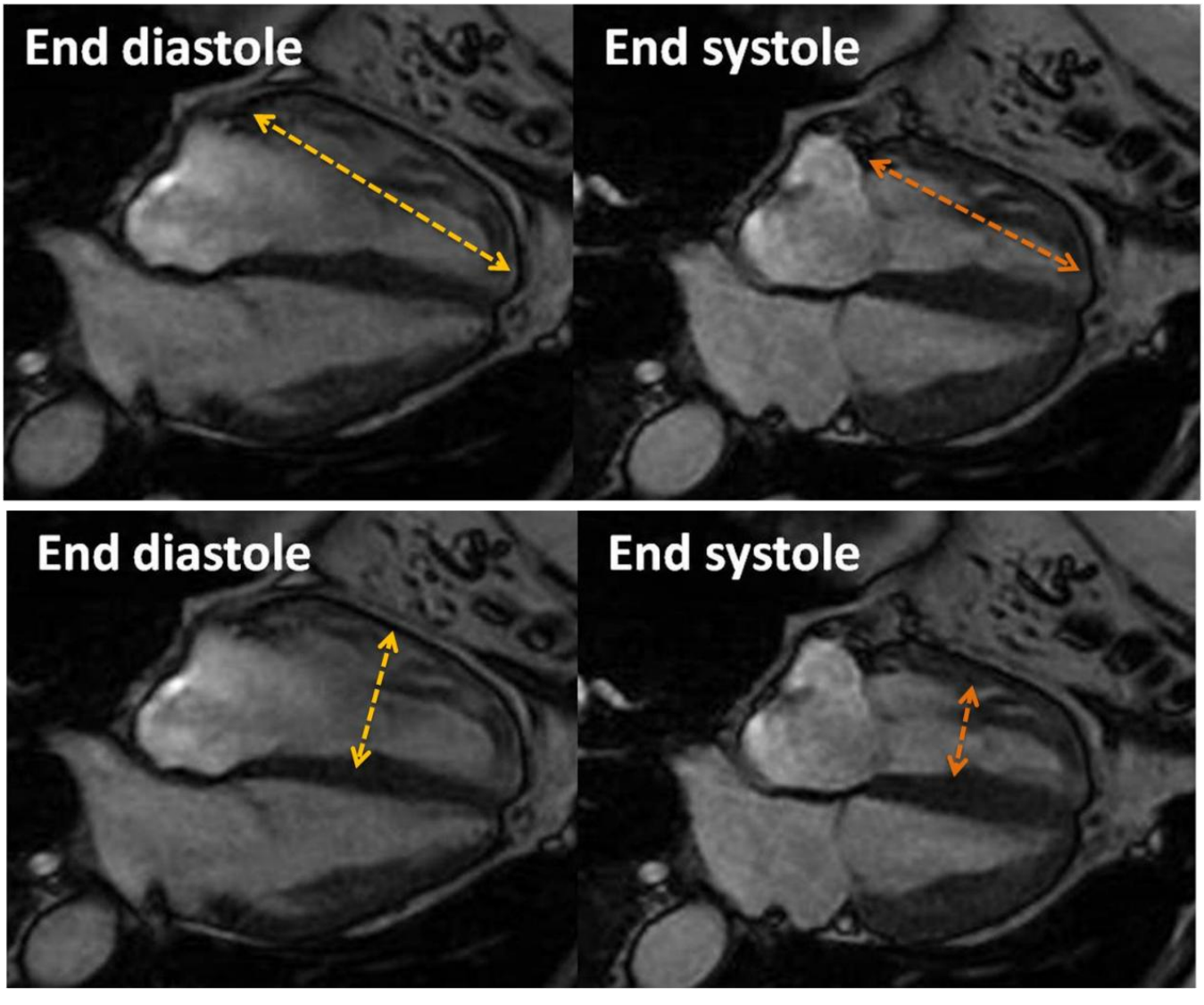

Figure 42: measurement of longitudinal (TAPSE) and transverse RV wall motion

Configuration of the interventricular septum:

The motion of the interventricular septum was visually analysed on short-axis and four-chamber views for presence or absence of paradoxical septal movement and are graded as normal, flattened and paradoxical septal position.

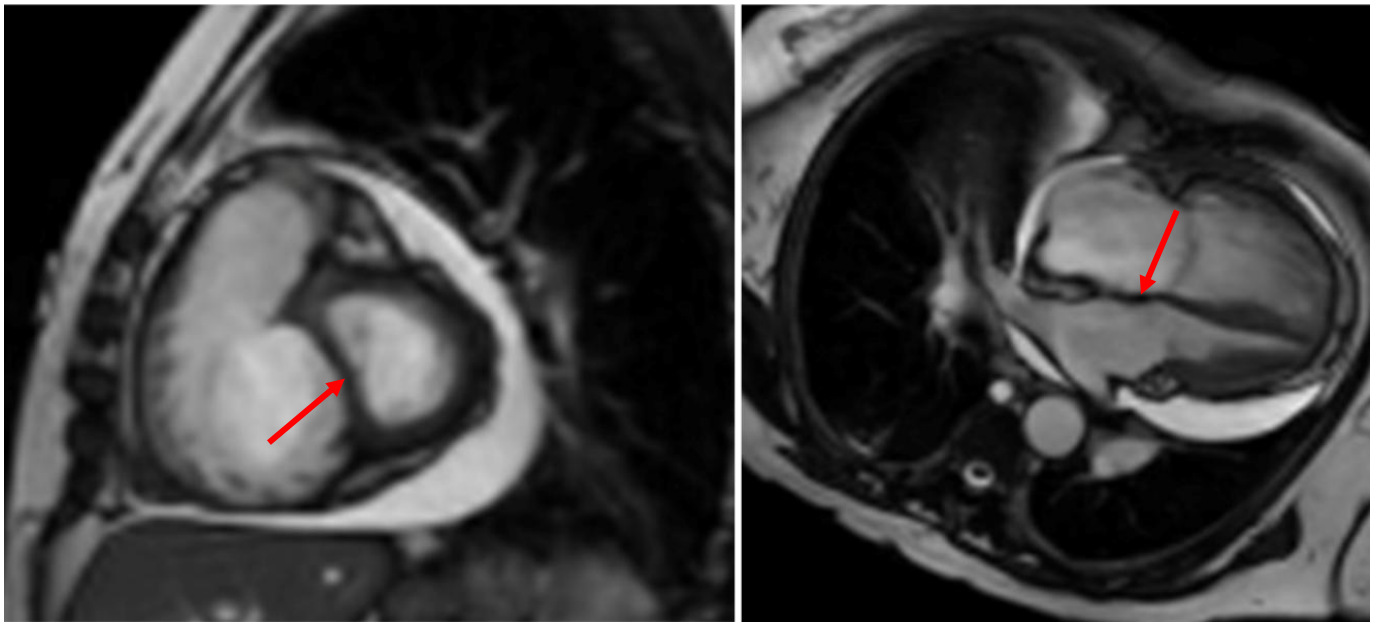

Figure 43: Short axis and 4 chamber cardiac views showing paradoxical shift of the interventricular septum to the left (red arrows)

Delayed myocardial enhancement:

Presence or absence of delayed myocardial enhancement was qualitatively noted. Presence of delayed myocardial enhancement was defined as area of hyperintensity at the interventricular septum insertion points on delayed mid-cavity short axis image following gadolinium administration.

2.8 Perfusion scintigraphy

The perfusion scintigraphy images were obtained with the patient in the supine position following intravenous administration of technetium 99m labelled macro-aggregated albumin (dose of 100-MBq; MAASOL; Amersham Health, Vienna, Austria). Scanning was performed on a gamma camera system (GE Millennium, GE Infinia, or Siemens Symbia gamma camera systems) with a 256 x 256 matrix using a 20% window centered over the 140-keV energy peak. Four standard images (anterior, posterior, right posterior oblique and left posterior oblique) were obtained for 500,000 to 750,000 counts each.

2.9 Statistical analysis

Comparisons of measurements between groups were performed using the independent t-test for continuous data and the chi-square test was used for categorical data. ANOVA testing was employed for multiple group comparisons. The diagnostic accuracy of a test was determined by deriving the sensitivity, specificity, negative and positive predictive value using Fisher's exact test. Diagnostic strength for the identification of patients with PH was assessed using receiver operated characteristic (ROC) curve analysis and was measured by the area under the ROC curve and a value closer to 1.0 was considered to have a greater the diagnostic utility. To determine the correlations between continuous variables Spearman's correlation coefficient was used. Kappa statistics were used to determine the extent of intra and inter-observer agreement for categorical data.

Event (death)-free survival from date of diagnosis was estimated using the Kaplan–Meier method with comparison between groups performed by the log-rank test. Cox regression analysis was used to assess individual predictors of survival.

Software

The statistical analyses were performed in GraphPad Prism 5.04 (GraphPad Software, San Diego, California and SPSS PASW 16 (Chicago, IL). A p-value of <0.05 was deemed statistically significant throughout.

2.10 Data handling

Patients identified for the study from the ASPIRE registry were given a unique encrypted patient identifier. The document linking the patient to this identifier was stored on a separate secured departmental computer and both the computer and the document were password protected. The datasheet on to which the MR and CT data were entered had no patient identifiable information clinical findings or right heart catheter haemodynamics.

3 CHAPTER 3: 3D contrast enhanced MR lung perfusion in Chronic Thromboembolic Pulmonary Hypertension

The work in this chapter is related to the manuscript published in Thorax "3D contrast enhanced lung perfusion MRI is an effective screening tool for chronic thromboembolic pulmonary hypertension: results from the ASPIRE Registry". Thorax, 2013 Jan 24 (doi: 10.1136/thoraxjnl-2012-203020).

This chapter of the thesis is focussed on patients with chronic thromboembolic pulmonary hypertension (CTEPH). Many patients with CTEPH frequently present with a previous history of pulmonary embolism. However there are also a significant proportion of patients who present with progressive breathlessness or unexplained PH without a history of embolic disease.

Currently perfusion scintigraphy is recommended as the first line investigation for diagnosing patients with CTEPH. As CTEPH is increasing being recognized as a treatable cause of PH, a non-ionizing screening tool that has the ability to provide RV functional and pulmonary vasculature structural information would be valuable.

This chapter is on the value of 3D MR lung perfusion as a diagnostic tool for identifying patients with CTEPH.

3.1 Abstract

Objective

CTEPH is an increasingly recognised complication of pulmonary embolism. Perfusion scintigraphy is currently advocated as the imaging modality of choice to exclude CTEPH in patients with unexplained PH or suspected CTEPH due to its high sensitivity. In this chapter the diagnostic utility of MR lung perfusion with currently available imaging modalities was compared.

Methods

Consecutive patients attending a PH referral centre undergoing lung perfusion magnetic resonance imaging, perfusion scintigraphy, CTPA and RHC within 14 days were enrolled. Contrast enhanced MR lung perfusion images were acquired on a 1.5 Tesla scanner using a time resolved 3D spoiled gradient echo sequence.

Results:

Of 132 patients, 78 patients had CTEPH. Six magnetic resonance images were classed as non-diagnostic due to artefact. Lung perfusion MRI correctly identified 76 patients as having CTEPH with overall sensitivity of 97%, specificity of 92%, positive predictive value of 95%, negative predictive value of 96% and accuracy of 95% compared to perfusion scintigraphy (sensitivity of 96%, specificity of 90% and accuracy of 94%). In total 222 lobes were identified as having perfusion defects on MR images compared to 209 on perfusion scintigraphy images. No cases of surgically accessible disease were missed with either modality.

Conclusion:

MR lung perfusion imaging has high sensitivity equivalent to that of perfusion scintigraphy, in diagnosing CTEPH but does not require ionising radiation making it an attractive initial imaging modality to assess patients with suspected CTEPH.

3.2 Background

In patients with surgically accessible CTEPH, pulmonary endarterectomy offers a prospect of cure whereas patients with surgically inaccessible disease may benefit from targeted drug therapies [116]. Consequently, there is increasing interest in identifying patients with CTEPH. Many are now seen in dedicated clinics after an episode of proven thrombo-embolism, but a significant proportion still present with breathlessness or unexplained PH with or without a history of embolic disease.

Perfusion scintigraphy is widely advocated in these patients as it benefits from being widely available and has high sensitivity for CTEPH even in inexperienced hands [54]. In contrast, subtle changes associated with chronic thromboembolic disease may be missed on CTPA. Consequently, perfusion scintigraphy is currently recommended as the initial investigation to exclude CTEPH [36].

3D contrast enhanced lung perfusion MRI tracks the dynamic passage of contrast bolus providing regional insight into pulmonary perfusion. Previous studies have demonstrated the feasibility of this technique and have compared it with perfusion scintigraphy in small mixed cohorts of patients with various underlying lung pathologies [93, 96, 126-128]. There is only limited data on the performance of 3D contrast enhanced lung perfusion MRI in diagnosing CTEPH in a high-risk population [91, 93, 129].

3.3 Objective

The aim of this study was to evaluate the diagnostic accuracy of 3D contrast enhanced lung perfusion MRI alongside currently available imaging modalities in the clinical setting to identify CTEPH in patients with unexplained PH or suspected CTEPH with a history of pulmonary thromboembolic disease.

3.4 Methods

3.4.1 Study cohort

This was a retrospective study of consecutive patients with suspected CTEPH or unexplained PH attending a pulmonary hypertension (PH) referral centre between October 2009 and September 2011. The systematic assessment practiced in our centre for evaluation of patients with suspected PH using a multi-modality imaging and right heart catheter approach is described in the ASPIRE Registry [130]. Inclusion criteria required MR lung perfusion imaging, perfusion scintigraphy and CTPA and RHC to be performed within 14 days.

3.4.2 Image acquisition

MR perfusion: Contrast enhanced 3D MR lung perfusion images were acquired using a time resolved 3D spoiled gradient echo sequence with view sharing (TRICKS)[125]. This sequence was acquired during full inspiratory breathhold after intravenous administration of 0.05 ml/kg of Gadovist (Schering, Berlin) injected at 4 ml/s followed by a 20ml saline flush. 40 3D image volumes were acquired consecutively depicting the passage of contrast bolus at an effective frame rate of two 3D volumes per second. To obtain full lung coverage an average of 24 slices were obtained with a total breath hold time of 25 seconds. The perfusion images were generated by subtraction of the pre-contrast data time frame from the peak enhancement post contrast time frame on a voxel-by-voxel basis on a MR workstation.

Perfusion scintigraphy: The perfusion scintigraphy images were obtained with the patient in the supine position following intravenous administration of technetium 99m labelled macro-aggregated albumin (dose of 100-MBq; MAASOL; Amersham Health, Vienna, Austria). Scanning was performed on a gamma camera system (GE Millennium, GE Infinia, or Siemens Symbia gamma camera systems) with a 256 x 256 matrix using a 20% window centered over the 140-keV energy peak. Four standard images (anterior, posterior, right posterior oblique and left posterior oblique) were obtained for 500,000 to 750,000 counts each.

CT pulmonary angiography: The CT was performed on a 64 slice MDCT scanner (Light-Speed General Electric Medical Systems, Milwaukee, WI). CTPA was performed during a single breath-hold following and standard acquisition parameters were used: 100 mA with automated dose reduction, 120 kV, pitch 1, rotation time 0.5 s and 0.625mm collimation. The field of view was 400x400 mm with an acquisition matrix of 512 x 512. 100ml of intravenous contrast agent (Ultravist 300; Bayer Schering, Berlin, Germany) was administered at a rate of 5ml/sec. The CTPA images were reconstructed using a soft filter to provide contiguous 0.625 mm axial slices from the apex of the lung to the diaphragm for review.

3.4.3 Image analysis

MR images: The MR images were independently analysed by two radiologists (2 years of experience in PH imaging) who were blinded to the results of other imaging studies and clinical information. The MRI images generated are peak enhancement maps of lung perfusion. Images were analysed in the coronal plane and the image quality was graded on a three-point scale [131]: 1) un-interpretable 2) interpretable but of marginal image quality, or 3) of sufficient image quality to obtain a confident diagnosis. The observers independently evaluated the perfusion images for perfusion defects. A perfusion defect was defined as a lung region with decreased or no visible contrast enhancement. A diagnosis of CTEPH was made when there were one or more segmental and / or circumscribed perfusion defects, based on evidence from previous studies [93, 132]. The distribution of perfusion defects was also recorded as upper, middle or lower zone in the right lung and upper and lower in the left lung. If the observers disagreed, a separate consensus reading took place and the consensus report was used in all further analysis. MR perfusion images were evaluated without referring to other MRI techniques as the purpose was to evaluate the standalone value of perfusion MRI.

Scintigraphy: Scintigraphy images were interpreted according to the modified PIOPED criteria [52] and a high-probability scan was suggestive of chronic thromboembolic pulmonary disease [52-53]. The perfusion scans were interpreted

by two specialist radiologists who are experienced (12 years) in reporting perfusion images. The indeterminate scan for the purpose of this study was considered as negative. A single dataset of perfusion analysis were obtained. In conventional practice ventilation scans are performed in the patients with indeterminate perfusion scans. This is not in our usual practice as for the final clinical decision making at the MDT the perfusion images were interpreted in conjunction with CTPA and MRA.

CTPA: CT findings of lack of contrast filling in the arterial vessel, intraluminal or eccentric contrast filling defects, calcified filling defects, recanalization, abrupt change in vessel calibre, strictures, post-stenotic dilatation, webs and parenchymal heterogeneity typical of perfusion abnormalities were considered suggestive of chronic thrombotic disease [61]. These CTPAs were interpreted by two radiologists with 10 years experience in reporting CTPA for presence or absence of chronic thromboembolic disease. A single dataset of CTPA analysis were obtained.

Final reference diagnosis

The final diagnosis of CTEPH or non-CTEPH was made at a multi-disciplinary meeting. This decision was based on clinical assessment, imaging findings (but not 3D MR perfusion maps) and right heart catheter haemodynamics. Imaging techniques of perfusion scintigraphy, MR angiography and CTPA were used as reference studies. Patients with a diagnosis of CTEPH were then referred to the national centre for pulmonary endarterectomy at Papworth and a final diagnosis of surgically accessible or inaccessible disease was made. Appropriate patients with surgically accessible disease were offered pulmonary endarterectomy. Follow-up data was retrieved on outcome following pulmonary endarterectomy.

3.4.4 Statistical analysis

Sensitivity, specificity, positive predictive value and negative predictive value were calculated with 95% confidence interval (CI) for detection of CTEPH on MR perfusion images, perfusion scintigraphy and CTPA. Kappa statistics were used to analyze inter-observer agreement and to measure agreement between imaging modalities for the detection and location of perfusion defects.

3.5 Results

The mean age of patients was 69±12 years. The mean time between right heart catheterisation and completion of multi-modality imaging was 1.8±6.5 days. 132 patients met the entry criteria for this study. Three patients had digital subtraction angiography. A summary of patient classification and demographics is outlined in figure 45 and table 6.

Non-diagnostic images: 6 patients (5%) had MR perfusion images that were considered to be of non-diagnostic quality due to patient breathing motion artefact. For the purpose of this study the non-diagnostic images were excluded when calculating the sensitivity, specificity and accuracy values. The results with the inclusion of the non-diagnostic images are shown in table 9 and 10.

Table 6: Patient demographics and right heart catheter parameters

	Whole Group n=126	CTEPH n=78	Non-CTEPH n=48	p-value
Age (yrs)	62(14)	59 (16)	64 (17)	0.47
Female (%)	58	56	66	0.9
mRAP (mmHg)	11(5)	11 (5)	10 (4)	0.67
mPAP (mmHg)	42 (13)	43 (11)	40 (14)	0.11
PCWP (mmHg)	12(6)	10(5)	14(6)	0.02
CI (L.min.m2)	2.7 (0.9)	2.9 (1)	2.7(1)	0.11
PVR (dyn.s.cm-5)	435 (365)	599(373)	429(365)	0.04
TPR ()	792 (267)	801(231)	789 (181)	0.4
mVO2 (%)	63 (8)	61(8)	66 (8)	0.008

mRAP-mean right atrial pressure; mPAP-mean pulmonary artery pressure; PCWP-pulmonary capillary wedge pressure; CI-cardiac index; PVR –pulmonary vascular resistance; TPR- total pulmonary resistance; mVO2 -mixed venous oxygen saturation (standard deviation in brackets)

Figure 44: Patient classification

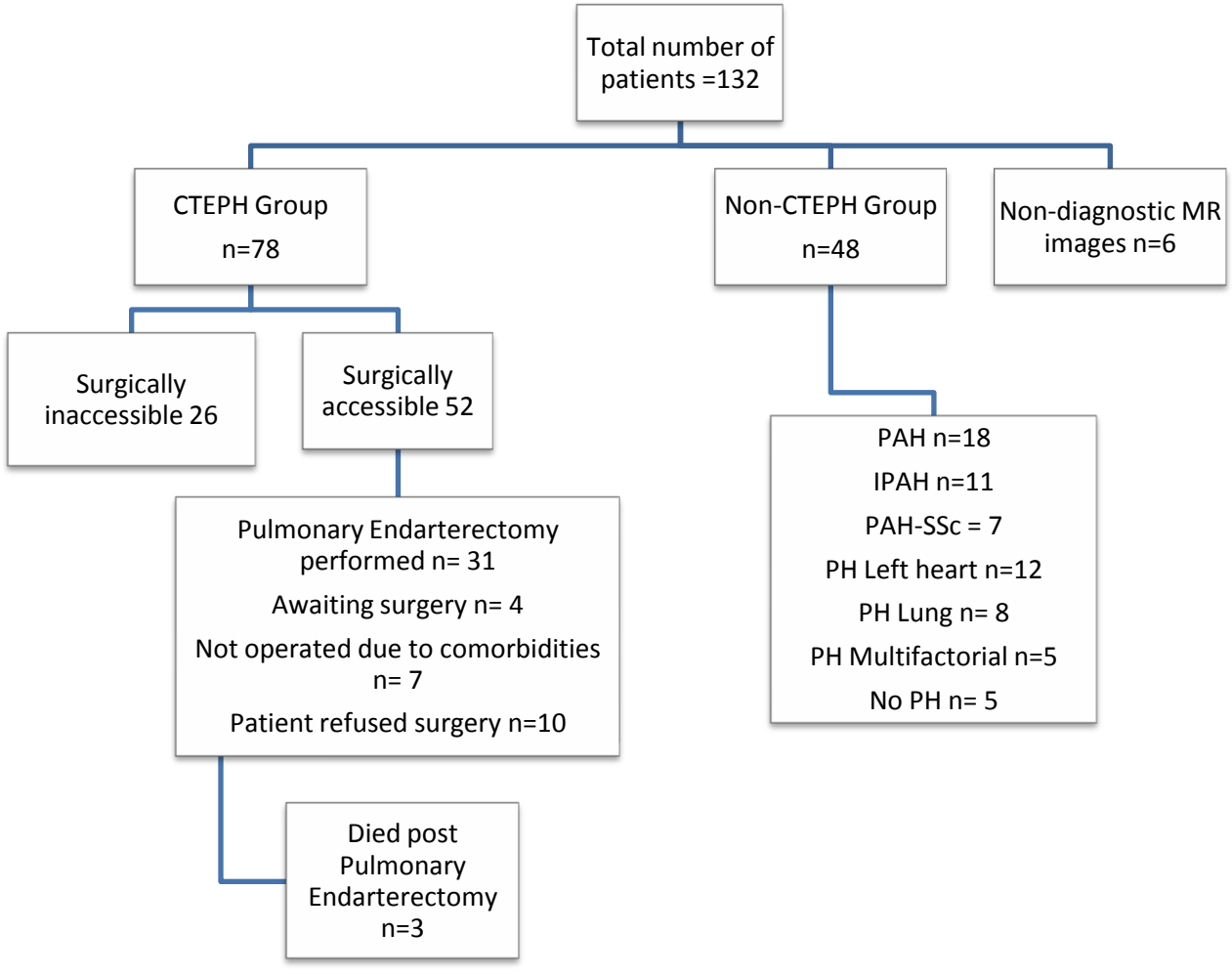

Abbreviations: CTEPH-chronic thromboembolic pulmonary hypertension; PH-pulmonary hypertension; IPAH – idiopathic pulmonary arterial hypertension; PAH- pulmonary arterial hypertension; SSc – Systemic Sclerosis

CTEPH group: 78 patients were diagnosed with CTEPH. In 52 patients (67%) disease was considered to be surgically accessible by the national centre for pulmonary endarterectomy. The MR perfusion sequence correctly identified 76 patients to have CTEPH. 2 patients were falsely reported as showing features suggestive of CTEPH, giving a sensitivity of 97% (95% CI: 91% to 99%), specificity of 92% (95% CI: 80% to 97%), positive predictive value (PPV) of 95% (95% CI: 88% to 99%) and negative predictive value (NPV) of 96% (95% CI: 85% to 99%). (Figure 46, Table 7 and table 8).

Table 7: Summary of results for perfusion scintigraphy, 3D MR perfusion and CT images

Groups	Perfusion scintigraphy		3D MR perfusion		CT	
	+	-	+	-	+	-
CTEPH (n=78)	75	3	76	2	73	5
Non-CTEPH (n=48)	5	43	4	44	1	47

Table 8: Summary of diagnostic performance of perfusion scintigraphy, MR perfusion and CTPA

	Q scan	MR perfusion*	CTPA
Sensitivity	96 (CI:0.89 to 0.99)	97 (CI:0.91 to 0.99)	94 (CI:0.85 to 0.98)
Specificity	90 (CI:0.77 to 0.97)	92 (CI:0.80 to 0.97)	98 (CI:0.88 to 0.99)
Positive predictive value	94 (CI:0.86 to 0.98)	95 (CI:0.88 to 0.99)	99 (CI:0.92 to 0.99)
Negative predictive value	93 (CI:0.82 to 0.99)	96 (CI:0.85 to 0.99)	90 (CI:0.78 to 0.96)
Accuracy	94	95	95

*__Inter-observer agreement__ for 3D-MR perfusion imaging for the presence or absence of CTEPH, kappa of 0.83; CI- confidence interval

Non diagnostic images: As an 'intention-to-analysis' the basis the sensitivity, specificity, PPV and NPV of 3D MR perfusion was calculated including the non-diagnostic MR images and the results are presented in tables 9 and 10.

Table 9: Summary of diagnostic performance of MR perfusion with the inclusion of the non-diagnostic scans

	MR perfusion
Sensitivity	93 (CI:0.85 to 0.97)
Specificity	92 (CI:0.80 to 0.97)
Positive predictive value	95 (CI:0.88 to 0.99)
Negative predictive value	88 (CI:0.77 to 0.96)
Accuracy	91

6 MR perfusion scan were non-diagnostic

Table 10: Summary of diagnostic performance of MR perfusion with the inclusion of the non-diagnostic scans

Groups	3D MR perfusion	
	+	-
CTEPH (n=82)	76	6
Non-CTEPH (n=50)	4	46

6 MR perfusion scan were non-diagnostic

Non-CTEPH group: 48 patients showed no evidence of CTEPH and were grouped as non-CTEPH. This group included patients with a diagnosis of no PH (n= 5), and all major forms of PH including pulmonary arterial hypertension (n= 18), PH associated with left heart disease (n= 12), PH associated with lung disease (n= 8) and PH multifactorial (n=5) [42]. 44 of 48 patients were reported as non-CTEPH and 4 patients were falsely identified as having CTEPH based on MR perfusion images.

In total, MR perfusion images identified perfection defects in 222 lobes compared to 209 identified by perfusion scintigraphy. The inter-observer agreement for the diagnosis of CTEPH on perfusion MRI was excellent with kappa of 0.83. Our results also showed CTPA to be effective in the diagnosis of CTEPH with a sensitivity of 94% (95% CI: 85% to 98%), specificity of 98% (95% CI: 88% to 99%), NPV of 99% (95% CI: 92% to 99%) and PPV 90% (95% CI: 78% to 96%). Mosaic pattern of pulmonary attenuation on CT was present in 55 % (43/78) of patients in the CTEPH group and in 17% (8/48) in the non-CTEPH group confirming that this feature is not specific for CTEPH [54, 133-134]. None of the imaging modalities missed any of the patients with surgically accessible CTEPH.

Interobserver agreement:

The overall inter-observer agreement was a kappa of 0.83 for diagnosing the presence or absence of CTEPH on 3D-MR perfusion images. The interobserver agreement on a perfusion defect by perfusion defect basics was 0.57.

Intermodality agreement:

There was an excellent overall agreement between perfusion scintigraphy and 3D-MR perfusion with kappa of 0.97 for diagnosing presence or absence of CTEPH. The inter-modality agreement however varied depending on the location of the defect, with better agreement in the upper lobes compared to lower lobes (Table 11).

Table 11: Agreement between MR perfusion and perfusion scintigraphy

Regions (Q scan/MRI)	Kappa
Right upper lobe	0.84
Right middle lobe	0.82
Right lower lobe	0.70
Left upper lobe	0.80
Left lower lobe	0.69
Overall diagnosis	0.97

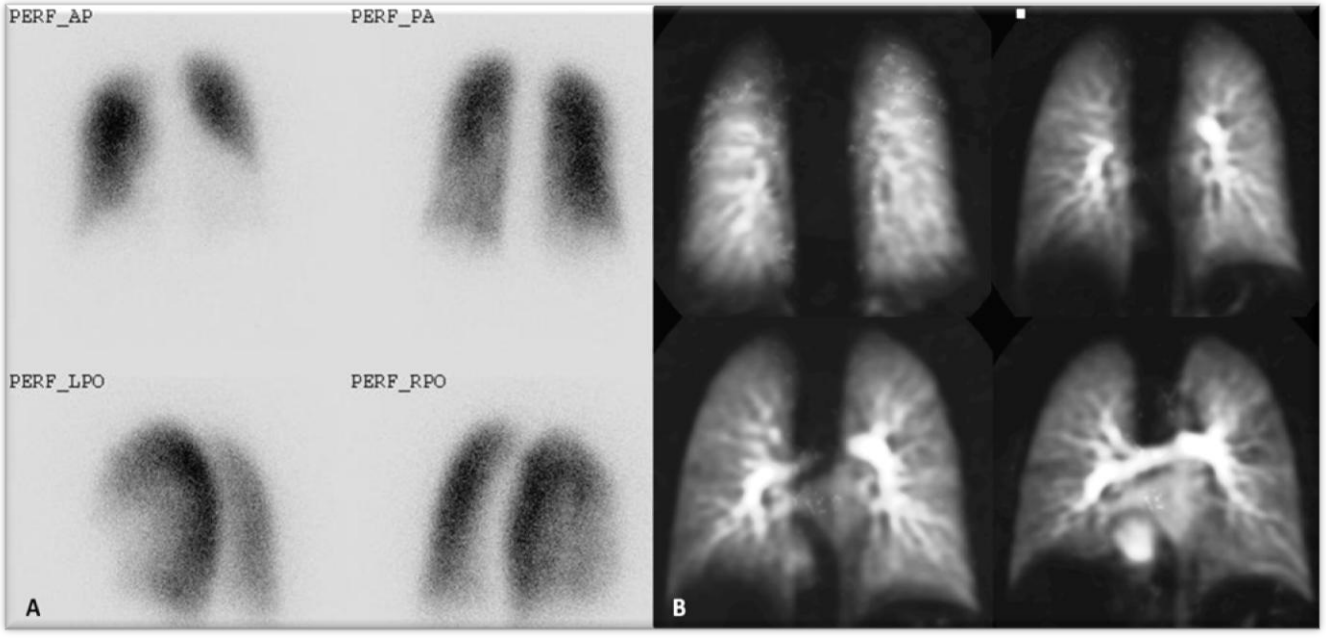

Figure 45: Example of a patient with normal lung perfusion on perfusion scintigraphy (A) and coronal representative MR perfusion images (B)

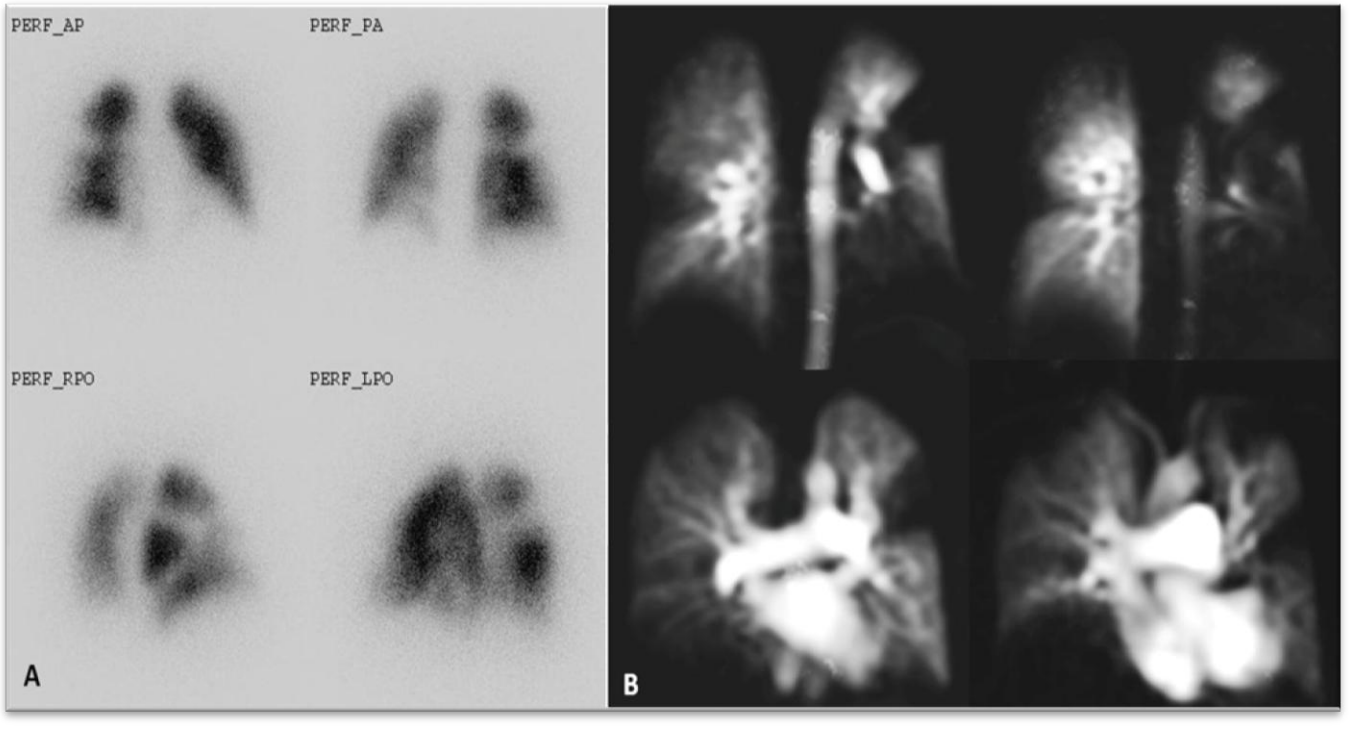

Figure 46: Bilateral multiple segmental perfusion defects on perfusion scintigraphy (A) and coronal MR perfusion images (B) consistent with a diagnosis of Chronic Thromboembolic Pulmonary Hypertension

Table 12: Summary of False-Positive perfusion MR, perfusion scintigraphy and CT images

Modality	Diagnosis
Perfusion MRI	1. Systemic sclerosis and pulmonary fibrosis (n=2) 2. PAH with background pulmonary emphysema (n=2)
Perfusion Scintigraphy	1. Scleroderma and pulmonary fibrosis (n=2) 2. PAH with background pulmonary emphysema (n=1) 3. PAH associated with congenital heart disease (n=1) 4. Pulmonary hypertension secondary to lung disease (n=1)
CT	1. PH associated with Pulmonary fibrosis (n=1)

PAH-pulmonary arterial hypertension; IPAH-idiopathic pulmonary arterial hypertension
Patients in 1 and 2 were the same for perfusion MRI and perfusion scintigraphy

The scan time for 3D perfusion MRI is fast. The images are acquired using a partial k-space view sharing algorithm [125] ; this combined with parallel imaging reduces the scan time making this 3D time resolved technique feasible even in symptomatic patients during typical breath-holds [96, 135]. The spatial resolution of 3D contrast enhanced lung perfusion MRI gives better regional characterisation of perfusion defects than the projection images of perfusion scintigraphy and contributes to superior depiction of patterns of lung perfusion. Moreover the 3D perfusion MRI can be viewed in any slice orientation when compared to the projection image of perfusion scintigraphy.

Few studies in the literature have evaluated contrast-enhanced MRI for the assessment of regional lung perfusion in a clinical context. Amundsen et al initially proved the feasibility of 2D MR lung perfusion imaging for detecting perfusion defects distal to pulmonary emboli [132]. Subsequently further studies have reported convincing correlations between 3D MR perfusion with perfusion scintigraphy in patients with mixed lung pathologies [93, 96, 126-128]. Fink et al

observed significant difference in signal-to-noise ratio (SNR) between normally perfused lung and areas of perfusion defects [135]. Furthermore, the temporal information from 3D dynamic contrast-enhanced MR perfusion also has been employed for quantitative spatio-temporal assessment of regional pulmonary perfusion [94, 106]. This quantitative type of analysis is fully compatible with our data acquisition strategy used here and in current work we are comparing map of blood volume and contrast agent transit time using tracer dilution theory.

Limitations

The patients included represent a selected population referred to a PH centre. Nonetheless this has allowed a large population of patients with CTEPH to be studied and represents a group at high risk of CTEPH where this imaging technique could clearly be employed. Secondly, we used as our gold standard for the identification of CTEPH, a multidisciplinary assessment with diagnosis validated at a national pulmonary endarterectomy centre. Pulmonary angiography is often quoted as the 'gold standard' investigation supplemented by right heart catheterisation for the diagnosis of CTEPH, however, our reference standard combined a number of imaging modalities. Thirdly, in this study of patients with suspected PH there was a low prevalence of lung disease and although this is representative of patients with severe PH undergoing evaluation, the diagnostic accuracy of this technique if applied to the general population in particular post pulmonary embolism is likely to be lower, although one would not expect this to affect the ability of this technique to exclude CTEPH. Finally, tomographic techniques such as single photon emission computed tomography (SPECT) lung perfusion scintigraphy that have been shown to perform better than planar perfusion scintigraphy [136]. This technique is, however, not currently routinely implemented in clinical practice and is associated with higher radiation exposure [137]. We have utilised the peak enhancement images to assess for perfusion defects of CTEPH. The Patients with CTEPH frequently have delayed pulmonary perfusion through bronchial and non-bronchial collateral circulations. By imaging using the first pass technique the delayed lung perfusion via the collateral circulation would be missed. Perfusion scintigraphy on the other hand gives the total lung perfusion as aggregates do not cross the pulmonary capillary bed and the acquisitions time is longer. Our results also show good interobserver agreement (kappa of 0.87) for diagnosing presence or absence of CTEPH however

the agreement for identifying defects at a segment–by-segment level was moderate with kappa of 0.57.

3.6 Conclusion

This study demonstrates that non-invasive assessment with non-ionising 3D-MR lung perfusion imaging has high diagnostic accuracy, comparable to that of perfusion scintigraphy, in patients with suspected CTEPH. This work demonstrates that normal MR lung perfusion excludes operable CTEPH and supports the further evaluation of MRI in the assessment of patients with suspected chronic thrombo-embolic pulmonary hypertension.

To enable translation of MR perfusion imaging into clinical practice the first step would be to prove the robustness of this technique in non-selected group of patients and to show the reproducibility of this technique across different lung perfusion findings. This would then be followed by replacing perfusion scintigraphy with MR lung perfusion especially in patients suspected with CTEPH. Secondly, the accuracy of MR perfusion imaging should also be evaluated for acute pulmonary embolism. By eventually replacing perfusion scintigraphy with MR lung perfusion unnecessary radiation dose can be avoided.

4 Chapter 4: Contrast-Enhanced MR Angiography in patients with Chronic Thromboembolic Pulmonary Hypertension

This chapter was published in part in the manuscript published in European Radiology "Diagnostic Accuracy of Contrast-Enhanced MR Angiography and Unenhanced Proton MR Imaging Compared with CT pulmonary angiography in Chronic Thromboembolic Pulmonary Hypertension" *Rajaram S, Swift AJ et al, European Radiology 2012 Feb; 22(2):310-7*

CTEPH is a major subtype of pulmonary hypertension that is potentially curable surgically and an imaging tool that provides accurate information on the extent and pattern of thromboembolic disease is essential for surgical planning. These patients frequently also require follow up imaging to assess for treatment response; hence the imaging method should ideally be reproducible and radiation-free.

In the previous chapter of thesis the value of 3D MR lung perfusion as a *screening tool* for identifying patients with CTEPH was demonstrated.

This chapter of thesis focuses on the value of MRI in characterizing the extent and pattern of the thrombus itself in chronic thromboembolic disease in patients with suspected CTEPH.

4.1 Abstract

Objectives:

To evaluate the diagnostic accuracy and characterize chronic thromboembolic disease with contrast enhanced MR angiography (ce-MRA) and to assess the added benefit of unenhanced proton MR angiography compared with CT pulmonary angiography (CTPA) in patients with chronic thromboembolic disease (CTE).

Methods:

A 2 year retrospective study of 53 patients with chronic thromboembolic pulmonary hypertension who underwent CTPA and MRI for suspected pulmonary hypertension and a control group of 36 patients with no CT evidence of pulmonary embolism. The MRI was evaluated for CTE and the combined diagnostic accuracy of ce-MRA and unenhanced proton MRA was determined.

Results:

The overall sensitivity and specificity of ce-MRA in diagnosing proximal and distal CTE were 98% and 94% respectively. The sensitivity improved from 50% to 88% for central vessel disease when ce-MRA images were analysed in parallel with unenhanced proton MRA. The ce-MRA identified more stenosis (29/18), post-stenosis dilatation (23/7) and occlusion (37/29) compared with CTPA.

Conclusion:

Ce-MRA has very high sensitivity and specificity for diagnosing CTE. The sensitivity of ce-MRA for visualisation of adherent central and lobar thrombus significantly improves with the addition of the unenhanced proton MRA that clearly delineates the vessel wall.

4.2 Background

Traditionally imaging techniques such as nuclear medicine ventilation-perfusion (V/Q) scintigraphy, pulmonary angiography and more recently CTPA have been used in the diagnostic work-up of patients with suspected CTEPH. Invasive pulmonary angiography depicts the angiographic changes of CTEPH and is considered to be the definitive investigation for assessment of surgically treatable CTEPH [138-139]. The main disadvantage of this technique is the invasive nature of this investigation and it can cause discomfort and comes with a mortality risk (0.5%), albeit small [20].

Patients with CTEPH will often require repeated studies to confirm the diagnosis, to assess the course of the disease and to monitor outcome and hence an alternative radiation-free imaging technique would be ideal. In the last decade, MRI techniques such as pulmonary MR angiography (MRA) and lung perfusion imaging have proved to be promising for the evaluation of patients with CTEPH [92, 140].

4.3 Objective

The aim of our study was to twofold

1. First to evaluate the diagnostic accuracy and characterize the disease on contrast enhanced MR angiography (CE-MRA) when compared to CTPA in patients with suspected CTEPH.
2. To assess the added benefit of unenhanced proton MRA using 2D balanced Steady State Free Precession (bSSFP) sequence alongside CE-MRA and compared with CTPA.

4.4 Methods

4.4.1 Study cohort

All patients referred to our institute for the evaluation of CTEPH in the period from January 2008 to March 2010 were considered for this study. The study patients belonged to the following two groups: 53 patients with CTEPH and 36 patients with no pulmonary hypertension (mPAP <25) at right heart catheterisation and no CT evidence of embolic disease. All patients included in this study underwent CT and MRI within a time interval of 48 hours.

4.4.2 Image acquisition

Contrast enhanced MRA was performed following an injection of 15ml contrast agent ensuring the total dose of contrast doesn't exceed 0.3ml/kg. This scan was preceded by a timing bolus of contrast agent (0.05ml/kg). The sequence parameters used were: 3D Coronal Spoiled Gradient Echo, TE 1.0ms, TR 2.8 ms, flip angle of 30°, FOV=48 cm2, 2x Asset, 300 x 200 Matrix, 125 kHz bandwidth, slice thickness of 3 mm and average of 60 slices. This was a breath-hold sequence acquired during inspiration.

Unenhanced proton MRA was performed as a stack of coronal 2D SSFP images, with the following parameters: TR 2.8 ms, TE 1.0ms, flip angle of 50°, FOV=48 cm x 43.2 cm, 256 x 256 matrix, 125-kHz bandwidth and slice thickness of 10 mm. This sequence was performed at full inspiration and with a total breath-hold time of 12 seconds.

CTPA was performed on a 64 slice MDCT scanner (Light-Speed General Electric Medical Systems, Milwaukee, WI). CTPA was performed during a single breath-hold following and standard acquisition parameters were used: 100 mA with automated dose reduction, 120 kV, pitch 1, rotation time 0.5 s and 0.625mm collimation. The field of view was 400x400 mm with an acquisition matrix of 512 x 512. 100ml of intravenous contrast agent (Ultravist 300; Bayer Schering, Berlin, Germany) was administered at a rate of 5ml/sec. The CTPA images were reconstructed using a soft filter to provide contiguous 0.625 mm axial slices from the apex of the lung to the diaphragm for review.

4.4.3 Image analysis

The CTPA and MRA were analysed by two radiologists (2 years of specialised experience in reporting CTPA and MRA for suspected CTEPH). The data was collected by the two radiologists resulting in two independent datasets. The volumetric MRA dataset and the MR maximum intensity projection (MIP) images were reviewed on a standard GE workstation by two radiologists blinded to the CT findings. The MR perfusion images were not available or used for interpretation of CT. In cases of discrepancy between observers, a consensus read was performed jointly by the two observers in a separate setting and this was used in all further analysis. The image quality was assessed subjectively and graded for artefacts as "none", "mild", "moderate" or "non-diagnostic". For CTPA all window settings including the lung window was available.

The ce-MRA images were examined for the presence of thromboembolic disease at central, lobar, segmental and sub-segmental vessels. The presence or absence of signs of chronic thromboembolism in the pulmonary artery such as complete or partial obstruction, adherent thrombus, bands, webs and post-stenotic dilatation was also studied. The unenhanced proton MRA was similarly evaluated for features of chronic thromboembolism and the combined diagnostic accuracy of ce-MRA and unenhanced proton MRA was assessed. The MR perfusion images discussed in the previous section was not used for the interpretation of MRA.

4.4.4 Statistical analysis

Direct comparison was made between MR and CTPA, using CTPA as the reference method. A Chi-squared test was used to establish sensitivity, specificity, positive and negative predictive values for detecting the presence and absence of PE. The Kappa statistic was used to determine the level of agreement between the independent observers. In cases of discrepancy between observers regarding abnormality detection, a final interpretation was obtained by consensus during a second session.

4.5 Results

Patient demographics:

One hundred and six patients underwent MRI and CT for suspected CTEPH. There were 63 patients with CTEPH and 43 patients with no evidence of pulmonary hypertension or pulmonary embolism and for the purposes of this study were considered 'normals'. The mean age of the patients was 61 years and the female to male ratio was 1.2. In 9 patients the renal function was impaired hence a ce-MRA was not performed.

Based on qualitative visual assessment of image resolution, clarity and breathing artefact, 33 MRI were deemed to have mild artefacts, 17 moderate artefacts and 8 were considered to be non-diagnostic. 89 MRI were of diagnostic quality (53 patients with CTEPH and 36 'normal' patients).

Figure 47: Flowchart representing study population and MRA quality

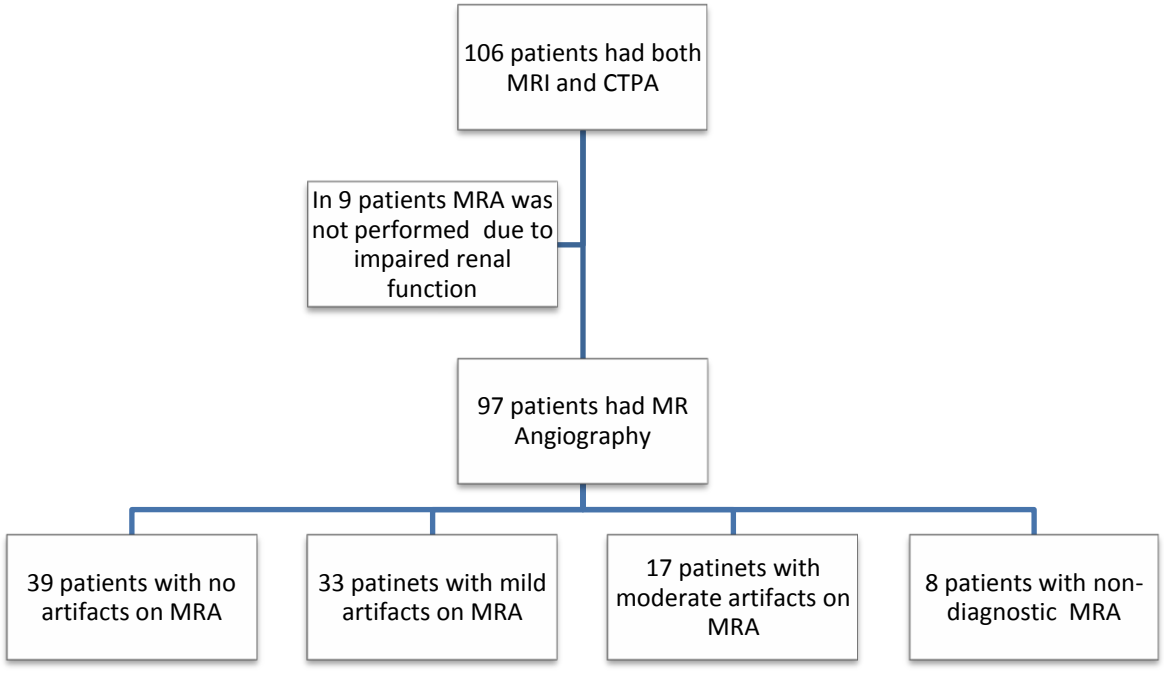

Diagnostic accuracy:

Of the 53 patients with CTEPH, 31 patients had proximal disease (involving central and lobar vessels) and 22 had distal disease (distal to lobar vessels). The overall sensitivity and specificity of ce-MRA in diagnosing CTE were 98% and 94% respectively with a positive predictive value of 96% and negative predictive value of 97%. 1 patient with isolated distal CTEPH was missed on ce-MRA and 2 patients were misdiagnosed to have CTEPH on ce-MRA. The non-diagnostic MRA images (8 scans) were excluded from this analysis.

Table 13: Overall sensitivity and specificity for ce-MRA compared with CTPA in diagnosing chronic thromboembolic disease

CTE	CTPA Present	CTPA Absent	Total
ce-MRA Present	52	2	54
ce-MRA Absent	1	34	35
Total	53	36	89

Sensitivity 98% (95% CI: 89–99), specificity 94% (81–99), positive predictive value 96% (87–99); Negative predictive value 97% (85–99); ce-MRA: contrast enhanced MR angiography

Table 14: Overall sensitivity and specificity for unenhanced MRA compared with CTPA for diagnosing proximal chronic thromboembolic disease

Proximal CTE	Present CTPA	Absent CTPA	Total
Present Non-contrast MRA	14	11	25
Absent Non-contrast MRA	17	35	52
Total	31	46	77

Sensitivity 45% (95% CI: 27–64), specificity 76% (61–87), positive predictive value 56% (35–76), negative predictive value 67% (53–80), 12 unenhanced MRA were non-diagnostic.

Non-diagnostic MR images: As an '*intention-to-analysis*' the basis the sensitivity, specificity, PPV and NPV of ce-MRA was calculated including the 8 non-diagnostic MR images and the results are presented in tables 15 and 16.

Table 15: Overall sensitivity and specificity for ce-MRA compared with CTPA in diagnosing CTE with inclusion of non-diagnostic scans

CTE	CTPA Present	CTPA Absent	Total
ce-MRA Present	52	2	54
ce-MRA Absent	3	40	43
Total	55	42	97

Sensitivity 94% (95% CI: 85–99), specificity 95% (84–99), positive predictive value 96% (87–99), Negative predictive value 93% (81–99); ce-MRA: contrast enhanced MRA
8 ce-MRA images were non-diagnostic.

Table 16: Overall sensitivity and specificity for unenhanced MRA compared with CTPA for diagnosing proximal chronic thromboembolic disease with inclusion of non-diagnostic scans

Proximal CTE	Present CTPA	Absent CTPA	Total
Present Non-contrast MRA	14	11	25
Absent Non-contrast MRA	21	43	64
Total	35	54	89

Sensitivity 40% (95% CI: 24–58), specificity 80% (66–89), positive predictive value 56% (35–76), negative predictive value 67% (54–78);
12 unenhanced MRA were non-diagnostic.

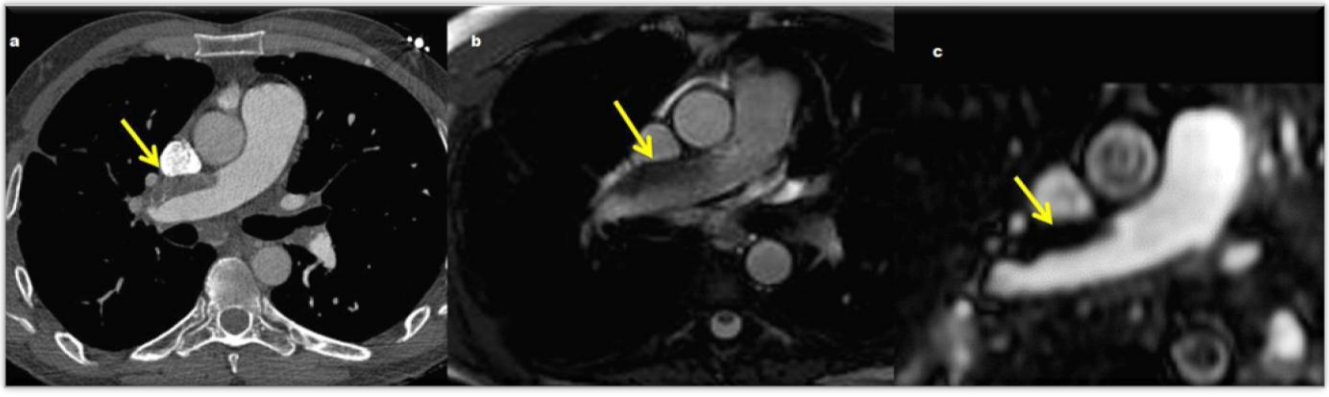

Figure 48: CTPA (a), unenhanced bSSFP MRI (b) and CE-MRA (c) show thromboembolic material adherent to the right main pulmonary arterial wall

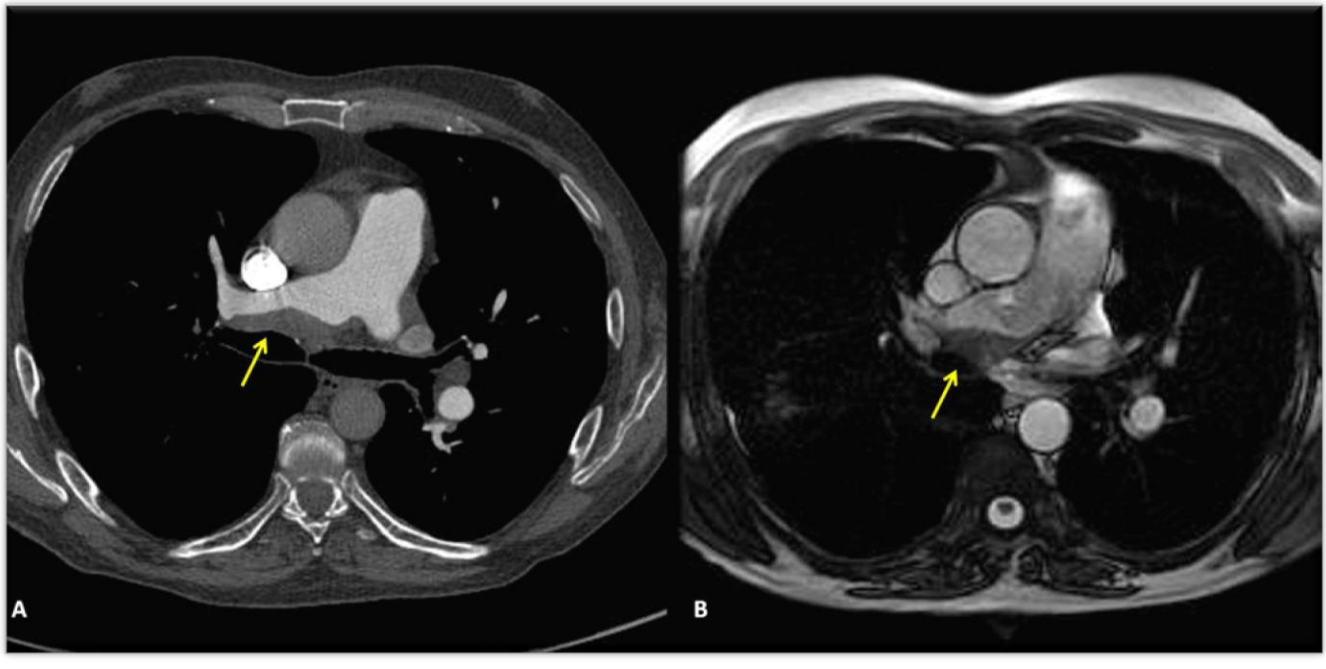

Figure 49: A wall-adherent chronic thromboembolism that was visualised better on CTPA (A) and unenhanced bSSFP sequence (B)

Level of disease:

The pulmonary vasculature was analysed for CTE at the central, lobar, segmental and sub-segmental levels and the ability of ce-MRA to identify disease at each of these levels is summarised in Table 17. Our results showed that the sensitivity for recognising lobar and segmental disease was 74% and 81% respectively. The sensitivity of ce-MRA for appreciating central disease was comparatively low at 50%, the reason being the poor contrast of smooth thromboembolic material adherent to the pulmonary vessel wall on ce-MRA images. With the addition of the b-SSFP unenhanced MRA sequence, which depicts the signal from vessel wall better, the sensitivity improved significantly from 50% to 88%. However we also found that using unenhanced proton MRA when viewed in isolation resulted in poor sensitivity (45%) and high false-positive rates for identifying proximal disease as shown in Table 17. 12 of the unenhanced MRA were non-diagnostic.

Table 17: Sensitivity of ce-MRA and the added benefit of unenhanced MRA in the diagnosis of CTEPH as a function of site of disease

	ce-MRA / CTPA	Sensitivity	kappa	ce-MRA + pMRA / CTPA	Sensitivity	kappa
Central	4/8	50%	1.0	7/8	87.9%	0.86
Lobar	20/27	74.07%	0.94	23/27	85.2%	0.79
Segmental	34/42	80.95%	0.86	34/42	80.95%	-
Sub-segmental	3/29	10.34%	0.74	3/29	10.34%	-

ce-MRA- contrast-enhanced MR angiography; pMRA- unenhanced proton MRA. Kappa in this context is the inter-observer agreement between the two readers for MRA.

Pattern of disease:

On assessing the various patterns of CTE disease appreciated on ce-MRA and CTPA, ce-MRA helps to recognise more stenosis (29 vs 18), post-stenosis dilatation (23 vs 7) and complete vessel obstruction (37 vs 29) when compared with CTPA. CTPA was superior to ce-MRA in identifying patients who had pulmonary wall adherent thromboembolic material and intra-luminal webs and bands (Table 18).

Table 18: Pattern of morphological changes found in ce-MRA and CTPA

Pattern of CTE	Ce-MRA	CTPA	kappa
Webs and bands	12	54	0.86
Stenosis	29	18	0.82
Post-stenotic dilatation	23	7	0.79
Occlusion	37	29	0.80
Adherent emboli	19	36	0.74

(Ce-MRA: contrast-enhanced MR angiography)

Kappa in this context is the inter-observer agreement between the two readers

Table 19: Interobserver agreement* for CTPA and ce-MRA for the level of CTE disease

Pattern of CTE	CT	MRA
Central	1.0	1.0
Lobar	0.96	0.94
Segmental	0.88	0.86
Sub-segmental	0.82	0.74

* Kappa analysis was used for interobserver agreement

Table 20: Interobserver agreement for CTPA and ce-MRA for the pattern of CTE disease

Pattern of CTE	CT	MRA
Webs and bands	0.92	0.86
Stenosis	0.89	0.82
Post-stenotic dilatation	0.86	0.79
Occlusion	0.90	0.80
Adherent emboli	0.85	0.74

* Kappa analysis was used for interobserver agreement

Interobserver agreement for MRA:

The interobserver agreement for the two radiologists for identifying the pattern of disease is as follows; kappa for presence of webs and bands is 0.86, stenosis is 0.82, post-stenotic dilatation is 0.79, occlusion is 0.80, adherent emboli is 0.74. For the level of disease the level of interobserver agreement between the two observers are for Central disease the kappa is 1.0, for lobar disease 0.94, segmental disease 0.86, sub-segmental disease is 0.74.

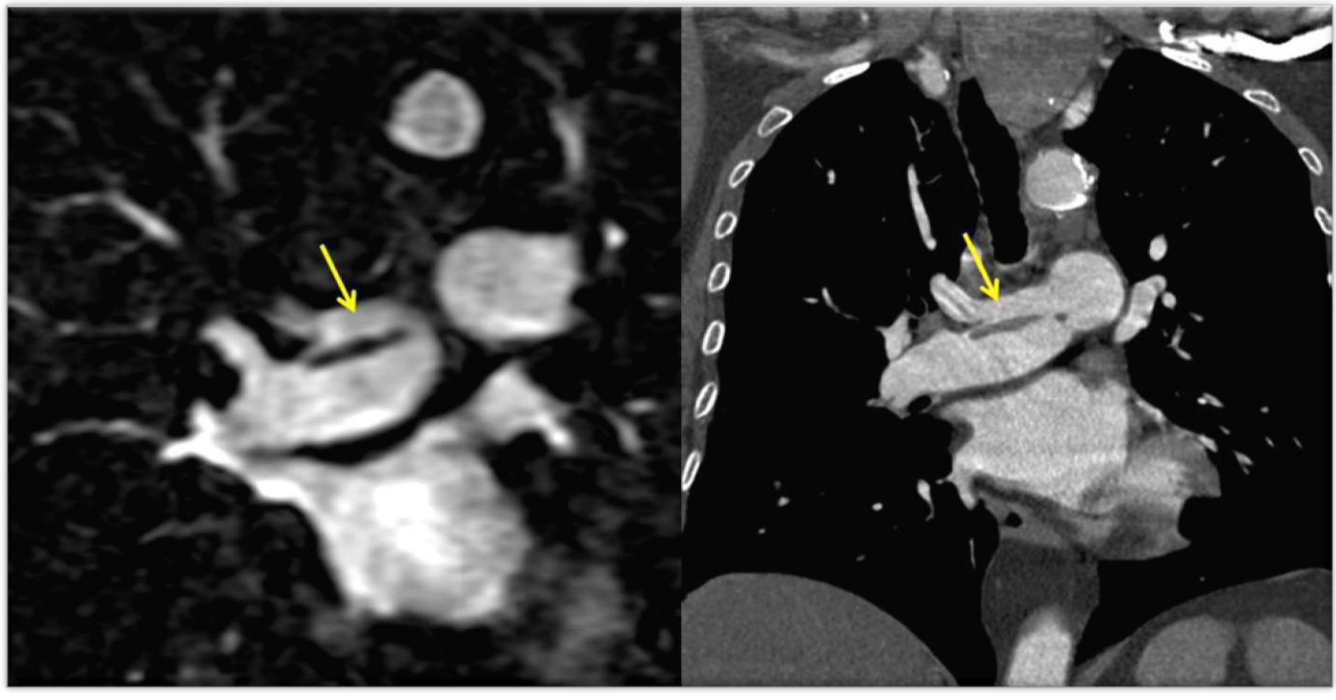

Figure 50: A central thrombotic web demonstrated clearly on CE-MRA and CTPA

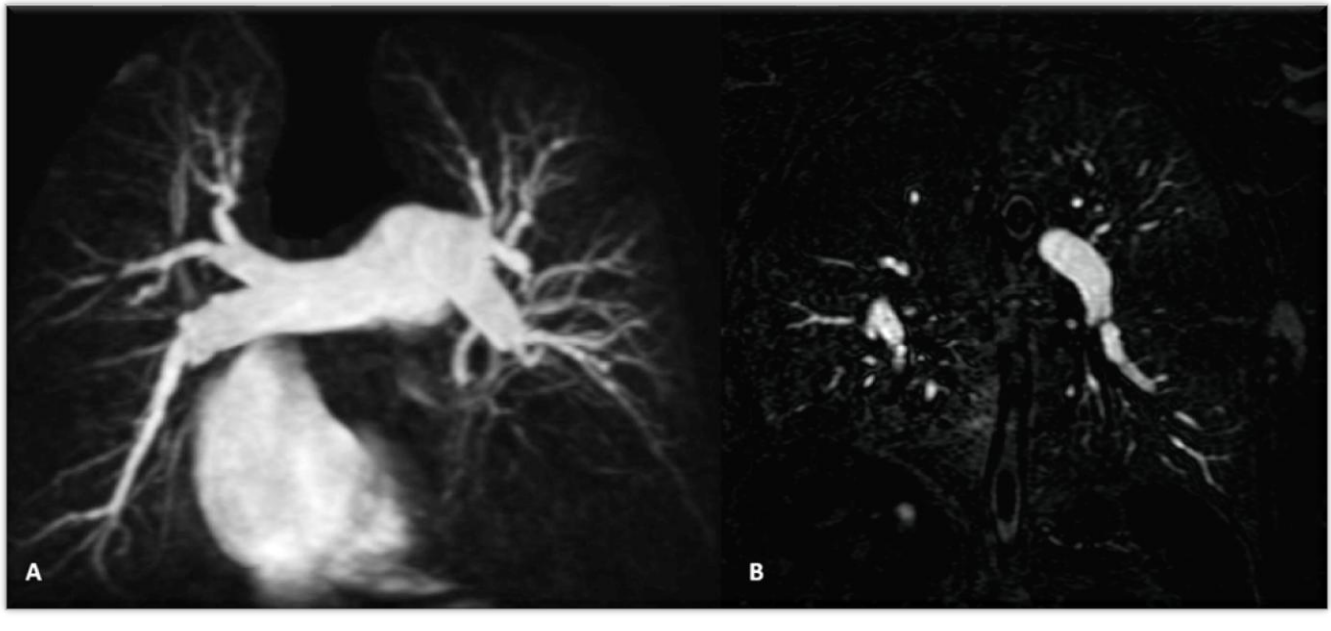

Figure 51: An example of a MIP generated from CE-MRA sequence showing complete occlusion of the left lower lobar branch and (B) a single slice showing stenosis with post stenotic dilatation (patient diagnosed with CTEPH)

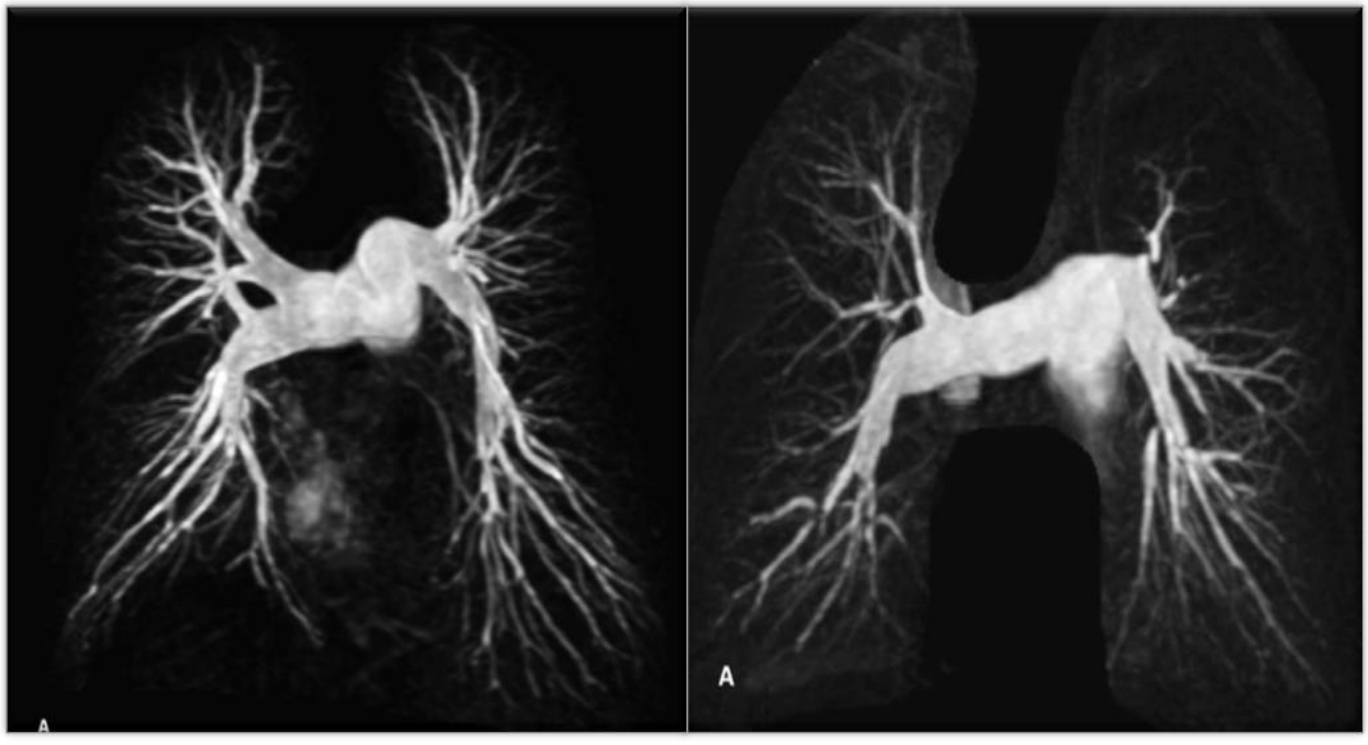

Figure 52: An example of a maximum intensity projection (MIP) image showing perfusion defects in a patient with CTEPH (right) and in a normal patient (left)

4.6 Discussion

Principal findings: We have demonstrated that ce-MRA has very high sensitivity and specificity in diagnosing the presence or absence of chronic thromboembolic disease in a population of patients with and without CTEPH undergoing evaluation for suspected PH. We have also shown that the addition of unenhanced proton MR improves the sensitivity of MR for the detection of proximal clot and that ce-MRA is superior in representing stenosis and post-stenotic dilatations compared with CTPA. The ce-MRA images were of sufficient quality to make a confident diagnosis in 92% of cases. To our knowledge, there have been no published studies analysing the added utility of this unenhanced proton MRA in demonstrating chronic thromboembolism.

Contrast-enhanced MRA is increasingly recognised as a valuable technique for imaging the pulmonary vasculature in patients with suspected CTEPH [73]. With the application of faster gradients and parallel imaging techniques, the duration of the breath-holding for the MRA sequences are significantly reduced and can rapidly characterise the pulmonary vasculature even in a symptomatic patient (breath-hold < 20 s). The presence of dilated bronchial arteries has been shown to correlate with a lower mortality rate after pulmonary endarterectomy and ce-MRA has been shown to accurately estimate the flow in the bronchial arteries in patients with CTEPH [141]. An MR technique that can demonstrate pulmonary vasculature without the use of contrast agent would be very useful and bSSFP is particularly suitable as it offers good contrast from the blood pool because of its inherent long T2 compared with tissue. Studies using this sequence in the imaging of coronary arteries have shown promising results [142-143]. One of the main difficulties of 3D SSFP coverage is the prolonged breath-hold time which can potentially be overcome by using a free-breathing navigator-gated technique [144].

Previous studies in patients with CTEPH have shown misdiagnosis of central wall-adherent thromboembolic material with both pulmonary angiography and CT and this was thought to be due to multiple factors [133, 145-146]. In chronic CTE, the residual thrombus is incorporated into the vessel wall and is covered by a new epithelial layer smoothing the intimal surface [145]. In ce-MRA, as in DSA and

CTPA, the vessel lumen is filled with contrast and in the absence of a wall irregularity an adherent thrombus may easily be missed.

The main problem in our study arose in viewing adherent thrombotic material that was flush with the vessel wall. One of the reasons for the insensitivity of ce-MRA in identifying central disease was that the vessel wall is not visualised in axial image data or the MIP images. This makes it difficult to appreciate the wall-adherent changes in some patients. In a 2D bSSFP image, the thrombus is demonstrated as an area of very low signal intensity compared with hyper-intensity surrounding flowing blood. As the vessel wall is clearly visualised with this sequence, any wall-adherent thromboembolic material is readily recognised. We have shown that addition of a simple unenhanced bSSFP MRA sequence the vessel wall is clearly delineated, which significantly improved the identification of the central and lobar adherent thrombotic disease.

Our study showed that there were false-positive results when unenhanced MRA images were used in isolation. The high false-positive rate was due to the relatively low spatial resolution of the bSSFP sequence (Figure 6), but this could be improved easily by increasing the data acquisition time or performing repeat imaging at higher resolution on selected slices of interest (Figure 7). Hence our recommendation is to use unenhanced MRA images as a routine adjunct to ce-MRA especially when assessing for proximal disease.

Limitations

There are several limitations to our study. The patients included were referred to a PH referral centre with suspected PH and represent a selected population and does not represent the wider general population. Secondly, we have compared MRA with CTPA rather than using pulmonary angiography. This we feel is acceptable as the aim was the compared the performance of MRA against CTPA that is widely used for the assessment of the embolic load. A recent report also showed ECG gated CTPA and MRA to be superior to pulmonary angiography in detecting CTEPH [147]. Although we have performed interobserver agreement for the pattern and level of disease a more thorough evaluation of a pattern-by-pattern basics would be more accurate.

4.7 Conclusion

In conclusion, ce-MRA has very high sensitivity and specificity in identifying patients with CTEPH. One of the limitations of ce-MRA, as with DSA, is the inability to accurately identify wall-adherent thromboembolic material. This can be overcome to an extent with the use of an unenhanced bSSFP sequence. The non-ionising nature of this investigation makes it attractive in the initial evaluation of patients with persisting breathlessness following acute PTE and in the follow-up of patients with CTEPH. This sequence also provides a parallel means of assessment of lung parenchyma (see chapter 7).

5 CHAPTER 5-CT features of pulmonary arterial hypertension and its major subtypes

The focus of the previous two chapters was on the usefulness of MRI in patients with CTEPH. In this chapter another major group of PH, pulmonary arterial hypertension, is studied with CT. Although this group share a similar clinical presentation, pathogenesis and treatment options, they are heterogenous disorders with varied outcome and imaging characteristics.

Patients with PAH commonly present with cardio-respiratory symptoms and routinely undergo thoracic CT. There are several features on thoracic CT that would point towards an underlying cause of pulmonary arterial hypertension. In this chapter the prevalence of these CT changes in each of the major subcategories of PAH is analysed and usefulness of CT as a prognostic tool is also evaluated.

This work forms the basis of a paper in preparation for *European journal of Radiology.*

5.1 Abstract

Objective: To study the prevalence and prognostic value of cardiac, vascular and parenchymal CT findings in PAH and its major subtypes from a large cohort of consecutive treatment naive patients.

Methods: 444 patients with PAH were identified from a major UK PH centre as part of the ASPIRE Registry. From this database, 292 patients who had mutlislice CTPA within 3 months of RHC were identified. Several measurements such as RV size, thickness of the RV free wall, aorto-pulmonary ratio, IVC size, pericardial effusion and tricuspid regurgitation. Images were also assessed for ground glass opacity (GGO), lymphadenopathy, bronchial collaterals, septal lines, ascites and oesophageal dilatation.

Results: The pulmonary artery: aortic ratio was 1.16(0.21) and significantly greater in PAH-CHD-Eisenmenger 1.46(0.45), $p<0.05$. Pulmonary artery calcification (13%) and thrombus (10%) were exclusively seen in PAH-CHD. Collateral vessels were most common in PAH-CHD-Eisenmenger (55%). The right to left ventricular (RV: LV) ratio was 1.25(0.42) with no statistically significant differences between groups. Pericardial (38%) and pleural effusions (11%) were found in PAH and were least common in PAH-CHD-Eisenmenger. Ground glass opacification (GGO) was commonly seen in PAH (41%) most common in PAH-CHD (60%) and least common in PAH-portal (21%), $p<0.05$. A central pattern of ground glass change was seen with high frequency in PAH-SSc. Lymphadenopathy was found in 19% of PAH and oesophageal dilation (46%) was most common in PAH-SSc. In multivariate analysis age, WHO functional Class, cardiac output, and CT measures including RV/LV ratio, size of pericardial effusion and inferior vena caval area predicted outcome. CTPA may suggest the form of PAH and provides prognostic information.

Conclusion: We have showed the prevalence of several cardiac, vascular and lung changes on a standard CT that is routinely preformed in patients with suspected PAH. Our results also show several CT features can predict outcome.

5.2 Background

Pulmonary hypertension (PH) is defined at right heart catheterisation as a mean pulmonary artery pressure of at least 25 mmHg. It ranges from a mild elevation in pressure commonly seen in severe cardiac and respiratory disease to rare conditions where severe elevation of pressure results in right heart failure and early death. The current system of classification identifies 5 major groups which define prognosis (1) and treatment. Whereas specific drug therapy can improve outcome in pulmonary arterial hypertension (PAH, Group 1) patients with chronic thrombo-embolic pulmonary hypertension (CTEPH, Group 4) can potentially be cured by surgery. Classification within subgroups is important. In patients with PAH, survival in idiopathic pulmonary arterial hypertension (IPAH) is superior to PAH associated with connective tissue disease (PAH-CTD) but inferior to PAH associated with congenital heart disease (PAH-CHD) (1). Accurate phenotyping of disease is therefore crucial to accurately estimate prognosis and define treatment.

The approach to the investigation of patients with suspected PH has evolved over the past decade [148]. Imaging is increasingly recognized as a valuable non-invasive tool in the assessment of pulmonary hypertension providing diagnostic and prognostic information [80, 87, 147, 149] that supplements data from right heart catheterisation. Perfusion scintigraphy has been traditionally used to exclude CTEPH, cardiac MR provides functional information on the performance of the right ventricle and pulmonary vasculature, whereas CT provides detailed structural information and depicts features such as emphysema, interstitial lung disease or thrombo-embolic disease which may cause PH. In addition CT demonstrates morphological changes such as right ventricular dilation seen as a consequence of PH. Previous studies that have attempted to describe CT features in PH have mainly been in mixed groups of patients and while a small number of CT parameters have been extensively studied only sporadic reports exist for many others. There is also interest in prognostic scores in PAH but limited information on the utility of CT markers in various forms of PAH.

5.3 Objective

- To evaluate the prevalence of several cardiac, vascular and parenchymal CT findings in pulmonary arterial hypertension and its 5 major subtypes namely idiopathic pulmonary arterial hypertension, PAH associated with systemic sclerosis, PAH associated with non systemic sclerosis connective tissue disease, PAH associated with portal hypertension and PAH associated with congenital heart disease.

- To explore the prognostic value of CT findings from a large cohort of treatment naive patients.

5.4 Methods

5.4.1 Study cohort

444 patients with PAH were identified from the ASPIRE Registry (Assessing the spectrum of pulmonary hypertension identified at a referral centre)[130]. We then retrospectively selected from this database consecutive patients who had undergone mutlislice CTPA. All patients included in the study had RHC except patients with Eisenmenger's Syndrome in whom RHC was not routinely required.

5.4.2 Image analysis

CTPA were analyzed by two radiologists (2 years of specialised experience in reporting CT for patients suspected with PH) who were blinded to haemodynamic parameters, clinical findings and outcome. They were jointly collected resulting in a single dataset. A randomly selected 50 patients were analysed for interobserver agreement for the various CT findings.

Cardiac changes:

Ratio of right to left ventricle (RV/LV ratio) was obtained as previously described in the methods section 2.6.2 and figure 26 to figure 31. From the axial mid-chamber view, right atrial length was measured from the centre of tricuspid annulus to the superior right atrial wall. The size of the right atrium was also qualitatively evaluated using a simple 3 point visual scale: mild, moderate and

severe. Displacement of the IV septum was evaluated on a three-point scale as normal, flattened and deviated septum [64]. Abnormal thickness of the right ventricular free wall was recorded from the axial images [119].

Vascular changes:

Pulmonary to aorta ratio (PA/AO ratio) and the maximum depth of pericardial effusion[63] were recorded. Reflux of contrast into the hepatic veins was assessed as previously described [66]. The size of the inferior vena cava (IVC) was measured by calculating the cross sectional area of the IVC above the level of the diaphragm, below the right atrium.

Lung and mediastinal changes:

The images were assessed for presence of ground glass opacity (GGO). When GGO was present the pattern was noted as centrilobular, panlobular homogenous, and panlobular heterogenous. The craniocaudal and anterioposterior distribution of GGO was also recorded [71].

CT scans were also assessed for the presence of fibrosis, pleural effusions, mediastinal lymphadenopathy, dilated bronchial collaterals, septal lines and oesophageal dilatation.

5.4.3 Statistical analysis

Continuous variables are presented as mean and standard deviation and tested between groups using analysis of variance. Categorical variables are presented as number and percentage. Prognostic value of CT signs and of baseline characteristics was assessed by means of both univariate and multivariate Cox proportional hazards.

5.5 Results

The study population is outlined in detail in figure 1. Of 444 consecutive patients with PAH identified from the ASPIRE registry, 292 patients had mutlislice CTPA within 3 months or right heart catheterisation and were included in the study. The mean age of the study population was 62 (± 16) years with a female preponderance of 73%. There were 74 patients with a diagnosis of idiopathic pulmonary arterial hypertension (IPAH), 95 patients with PAH associated with

Systemic Sclerosis (PAH-SSc), 39 with PAH associated with other connective tissue disease (PAH-CTD not SSc), 63 patients had PAH with congenital heart disease (PAH-CHD) of which 31 had Eisenmenger syndrome, 14 patients with PAH associated with porto-pulmonary hypertension (PAH-portal), 3 patients with Haemolytic anaemia, 2 with drug induced PAH and 2 with familial PAH. Table 19 summarizes baseline hemodynamic and demographic characteristics for the 5 main subgroups of PAH.

Figure 53: Study characteristics

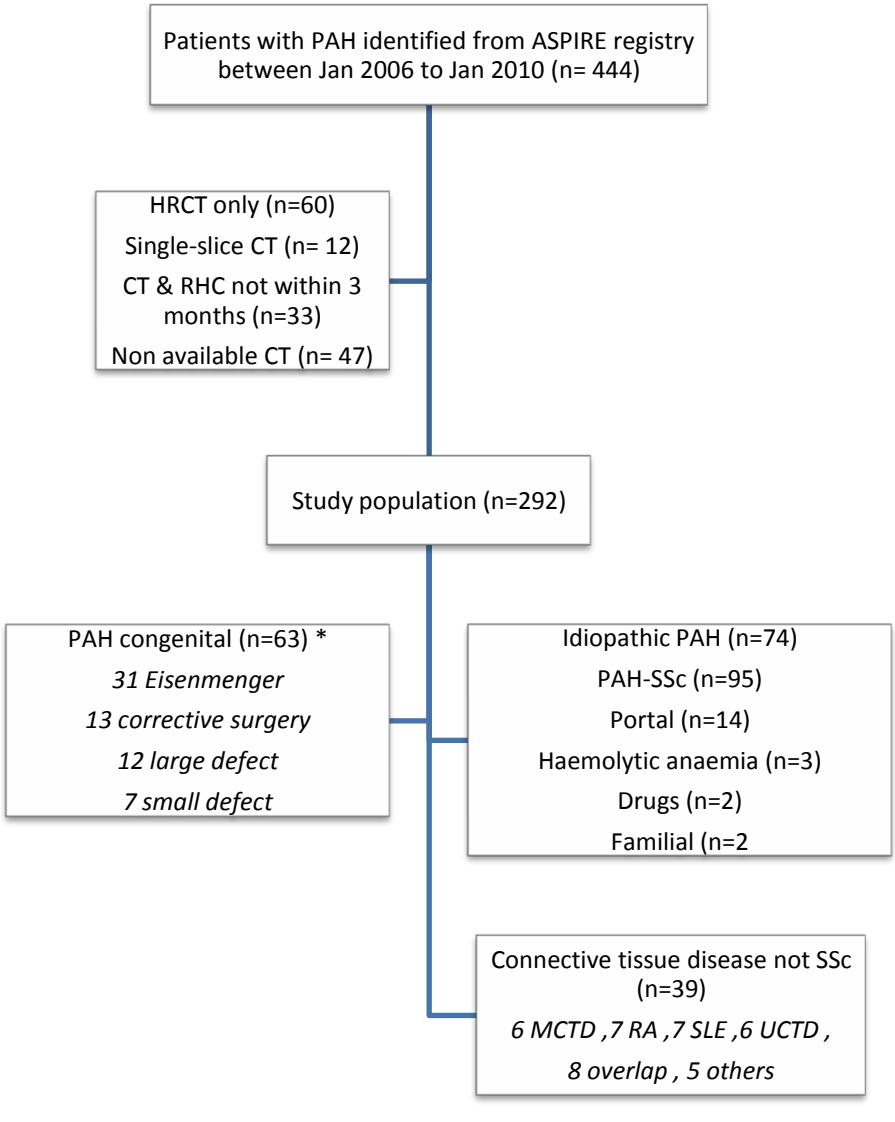

**RHC not performed in 26 pts with PAH-Congenital*

Table 21: demographics and haemodynamics of the study population

Characteristics	PAH	IPAH	PAH-SSc	PAH-CTD nonSSc	PAH-Portal	PAH-CHD
No. of patients	292	74	95	39	14	63
Age (yrs)	62 (16)	62 (16)†‡	69 (9) $^{*\dagger\#}$	60 (16)†‡	59 (12)	51 (18)$^{*\#\ddagger}$
Female (%)	73	59$^{\ddagger\#}$	85*	84*	64	71
WHO III/IV (%)	62:11	69: 12	69: 13	74: 10	64:0	59: 10
mRAP (mmHg)	9 (5)	10 (6)$^{\#\ddagger}$	6 (5)*	7 (4)*	9 (7)	-
mPAP (mmHg)	46 (14)	51 (11)$^{\#\ddagger}$	42 (14)*	43 (11)*	47(10)	-
PCWP (mmHg)	10 (4)	10 (3)	10 (4)	9 (4)	11 (2)	-
CI (L.min.m2)	2.8 (0.9)	2.4 (0.7)$^{\#\ddagger\S}$	3 (0.83)*	3.2 (1.03)*	3.4 (0.8)*	-
PVR (dyn.s.cm-5)	702 (431)	889 (415)	568 (378)	586 (398)	482 (202)	-
mVO2 (%)	65 (9)	62 (7)	66 (9)	65 (8)	70 (8)	-
FVC (%)	89 (19)	95 (11)†	95 (14)†	85 (18)†	94 (20)†	72 (23)$^{*\ddagger\S\#}$
FEV1 (%)	74 (20)	83 (15)$^{\#\dagger}$	80 (17)†	73 (17)*	77 (18)†	64 (20)*‡§
TLCO (%)	55 (23)	50 (19)†‡	37 (16)†§*	48 (8)†§	66 (7)$^{\#\ddagger}$	71 (23)$^{*\ddagger\#}$
ISWD (m)	185 (160)	176 (179)†‡	166 (137)$^{*\dagger\#}$	130 (95)‡	236 (126)	213 (123)*‡

Cardiac changes Table 22:

The RV/LV ratio for patients PAH was 1.25±0.42 (mean ±standard deviation) and among the subgroup, patients with IPAH had the highest value (1.37±0.46) although there were no statistically significant differences between groups. The mean right ventricle wall thickness (RVWT) was 6±2.7 mm for the whole group and within subgroups a lesser degree of RV hypertrophy was seen in patients with PAH-connective tissue disease (4±1.78 and 4±3.21 for PAH SSc and PAH non SSc respectively).

Qualitative visual grading of the right atrium showed a large number of patients with PAH (82%), and in particular those with IPAH (79%) and PAH-CHD (83%) had RA enlargement. A higher proportion of patients with IPAH (24%) and PAH-CHD (27%) were graded to have severe RA enlargement compared to other subgroups. The mean RA size for patients with PAH was 55mm±12.1 and was based on quantitative measurement of the long axis length of the RA. Deviation of the interventricular septum towards the left ventricle was evident in 27% of patients with PAH and 41% of patients with IPAH. 38% of patients with PAH had pericardial effusion with maximum mean depth of 12±5mm. Within the subgroup, pericardial effusion was particularly prevalent in patients with PAH-CTD-nonSSc (71%) and was relatively less frequent is patients with PAH-CHD-Eisenmenger (22%).

Table 22: Frequency (expressed in percentage) of cardiac features in PAH and its major subgroups

Cardiac **CT Parameters**	**PAH (n=292)**	**IPAH (n=74)**	**PAH-SSc (n=95)**	**PAH-CTD-nonSSc (n=39)**	**PAH-Portal (n=14)**	**PAH-CHD (n=63)**	**PAH-CHD-Eisenmenger (n=31)**
RV/LV ratio~	1.25(0.42)	1.39(0.46)	1.19(0.48)	1.19(0.36)	1.25(0.35)	1.15(0.30)	1.23(0.38)
RVH (mm) ~	6(2.7)	6(2.3)	4(1.78)	4(3.21)	6(1.89)	7(4.26)	8(2.5)
RA size (mm) ~	55(12.1)	57(10.9)	53(12.5)	52(13.1)	56(17.2)	59(13.4)	59(14.6)
RA size							
Mild	25	20	30	31	28	21	16
Moderate	28	35	20	26	36	35	42
Severe	19	24	16	10	14	27	22
IV septum							
Normal	42	24	57	59	36	37	42
Flattened	31	35	24	26	43	30	29
Deviated	27	41	19	15	21	33	29
Pericardial effusion							
Present	38	31	42	71	36	22	19
Depth (mm)**~**	12(5)	8 (7)	14 (6)	13 (6)	14 (5)	13 (4)	11(4)

Numbers represent percentages; ~ mean (standard deviation)

Vascular changes Table 23:

The average pulmonary artery-aorta ratio (PA/Ao ratio) for patients with PAH in our study was 1.16±0.21. This ratio was highest for patients with PAH-CHD-Eisenmenger (1.46±0.45) followed by patients with IPAH who had an average of 1.19±0.18. Regurgitation of contrast into the hepatic veins was frequent across the major subgroups with grade 4 reflux (contrast into the distal hepatic veins) seen in 24% of patients with IPAH and 28% of patients with PAH-CHD. A higher degree of IVC dilatation was observed in patients with PAH-portal and PAH-CHD with average IVC size of 632±156mm^2 and 647±209 mm^2, respectively. Pulmonary artery calcification and mural thrombus were noted only in patients with PAH-CHD and occurred in 16% (calcification) and 13% (mural thrombus) in PAH-CHD-Eisenmenger group.

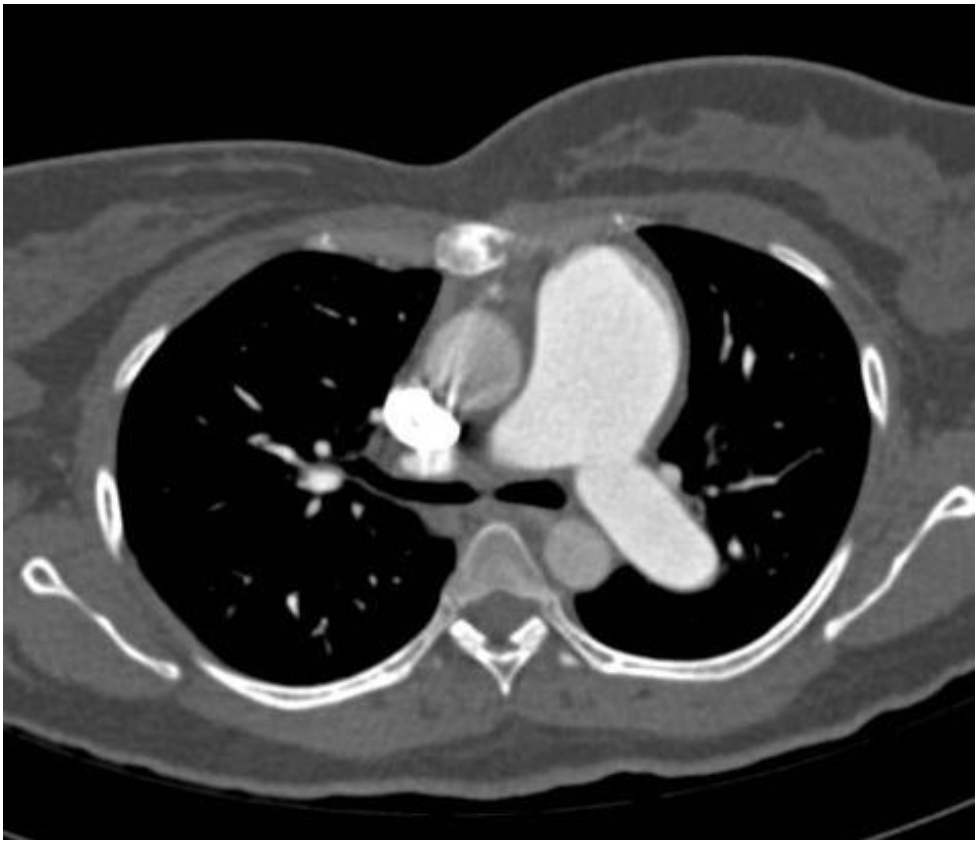

Figure 54: There is marked dilatation of the pulmonary artery with PA/Ao ratio of 2.1 in this patient with IPAH.

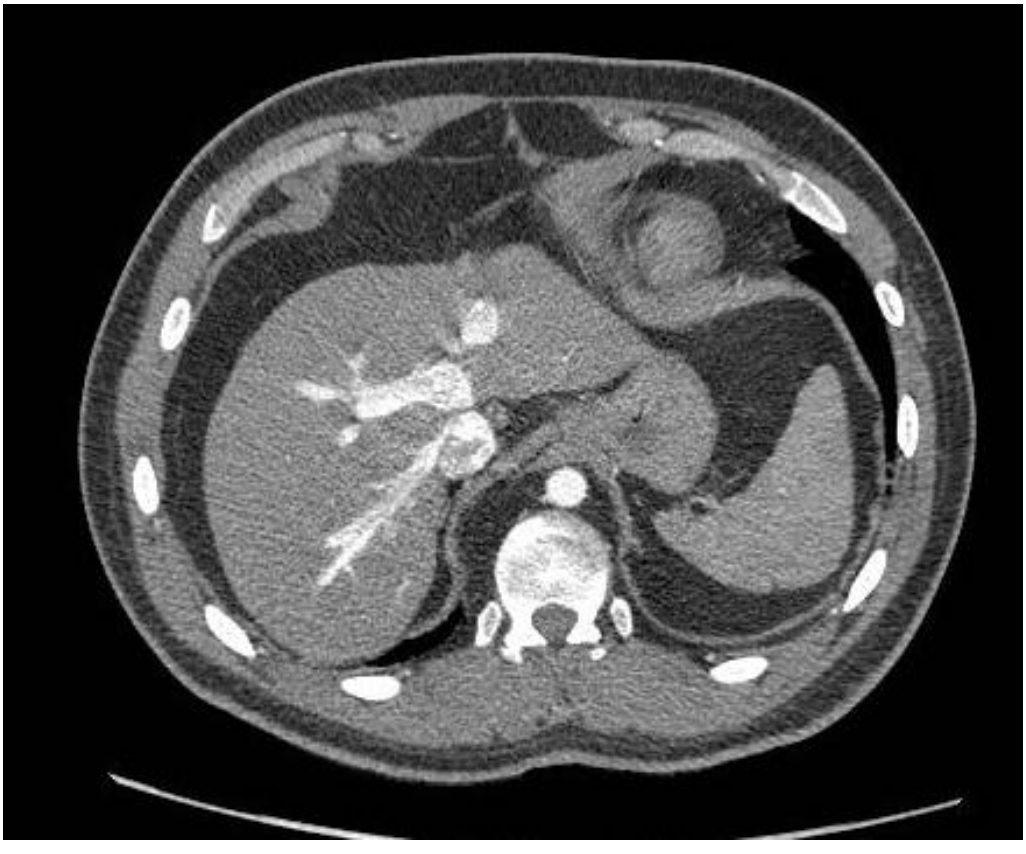

Figure 55: Grade 5 tricuspid regurgitation with contrast refluxing into the distal hepatic veins

Table 23: Frequency (expressed in percentage) of vascular features in PAH and its major subgroups

Vascular signs **CT Parameters**	**PAH (n=292)**	**IPAH (n=74)**	**PAH-SSc (n=95)**	**PAH-CTD-nonSSc (n=39)**	**PAH-Portal (n=14)**	**PAH-CHD (n=63)**	**PAH-CHD-Eisenmenger (n=31)**
PA/Ao ratio~	1.16 (0.21)	1.19 (0.18)	1.04(0.16)	1.07 (1.16)	1.08 (0.17)	1.26 (0.40)	1.46(0.45)
IVC size(mm^2) ~	596(207)	583 (200)	570 (203)	546 (206)	632(156)	647 (209)	659(212)
TR Present	73	80	67	62	57	85	93
Grade 1	18	15	20	23	36	14	16
Grade 2	21	24	23	15	14	22	23
Grade 3	12	24	13	13	0	21	22
Grade 4	22	24	12	10	7	28	32
Calcification in PA	3	0	0	0	0	13	16
Thrombus in PA	2	0	0	0	0	10	13

Lung and mediastinal changes (table 24):

Ground glass opacities were a frequent finding in patients with PAH (41%) and occurred mostly commonly in patients with PAH-CHD (60%). Patients with IPAH and PAH-CTD had a higher intensity of GGO with 58% of IPAH, 50% of PAH-CTD-nonSSc and 47% of PAH-SSc graded as having GGO in more than two-thirds of the lung (grade 3). The predominant pattern of GGO in PAH (55%) and its major subgroup was centrilobular pattern (61% in PAH-SSc, 60% in PAH-CTD-nonSSc, PAH-portal and PAH-CHD). In patients with IPAH centrilobular and panlobular changes occurred in equal frequency (55% of centrilobular and 52% of panlobular heterogenous). When panlobular involvement of GGO occurred, it was principally in a heterogenous (38%-PAH) rather than a homogenous distribution (8%-PAH). Assessment of distribution of GGO in anterioposterior and craniocaudal direction showed the distribution was mainly random (79% random for anterioposterior and 86% random for craniocaudal) except in patients with PAH-SSc. In patients with PAH-SSc 51% of patients had central distribution of GGO and 49% had non central distribution; compared to low occurrence of central distribution in other subgroups. Dilated collateral vessels were most prevalent in patients with PAH-CHD (35%) and within this subtype occurred 55% of patients with Eisenmenger syndrome. 19% of patients with PAH had enlarged mediastinal lymph nodes and it was relatively more frequent in IPAH (22%) and PAH-CTD subgroup (25% of PAH-SSc and 27% of PAH-CTD-nonSSc). Oesophageal dilatation was appreciated mainly in patients with PAH-CTD (46% of PAH-SSc and 36% of PAH-CTD-nonSSc) compared to other subgroups.

Table 24: Frequency (expressed in percentage) of lung and other features in PAH and its major subgroups

Lung and mediastinal **CT Parameters**	**PAH (n=292)**	**IPAH (n=74)**	**PAH-SSc (n=95)**	**PAH-CTD-nonSSc (n=39)**	**PAH-Portal (n=14)**	**PAH-CHD (n=63)**	**PAH-CHD-Eisenmenger (n=31)**
GGO Present	41	42	38	26	21	60	58
Intensity 1/ 2/ 3	20/34/46	16/26/58	25/28/47	0/50/50	67/33/0	18/55/27	17/50/33
centri/pan homo/pan hetero	55/8/38	48/0/52	61/22/19	60/0/40	67/33/0	53/0/47	56/0/44
central /random/peripheral	21/79/0	10/90/0	51/49/0	10/90/0	0/67/33	5/95/0	6/94/0
upper/random/lower	10/86/4	6/81/13	11/86/3	10/90/0	33/67/0	11/89/0	22/78/0
Septal lines	21	30	23	5	21	18	23
Collaterals vessel	11	9	1	8	0	35	55
Lymphadenopathy	19	22	25	27	0	10	16
Pleural effusion	11	14	15	8	14	5	3
Right/left/bilateral	25/22/53	10/40/50	21/15/64	33/0/67	50/50/0	67/0/33	1/0/0
Oesophageal dilatation	23	7	46	36	7	6	10
Ascites	5	5	4	8	14	2	0

Survival result:

The maximal duration of follow up was 6 years with a mean follow-up of 3 years. During this period there were 112 deaths. For all PAH univariate Cox regression analysis demonstrated that cardiac parameters of RV/LV ratio, right atrial size, deviation of interventricular septum and presence and depth of pericardial effusion to predict outcome. Reflux of contrast into the distal hepatic veins and size of IVC and lung changes of septal lines, presence of pleural effusion and mediastinal lymphadenopathy also concurred with poor outcome in patients with PAH. Multivariable Cox proportional hazard analysis incorporating hemodynamic and CT parameters showed that the RV/LV ratio, the depth of pericardial effusion and inferior vena caval size were all significant predictors of death. Univariate predictors of outcome in the 5 major groups of PAH are shown in Table 25.

Table 25: Univariate and Multivariate survival analysis

Parameters	Univariate HR(CI)	P -value	Multivariate HR(CI)	P -value
Age	1.04(1.02-1.05)	<0.05	1.18(0.75-1.04)	<0.05
Gender				
WHO classification	1.68(1.35-2.08)	<0.05	1.01(0.70-1.08)	<0.05
mRAP	1.01(0.98-1.05)	0.39		
mPAP	0.99(0.98-1.01)	0.91		
Cardiac output	0.83(0.73-0.94)	<0.05	1.37(1.14-1.64)	<0.05
PVR	1.10(1.00-1.21)	<0.05	1.00(1.00-1.00)	0.07
smVO2	0.95(0.95-0.98)	<0.05	0.98(0.94-1.01)	0.31
Cardiac signs				
PA/Ao ratio	0.49(0.24-1.10)	0.09		
RV/LV ratio	2.59(1.89-3.57)	<0.05	1.93(1.00-3.72)	<0.05
RA size	1.35(1.17-1.56)	<0.05	1.18(0.95-1.45)	0.12
RV hypertrophy	1.00(0.94-1.06)	0.96		
IV septal position				
Normal	Reference		Reference	
Straightening	1.49(0.91-2.42)	0.11	1.19(0.91-2.41)	0.11
Deviated	3.10(1.98-4.86)	<0.05	2.11(1.80-3.86)	0.12
Pericardial effusion				
presence	1.65(1.17-2.47)	<0.05	1.04(0.70-1.54)	0.82
Depth	1.71(1.28-2.11)	<0.05	1.84(1.01-3.35)	<0.05
Vascular signs				
IVC size	1.0(1.00-1.002)	<0.05	1.11(1.00-1.24)	<0.05
Hepatic vein reflux				
None	Reference			
trace into IVC	1.40(0.73-2.50)	0.25		
proximal hepatic vein	1.45(0.83-2.52)	0.19		
mid hepatic vein	1.27(0.63-2.53)	0.49		
distal hepatic vein	1.79(1.05-3.06)	<0.05		
Collaterals	0.55(0.28-1.10)	0.09		
Lung signs				
GG nodules				
Present	1.00(0.69-1.47)	0.96		
extent <1/3rd	Reference			
1/3rd-2/3rd	0.88(0.39-1.98)	0.75		
>2/3rd	0.95(0.45-2.01)	0.89		
centrilobular vs panlobular	1.04(0.57-1.86)	0.91		
central vs non-central	1.71(0.72-4.04)	0.22		
Pleural effusion	3.21(2.05-5.08)	<0.05	1.42(0.70-2.86)	0.32
Septal lines	2.64(1.78-3.95)	<0.05		
Lymphadenopathy	1.71(1.13-2.60)	<0.05	0.75(0.42-1.36)	0.35

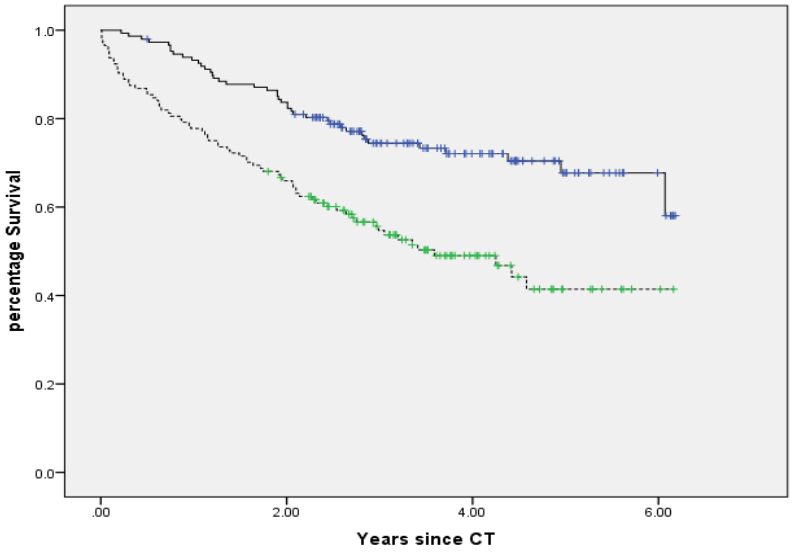

Figure 56: Kaplan Meier Plots for RV/LV ratio above and below median value (1.18) in patients with PAH (Chi square – 18.09; p value - 0.00.)

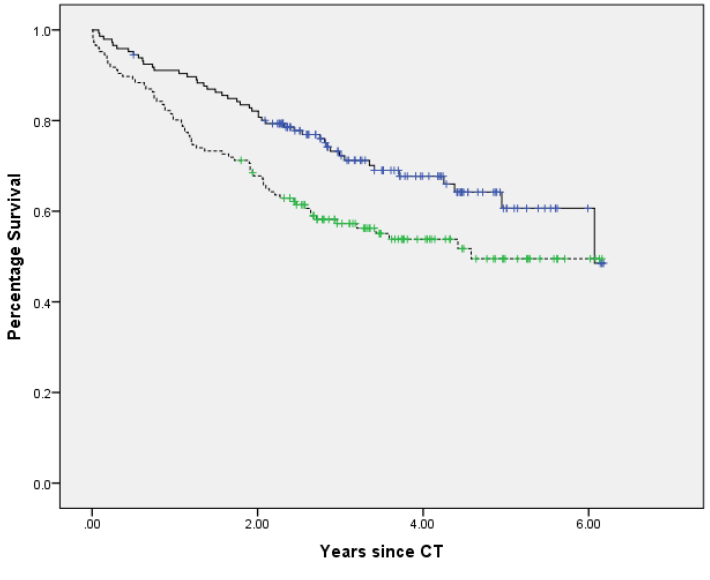

Figure 57: Kaplan Meier Plots for IVC size above and below median value (559) in patients with PAH (Chi square – 6.73; p value - 0.009)

5.6 Discussion

Principle findings: This study is the first comprehensive report of the prevalence of vascular, cardiac, and lung parenchymal and mediastinal changes on CT in patients with PAH and its major subgroups. It has shown that certain features such as oesophageal dilation and pulmonary artery calcification are more common in certain forms of PAH and features usually associated with intrinsic lung disease such as ground glass change are frequently seen in all forms of PAH. We have also demonstrated that cardiac and vascular morphology can independently predict outcome in PAH and that simply made measures at CT such as RV/LV ratio and pericardial and IVC size are of independent predictive prognostic value.

In addition to well established features such as a high PA/Ao ratio several quantifiable CT findings including elevated RV/LV ratio, deviated interventricular septum, dilated right atrium, hypertrophy of the RV free wall, pericardial effusion, contrast regurgitation into the hepatic veins and presence of ground glass opacities occur frequently in patients with PAH and its major subgroups. Patients with IPAH and PAH-CHD-Eisenmenger have a higher proportion of patients with severe RA dilatation, contrast regurgitation into the hepatic veins and ground glass opacities. However, while more patients with IPAH have deviated interventricular septum and greater RV/LV ratio, the Eisenmenger group had a higher PA/Ao ratio, pulmonary artery calcification and mural thrombus and dilated collaterals vessels. Interestingly we also noted that central distribution of ground glass opacity was particularly frequent in patients with PAH-SSc whereas a centrilobular pattern was more common in IPAH and PAH-CHD-Eisenmenger. Pulmonary artery size and pulmonary artery-aortic ratio have been extensively studied and shown to have diagnostic accuracy but do not reflect disease severity. In our study, patients with Eisenmenger syndrome had the highest pulmonary artery to aorta ratio.

We have also shown that CT features can predict outcome in treatment naive patients with PAH at the time of initial diagnosis. These CT features include simple measurements such as ratio of the right to left ventricle, right atrial size, position of interventricular septum, inferior vena caval size, the presence of pericardial and pleural effusions, mediastinal lymphadenopathy and septal lines. Most of these parameters also predict survival in individual major subgroups. A number of these measures including RV/LV ratio, pericardial and IVC size were predictors of outcome

independent of pulmonary haemodynamic variables and WHO functional class, highlighting the potential prognostic value of CT. In this study PA size was not a predictor or outcome, however, a recent study has shown that marked pulmonary artery dilation was a n independent risk factor for IPAH with marked dilation >4.8cm being associated with a 7 fold increase risk of unexpected death (Chest 2012;142:1406). A recent work showed mediastinal lymphadenopathy was not associated with right heart haemodynamic in patients with IPAH [150].

In PAH right ventricular function is a major prognostic determinant [151-152]. The increase in ventricular pressure in PAH stretches the right ventricular wall, which leads initially to RV hypertrophy. Over time, this response cannot be sustained and eventfully the RV starts to dilate. As the RV expands, the crescentic shape of the RV cavity is lost and the interventricular septum bulges towards the LV cavity [153-155]. Displacement of the interventricular septum and dilatation of RV as shown by a high RV/LV ratio on CT are likely to reflect a failing RV and it is not surprising that they have prognostic significance. A failing RV and tricuspid regurgitation also elevate right atrial pressure. This impedes the mediastinal lymphatic and venous drainage [156-157] results in the development of septal lines, mediastinal lymphadenopathy and pleural and pericardial effusions. These features which can be easily quantifiable on CT are not surprisingly associated with a poor outcome. Reflux of contrast into the inferior vena cava and hepatic veins is thought to reflect tricuspid regurgitation [66] and our results have demonstrated that a significant number of patients with PAH have features which would be consistent with tricuspid regurgitation. Severity of TR on echocardiography has been shown to be a significant predictor of outcome[158-159]; however this was not seen using CT estimates and is likely to reflect how TR is estimated using CT. Tricuspid valve insufficiency is measured behind the level of tricuspid valve leaflets on echocardiography using colour flow Doppler [160], however, the severity of TR on CT is estimated using indirect measures such as reflux flow of contrast into the hepatic veins. This method is influenced by factors such as the extent and phase of breath hold and rate of contrast injection [161]. Interestingly inferior vena caval size has demonstrated to be a strong predictor of outcome. This is not surprising as vena caval diameter reflects the pressure in the right atrium [162] which is an important prognostic marker in PH[158, 163].

Ground glass attenuation is a documented finding in patients with PH [68-69] and our results show that GGO is seen in all major subgroups of PAH. The histology of GGO

is poorly understood, one study in patients with Eisenmenger's syndrome demonstrated centrilobular GGO to correlate with dilated capillary networks in alveolar spaces [62] while another isolated study showed them to represent cholesterol granulomas [70]. A more recent study has correlated centrilobular ground glass changes with histopathological changes in a small number of patients with IPAH, pulmonary capillary haemangiomatosis and pulmonary veno-occlusive disease. They demonstrated that patients with PCH had larger vascular abnormalities which corresponded to larger areas of ground glass on CT. Interestingly In a study by Resten et al[71] centrilobular pattern of GGO correlated with poor outcome following treatment in patients with PAH, however in our study this finding was restricted to patients with IPAH and was not appreciated in other major subgroups. Finally an interesting observation that has not been reported previously is that the central pattern of ground glass attenuation was seen more frequently in patients with PAH-SSc (51%) compared to other subgroups of PAH.

Limitations: Firstly, we have used non-gated axial images for assessment of cardiac morphology. Given the complex nature of cardiac anatomy, relying on simple measurement might only provide limited information. However, our study in a large patient cohort shows the value of uncomplicated measurements in a non-gated CT that is frequently performed as a first line examination. Secondly, our analysis involved relatively few patients in less common subgroups of PAH such as patient with HIV, drugs related PAH and this precluded the detailed analysis of these subgroups. Finally, a rare category of PAH, pulmonary veno-occlusive disease (PVOD) has several overlapping clinical and pathological features with IPAH which can be difficult to recognise without lung biopsy or until transplantation. It is possible that a number of patients with IPAH in our cohort may have had an element of PVOD. Resten et al, found that a proportion of patients with GGO have PVOD at post-mortem examination, although this was a small number of patients[71]. This is a large set of data on various CT changes and the next stage of this work is to perform an interobserver agreement on the various measurable and qualitative CT changes.

5.7 Conclusion

We report features of PAH and its major subgroups on a pre-treatment CT and also show parameters that predict outcome in this patient group. There are many

characteristic features on a standard CT that are suggestive of PAH and a few distinctive features that are more prevalent in certain subgroups of PAH. Presence of dilated right atrium and ventricle, deviated interventricular septum, pleural and pericardial effusions on CT are associated with worse survival.

6 CHAPTER 6: Diagnostic value of MR and CT in patients with PH secondary to connective tissue disease

This chapter is based on the paper published in *Journal of Rheumatology*
"Cardiac MRI predicts mortality and is superior to thoracic CT in the assessment of suspected pulmonary arterial hypertension in connective tissue disease"
Rajaram S et al, Journal of Rheumatology 2012 Jun; 39(6):1265-74.

In the previous chapters the roles of MRI and CT in distinctive subgroups of patients with PH have been studied. In this chapter the focus is on a unique subgroup of patients with connective tissue disease. These patients are at risk of developing PH which is a leading cause of mortality for this group.

Physical limitation and non-specific symptoms are common with CTD and when these patients develop PH it is often overlooked. To date the optimal screening tool is echocardiography however it is not without flaws often resulting in unnecessary right heart catheterization.

This chapter investigates the diagnostic and prognostic utility of CT and MRI that would aid in risk stratification of patients with connective tissue disease.

6.1 Abstract

Background:

PAH is a life threatening complication of connective tissue diseases. The aim of this study was to compare the diagnostic utility of non-invasive modalities, MRI and CT in the evaluation of these patients.

Methods:

81 consecutive patients with CTD and suspected PH underwent cardiac MRI, CT and RHC within 48 hours. Functional cardiac parameters: ventricle areas and ratios, delayed myocardial enhancement, position of the inter-ventricular septum, RV mass and pulmonary artery distensibility were all evaluated. The PA size, PA/Ao ratio, RV/LV ratio, RV wall thickness and grade of tricuspid regurgitation were measured on CT.

Results:

In our study of 81 patients with CTD, 55 patients had PAH and 22 patients had 'no PH'. There was a good correlation between mPAP measured at RHC and MR derived RV mass (r_0.71 p <0.001), systolic (r_0.70 p <0.001) and diastolic (r_0.64 p <0.001) RV/LV area ratios. In contrast parameters measured from CT demonstrated only a moderate correlation with mPAP (RV/LV ratio r_0.43 p 0.0008; hepatic vein reflux r_ 0.53 p 0.001 and right ventricle wall thickness r_ 0.47 p 0.0002). MR performed better as a diagnostic test for PAH than CT derived parameters: PA-distensibility had a sensitivity of 80%, specificity 78% and likelihood ratio (LR) of 3.6. Univariate Cox regression analysis showed the MR parameters to better predict mortality. Patients with a RVEDV of <135ml had a better prognosis than those with a value >135ml with a 1 year survival of 95% vs 66 % (log rank test of 0.024).

Conclusion:

In patients with CTD and suspected PAH, MR is superior to CT in the identification of PAH and in risk stratification.

6.2 Background

Pulmonary arterial hypertension (PAH) is a serious complication of connective tissue disease and is one of the leading causes of mortality [164]. The prevalence of connective tissue disease associated PAH (CTD-PAH) is estimated to be as high as 13% based on right heart catheterization (RHC) [165]. This is most commonly seen in the setting of systemic sclerosis (SSc), whereas in patients with System Lupus Erythematosus (SLE) the estimated prevalence is less than 1% [112]. Patients with CTD-PAH generally have a poor outcome compared to idiopathic pulmonary artery hypertension (IPAH) [112, 130, 166]. Within this group, patients with PAH associated with SSc have the poorest prognosis.

Diagnostic tools capable of identifying the presence of PAH with a high degree of accuracy and identifying patients at increased risk of early mortality are highly desirable in this patient population. Currently echocardiography is recommended as a screening test, with annual echocardiography recommended in patients with SSc and in other forms of CTD when patients have symptoms of breathlessness. However, estimates of pulmonary artery pressure cannot always be made and echocardiography can both underestimate and overestimate pulmonary artery pressure. RHC remains the gold standard investigation to confirm a diagnosis of pulmonary hypertension but this is an invasive investigation. In addition it only gives limited information on the cause of PH and gives no detail of the morphology of the cardiac chambers or the pulmonary vascular bed. A non-invasive test that may aid the clinician in risk stratification of patients with CTD, who have a poor quality echocardiogram or in whom the results are equivocal, would clearly be of value in both diagnosing the presence of PH and aiding classification.

6.3 Objective

- To compare the diagnostic utility of various MR, CT and echo-cardiographic parameters with RHC in patients with CTD and suspected PH
- To evaluate the ability of the above imaging modalities to assess PAH severity and predict mortality.

6.4 Methods

6.4.1 Study cohort

This was a retrospective study of 81 consecutive patients suspected with CTD-PH identified from patients referred to our centre with suspected PH. Patients were referred to our centre for further evaluation of clinical features suggesting pulmonary hypertension or after implementation of a screening protocol using the combination of echocardiography, lung function testing and assessment of symptoms of breathlessness. From the screening programme, patients underwent cardiac catheterisation if i) Tricuspid Gradient (TG) ≥ 40 mmHg, ii) if the TG was ≥ 30mmHg but < 40 mmHg with a TLco < 50% or iii) in the presence of symptoms of unexplained progressive breathlessness regardless of the results of the echocardiogram [167]. The diagnosis of CTD was made according to standard criteria and in most cases this was by the referring physician [168-170]. The patients included in the study were required to have had CT, MRI and RHC performed within 48 hours. For comparison with echocardiography this had to be performed at our centre within 3 months of RHC. All the CT and MRI were reviewed by two chest radiologists blinded to RHC haemodynamics.

The study included patients from January 2008 to March 2010 with a median follow-up of 24 months. The census date for mortality was 31st March 2011. Patients were treated according to national guidelines and prescription of therapies was in accordance with the UK national commissioning policy.

6.4.2 Image acquisition

CTPA was performed during a single breath-hold following and standard acquisition parameters were used: 100 mA with automated dose reduction, 120 kV, pitch 1, rotation time 0.5 s and 0.625mm collimation. The field of view was 400x400 mm with an acquisition matrix of 512 x 512. 100ml of intravenous contrast agent (Ultravist 300; Bayer Schering, Berlin, Germany) was administered at a rate of 5ml/sec. The CTPA images were reconstructed using a soft filter to provide contiguous 0.625 mm axial slices from the apex of the lung to the diaphragm for review.

MR imaging was performed on a 1.5 Tesla GE HDx Scanner (GE Healthcare, Milwaukee, USA) with peak gradient strength40 mT/m and slew rate 120 mT/m/ms. An 8 channel cardiac receive array RF coil (GE, Aurora, Ohio, USA) was used throughout.

SSFP is performed in the coronal plane as a stack of 2D SSFP images (GE FIESTA sequence). This sequence was performed in full inspiration with a breath hold time of 12 seconds. The imaging parameters are as follows: TR 2.8 ms, TE 1.0ms, Flip angle of 50°, FOV=48 cm x 43.2 cm, 256 x 256 Matrix, 125 kHz bandwidth and slice thickness of 10mm. This sequence is also used for scout images for planning the geometry of the cine cardiac scans.

CINE cardiac imaging: Four chamber view and contiguous cine short-axis views are acquired using cardiac gated SSFP imaging at end-expiratory breath-holds. The following parameters are used: 20 frames per cardiac cycle, slice thickness 8-10mm, FOV 48, matrix 256 x 256, BW 125 KHz/pixel, TR/TE 3.7/1.6 ms).

6.4.3 Image analysis

The CT and MRI images are analysed by two radiologists with 2 years of specialized experience in interpreting CT and MR images for patients with suspected PH. The data was collected by two radiologists and a single dataset was obtained at the end.

CT: The following CT parameters were measured: The following parameters were calculated using the method described in the methods section. Pulmonary artery to aorta ratio, ratio of the short axis distance between right to left ventricle, reflux of contrast into the hepatic views were graded. The HRCT images were also graded for presence or absence of interstitial ling disease (ILD) using a scoring system used by Bezante [171].

MRI: The RV end diastolic volume (RVEDV), RV end systolic volume (RVESV), RV ejection fraction (RVEF), stroke volume (SV) and cardiac output (CO) were subsequently calculated as described in the methods section. The systolic and diastolic areas of the RV and LV chambers were measured on the mid 4 chamber view and a ratio was derived. The RV end diastolic mass (RVEDM), left ventricular

end diastolic mass (LVEDM) and the ventricular mass index as the ratio of RVEDM/LVEDM (VMI) were calculated from the end diastolic short axis stack of images [78]. Tricuspid annular systolic excursion (TAPSE) and septum-free-wall distance (SFD) were also recorded [80]. From the mid 4-chamber image the RV relative area change (RV area in end diastole−RV area in end systole/RV area in end diastole×100) and systolic and diastolic RV/LV area ratios were measured. Phase-contrast MR images were processed using specialized software. The contours of the main PA were traced simultaneously on magnitude and velocity-map images and peak velocity, pulmonary artery blood flow and pulmonary artery distensibility were calculated [172]. The motion of the interventricular septum was visually analysed on short-axis and four-chamber views for presence or absence of paradoxical septal movement. The presence or absence of myocardial delayed enhancement at the interventricular septum insertion points was also noted. The degree of delayed myocardial enhancement was not quantified.

6.4.4 Statistical analysis

To compare CT and MR parameters between patients with PH and no PH subjects, the independent t-test and χ^2 tests were used as appropriate. To determine the correlations between imaging and RHC parameters a Pearson's test was used. Diagnostic strength, for the identification of patients with PAH, was assessed using receiver operated characteristic (ROC) curve analysis. The survival curves were derived using the Kaplan-Meier method and were compared using a log-rank test. Median values were used to separate continuous variables into two groups. The univariate Cox regression analysis was used to calculate the hazard ratio and confidence interval for the following predictors: age, mean right atrial pressure (mRAP), mixed venous oxygen saturation ($mSVO_2$), cardiac index (CI), mPAP, PVR, RVEDM, RVEDV, PA/Ao ratio and RV wall thickness. A *P* value of less than 0.05 was considered to be statistically significant for all statistical analysis.

6.5 Results

Demographics:

81 patients were identified with CTD of whom 55 patients had PAH and 4 patients had PH owing to left heart disease. 22 patients with CTD had 'no PH'. Phase contrast MRI was performed in 51 patients and the ventricular mass was available for 62 patients. The median time interval between echocardiogram and RHC was 34 days (interquartile range of 3 to 59 days). In 9 patients the echocardiogram data was not available.

The study profile is outlined in figure 1 and demographic details of the patients are summarized in table 26.

Table 26: Patient classification

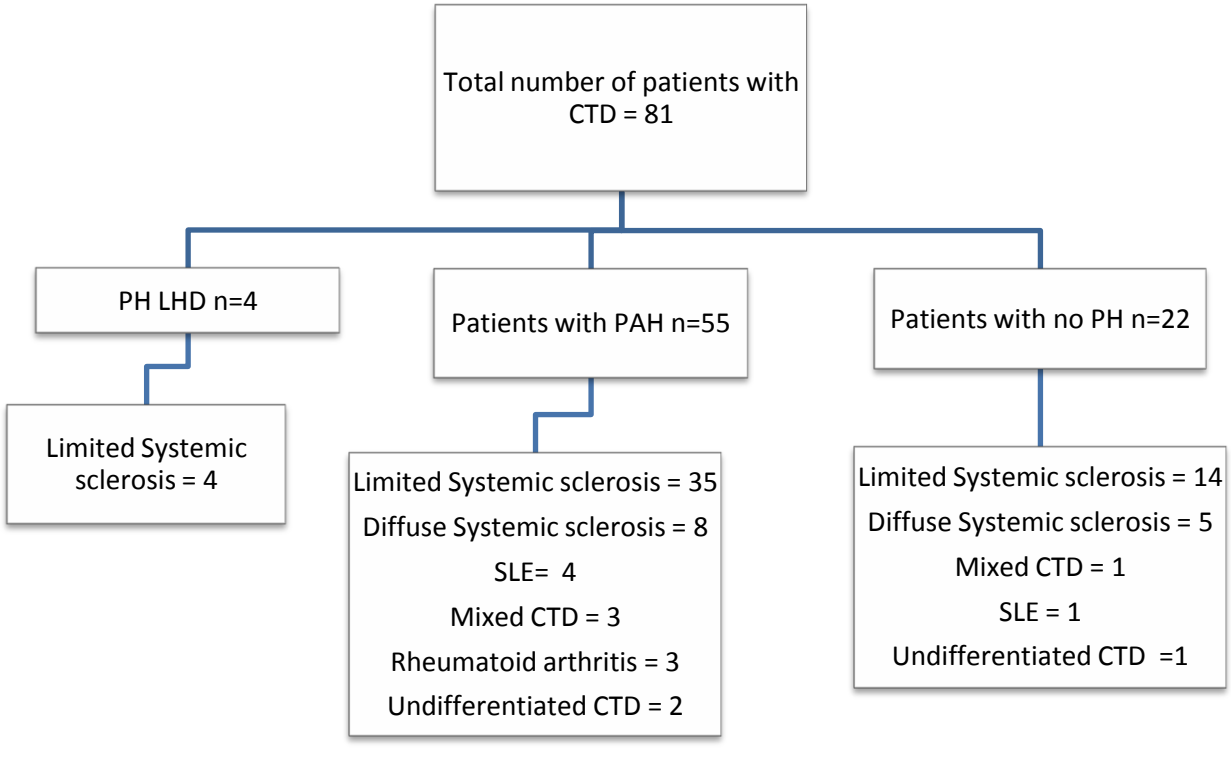

Table 27: Patient classification

	Whole Group n=81	No PH n=22	PAH n=55	p-value
Age (yrs)	62(14)	59 (16)	64 (17)	0.47
Female (%)	85	85	85	0.90
WHO II/III/IV (%)	25:63:9	40:55:0	20:66:13	<0.001
FVC (% predicted)	85 (22)	91 (15)	82 (24)	0.11
TLCO (% predicted)	47 (19)	67 (21)	40 (12)	<0.001
mRAP (mmHg)	8 (5)	6 (3)	9 (5)	0.007
mPAP (mmHg)	35 (15)	19 (3)	40 (14)	<0.001
CI (L.min.m2)	3.3 (0.8)	3.7 (0.8)	3.2 (0.7)	0.004
PVR (dyn.s.cm-5)*	417 (393)	112 (46)	524 (404)	<0.001
mVO2 (%)	69 (8)	73 (7)	67 (8)	0.008

FVC-forced vital capacity; TLCO-gas transfer; mRAP-mean right atrial pressure; mPAP-mean pulmonary artery pressure; PVR-pulmonary vascular resistance; mVO2-mixed venous saturation; CI-cardiac index; PVR -pulmonary vascular resistance; mVO -mixed venous oxygen saturation (n=4 patients with LHD are included within the whole group)

Assessment of severity:

Table 28 summarises the correlations between MR measurements and RHC derived mPAP and PVR. Good correlation was found between mPAP and PVR and VMI, RVEDM, systolic and diastolic RV/LV area ratio and a moderate correlation was found with TAPSE, PA distensibility and RV RAC. The pulmonary artery average blood flow measured from phase contrast MR showed a moderate correlation with RHC derived cardiac output (r_0.59 p<0.001) but not with mPAP or PVR. For parameters measured from CT; PA size, PA/Ao, RV wall thickness, RV/LV ratio and graded hepatic vein reflux showed only a moderate correlation with the mPAP and PVR. Tricuspid gradient from echocardiography correlated strongly with mPAP and PVR measured at RHC (mPAP =0.84, P < 0.001 and PVR =0.76, P < 0.001).

Table 28: Correlations of cardiac MR parameters with mPAP and PVR

	mPAP		PVR	
	r value	*p*-value	r value	*p*-value
RV Mass ** (g/cm3)	0.70	<0.001	0.60	<0.001
Systolic RV/LV area ratio	0.69	<0.001	0.68	<0.001
Diastolic RV/LV area ratio	0.64	<0.001	0.64	<0.001
PA distensibility* (%)	-0.58	0.0011	-0.54	0.0012
RVRAC (%)	-0.53	<0.001	-0.56	<0.001
TAPSE (cm)	-0.55	<0.001	-0.58	<0.001
SFD (cm)	-0.39	0.0019	-0.44	<0.001
RVEF (mL)	-0.44	<0.001	0.50	<0.001
RVESV (mL)	0.40	<0.001	0.43	<0.001
RVEDV (mL)	0.24	0.09	0.20	0.12
RVSV (mL)	-0.37	0.0026	-0.41	<0.001

N=81(study group) *N=51 (PA distensibility) **N=62 (RV Mass). RVEDV – right ventricle end diastolic volume; RVESV–right ventricle end systolic volume; RVEF–right ventricle ejection fraction; SV–stroke volume; RVEF–right ventricle ejection fraction; TAPSE-transverse annular systolic excursion; SFD–septal-free wall distance; RVRAC- RV relative area change; RV mass–right ventricle mass

Table 29: Correlations of CT parameters with mPAP and PVR

	mPAP		PVR	
	r value	p-value	r value	*p*-value
RV wall thickness	0.47	<0.001	0.35	0.007
PA size	0.37	0.003	0.28	0.03
PA/Ao ratio	0.43	<0.001	0.36	0.004
RV/LV ratio	0.40	0.005	0.35	0.015
Hepatic vein reflux	0.53	0.001	0.58	0.001

RV/LV ratio–right ventricle left ventricle transverse distance ratio; PA/Ao ratio–Pulmonary artery Aorta ratio; PA– Pulmonary artery; RVWT–right ventricle wall thickness

Diagnostic value:

The performance of the MR and CT are outlined in table 30 and 31. VMI was the best performing MR parameter with a cut off value ≥ 0.45 as determined by the ROC analysis (AUC 0.87) having a sensitivity of 85%, specificity 82% and likelihood ratio of 4.5. PA distensibility with the cut off point ≤ 15 (AUC 0.85) had a sensitivity of 80%, specificity 78% and LR 3.6. Of the CT parameters evaluated, presence of PA/Ao ratio of ≥1 (AUC 0.71) had a low sensitivity of 59%, specificity 73% and LR 2.2. RV wall thickness ≥ 3.5mm as determined by the ROC analysis (AUC 0.73) showed a sensitivity of 65%, specificity 67% and LR 1.9. Although the presence of pericardial effusion had 100% specificity, the sensitivity was poor (23%) as this was present in only 12 patients. Tricuspid gradient performed strongly as a diagnostic test for the group in our study (AUC 0.87). The strongest TG threshold for diagnosing PH was 40 mmHg and at this cutoff point the sensitivity was 86%, specificity was 82% and LR of 4.6 for diagnosing PH.

Table 30: Diagnostic performance of MR parameters

Variables	sensitivity / specificity	PPV/NPV	LR	ROC AUC
PA distensibility ≤ 15	80/78	90/59	3.60	0.85
RV Mass ≥ 30	72/80	91/50	3.57	0.84
RV area change≤36%	69/75	89/47	2.76	0.70
Systolic RV/LV area ratio ≥ 0.8	67/75	88/45	2.70	0.78
Diastolic RV/LV area ratio ≥0.8	60/75	87/40	2.40	0.73
Transverse excursion ≤2cm	67/65	83/45	1.9	0.70
Septal free wall distance ≤1	70/60	81/45	1.73	0.67
Delayed Myocardial Enhancement	74/82	89/63	4.09	-
Paradoxical Septal Movement	23/100	100/35	-	-

PPV-positive predictive value; NPV- negative predictive value; LR- likelihood ratio; ROC AUC- receiver operator characteristics are under the curve; TAPSE-transverse annular systolic excursion; SFD–septal-free wall distance; RVRAC- RV Relative area change; PA distensibility – pulmonary artery distensibility; RV mass–right ventricle mass.

Table 31: Diagnostic performance of CT parameters

Variables	sensitivity/ specificity	PPV/NPV	LR	ROC AUC
PA size ≥ 2.9	59/73	87/37	2.1	0.71
PA/Ao ratio ≥ 1	54/74	87/40	2.2	0.73
RV/LV ratio	55/53	76/30	1.2	0.54
RV wall thickness≥ 3.5 mm	65/67	88/35	1.9	0.74
Hepatic vein reflux (present/absent)	41/85	89/35	2.7	0.73

PPV-positive predictive value; NPV- negative predictive value; LR- likelihood ratio; ROC AUC- receiver operator characteristics are under the curve; RV/LV ratio–right ventricle left ventricle transverse distance ratio; PA/Ao ratio–Pulmonary artery Aorta ratio; PA– Pulmonary artery; RVWT–right ventricle wall thickness

Survival analysis:

The mean follow up period was 24 months and there were 10 deaths during the study period. Univariate Cox regression analysis demonstrated that mean RA pressure, mixed venous oxygen saturation, RVEDV, RVESV, VMI and RVEDM predicted mortality in PAH (Table 32). Kaplan Meier survival curves showed patients with a RVEDV < 135ml had significantly better survival than those with RVEDV >135ml (log rank test, P 0.024). The Kaplan Meier survival curve for RVEDV is shown in Figure 59. In our group of patients, Kaplan Meier survival curve for VMI using a median value of 0.75 also predicted mortality with a p-value of 0.04 (Figure 60). A multi-variable analysis was not performed due to the low number of deaths.

Table 32: Univariate predictors of mortality in CTD-PH patients

Variables	Hazard Ratio	95% CI	*p*-value
Age (yr)	1.00	0.95–1.05	0.93
mRAP (mm Hg)	1.2	1.06–1.35	0.003
mPAP (mm Hg)	1.01	0.96–1.06	0.009
mVO_2 (%)	0.91	0.84–0.98	0.02
Cardiac index ($L/min^{-1}/m^{-2)}$	0.59	0.21–1.68	0.328
PVR ($dyne/s/cm^{-5)}$	1.00	0.99–1.00	0.307
RV systolic volume($mL/mm\ Hg^{-1}$)	1.01	0.98–1.04	0.186
RV ejection fraction	0.99	1.05–1.03	0.923
RV end diastolic volume (mL)	1.02	1.01–1.03	0.002
RV end systolic volume (mL)	1.01	1.00–1.02	0.027
RV end diastolic mass (g/cm3)	1.03	1.00–1.06	0.040
PA distensibility (%)	0.87	0.64-1.18	0.388

RVEF–right ventricle; mRAP-mean right atrial pressure; mPAP- mean pulmonary artery pressure; PVR-pulmonary vascular resistance; mVO2-mixed venous saturation

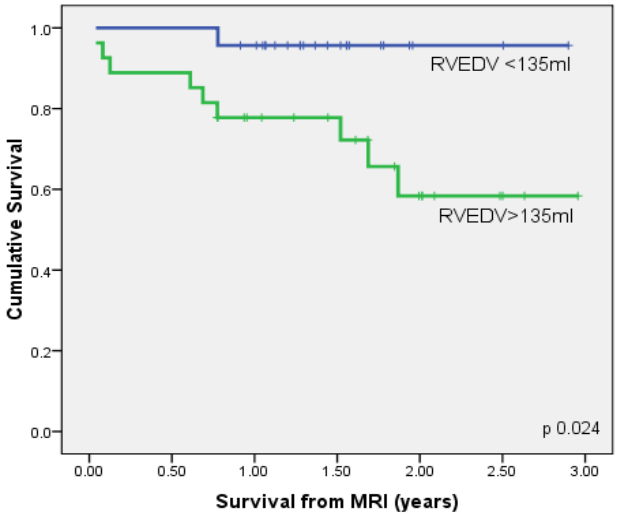

Figure 58: Kaplan-Meier survival curve for patients with Connective Tissue Disease associated Pulmonary Hypertension based on right ventricle end diastolic volume

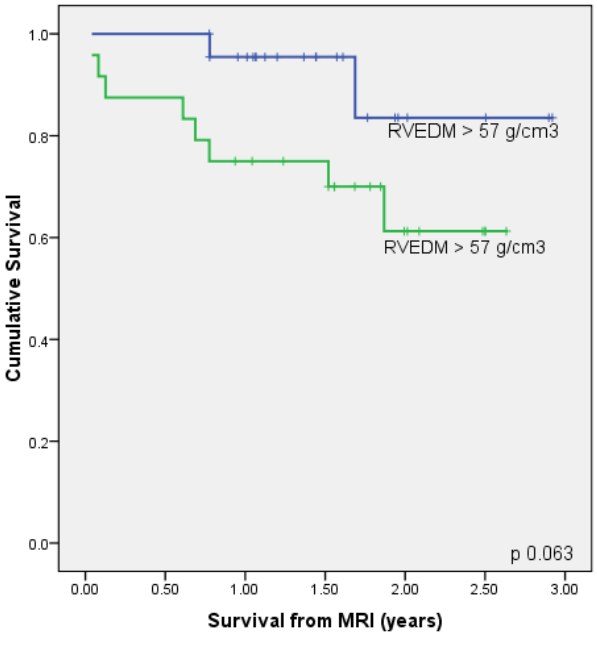

Figure 59: Kaplan-Meier survival curve for patients with Connective Tissue Disease associated Pulmonary Hypertension based on right ventricle end diastolic mass

6.6 Discussion

Principal findings: We have compared the diagnostic utility of MRI with CT and selected echocardiographic parameters, for the first time, in a large unselected group of patients with CTD and suspected PAH. We have demonstrated that both MR and echocardiographic indices have a good correlation with mPAP and PVR made at right heart catheter and performed well in predicting the presence of PAH in a high risk population. In addition, MR derived measures of volume and mass predicted outcome. In contrast, CT indices correlated only moderately with invasive measures of pulmonary haemodynamics and had poorer diagnostic utility for PAH. To the best of our knowledge, our study is the first to analyse several quantitative MR measures in a subgroup of patients with CTD and suspected PAH in comparison to 'gold standard' RHC.

There are interests in measures that are likely to reflect the remodelling process such as RV mass and fluid overload as reflected by change in chamber volume. In our cohort, right ventricular mass showed the best correlation with mPAP (RVEDM = r_0.70; VMI r_0.68) and this is not surprising as RV mass partially reflects the effect of RV afterload [76]. We and others, have previously shown that VMI can predict disease severity in patients with PAH [78-79], however both acquisition and post-processing for RV mass assessment is a time consuming process. In this study we have demonstrated that simpler and quicker to perform measurements such as RV/LV systolic area ratio also show good correlation with the catheter hemodynamics (mPAP r_0.68; PVR r_0.69). A simple approach to quantify systolic RV function has been to measure RV wall motion. Tricuspid annular plane systolic excursion (TAPSE) quantifies the longitudinal motion and SFD the transverse motion of the RV. Both these parameters have previously been applied in MRI in patients with IPAH [80, 173] and our results showed a better relationship of TAPSE with mPAP compared to SFD. Primary myocardial involvement has been reported in systemic sclerosis and established myocardial involvement characteristically results in myocardial fibrosis [174]. Our study examined the prevalence of delayed myocardial enhancement in patients with suspected PAH and interestingly 4 patients with systemic sclerosis had delayed myocardial enhancement in the absence of PAH based on right heart

catheterization. The process of 'Primary' myocardial involvement in systemic sclerosis may account for this finding in our study patients without PAH [175].

The development of PAH in patients with CTD is known to have a major impact on survival and this group of patients have poorer prognosis compared to other forms of PAH [112, 166, 176]. VMI was noted to predict outcome in a selected group of patients with systemic sclerosis associated PAH [78]. In a further work, Van Wolferen et al found low stroke volume, RV end diastolic volume index and impaired left ventricular filling to independently predict mortality in patients with PAH [76]. We have shown that these findings are broadly applicable in patients with CTD-PAH and have demonstrated the ability of MR measure of RV volume and ventricular mass index to identify patients with better outcome.

In a recent study, we have demonstrated moderate correlation between CT measured RV/LV ratio and reflux of contrast into hepatic veins and pulmonary haemodynamics [177]. However, as individual measurements, the role of morphological CT parameters appears to be limited as a prognostic and diagnostic tool. We have reproduced a similar correlation in a subgroup of patients with CTD using non-cardiac gated CT. This study, however, does establish that MRI has greater diagnostic accuracy than CT, which is not surprising given the gated nature of the acquired images and the functional information that can be gleaned from MRI.

Limitations

There are limitations to our study. The study was carried out in a quaternary referral centre for PH where patients were referred with suspected PH either from screening programmes or due to the presence of symptoms. This group are at particularly high risk of having PAH. They are therefore an important group of patients in whom it would be most appropriate to consider further non-invasive assessment. The CTPA that was used for evaluation of the cardiac measurements was not cardiac-gated. However CT performed for suspected PH is not routinely cardiac-gated and our study reflects the utility of CT that is typically performed in a routine clinical setting. Finally delayed myocardial enhancement have previously been quantified and have shown to predict outcome in patients with PH, in our group delayed myocardial enhancement was not quantified although qualitative analysis showed a relationship with mortality [178].

6.7 Conclusion

In conclusion, our results show that cardiac MR had similar diagnostic accuracy to TG, when this could be assessed using echocardiography and is superior to CT in assessing the severity of disease and diagnosing PAH in patients with CTD who are at high risk of having PAH. MR can identify with a high degree of certainty patients likely to have PAH and may be of particular value in patients with suspected PAH who have poor quality echocardiograms or in patients reluctant to have invasive investigation in establishing a positive diagnosis of PAH. In addition, cardiac MR also offers the added advantage of predicting mortality in this subgroup of patients with CTD-PAH and may be valuable in identifying patients for more aggressive therapy. Neither imaging test can confidently exclude PAH nor does right heart catheterisation remain the definitive investigation to do so in patients with on-going symptoms despite re-assuring non-invasive investigations.

7 CHAPTER 7: Balanced steady-state Free Precession MRI for imaging Lung parenchyma

This chapter is based a paper published in *Radiology* "Lung morphology assessment with balanced steady state free precession (bSSFP) MRI compared to computed tomography " *Rajaram S et al, Radiology 2012 May; 263(2):569-77.*

As we are aware chest radiography and CT have traditionally been considered as the modalities of choice for imaging lung parenchyma and CT gives excellent anatomical detail of the lung. However regardless of the low radiation dose volume CT protocols radiation exposure is still a great concern in paediatric patients and pregnant women. Furthermore, patients with chronic lung disorders may require multiple CT scans resulting in a high cumulative dose of radiation. Hence a radiation free screening tool for the lung is desirable particularly in high risk patients.

This final chapter of the thesis utility of balanced steady state free precession lung MRI is compared to CT for imaging morphological lung changes.

7.1 Abstract

Objective:

The purpose of this study was to evaluate the utility of 1.5T non-contrast MR imaging of the lung parenchyma and compare it to CT in the assessment of interstitial lung disease and other morphological lung abnormalities.

Methods:

236 patients who underwent MRI and CT investigations as part of their assessment for suspected PH were included in this study. Lung MRI was performed on a 1.5 T system as a stack of coronal 2D Steady State free precession acquisitions. Two radiologists independently evaluated the CT and MRI images for various morphological abnormalities such as pulmonary fibrosis, pleural and mediastinal disease, solid lesions, bronchial disease and emphysema.

Results:

The sensitivity and specificity of MRI in identifying pulmonary fibrosis (n=47) was 89% and 92% respectively. 80% of cases of mild fibrosis and 100% of severe fibrosis were seen on proton SSFP MRI. In comparison to CT, MRI demonstrated 75% of ground glass opacification. 9 out of the 12 non-calcified nodules were identified on MRI. Bronchial changes and effusion were also well visualized on MRI. MRI was however less effective in depicting emphysema, minor fibrosis and nodules less that 5mm in size.

Conclusion:

bSSFP MRI is inferior to CT in imaging parenchymal lung disease. This study does however demonstrate a potential role for the bSSFP sequence as an alternative radiation free, non-contrast imaging modality for young patients, pregnant women and in follow-up of patients with known lung disease.

7.2 Background

Until recently, MR imaging of the lung has been a challenge. This is principally due to poor inherent proton density of normal lung tissue resulting in low signal to noise ratio (SNR). Secondly, there is degradation of the signal from the lung parenchyma due to T2* dephasing from magnetic susceptibility gradients at the air-soft tissue interfaces [23]. Cardiac pulsation and breathing motion add further challenges to image quality.

The advent of newer MRI techniques that exploit developments in MR hardware namely faster switched field gradients and parallel imaging have opened up new scope for imaging lung parenchyma [179]. Techniques such as short echo time three dimensional (3D) breath-hold gradient echo [180-181], single shot fast spin echo [182-183] and post contrast T1 weighted gradient echo [184-185] have been considered for structural lung imaging. Studies and experimental work using these MRI sequences have shown them to be helpful in the assessment of malignant and benign lung changes [186-188]. More recently Failo et al [189] showed good visualization of lung parenchyma in patients with cystic fibrosis (CF) using a non-contrast, short TR/TE 2D balanced steady state free precession (bSSFP) technique. Nevertheless, experience with this bSSFP sequence for imaging lung morphology has been limited to comparisons with gradient echo methods in dynamic breathing studies [190]. Moreover comparison of bSSFP with CT in adult patients with lung disease has not been previously reported.

7.3 Objective

The purpose of this study was to evaluate the utility of 1.5T non-contrast MR imaging of the lung parenchyma and compare it to CT in the assessment of interstitial lung disease and other morphological lung abnormalities.

7.4 Methods

7.4.1 Study cohort

This was a retrospective study of 236 consecutive patients who underwent MRI and CT investigations as part of their routine assessment for suspected pulmonary hypertension between January 2008 and March 2010. All patients included in this study had CT and MRI performed within a time interval of 48 hours. 11 patients did not undergo MRI either due to claustrophobia or presence of MR incompatible metallic device. The study group included patients with no PH (n=36), and all major forms of PH [42] including pulmonary arterial hypertension (n= 81), chronic thromboembolic PH (n= 63), PH owing to left heart disease (n= 26) and PH owning to lung disease (n= 30). CT was considered as the 'reference standard' imaging modality for morphological imaging of the parenchyma.

7.4.2 Image acquisition

MR: A stack of coronal two dimensional bSSFP (GE Fiesta sequence) images were acquired, with the following parameters: TR 2.8 ms, TE 1.0ms, Flip angle of 50°, FOV=48 cm x 43.2 cm, 256 x 256 Matrix, 125 kHz bandwidth and slice thickness of 10mm. The lung apex to the diaphragm was covered in a single breath hold. This sequence was performed in full inspiration and with a breath hold time of 12 seconds. As part of the patients' workup for evaluation of PH, these bSSFP breathhold scans serve as scout images for planning the geometry of the cine cardiac scans used to assess right heart function.

The CT was performed on a 64 slice MDCT scanner (Light-Speed General Electric Medical Systems, Milwaukee, WI).

CTPA: CTPA was performed during a single breath-hold following and standard acquisition parameters were used: 100 mA with automated dose reduction, 120 kV, pitch 1, rotation time 0.5 s and 0.625mm collimation. The field of view was 400x400 mm with an acquisition matrix of 512 x 512. 100ml of intravenous contrast agent (Ultravist 300; Bayer Schering, Berlin, Germany) was administered at a rate of 5ml/sec. The CTPA images were reconstructed using a soft filter to

provide contiguous 0.625 mm axial slices from the apex of the lung to the diaphragm for review.

HRCT: 1.25mm HRCT slices were also reconstructed every 10mm from the contrast enhanced acquisition using a high spatial resolution filter.

7.4.3 Image analysis

The MR images were reviewed on a standard GE workstation by two independent radiologists blinded to the CT findings. For evaluation of pulmonary fibrosis, bronchial disease and emphysema, HRCT images were used. CTPA was used for assessment of pleural and mediastinal disease and solid lung lesions.

The images were evaluated for the presence or absence of the following morphological abnormalities: pulmonary fibrosis, pleural and mediastinal disease, solid lesions, bronchial disease and emphysema. The criteria for positive interpretation of fibrosis on CT and MRI included one or more of the following: interlobular septal thickening, intra-lobular interstitial thickening, honeycombing and traction bronchiectasis or ground-glass opacity [121-122]. Ground glass opacity on MR was defined as an area of increased signal intensity without obscuration of the pulmonary vessels as shown on a previous work by Muller et al [191].

Interstitial lung changes were graded based on a grading system used by Gay et al [123] and is outlined in table 33. Each lung was divided into 3 zones defined as follows: upper zone was defined as above the aortic arch, the middle zone was defined as between the aortic arch and pulmonary veins, and the lower zone was defined as below the pulmonary veins [124]. The sum of the scores for all zones for each patient was obtained (a minimum score was 0 and the maximum score was 30).

The CT and MR images were also studied for pleural and pericardial effusions and enlarged mediastinal lymph nodes.

Calcified and non-calcified pulmonary nodules and consolidation were assessed under ‘solid lesions’. The nodules were measured along their largest diameter.

Consolidation on MR was defined as homogenous increase in signal intensity with obscuration of margins of the vessels [192].

Bronchiectasis was considered when there was cylindrical dilatation. Emphysema on MRI was defined as area of low signal intensity with sparsity of pulmonary vasculature [193].

7.4.4 Statistical analysis

Exact 95% confidence interval (CI) of sensitivity, specificity, and positive and negative predictive values for presence or absence of pulmonary fibrosis were computed by using the binomial distributions. Kappa analysis was used to determine the extent of agreement between the two observers. In cases of discrepancy between observers regarding abnormality detection, a final interpretation was obtained by consensus during a second session.

7.5 Results

236 patients underwent MRI and CT within 48 hours and were included in the study. The mean age was 62 years ± 13 (± standard deviation); (149 women; mean age, 62 years ± 14; 87 men; mean age, 62 years ± 12). 224 MRI scans were of diagnostic quality, only 12 (12/236- 5.08%) had significant artefacts and were considered to be non-diagnostic. 33 patients had no lung or mediastinal disease on CT and for the purpose of this paper were considered as 'normals'. The interobserver agreement was performed for MRI but not CT data.

Fibrosis

Forty seven patients had pulmonary fibrosis on CT and the sensitivity and specificity of MRI for identifying pulmonary fibrosis was 89 % (95% CI: 77 to 96) and 91% (95% CI: 76 to 98) respectively with a positive and negative predictive value of 93% (95% CI: 82 to 99) and 86% (95% CI: 70 to 95) (Table 34). The bSSFP MRI identified (12/18) 78% of patients with total fibrosis score of 1-5 and (5/5) 100% patients with total fibrosis score of >15. In comparison to CT, MRI demonstrated 75% (9/12) of ground glass opacification, 67% (10/15) of traction bronchiectasis and 45% (5/11) of cystic reticular changes (Table 35). All the images were reviewed by two radiologists with 5 years of clinical experience with

substantial inter-observer agreement with inter-observer kappa of 0.79 (Table 36).

Table 33: HRCT interstitial score

Score	Characteristics
0	No interstitial disease
1	Interlobular septal thickening (no discrete honeycombing)
2	Honeycombing involving up to 25% of the zone
3	Honeycombing involving 25 to 49% of the zone
4	Honeycombing involving 50 to 75% of the zone
5	Honeycombing involving > 75% of the zone

*Adapted from Gay et al [123] based upon the relative quantity of honeycombing

Table 34: Overall accuracy of MRI in the overall diagnosis of pulmonary fibrosis

Fibrosis	CT Present	CT Absent	Total
MR Present	41	3	44
MR Absent	5	30	35
Total	46	33	79

Sensitivity 89.13% (95% CI: 77 - 96), specificity 91% (95% CI: 76 - 98), positive predictive value 93% (95% CI: 82 - 99), negative predictive value 86% (95% CI: 70 - 95)

Table 35: Sensitivity of MRI in the diagnosis of pulmonary fibrosis

		MR/CT	Sensitivity	95% CI	Kappa** (p value)
Degree of Fibrosis*	Score 1-5	12/18	66.67%	41 to 87	0.79
	Score 6-15	22/23	95.65%	78 to 99	
	Score >15	5/5	100%	48 to 100	
Pattern of Fibrosis	Ground glass opacification	9/12	75%	43 to 94	0.58
	Traction bronchiectasis	10/15	66.67%	38 to 88	0.61
	honeycombing involving ≤ 25% of a zone on CT	22/27	81.48%	61 to 93	0.43
	honeycombing involving ≥ 25% of a zone on CT	19/19	100%	82 to 100	0.62

*based on sum of the scores in 6 zones (minimum score was 0 and the maximum score was 30)
**Inter-observer agreement (Kappa) between the two readers for MRI; CI -confidence interval

Table 36: Inter-observer variation between two observers for diagnosis of fibrosis on MRI

	Observer 1		Total
	Fibrosis absent	Fibrosis present	
Observer 2			
Fibrosis absent	32	6	38
Fibrosis present	2	40	42
Total	34	46	80

Inter-observer agreement 90%, kappa=0·79 for presence of absence of fibrosis.
In 8 patients consensus reading on a second session was required.

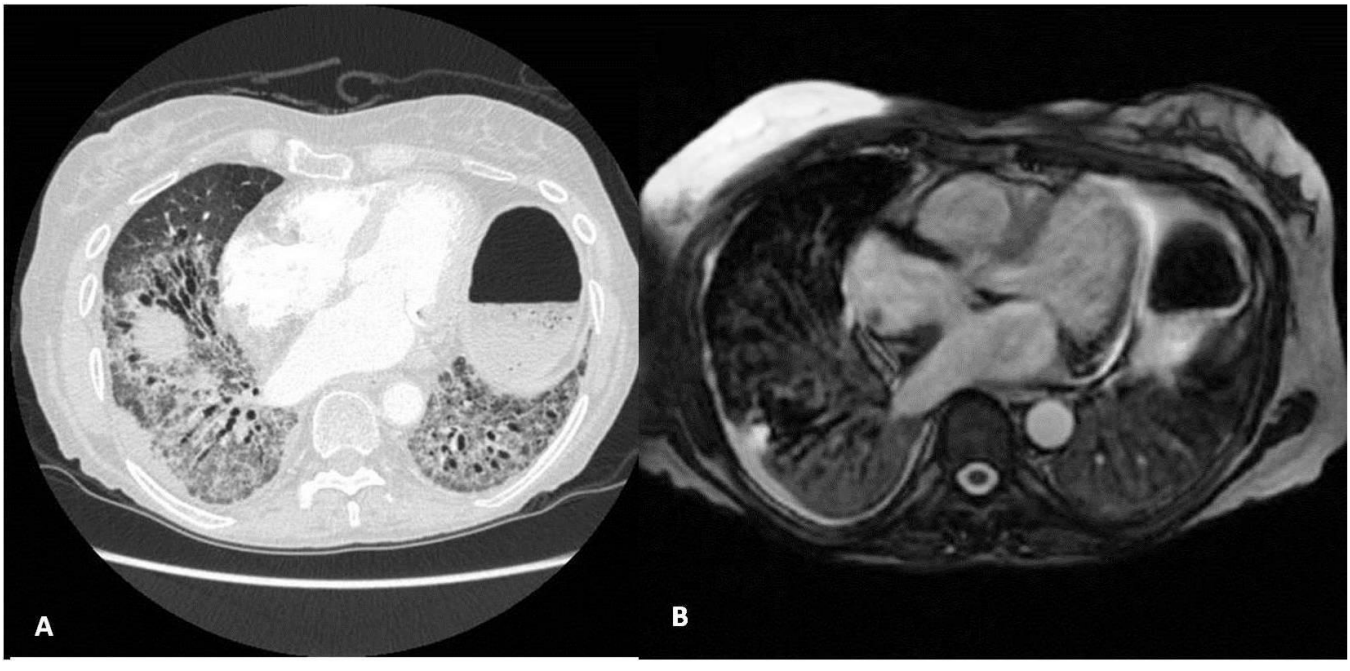

Figure 60: Typical NSIP pattern of fibrosis with presence traction bronchiectasis appreciated on both CT (A) and bSSFP MRI (B)

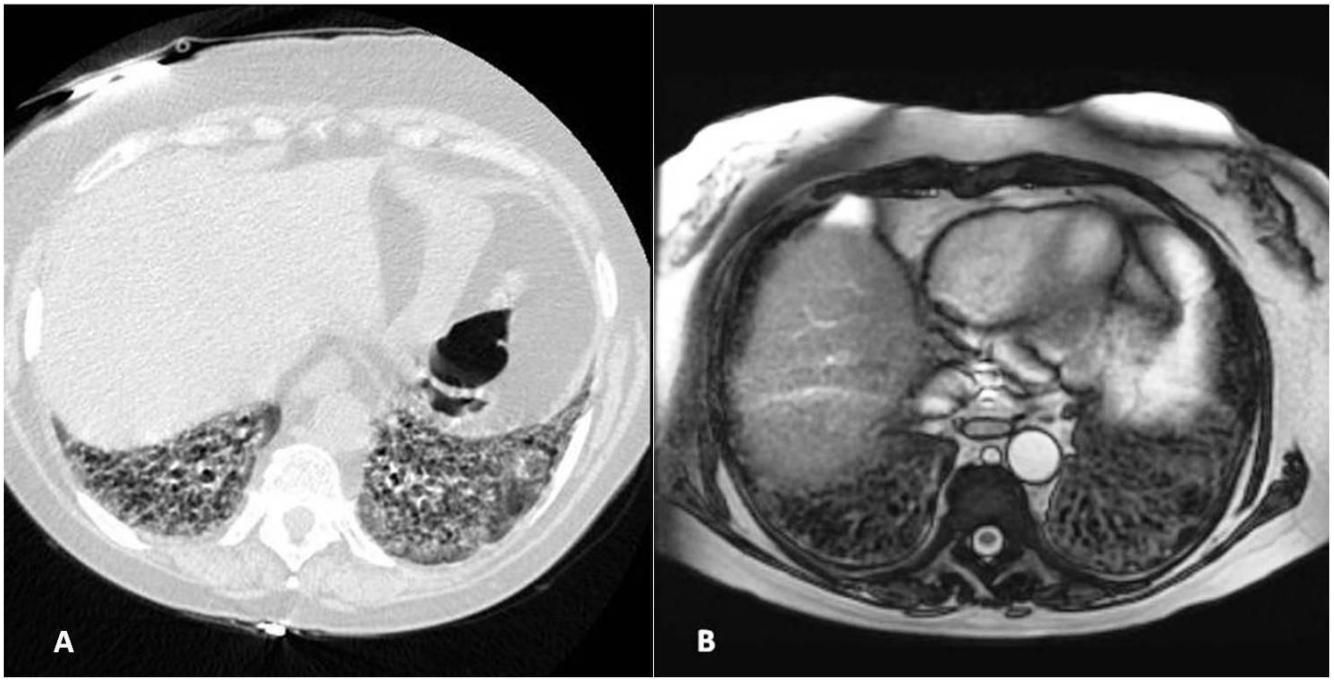

Figure 61: CT (A) and bSSFP MRI images (B) show the presence of cystic reticular pattern of fibrosis in the lung bases

Solid lesions:

Twelve non calcified lung nodules and 2 consolidations were seen on CT in 7 patients. MRI identified 9 of 12 non calcified lung nodules. The nodules ranged in size from 4 to 20mm and MRI identified 75% (6/8) of nodules between 6-10mm and 100% (6/8) of nodules above 11mm (3/3). In one patient with background pulmonary fibrosis, a 6mm nodule was hyperintense and hence was appreciated better on MRI than CT. MRI failed to identify an additional 12 calcified granulomas that were visualized on CT. The sensitivity was also poor for mosaic pattern of attenuation with MRI demonstrating only 3 of 33 patients (9.09%) (3/33).

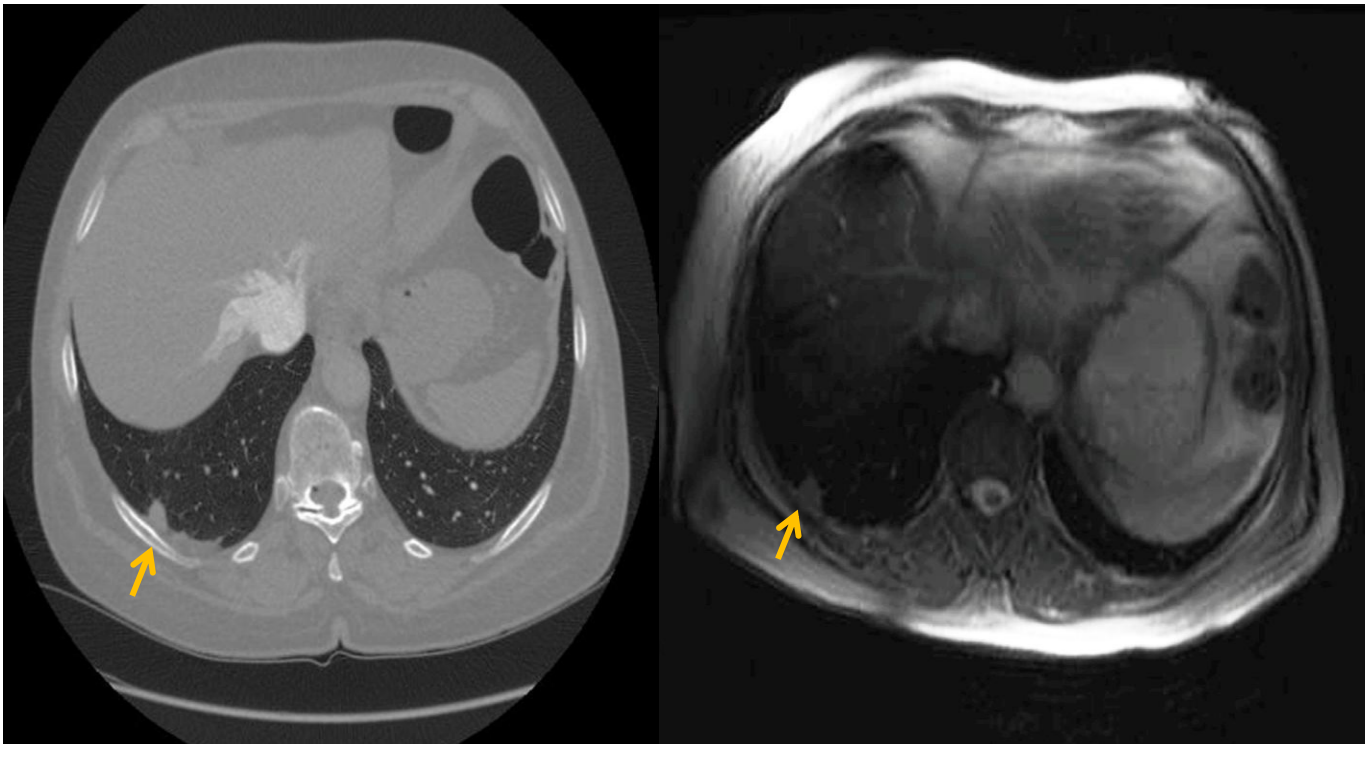

Figure 62: Small pleural based nodule seen on CT and MRI

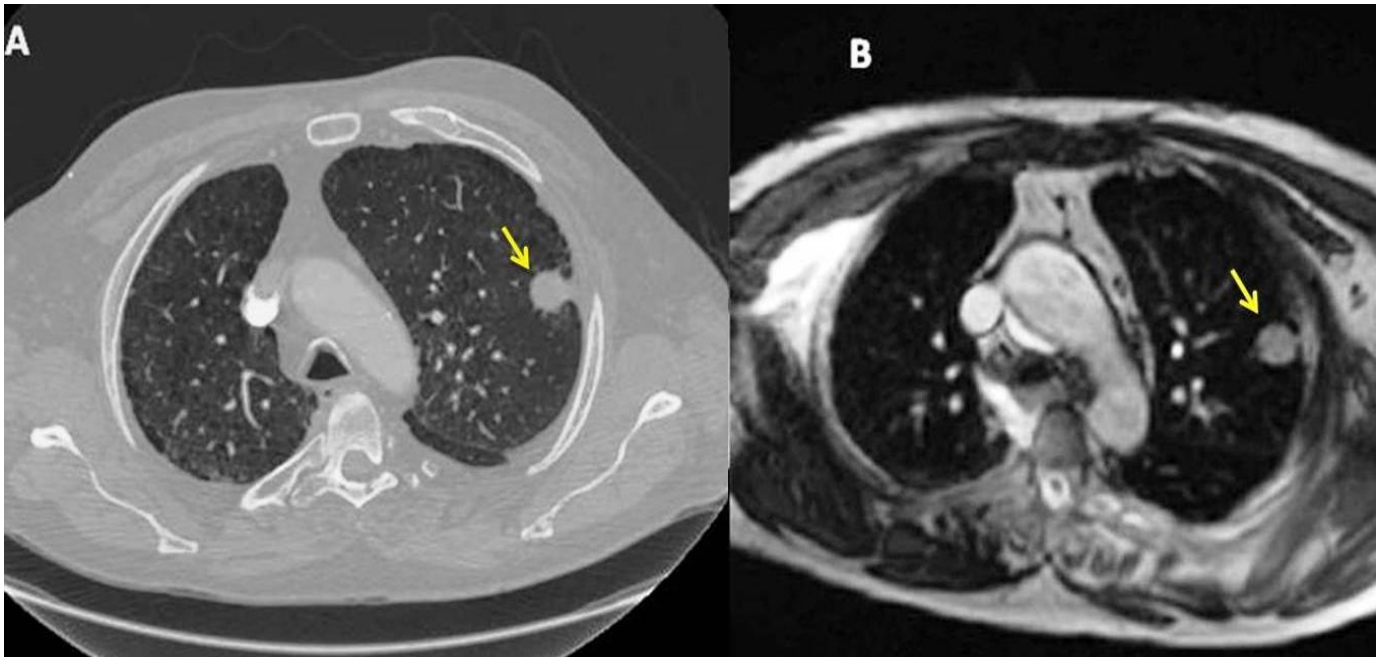

Figure 63: A peripheral 12mm lung nodule seen on both CT (A) & bSSFP MRI (B)

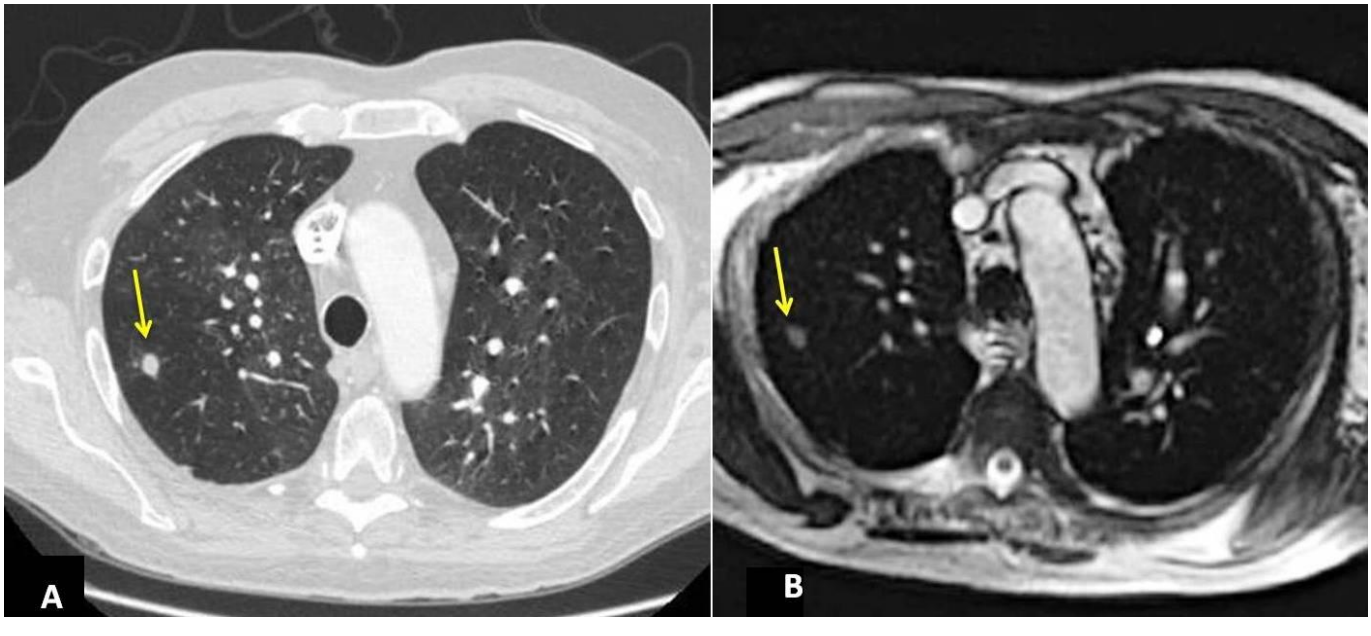

Figure 64: A peripheral nodule in the right upper lobe is appreciated on MRI (B) and CT (A)

Pleural and mediastinal disease:

MRI identified all patients with pleural (n=15) and pericardial effusions (n=12). Seventeen patients had enlarged mediastinal and hilar lymph nodes on CT, visualized in 12 patients on MRI with sensitivity of 70.58% (12/15)

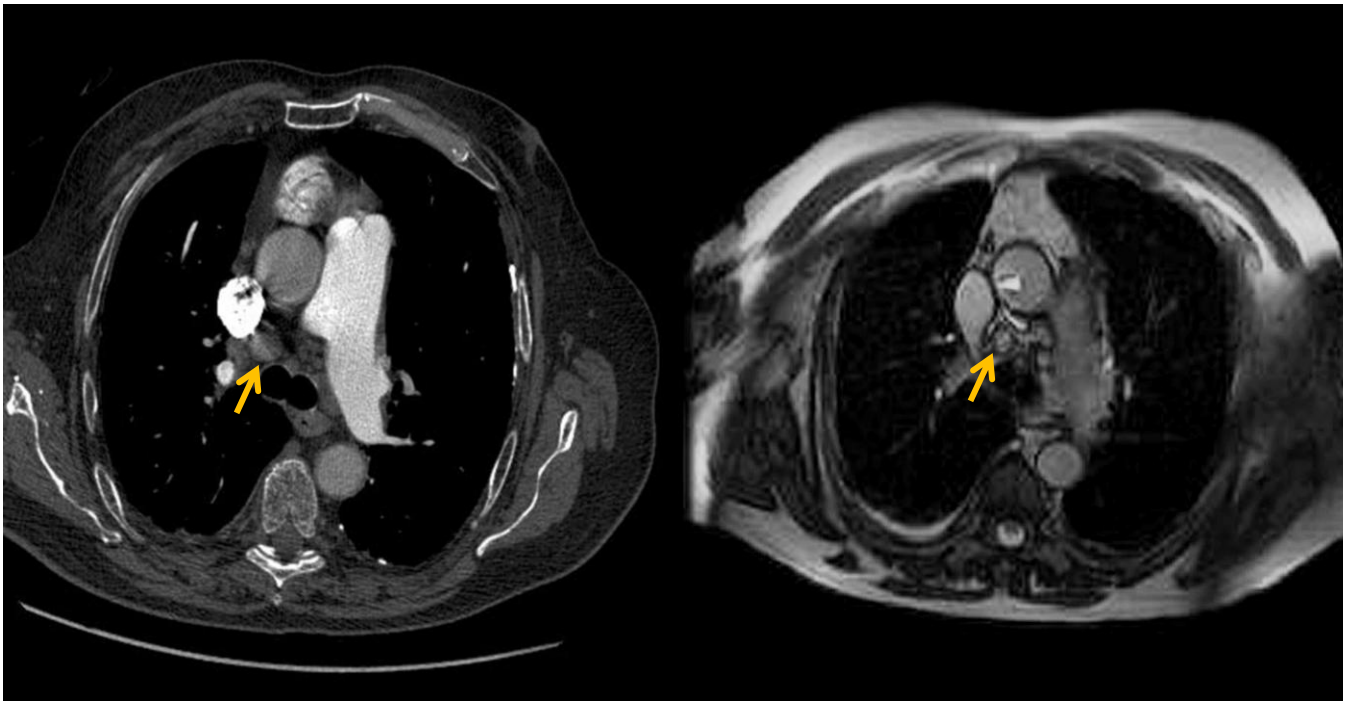

Figure 65: Small lymph node in the mediastinum and tiny right side effusion

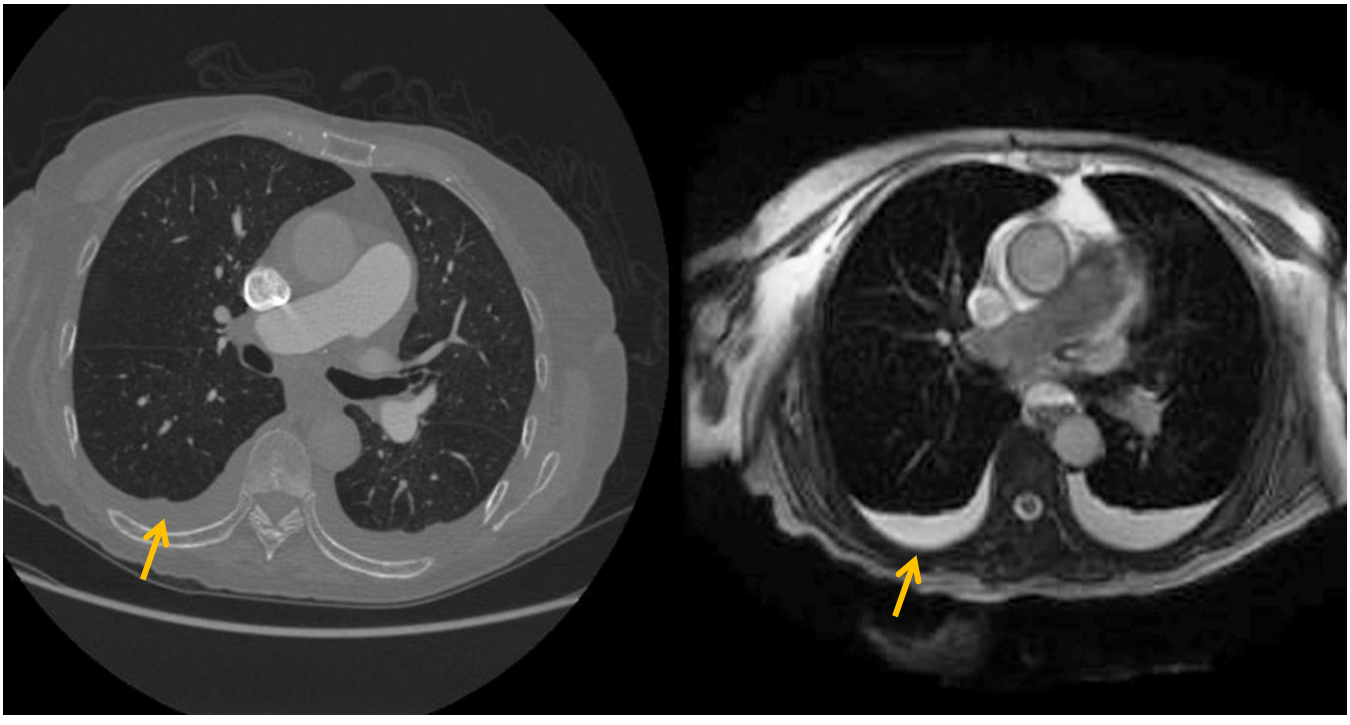

Figure 66: Small pleural effusion in both lungs

Bronchial disease:

Six patients had bronchiectasis on CT. MRI depicted 4 patients with central disease (4/6; 67%), but 2 patients with peripheral disease were missed. Two patients were thought to have mucus plugging on CT and this was confirmed on MRI with characteristic hyperintensity in the bSSFP signal [189]. Patients with traction bronchiectasis secondary to pulmonary fibrosis on CT were analysed under the pulmonary fibrosis group.

Emphysema:

Forty five patients had emphysematous changes on CT. On CT assessment, 13 patients had severe disease, 9 patients had moderate and 23 patients had mild disease. Bullous emphysema was seen in 5 patients. MRI was able to identify 7 emphysematous patients, of which 4 had bullous disease and 3 had severe emphysema with marked sparsely of pulmonary vasculature. None of the cases of mild centrilobular or paraseptal emphysema (n=21) were recognised on MRI.

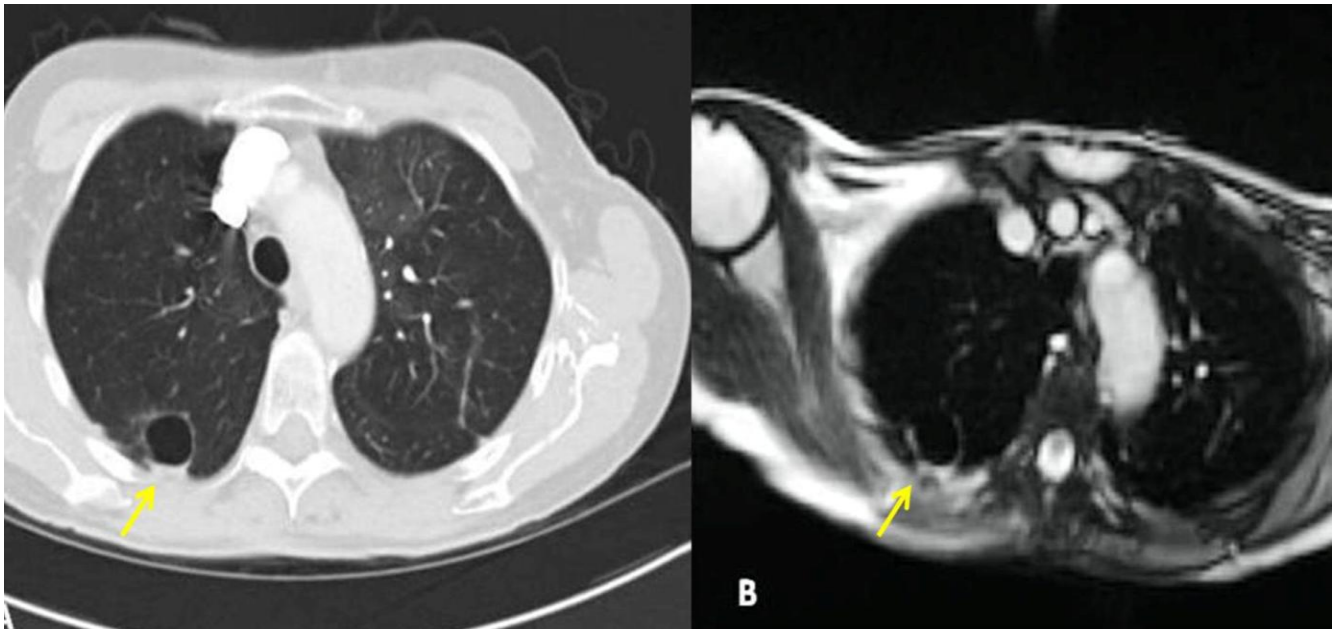

Figure 67: Bullae in the right apex

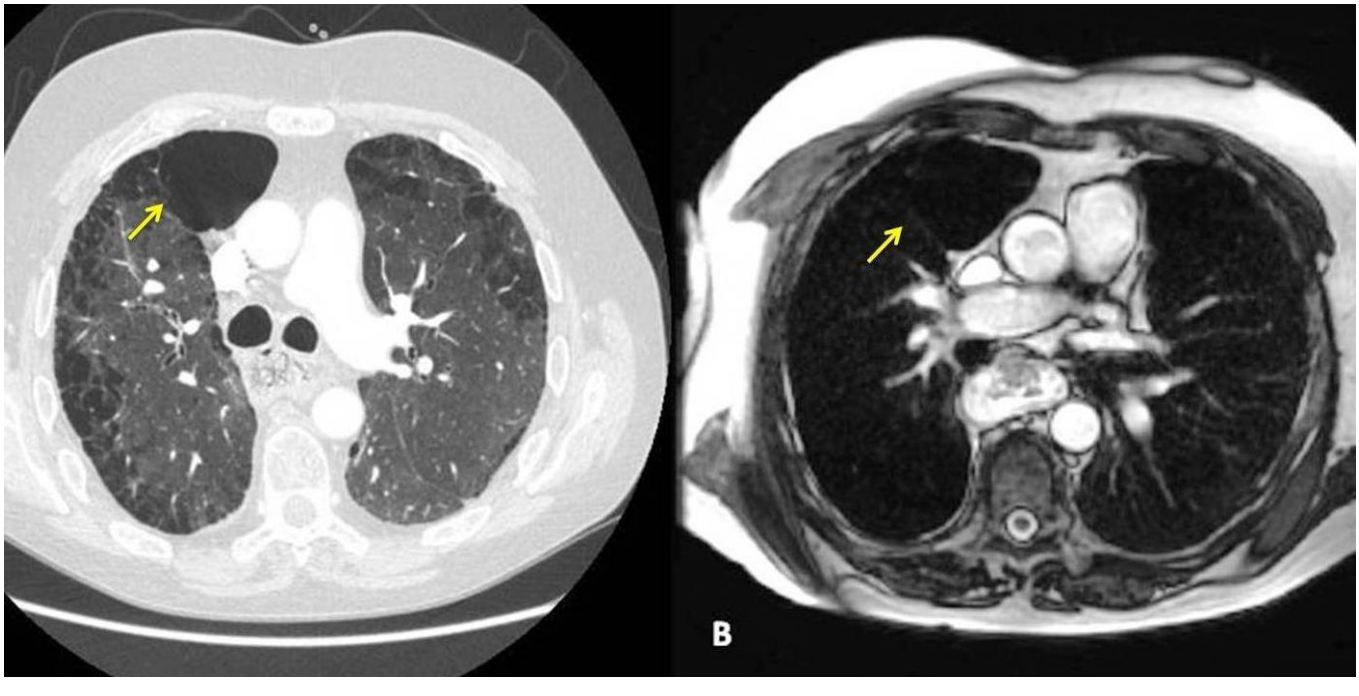

Figure 68: A peripheral bulla in the right middle lobe is appreciated on MRI

Table 37: Sensitivity of MRI in the diagnosis of various morphological lung abnormalities and inter-observer agreement (Kappa) between the two readers for MRI

	Sensitivity (%)	No. detected on MRI	No. detected on CT	Kappa (*p* value)*
Pleural effusion	100	15	15	0.89
Pericardial effusion	100	12	12	0.83
Consolidation	100	2	2	0.66
Fibrosis	89	41	46	0.79
Nodules	75	9	12	0.71
Lymph nodes	71	12	17	0.65
Bronchiectasis *	67	4	6	0.61
Atelectasis	64	20	31	0.75
Mucus plugging	50	2	4	0.56
Emphysema	16	7	45	0.60
Mosaic pattern	9	3	33	0.53

*non cystic fibrosis patients; patients with traction bronchiectasis not included

7.6 Discussion

In this study an ultra-short TR/TE 2D bSSFP MRI sequence has been used. In an observational study in healthy volunteers and phantom models [190], bSSFP was shown to provide good quality images with superior spatial resolution and signal, and equal temporal resolution to spoiled gradient echo. More recently, Failo et al [189] showed bSSFP to be effective in the detection of clinically relevant structural abnormalities such as bronchiectasis, mucus plugging and atelectasis in children with cystic fibrosis. Our study is the first to assess bSSFP MRI against CT in a large group of adult patients with various lung abnormalities and in particular a large group of patients with pulmonary fibrosis. The potential advantages of 2D bSSFP when compared to the 3D gradient echo (VIBE) sequence described in [180] are the shorter acquisition times that facilitate volume coverage in a single breath-hold as opposed to multiple 3D slabs in separate breaths. The bSSFP protocol we used provided a fast and efficient means of quick assessment of structural and vascular abnormality in the patients chosen. The 2D bSSFP method could also be readily extended to 3D acquisition with an associated increase in acquisition time. Caution should be taken with regard to characteristic off-resonance banding artefacts that are seen with bSSFP in regions of magnetic inhomogeneity such as close to the diaphragm. As the lung signal is intrinsically dark, the propagation of such a banding artefact into the lung field could obliterate focal hyperintense signal from nodules and vessels. Care was taken to scrutinise for such artifacts in this work and these could be further reduced with a shorter TE. The VIBE sequence described in [180] could potentially be accelerated further in to a single breathhold with shorter TE and TR now achievable on state of the art systems. A side-by-side evaluation of the different contrasts and sensitivity to different lung pathologies offered by bSSFP, HASTE and VIBE for structural lung imaging alongside ultra-short echo time radial imaging is work in progress in our institute and is beyond the scope of this paper [194].

Further work is also required to assess the most sensitive MR sequence for detection of fibrosis, presence of inflammation and pulmonary nodules which currently may be pre- and post-contrast breath-hold 3D gradient echo sequences [180].

The potential advantages of the bSSFP sequence over the HASTE sequence are; the shorter TE, acquisition time and lower Specific Absorption Rate (SAR) intensity. bSSFP also offers a different mixed T2 and T1 contrast as compared to the T2 weighted contrast of HASTE. The faster acquisition times explain the absence of cardiac motion artefact. This sequence does not require intravenous contrast and hence can be performed in patients with impaired renal function. The normal lung parenchyma has a low signal-to-noise ratio (SNR) in MRI and in a small representative sample in our study, the normal lung parenchyma showed a mean signal intensity of 30.4±12.15 with the mean background noise signal of 23.19±7.45. With further decreases in echo time the SNR of the lung parenchyma could be further improved which could open up increased sensitivity to emphysema. The MR signal intensity of the lung parenchyma also visually increases on expiration compared to inspiration on MRI and this may be used for the assessment of air trapping and emphysema. The pathological changes usually have higher proton density and hence appear brighter due to increased signal intensity. Therefore, the lung abnormalities are more conspicuous in MRI [195]. This could be a potential solution to the problem of imaging the pregnant women without the use of contrast agent or exposing to them harmful effects of ionising radiation.

The high tissue contrast of MRI is generally expected to be useful for differentiation of active inflammation from fibrosis in ILDs, thereby aiding in the management. Initial studies showed the presence of high signal intensity lesions were a useful predictor of treatment response and clinical outcome [191, 196]. Subsequent reports focused on the enhancement pattern in the areas of active alveolitis [197-198]. Our results show that bSSFP MRI has a good specificity and sensitivity for anatomical resolution of pulmonary fibrosis, especially in patients with severe disease. Areas of ground glass attenuation, traction bronchiectasis and cystic reticular change were appreciated on MRI. Patients with chronic interstitial lung disease have relapsing and remitting symptoms and need frequent imaging to assess disease status and also response to treatment. MRI could potentially be used as a follow up in patients with known lung changes visible on MRI and thus preventing multiple radiation exposures. Although sensitivity of detection of pulmonary nodules greater than 5mm was 81% (9/11), the detection of small pulmonary nodules and even larger ground glass nodules,

especially when patients do not breath-hold adequately, was significantly decreased. This mandates that we continue to offer patients CT as a first line means of follow-up for pulmonary fibrosis, given the increased risk of lung cancer in these patients. MRI was able to identify bullae in a background of normal or fibrosed lung tissue. In few patients, severe emphysema was appreciated due to marked paucity of pulmonary vasculature. However, due to decreased lung tissue in emphysematous patients, MRI was generally poor in depicting subtle emphysematous changes. By virtue of the inherent hyper-intensity of bSSFP images to fluid signals, pleural and pericardial effusions were more easily depicted by MRI and the findings in the small number of patients with bronchiectasis were also encouraging Overall bSSFP MRI does demonstrate a wide range of parenchymal lung abnormalities and our findings were comparable to other studies with different sequences [199].

Limitations

One of the limitations of our study was that, despite a large number of study patients, the number of patients for some morphological changes was low and hence the true positive and negative predictive values could not be assessed. The MR sequence was performed without intravenous contrast and the potential role of the contrast enhanced b-SSFP sequence to differentiate active inflammation from fibrosis and detection of smaller lung nodules has not been explored. This was a retrospective review of patients undergoing imaging investigations as part of the routine assessment of suspected PH and hence a highly selected group of patients. Although MR images were reported in isolation some features such as oesophageal dilatation may have influenced the diagnosis of lung fibrosis. Given the number of patients studied, our results prove the feasibility of MRI in interpreting a wide variety of pulmonary pathologies in a non-specific consecutive group of subjects with and without lung disease.

7.7 Conclusion

In conclusion, bSSFP MRI is inferior to CT in imaging parenchymal lung disease. However, the study does demonstrate that there is a potential role for the bSSFP sequence as an alternative radiation free, non-contrast imaging modality. In particular we have demonstrated for the first time the utility of this potential

technique in the evaluation of the severity of pulmonary fibrosis. A larger study on the utility of MR in diagnosing fibrosis in a non-selected population is required before this can be applied in clinical practice.

8 Future directions

This body of research has shown that several simple and reproducible CT and MRI indices and pulse sequences have value in the assessment of subgroups of patients with pulmonary hypertension and associated lung disease. These imaging modalities have been compared with the 'gold standard' methods and have shown promising results.

From this thesis, MR angiography is a valuable tool for the assessment of the pulmonary vasculature. The data also proves that 3D MR perfusion has a high diagnostic accuracy similar to perfusion scintigraphy in the assessment of thromboembolic disease. Pulmonary embolism has a quoted incidence of 42 per 100000 (95% CI, 39-46) [200] and is increasingly being recognized and suspected in clinical practice. The average radiation dose from the current standard investigation CT pulmonary angiography is 7-8mSV. Using MR angiography combined with 3D MR perfusion imaging for investigating acute pulmonary embolism will provide a radiation free alternative and this need to be explored further for future patient benefit. Newer non-contrast MR angiographic techniques are emerging and value of these techniques for identifying pulmonary embolism should be examined as they would provide an ideal investigation tool for pregnant patients with suspected pulmonary embolism.

This body of work also shown for the first time that several uncomplicated indices on a standard CT can identify subgroups of patients with pulmonary arterial hypertension and can also recognise patients who are at risk of having a poor outcome with disease process. This thesis has highlighted the potential value of morphological MRI and CT indices in comparison to invasive right heart catheter measurements in the diagnostic work-up of patients presenting with suspected PH. Furthermore, it has also shown the utility of these techniques in assessing disease severity and prognosticating the outcome. Similar analysis in other groups in particular PH owing to left heart disease or PH secondary to chronic thromboembolic disease must be done to evaluate the diagnostic impact and sensitivity across groups of pulmonary hypertension.

This should also be performed in multiple centres to find the efficiency of recognising these changes by general and specialist radiologists.

Another important outcome of this thesis is that for the first time the diagnostic value of balanced SSPF MRI for detecting lung parenchymal abnormalities has been studied. The results show that although inferior to CT, MRI has a good accuracy for identifying moderate to severe fibrosis. This improved anatomic resolution of balanced SSFP sequence can be utilized, for instance, to differentiate inflammation and fibrosis-predominant lesions in the patients with interstitial lung disease types such as usual and nonspecific interstitial pneumonias.

Techniques such as utrashort echo time (UTE) MRI have been shown to demonstrate much higher signal intensity in the lung parenchyma and finer pulmonary structures. The balanced SSFP sequence must also be compared with these sequences for anatomical resolution of lung parenchymal changes and radiological comparison are fully made.

9 Appendix A – publications, presentations and posters

PUBLISHED PAPERS (DIRECTLY RELATED TO THIS THESIS)

Rajaram S, Swift AJ, Capener D, Telfer A, Davies C, Hill C, Condliffe R, Elliot C, Hurdman J Wild JM, Kiely DG. *3D contrast-enhanced lung perfusion MRI is an effective screening tool for chronic thromboembolic pulmonary hypertension: results from the ASPIRE Registry.* Thorax 2013 doi:10.1136/thoraxjnl-2012-203020

Rajaram S, Swift AJ, Capener D, Telfer A, Davies C, Hill C, Condliffe R, Elliot C, Hurdman J, Kiely DG, Wild JM. *Lung morphology assessment with balanced steady-state free precession MR imaging compared with CT*. Radiology. 2012 May;263(2):569-77. Epub 2012 Mar 6.

Rajaram S, Swift AJ, Capener D, Telfer A, Davies C, Hill C, Condliffe R, Elliot C, Hurdman J, Kiely DG, Wild JM. *Diagnostic accuracy of contrast-enhanced MR angiography and unenhanced proton MR imaging compared with CT pulmonary angiography in chronic thromboembolic pulmonary hypertension*. Eur Radiol. 2012 Feb;22(2):310-7. Epub 2011 Sep 2

Rajaram S, Swift AJ, Capener D, Elliot CA, Condliffe R, Davies C, Hill C, Hurdman J, Kidling R, Akil M, Wild JM, Kiely DG. *Comparison of the diagnostic utility of cardiac magnetic resonance imaging, computed tomography and echocardiography in assessment of suspected pulmonary arterial hypertension in patients with connective tissue disease*. J Rheumatol. 2012 Jun;39(6):1265-74. Epub 2012 May 15.

PAPERS FOR SUBMISSION (DIRECTLY RELATED TO THE THESIS)

Rajaram S, Swift AJ, Elliot CA, Condliffe R, Davies C, Hill C, Hurdman J, Wild JM, Kiely DG, *CT features of pulmonary arterial hypertension and its major subtypes: a study of 292 patients.*

CO-AUTHORED PUBLISHED PAPERS (INDIRECTLY RELATED TO THE THESIS)

Swift AJ, **Rajaram S**, Condliffe R, Capener D, Hurdman J, Elliot CA, Wild JM, Kiely DG. Diagnostic accuracy of cardiovascular magnetic resonance of right ventricular morphology and function in the assessment of suspected pulmonary hypertension. J Cardiovasc Magn Reson. 2012 Jun 21;14(1):40.

Condliffe R, Radon M, Hurdman J, Davies C, Hill C, Akil M, Guarasci F, **Rajaram S**, Swift AJ, Wragg Z, van Beek E, Elliot CA, Kiely DG CT pulmonary angiography combined with echocardiography in suspected systemic sclerosis-associated pulmonary arterial hypertension. Rheumatology (Oxford). 2011 Mar 29.

Swift AJ, **Rajaram S**, Condliffe R, Capener D, Hurdman J, Elliot CA, Kiely DG, Wild JM,. Pulmonary artery relative area change detects mild elevations in pulmonary vascular resistance and predicts adverse outcome in pulmonary hypertension. Invest Rad. 2012 Oct;47(10): 571-577

Marshall H, Deppe MH, Parra-Robles J, Hillis S, Billings CG, **Rajaram S**, Swift AJ, Miller SR, Watson JH, Wolber J, Lipson DA, Lawson R, Wild JM. Direct visualisation of collateral ventilation in COPD with hyperpolarised gas MRI. Thorax. 2012 Jul;67(7):613-7. Epub 2012 Jan 27.

Swift AJ, **Rajaram S**, Marshall H, Condliffe R, Capener D, Hill C, Davies C, Hurdman J, Elliot CA, Wild JM, Kiely DG. Black blood MRI has diagnostic and prognostic value in the assessment of patients with pulmonary hypertension. Eur Radiol. 2012 Mar;22(3):695-702.

INTERNATIONAL ORAL PRESENTATIONS

Rajaram S, Swift AJ, Marshall H, Capener D, Condliffe R, Hurdman J, Elliot C, Kiely DG, Wild JM. Cardiac MRI in connective tissue disease patients with suspected pulmonary hypertension: correlation between morphological and functional parameters and invasive measurements. EULAR 2011

Rajaram S, AJ Swift, D Capener, C Davies, C Hill, R Condliffe, C Elliot, J Hurdman, JM Wild, DG Kiely Accuracy of contrast enhanced MR lung perfusion compared to perfusion scintigraphy in diagnosing Chronic Thromboembolic Pulmonary Hypertension. BTS 2011

Rajaram S, AJ Swift, D Capener, C Davies, C Hill, R Condliffe, C Elliot, J Hurdman, JM Wild, DG Kiely Connective tissue disease patients with suspected pulmonary hypertension: correlation between MR and CT parameters and invasive measurement. RSNA 2011

POSTER PRESENTATIONS

Rajaram S, Swift AJ, Marshall H, Capener D, Condliffe R, Hurdman J, Elliot C, Kiely DG, Wild JM Diagnostic Accuracy of Contrast-Enhanced MRA and Non-Contrast Proton MRI Compared with CTPA in Chronic Thromboembolic Pulmonary Hypertension. ISMRM 2011

Rajaram S, Swift AJ, Marshall H, Capener D, Condliffe R, Hurdman J, Elliot C, Kiely DG, Wild JM Assessment of lung morphology with steady state free precession (SSFP) MRI compared to computed tomography. UPenn 2011

Rajaram S, Swift AJ, Marshall H, Capener D, Condliffe R, Hurdman J, Elliot C, Kiely DG, Wild JM Comparative study of SPSS lung MRI with HRCT in patients with interstitial lung fibrosis. ISMRM 2011

Rajaram S, Swift AJ, Marshall H, Capener D, Condliffe R, Hurdman J, Elliot C, Kiely DG, Wild JM. Effect of pulmonary fibrosis on pulmonary artery size in predicting pulmonary hypertension. ESTI 2011

Rajaram S, AJ Swift, D Capener, C Davies, C Hill, R Condliffe, C Elliot, J Hurdman, DG Kiely, JM Wild. Diagnostic Accuracy of Contrast-Enhanced MRA and Non-Contrast Proton MRI Compared with CTPA in Chronic Thromboembolic Pulmonary Hypertension. ISMRM 2011

S Rajaram, AJ Swift, D Capener, C Davies, C Hill, R Condliffe, C Elliot, J Hurdman, DG Kiely, JM Wild. Diagnostic Accuracy of Contrast-Enhanced MRA and Unenhanced Proton MRI Compared with CTPA in Chronic Thromboembolic Pulmonary Hypertension. National CTEPH meeting 2011

S Rajaram, AJ Swift, D Capener, C Davies, C Hill, R Condliffe, C Elliot, J Hurdman, DG Kiely, JM Wild. Delayed myocardial enhancement predicts mortality in patients with Pulmonary Hypertension. RSNA 2011

Swift AJ, **Rajaram S**, Capener D, Sproson TW, Elliot C, Condliffe R, Kiely DG, Wild JM Prognostic value of ventricular volumes and function in patients with pulmonary hypertension due to chronic obstructive pulmonary disease. ERS 2012

Swift AJ, **Rajaram S**, Capener D, Marshall H, Hill C, Davies C, Hurdman J, Condliffe R, Elliot C, Wild JM, Kiely DG. Black blood MRI has high diagnostic accuracy in patients with suspected pulmonary hypertension. ATS 2011

Swift AJ, **Rajaram S**, Capener, Condliffe R, Hurdman J, Elliot C, Wild JM and Kiely DG MR LV Systolic Eccentricity Index Compared to Established Cardiac MR Parameters for the Diagnosis of PH: Correlation with Right Heart Catheterization. ATS 2011

Swift AJ, **Rajaram S**, Capener D, Hurdman J, Condliffe R, Elliot C, Kiely DG, Wild JM. Relative Area Change (RAC) Better Reflects Right Ventricular Ejection Fraction (RVEF) than Longitudinal or Transverse Functional Measurements in PH Patients. ISMRM 2011

Swift AJ, **Rajaram S**, Capener D, Hill C, Davies C, Condliffe R, Hurdman J, Elliot C, Wild JM, Kiely DG. 3D MR Pulmonary Perfusion in Connective Tissue Disease Patients: a non-invasive method of PVR estimation. EULAR 2011

Swift AJ, Telfer A , Marshall H, **Rajaram S** Capener D, Condliffe R, Hurdman J, Elliot C, Kiely DG, Wild JM 3D MR Pulmonary Perfusion in Patients with Pulmonary Arterial Hypertension: Regional Analysis of Contrast Transit Times. UPenn 2011

Swift AJ, Telfer A , Marshall H, **Rajaram S** Capener D, Condliffe R, Hurdman J, Elliot C, Kiely DG, Wild JM. 3D Time-resolved MR Perfusion in Patients with Chronic Thromboembolic Pulmonary Hypertension. National CTEPH meeting 2011

Swift AJ, **Rajaram S**, Marshall H, Capener D, Condliffe R, Hurdman J, Elliot C, Kiely DG, Wild JM. Novel Method for the Estimation of PCWP using CINE Cardiac MRI in Patients with Pulmonary Hypertension. ERS 2011

10 Appendix B – CT Physics

The basic principle of CT is that it generates two-dimensional cross-sectional images of the body by using X-rays. The X-rays are generated by the X-ray tube that rapidly rotates 360° around the patient. The transmitted radiation is then measured by a ring of sensitive radiation detectors located on the gantry around the patient. Finally, the acquired images from multiple X-ray projections are reconstructed using appropriate algorithm depending of the body parts imaged and the clinical situation.

There are two modes of CT scan, step and shoot technique or the helical or spiral CT. The step and shoot (which is two alternate stages of data acquisition and patient positioning) is replaced by the spiral CT scanners. With spiral CT, X-ray tube rotates continuously in one direction whilst the table mechanically moves forward. The patient is thus exposure to a helical or spiral beam of radiation and with this technique the information can be acquired as a continuous volume of contiguous slices. The scan time is exponentially faster with this technique.

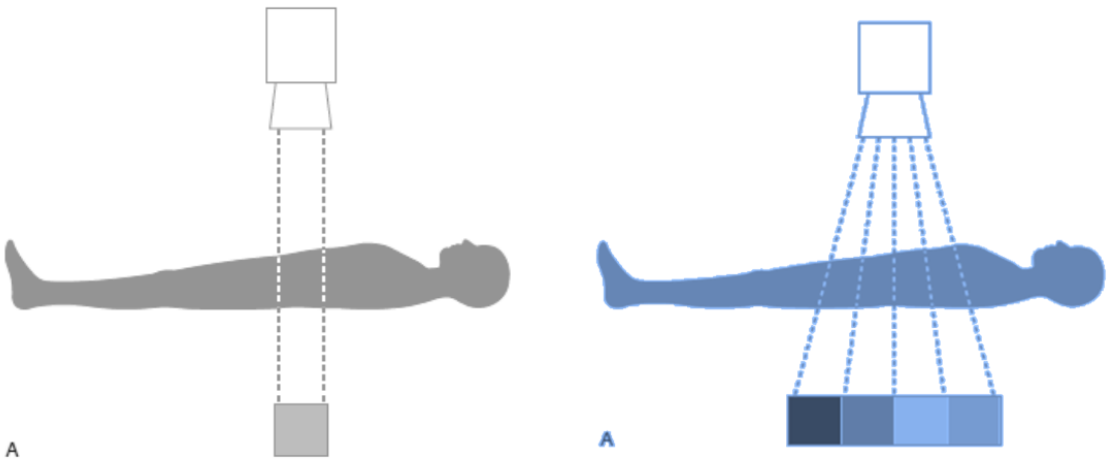

Figure 69: A represents a single slice system and B represents a mutlislice system

A major turning point for using CT for clinical imaging was the introduction of mutlislice CT. The key difference between a single and mutlislice CT is in the detector array design. Single slice CT consists of a large detector element in a single row to intercept the transmitted radiation across the slice. It is mono directional and controls both the slice thickness and resolution. In MSCT, detector elements are divided into several smaller detector elements, forming a 2-dimensional array forming multiple parallel rows of detectors unlike single row of detectors intercepting the X-ray fanbeam.

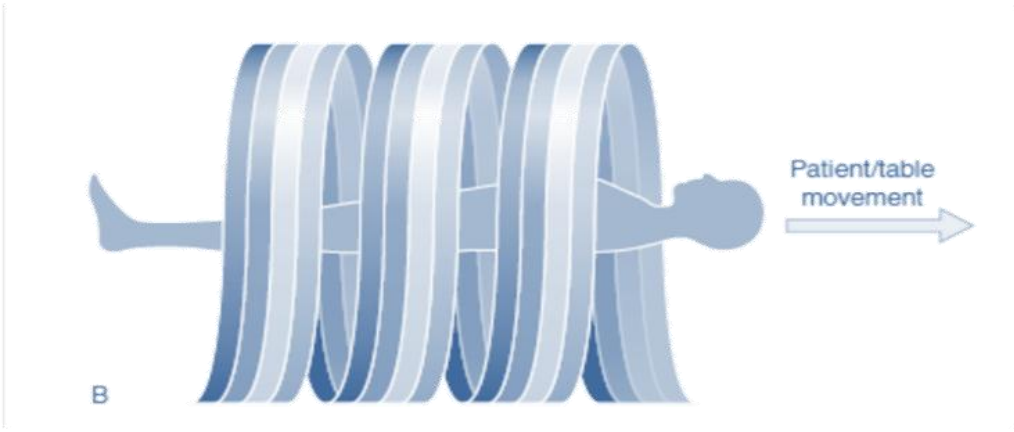

Figure 70: This represents a helical mutlislice system with four detectors. The X-ray tube rotates continuously and the patient moves through the X-ray beam at a constant rate.

Most mutlislice scanners are based on the third generator CT platform. In this design the detector array is rigidly linked to the x-ray tube, so that both the tube and the detectors rotate undergo a single rotational motion together around the patient.

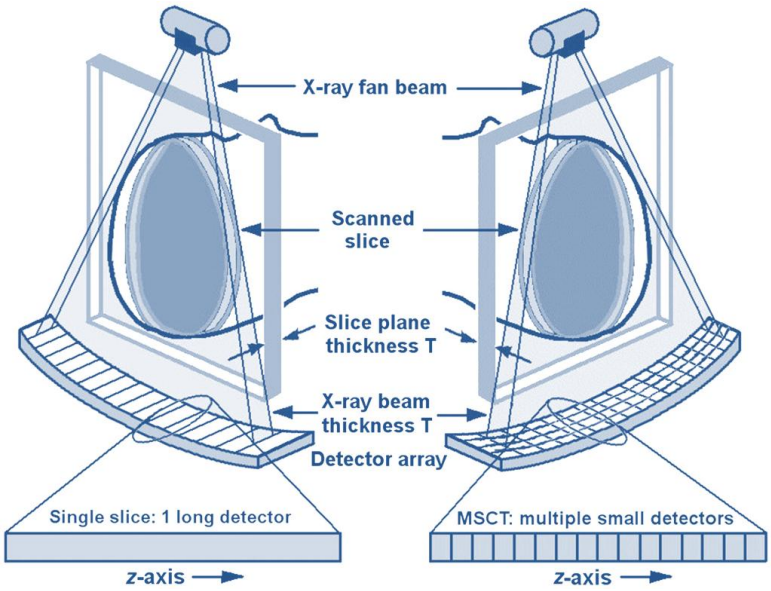

Figure 71: Single slice CT detectors containing single array of long elements along z-axis. (Right) while mutlislice CT arrays have several rows of small detector elements. Diagrams taken from [201]

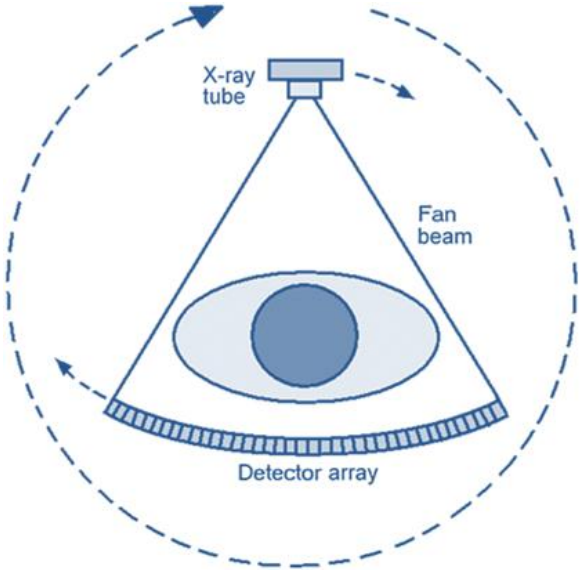

Figure 72: This is an example of third-generation CT detectors. Tube and detectors were rigidly linked and underwent single rotational motion and large array of detectors measure data across width of fan [201]

Finally, cardiac gated CT techniques minimizes imaging artifacts caused by cardiac motion and improve temporal resolution of the images. There are two approaches to ECG gating; one is prospective ECG triggering and the other is retrospective ECG gating. The total radiation dose is substantially higher with retrospective gating as the X-ray tube is 'on' throughout the examination and while with prospective gating the X-ray tube is on only during a short burst ('step-and-shoot' method). With both approaches, the imaging data from the same point in the cardiac cycle at every heart beat are combined together to create a 3D volume for each desired cardiac phase.

11 Appendix C – MRI sequences

When a patient enters the magnetic field randomly moving protons in the body align under the influence of an external magnetic field. The direction in which the net magnetization (Z axis) aligns is represented as longitudinal magnetization. By sending a *radiofrequency* (RF) pulse of certain strength and for a certain period of time it is possible to rotate or 'flip' (*flip angle*) the net magnetization into a plane perpendicular to the Z axis called the transverse magnetization (X-Y axis).

This process of excitation with the radiofrequency pulse sends the protons into a higher energy state and the process of returning back to equilibrium or original state results in *T1 relaxation*. The T1 relaxation time is different for each tissue and depends on the molecular binding in the tissue; tightly bound protons such as fat tissue will release their energy much quicker than the protons that are loosely bound. The RF pulse also causes phase coherence of proton along transverse magnetization and the de-phasing of protons is named as the *T2 relaxation time*.

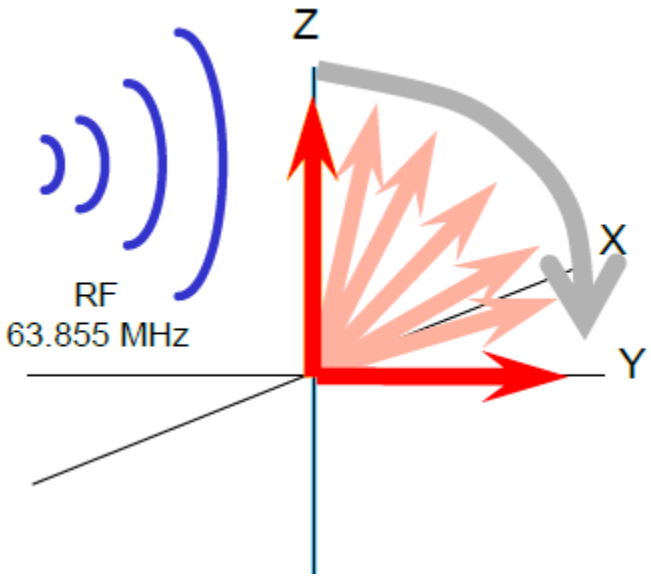

Figure 73: RF pulse of certain amplitude and for a period of time can rotate the net magnetization vector (red arrows) into a plane perpendicular to the Z axis, which is X-Y

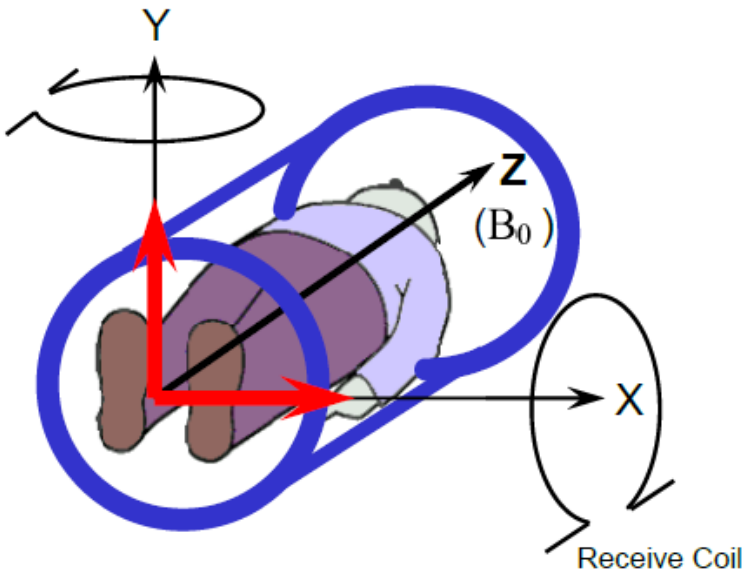

Figure 74: B0 represents the main magnetic field. The receive coil must be positioned at right angles to the main magnetic field to achieve maximum signal

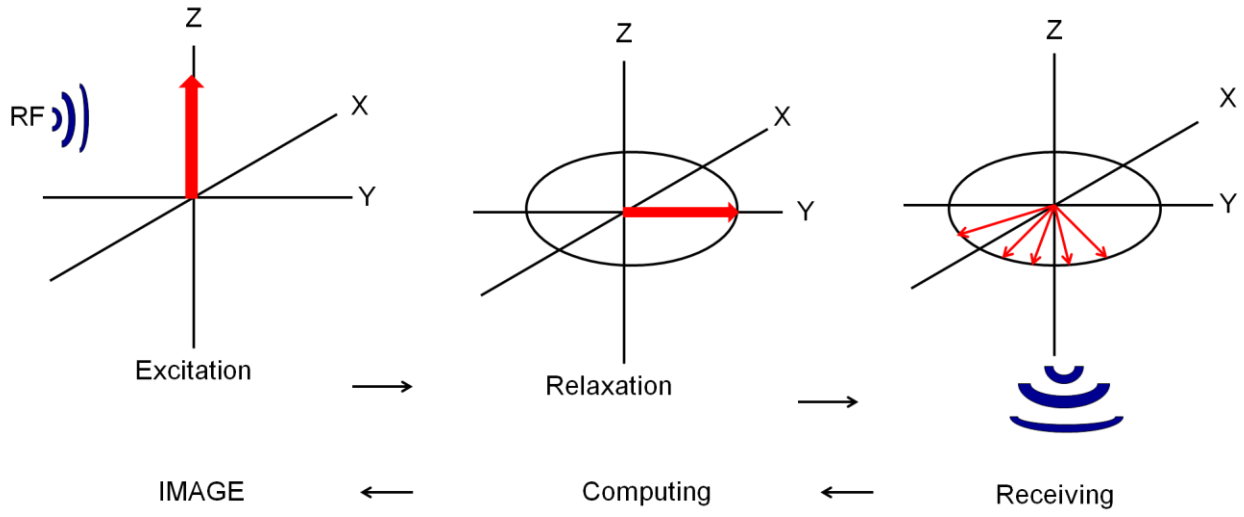

Figure 75: The RF signal causes the net magnetization to flip from Z axis to X-Y direction, this causes dephasing of the signals and the output that is received is analysed and a MR image is generated on the screen. This figure shows the entire process graphically

MR terms

Repetition Time: TR is the time between two 90º excitation pulses.

Echo Time: This is the time between the 90º excitation pulse and the echo.

Flip Angle: Refers to the degree the net-magnetization is flipped into the X-Y plane.

Phase encoding: The phase of proton spins in one dimension is altered with a pulsed magnetic field gradient. This process localizes the MR signal along that dimension prior to the acquisition of the signal.

Frequency encoding: The process of spatial localization of MR signals by modifying the Larmor frequencies in the horizontal direction throughout the time it is applied.

SNR: signal to noise ratio

The MRI pulse sequence is a sequence of events needed to acquire a MR image and two of the principal pulse sequences that the widely used highlighted below.

Spin Echo Sequence:

This is one of the most common pulse sequences used in MR imaging. It uses a 90° radiofrequency (RF) pulses to excite the magnetization and one or more 180° pulses to refocus the spins to generate spin echoes.

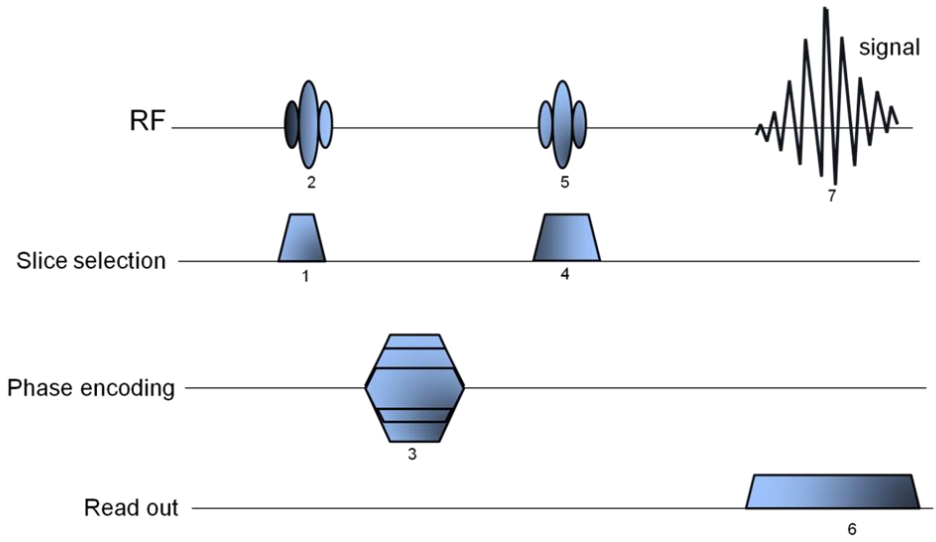

Figure 76: illustrated diagram of spin echo sequence

The slice to be imaged is selected by switching the slice select gradient. A 90º RF pulse is applied to flip the net magnetization into the X-Y plane. The phase encoding gradient is switched on. A 180º rephasing pulse is applied at the sometime as the slice select gradient is switched on. The 180º pulse causes the dephasing protons in the X-Y plane re-phase and when all the spins are re-phase the signal is high. Finally the frequency encoding or the read out gradient is applied and the signal or echo is sampled.

The advantages of the spin echo sequence are that the signal is strong and there is compensation for local field inhomogeneities with lesser artifacts. It also generates “true” T1 and T2 images. However rephasing pulse takes time and thus the total scan time is more and it is also susceptible to motion artifacts.

Gradient Echo Sequence:

In the Gradient echo (GE) sequence there is no refocusing RF pulse, it uses a single RF pulse followed by a pulse gradient to create the echo, which also measures the signal intensity [202]. This is achieved by using a bipolar gradient; a negative pulse gradient to dephase the spins followed by a positive pulse gradient of opposite polarity to re-phase the spins to generate the echo.

The main advantage of this sequence is that the short TR facilitates a short scan time and enables acquisitions in a single breath-hold and allows dynamic imaging. However this sequence is sensitive to T2* inhomogeneity artefacts and also has a lower signal compared to spin echo sequence.

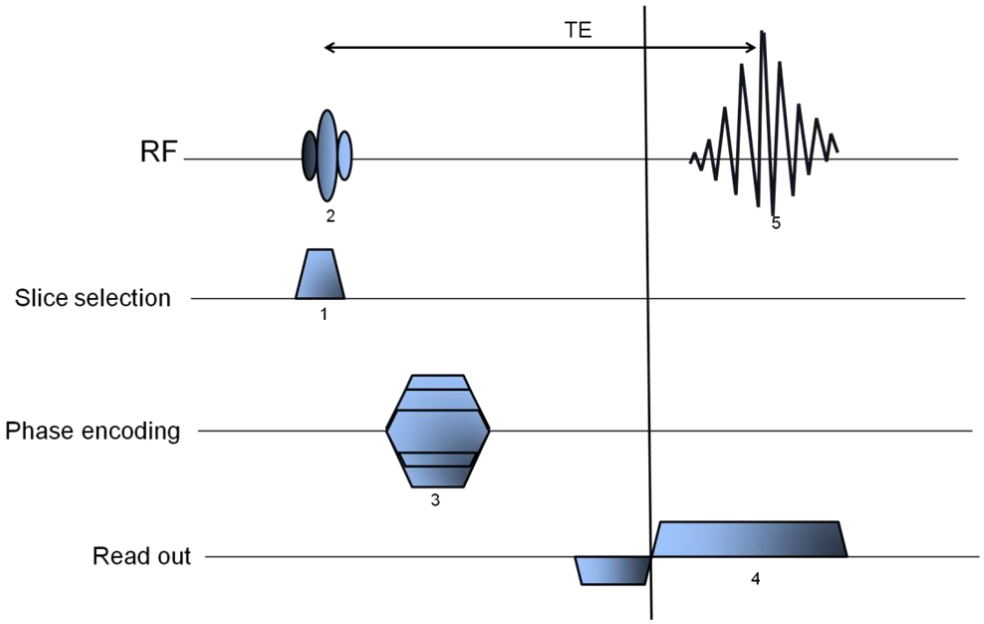

Figure 77: Illustrated diagram of gradient echo pulse sequence

The first slice selection gradient is switched on and the excitation pulse applied. Then phase encoding takes place. Next the read out or frequency encoding gradient is switched on, first with negative polarity and then changed to positive polarity. Finally the signal is obtained.

11.1 Cardiac MRI - GE sequences used for contrast MR angiography and perfusion

11.1.1 Balanced Steady State Free Precession sequence

Steady state free precession is a type of gradient echo sequence in which non-zero steady state develops for both transverse and longitudinal magnetization. This is achieved by using a repetition time that is shorter than the T2

relaxation time of tissue so that the MR signal never completely decays and the spin along the transverse magnetization never completely dephase. When the same sequence of RF excitation and relaxation are repeated, a steady state is reached in which the magnetization becomes constant from one repetition to the next. Balanced SSFP (bSSFP) is a type of SSFP sequence where the net gradient-induced dephasing within the repetition time is exactly zero and is achieved by refocusing all of the three encoding gradients in each repetition interval to keep the gradient moment constant [202-203].

There are several factors that make this sequence ideal for cardiac imaging. The contrast in bSSFP depends on the T1/T2 ratio and this ratio is higher for blood than the myocardium. This high blood myocardial contrast enables better delineation between ventricular myocardial borders facilitating reliable segmentation of the ventricles. It has an intrinsically high signal to noise ratio (SNR) that makes it possible to image at a very short TR and hence faster acquisition speed. Finally this sequence is also insensitive to flow. The features make this sequence ideal for anatomical imaging of the heart and assessment of the myocardium [202].

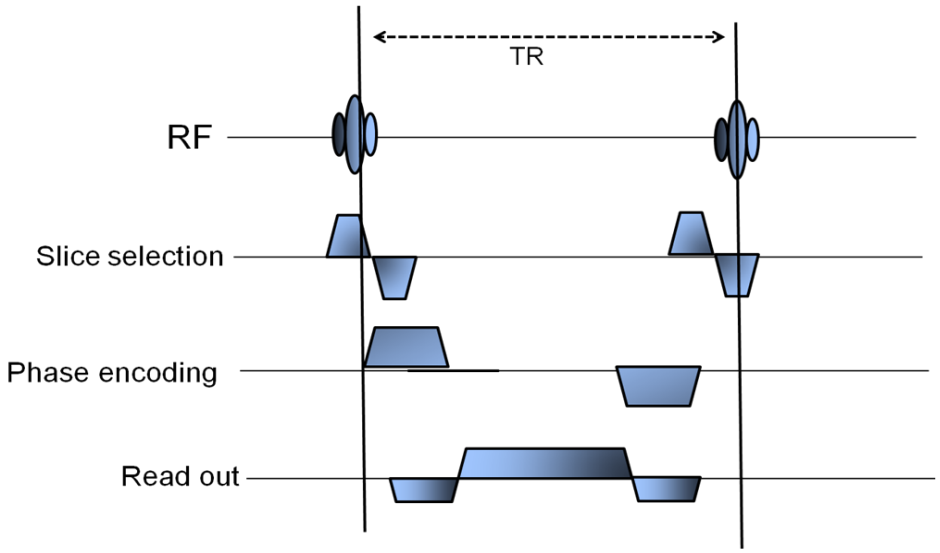

Figure 78: illustrated diagram of balanced steady state free precision sequence

11.1.2 Double inversion recovery black blood technique

Double inversion recovery (DIR) MRI is a T1 weighted black blood MR sequence where the signal from the blood is suppressed. The readouts are acquired when the longitudinal magnetization of blood reaches the zero and thus the blood in the imaged slice gives no signal or appears 'black'. In cases where the images are obtained in-plane or the blood flow is slow the suppression of the signal from blood becomes incomplete.

DIR sequences can be fast spin echo technique with longer acquisition time performed with separate breath hold or fast spin-echo and single-shot techniques single shot acquired in one breath hold. This technique is performed during breathhold with one image per acquisition and the DIR images can also be cardiac gated to remove the motion artefacts from the images. The advantage of this technique is that it provides fine details of the boundaries between the vessel lumen and the wall of the cardiac chambers and pericardium, and mediastinum.

11.1.3 Phase contrast MR angiography

In a magnetic field, protons flowing in the direction of the magnetic field gradient acquire a phase shift compared to the stationary protons and phase contrast MRI utilizes this phase change to quantify velocity. This is achieved by applying paired gradients, one with no flow sensitivity and a second gradient that is a flow sensitive sequence. The stationary tissue undergoes no effective phase change after the application of the two gradients while a phase shift is created in the flowing blood due to different spatial localization of flowing blood compared to stationary tissue. The two raw data sets are subtracted and an accurate degree of motion induced phase change determined. Signal intensities from MR imaging data are processed into a magnitude image (anatomical image) and a phase or velocity image where pixel brightness is proportional to spatial velocity. Thus on phase contrast MR images signal from stationary tissue appear grey while flow in one direction of the magnetic field appears brighter and flow in the opposite direction has darker signal intensity. Both 2D and 3D acquisition techniques can be applied with this technique.

Clinical applications of this technique include evaluation of vascular flow through aorta, pulmonary arteries and cerebrovascular arteries. Quantification of cardiac output and diastolic dysfunction and evaluation of intra-cardiac shunts are also feasible with this technique [204-205].

11.1.4 Contrast enhanced MR angiography

Contrast enhanced MR angiography utilizes the T1 shortening effect of gadolinium and causes the blood to appear bright thereby creating an angiographic effect. This technique unlike time-of-flight MR angiography and phase contrast MR angiography is not dependent on the phase shift or in-flow velocity of the flowing blood. This sequence is performed with a short TR to have low signal from the stationary tissue and short TE to minimize T2* effects. The contrast agent injection is timed in such a way that the period of maximum arterial concentration corresponds to the k-space acquisition to obtain maximum enhancement and there are different techniques such as bolus timing or automatic bolus detection to ensure optimal contrast in the arteries.

Images of the region of interest are performed with 3D spoiled gradient echo pulse sequences. 3D MRA has the freedom of plane orientation which allows greater vessel coverage which can be obtained at high resolution with fewer slices.

11.1.5 Cardiac gated MRI

MR applications can be synchronized with the cardiac cycle to minimize cardiac pulsation artifacts. An electric trigger that corresponds with the patient's cardiac cycle is used to 'activate' the RF excitation for the MR image acquisition and an ECG voltage source is used as this electric trigger. In the ECG voltage, the R wave is used as the trigger because it voltage peak is usually much higher than the other points of the ECG waveform thereby allowing easier detection. In simple cardiac gating, a single image line is acquired in each cardiac cycle. Lines for multiple images can then be acquired successively in consecutive gate intervals. By using the standard multiple slice imaging and a spin echo pulse sequence, a number of slices at different anatomical levels can

be obtained. The repetition time during an ECG-gated acquisition equals the RR interval, and the RR interval defines the minimum possible repetition time. If longer TRs are required, multiple integers of the RR interval can be selected. When using a gradient echo pulse sequence, multiple phases of a single anatomical level or multiple slices at different anatomical levels can be acquired over the cardiac cycle. Using this application desired phases in the cardiac cycle such as the diastolic or systolic phase can be imaged. There are also other cardiac compensation techniques such as phase-encode reordering and retrospective gating can minimize the cardiac pulsation artifacts [206-207].

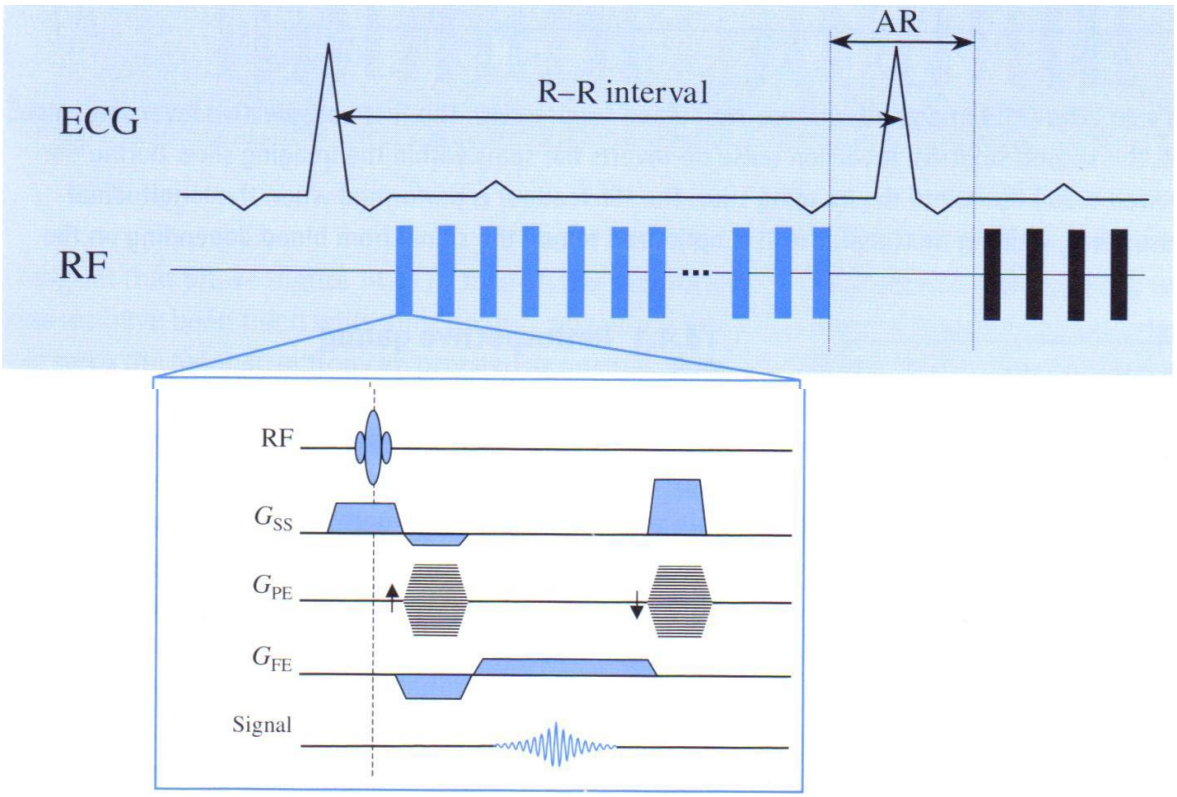

Figure 79: This diagram representing cardiac gated MRI. The R wave is used as the trigger due to its high voltage peak. Using this technique multiple images can then be acquired successively in consecutive gate interval

11.2 Lung imaging

11.2.1 Challenges

Proton MR imaging of the lung has been more difficult than proton imaging of the other organs in the body. One of the reasons for this is that the lung parenchyma is mainly comprised of numerous air-containing alveoli and air passages and the soft tissue constitutes only about 10% of the lung [208]. This causes poor inherent proton density from the normal lung tissue resulting in a low signal to noise ratio (SNR). Secondly, inflated lung has a unique combination of air soft tissue and blood interfaces with different magnetic susceptibilities. This induces local magnetic field gradients at each of these air-tissue interfaces. This affects the homogeneity of the static magnetic field and shortens the T2 and T2* relaxation times resulting in significant susceptibility artifact [23]. Finally, physiological cardiac pulsation and breathing motion further compound the challenges for fast imaging. Several MR techniques have been proposed to overcome these limitations and to improve image quality and are discussed in detail under MR sequences.

11.2.2 Respiratory gated MRI

Strategies such as cardiac gating and respiratory gating can minimize image degradation due to motion artefacts. Using faster MRI techniques and performing the acquisition in a breathhold is the simplest way to avoid respiratory blurring. For longer acquisitions, images can be acquired in free breathing by using respiratory gating. In a respiratory triggered sequence, all images are acquired at identical position of the diaphragm. This can be achieved either through pneumatochographic or navigator triggering. With pneumatochographic triggering, a monitoring belt is used to record breathing motion with the aid of a pressure sensor or infrared reflector [209]. In the navigator technique a prepulse readout projection sequence records the position of the diaphragm and imaging data are only accepted when the position of the interface falls within a range of pre-specified range [210].

11.2.3 Spin echo sequence with short echo time

The use of spin echo sequence with short echo time (TE) can minimize the signal loss of both T2 and T2* and improve visualization of the lung parenchyma [211]. Mayo et al showed an increase in the SNR by 3.5-fold with a short TE (7ms) when compared with the conventional SE with TE of 20ms [212]. The short TE also reduces motion artifacts. The reduced TE makes this sequence relatively T1 weighted and thus very sensitive to effect of contrast agents. Several studies have shown this MR sequence to detect pulmonary nodules and infiltrative lung disease when compared to CT [186, 191, 213-215]. Disadvantages of the sequence are the long acquisition time necessitated by the multiple TR periods and longer TR needed to refocus a spin echo.

11.2.4 Fast spin echo

Fast Spin Echo (FSE) also described as Turbo Spin Echo (TSE) or Rapid Acquisition with Refocusing Echoes (RARE) is characterized by a series of rapidly applied multiple 180° RF refocusing pulses changing the phase encoding gradient for each echo [216]. In this sequence, the scan time is vastly reduced and this enables breath-hold imaging of the chest. The susceptibility artifact is also minimized and the images are T2 weighted with an effective echo time representing the point in time in the echo time that the centre of k-space is crossed. Kersjes et al evaluated 23 patients and showed that a T2-weighted TSE sequence enabled correct identification of 286 of 340 pulmonary metastases [217]. This sequence has also been proved to be feasible in determining disease activity in patients with interstitial lung disease and detecting pneumonia [192, 197-198]. Shortening the inter-echo spacing has the advantage of reducing imaging time, thus reducing artifacts due to cardiac and respiratory motion [218].

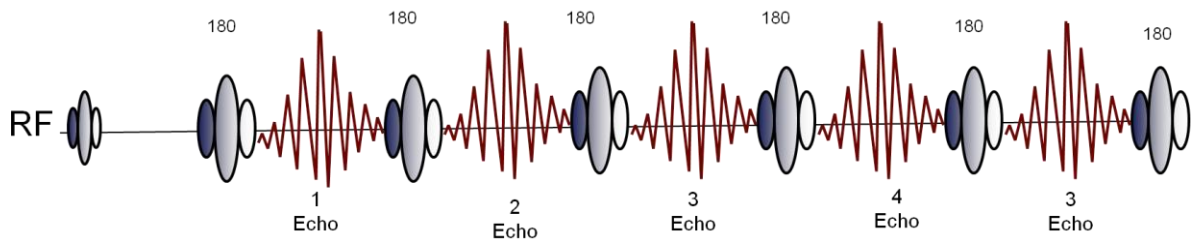

Figure 80: The fast spin echo sequence also makes use of the multi-echo principle. In fast spin echo sequence the 90º RF pulse is followed by a series of 180º pulses. Each 180º pulse generates an echo.

11.2.5 Short TI Inversion Recovery

Short TI Inversion Recovery (STIR) is an inversion recovery FSE pulse sequence with suppression of signal from fat. The advantage of this sequence is that it offers fat signal suppression with low sensitivity to magnetic field heterogeneities. This sequence has additive T1 and T2 characteristics inherent to the FSE readout and a high contrast of disease tissue. The fat suppression allows easy distinction between lung pathology from adjacent mediastinal and pericardial fat and this is particularly helpful for identification of lung nodules [214]. Comparative studies showed a high sensitivity of the STIR sequence (82 %) for identifying pulmonary nodules when compared to conventional T2-weighted SE [186, 214].

11.2.6 Half-Fourier-acquisition single-shot turbo spin-echo

Half-Fourier-acquisition single-shot turbo spin-echo (HASTE) is a rapid form of single shot FSE or RARE, where the initial RF excitation pulse is followed by a very long echo train of multiple 180 pulses over which all phase encode steps are acquired. A partial Fourier technique is used to reduce the number of phase-encoding steps and decreasing the acquisition time. As a result, this technique is relatively insensitive to motion artifacts and allows the entire chest to be imaged in a single breath-hold [207]. The multiple spin echoes also minimize magnetic susceptibility by limiting T2* decay [202].

The SNR from the lung parenchyma is higher on the HASTE sequence when compared to SE, FSE and GRE (that are attainable at modest echo times of 1.5 ms) techniques [183, 218]. Various pulmonary disorders such as bronchogenic cancers, lymphadenopathy and bronchial wall thickening have been appreciated using this sequence [183, 219]. Schroeder et al showed 95% sensitivity for detecting lung nodules greater than 5mm. Most cancerous tissue, due to hypervascularity, have an intrinsic high signal on T2 weighted images and the high T2 of the HASTE sequence makes lung nodules more conspicuous. Furthermore, arteries and veins are less apparent in HASTE as a result of signal void. Hence this sequence is particularly preferred for visualization of lung nodules. [182].

11.2.7 Gradient echo sequence

A study using a dynamic GE sequence showed higher signal intensity for malignant lung nodules during the first transit of contrast agent and showed its potential to characterize lung nodules [206, 220]. However this sequence is more sensitive to magnetic field inhomogeneities, therefore magnetic susceptibility artifacts are more pronounced on GE sequences compared to SE sequences for a given TE [202, 221].

11.2.8 3D Gradient-Echo Technique

The main advantage of the 3D gradient-echo technique over 2D is its ability to rapidly acquire a volumetric data set during a single breath-hold, which enables acquisition of contiguous thin-slice images with no inter-slice gap.

Volumetric interpolated breath-hold examination (VIBE), a type of rapid 3D gradient-echo MR sequence was initially applied for abdominal imaging. Few studies have confirmed the feasibility of VIBE sequence for lung imaging and demonstrated its ability for the assessment of various lung abnormalities including lung nodules [180, 187, 219]. A comparative study of 2D GE sequence and VIBE proved VIBE to have a better image quality with statistically lower degree of phase contrast artifacts. The degree of image graininess, however,

was significantly higher on the 3D gradient-echo VIB images than on the 2D gradient-echo images [185].

11.2.9 Balanced Steady State Free Precession sequence

When compared to all other MR sequences, bSSFP has the highest SNR and this makes it an ideal technique for imaging the lung parenchyma. In this relatively fast acquisition, the quality is very dependent on the homogeneity of the magnetic field or shim, if the shim is poor, there can be dark banding artifacts which may be difficult to discern in the context of the low SNR in the lung. Failo et al [189] showed good visualization of lung parenchyma in patients with cystic fibrosis (CF) using a non-contrast, short TR/TE 2D bSSFP technique.

12 Appendix D – Abbreviations

Balanced Steady State Free Precession: bSSFP

Cardiac output: CO

Cardiac index: CI

Chronic thromboembolic disease: CTE

Chronic thromboembolic pulmonary hypertension: CTEPH

Computed tomography: CT

Connective tissue disease: CTD

Contrast-enhanced MR angiography: ce-MRA

CT pulmonary angiography: CTPA

Forced vital capacity: FVC

Gas transfer: TLCO

Idiopathic pulmonary arterial hypertension: IPAH

Magnetic resonance angiography: MRA

Magnetic resonance imaging: MRI

Mean pulmonary artery pressure: mPAP

Mean right atrial pressure: mRAP

Mixed venous oxygen saturation: mVO2

Left heart disease: LHD

Pulmonary arterial hypertension: PAH

Pulmonary capillary wedge pressure: PCWP

Pulmonary embolism: PE

Pulmonary hypertension: PH

Pulmonary vascular resistance: PVR

Systemic sclerosis: SSc

Total pulmonary resistance: TPR

Ventilation perfusion: V/Q

13 References

1. Hansell, D.M. and I.H. Kerr, *The role of high resolution computed tomography in the diagnosis of interstitial lung disease.* Thorax, 1991. **46**(2): p. 77-84.
2. McAdams, H.P., et al., *Recent advances in chest radiography.* Radiology, 2006. **241**(3): p. 663-83.
3. Hull, R.D., et al., *Diagnostic value of ventilation-perfusion lung scanning in patients with suspected pulmonary embolism.* Chest, 1985. **88**(6): p. 819-28.
4. Gottschalk, A., et al., *Ventilation-perfusion scintigraphy in the PIOPED study. Part II. Evaluation of the scintigraphic criteria and interpretations.* J Nucl Med, 1993. **34**(7): p. 1119-26.
5. *Value of the ventilation/perfusion scan in acute pulmonary embolism. Results of the prospective investigation of pulmonary embolism diagnosis (PIOPED). The PIOPED Investigators.* JAMA, 1990. **263**(20): p. 2753-9.
6. Leblanc, M., F. Leveillee, and E. Turcotte, *Prospective evaluation of the negative predictive value of V/Q SPECT using 99mTc-Technegas.* Nucl Med Commun, 2007. **28**(8): p. 667-72.
7. Committee, A.o.R.S.A., 2006.
8. Notghi, A. and C.S. Low, *Myocardial perfusion scintigraphy: past, present and future.* Br J Radiol, 2011. **84 Spec No 3**: p. S229-36.
9. Dvorak, R.A., R.K. Brown, and J.R. Corbett, *Interpretation of SPECT/CT myocardial perfusion images: common artifacts and quality control techniques.* Radiographics, 2011. **31**(7): p. 2041-57.
10. Hagan, G., et al., *(18)FDG PET imaging can quantify increased cellular metabolism in pulmonary arterial hypertension: A proof-of-principle study.* Pulm Circ, 2011. **1**(4): p. 448-55.
11. Hartmann, I.J., R. Wittenberg, and C. Schaefer-Prokop, *Imaging of acute pulmonary embolism using multi-detector CT angiography: an update on imaging technique and interpretation.* Eur J Radiol, 2010. **74**(1): p. 40-9.
12. Ghaye, B., et al., *Peripheral pulmonary arteries: how far in the lung does multi-detector row spiral CT allow analysis?* Radiology, 2001. **219**(3): p. 629-36.
13. Kang, M.J., et al., *Dual-energy CT: clinical applications in various pulmonary diseases.* Radiographics, 2010. **30**(3): p. 685-98.
14. Karcaaltincaba, M. and A. Aktas, *Dual-energy CT revisited with multidetector CT: review of principles and clinical applications.* Diagn Interv Radiol, 2011. **17**(3): p. 181-94.
15. Schenzle, J.C., et al., *Dual energy CT of the chest: how about the dose?* Invest Radiol, 2010. **45**(6): p. 347-53.
16. Hoey, E.T., et al., *Dual energy CT pulmonary angiography: findings in a patient with chronic thromboembolic pulmonary hypertension.* Thorax, 2009. **64**(11): p. 1012.
17. Nikolaou, K., et al., *Diagnosing pulmonary embolism: new computed tomography applications.* J Thorac Imaging, 2010. **25**(2): p. 151-60.
18. Auger, W.R., et al., *Chronic major-vessel thromboembolic pulmonary artery obstruction: appearance at angiography.* Radiology, 1992. **182**(2): p. 393-8.
19. Coche, E., S. Vynckier, and M. Octave-Prignot, *Pulmonary embolism: radiation dose with multi-detector row CT and digital angiography for diagnosis.* Radiology, 2006. **240**(3): p. 690-7.
20. Stein, P.D., et al., *Complications and validity of pulmonary angiography in acute pulmonary embolism.* Circulation, 1992. **85**(2): p. 462-8.
21. Damadian, R., *Nuclear magnetic resonance: a noninvasive approach to cancer.* Hosp Pract, 1977. **12**: p. 63-70.
22. Biederer, J., C. Hintze, and M. Fabel, *MRI of pulmonary nodules: technique and diagnostic value.* Cancer Imaging, 2008. **8**: p. 125-30.

23. Bergin, C.J., et al., *MR imaging of lung parenchyma: a solution to susceptibility.* Radiology, 1992. **183**(3): p. 673-6.
24. Mayo, J.R., J. Aldrich, and N.L. Muller, *Radiation exposure at chest CT: a statement of the Fleischner Society.* Radiology, 2003. **228**(1): p. 15-21.
25. Lee, K.S., et al., *Chronic infiltrative lung disease: comparison of diagnostic accuracies of radiography and low- and conventional-dose thin-section CT.* Radiology, 1994. **191**(3): p. 669-73.
26. Charles, M., *UNSCEAR report 2000: sources and effects of ionizing radiation. United Nations Scientific Comittee on the Effects of Atomic Radiation.* J Radiol Prot, 2001. **21**(1): p. 83-6.
27. Mettler, F.A., Jr., et al., *CT scanning: patterns of use and dose.* J Radiol Prot, 2000. **20**(4): p. 353-9.
28. Nelson, C.B., J.S. Puskin, and D.J. Pawel, *Adjustments to the baseline lung cancer mortality for radon-induced lung cancers in the BEIR VI risk models.* Radiat Res, 2001. **156**(2): p. 220-1.
29. BEIR-VII, C.t.A.H.R.f.E.t.L.L.o.I.R., *National Research Council. Health risks from exposure to low levels of ionizing radiation: BEIR VII – Phase 2.* Washington, DC: National Academies Press, 2006.
30. Berrington de Gonzalez, A., et al., *Projected cancer risks from computed tomographic scans performed in the United States in 2007.* Arch Intern Med, 2009. **169**(22): p. 2071-7.
31. Brenner, D.J. and E.J. Hall, *Computed tomography--an increasing source of radiation exposure.* N Engl J Med, 2007. **357**(22): p. 2277-84.
32. Winer-Muram, H.T., et al., *Pulmonary embolism in pregnant patients: fetal radiation dose with helical CT.* Radiology, 2002. **224**(2): p. 487-92.
33. Matthews, S., *Short communication: imaging pulmonary embolism in pregnancy: what is the most appropriate imaging protocol?* Br J Radiol, 2006. **79**(941): p. 441-4.
34. O'Neill, J., et al., *Effect of the introduction of helical CT on radiation dose in the investigation of pulmonary embolism.* Br J Radiol, 2005. **78**(925): p. 46-50.
35. McCollough, C.H., M.R. Bruesewitz, and J.M. Kofler, Jr., *CT dose reduction and dose management tools: overview of available options.* Radiographics, 2006. **26**(2): p. 503-12.
36. Galie, N., et al., *Guidelines for the diagnosis and treatment of pulmonary hypertension: the Task Force for the Diagnosis and Treatment of Pulmonary Hypertension of the European Society of Cardiology (ESC) and the European Respiratory Society (ERS), endorsed by the International Society of Heart and Lung Transplantation (ISHLT).* Eur Heart J, 2009. **30**(20): p. 2493-537.
37. Morrell, N.W., et al., *Cellular and molecular basis of pulmonary arterial hypertension.* J Am Coll Cardiol, 2009. **54**(1 Suppl): p. S20-31.
38. Rich, S., et al., *Primary pulmonary hypertension. A national prospective study.* Ann Intern Med, 1987. **107**(2): p. 216-23.
39. Humbert, M., et al., *Pulmonary arterial hypertension in France: results from a national registry.* Am J Respir Crit Care Med, 2006. **173**(9): p. 1023-30.
40. Peacock, A.J., et al., *An epidemiological study of pulmonary arterial hypertension.* Eur Respir J, 2007. **30**(1): p. 104-9.
41. Pietra, G.G., et al., *Pathologic assessment of vasculopathies in pulmonary hypertension.* J Am Coll Cardiol, 2004. **43**(12 Suppl S): p. 25S-32S.
42. Simonneau, G., et al., *Updated clinical classification of pulmonary hypertension.* J Am Coll Cardiol, 2009. **54**(1 Suppl): p. S43-54.
43. Tuder, R.M., et al., *Development and pathology of pulmonary hypertension.* J Am Coll Cardiol, 2009. **54**(1 Suppl): p. S3-9.
44. Humbert, M., *Pulmonary arterial hypertension and chronic thromboembolic pulmonary hypertension: pathophysiology.* Eur Respir Rev, 2010. **19**(115): p. 59-63.
45. Moser, K.M. and C.M. Bloor, *Pulmonary vascular lesions occurring in patients with chronic major vessel thromboembolic pulmonary hypertension.* Chest, 1993. **103**(3): p. 685-92.

46. Peacock, A., G. Simonneau, and L. Rubin, *Controversies, uncertainties and future research on the treatment of chronic thromboembolic pulmonary hypertension.* Proc Am Thorac Soc, 2006. **3**(7): p. 608-14.
47. Egermayer, P., *Chronic thromboembolic pulmonary hypertension and upper limb thrombosis.* Eur Respir J, 2000. **16**(1): p. 187.
48. Hoeper, M.M., et al., *Chronic thromboembolic pulmonary hypertension.* Circulation, 2006. **113**(16): p. 2011-20.
49. Blyth, K.G., et al., *NT-proBNP can be used to detect right ventricular systolic dysfunction in pulmonary hypertension.* Eur Respir J, 2007. **29**(4): p. 737-44.
50. Warwick, G., P.S. Thomas, and D.H. Yates, *Biomarkers in pulmonary hypertension.* Eur Respir J, 2008. **32**(2): p. 503-12.
51. Schmidt, H.C., et al., *Pulmonary hypertension in patients with chronic pulmonary thromboembolism: chest radiograph and CT evaluation before and after surgery.* Eur Radiol, 1996. **6**(6): p. 817-25.
52. Freitas, J.E., et al., *Modified PIOPED criteria used in clinical practice.* J Nucl Med, 1995. **36**(9): p. 1573-8.
53. Freeman, L.M., B. Krynyckyi, and L.S. Zuckier, *Enhanced lung scan diagnosis of pulmonary embolism with the use of ancillary scintigraphic findings and clinical correlation.* Semin Nucl Med, 2001. **31**(2): p. 143-57.
54. Tunariu, N., et al., *Ventilation-perfusion scintigraphy is more sensitive than multidetector CTPA in detecting chronic thromboembolic pulmonary disease as a treatable cause of pulmonary hypertension.* J Nucl Med, 2007. **48**(5): p. 680-4.
55. Ryan, K.L., et al., *Perfusion scan findings understate the severity of angiographic and hemodynamic compromise in chronic thromboembolic pulmonary hypertension.* Chest, 1988. **93**(6): p. 1180-5.
56. Gopalan, D., et al., *Imaging in pulmonary hypertension, part 3: small vessel diseases.* Postgrad Med J, 2012. **88**(1041): p. 397-406.
57. Lisbona, R., et al., *Perfusion lung scanning: differentiation of primary from thromboembolic pulmonary hypertension.* AJR Am J Roentgenol, 1985. **144**(1): p. 27-30.
58. Tan, R.T., et al., *Utility of CT scan evaluation for predicting pulmonary hypertension in patients with parenchymal lung disease. Medical College of Wisconsin Lung Transplant Group.* Chest, 1998. **113**(5): p. 1250-6.
59. Devaraj, A., et al., *The effect of diffuse pulmonary fibrosis on the reliability of CT signs of pulmonary hypertension.* Radiology, 2008. **249**(3): p. 1042-9.
60. Revel, M.P., et al., *Pulmonary hypertension: ECG-gated 64-section CT angiographic evaluation of new functional parameters as diagnostic criteria.* Radiology, 2009. **250**(2): p. 558-66.
61. Remy-Jardin, M., et al., *Systemic collateral supply in patients with chronic thromboembolic and primary pulmonary hypertension: assessment with multi-detector row helical CT angiography.* Radiology, 2005. **235**(1): p. 274-81.
62. Sheehan, R., et al., *Pulmonary neovascularity: a distinctive radiographic finding in Eisenmenger syndrome.* Circulation, 2005. **112**(18): p. 2778-85.
63. Baque-Juston, M.C., A.U. Wells, and D.M. Hansell, *Pericardial thickening or effusion in patients with pulmonary artery hypertension: a CT study.* AJR Am J Roentgenol, 1999. **172**(2): p. 361-4.
64. Reid, J.H. and J.T. Murchison, *Acute right ventricular dilatation: a new helical CT sign of massive pulmonary embolism.* Clin Radiol, 1998. **53**(9): p. 694-8.
65. Devaraj, A., et al., *Detection of pulmonary hypertension with multidetector CT and echocardiography alone and in combination.* Radiology, 2010. **254**(2): p. 609-16.
66. Groves, A.M., et al., *Semi-quantitative assessment of tricuspid regurgitation on contrast-enhanced multidetector CT.* Clin Radiol, 2004. **59**(8): p. 715-9.

67. Simon, M.A., et al., *Phenotyping the right ventricle in patients with pulmonary hypertension.* Clin Transl Sci, 2009. **2**(4): p. 294-9.
68. Sherrick, A.D., S.J. Swensen, and T.E. Hartman, *Mosaic pattern of lung attenuation on CT scans: frequency among patients with pulmonary artery hypertension of different causes.* AJR Am J Roentgenol, 1997. **169**(1): p. 79-82.
69. Griffin, N., et al., *Eisenmenger syndrome and idiopathic pulmonary arterial hypertension: do parenchymal lung changes reflect aetiology?* Clin Radiol, 2007. **62**(6): p. 587-95.
70. Nolan, R.L., et al., *Pulmonary cholesterol granulomas in patients with pulmonary artery hypertension: chest radiographic and CT findings.* AJR Am J Roentgenol, 1999. **172**(5): p. 1317-9.
71. Resten, A., et al., *Pulmonary arterial hypertension: thin-section CT predictors of epoprostenol therapy failure.* Radiology, 2002. **222**(3): p. 782-8.
72. Perloff, J.K., et al., *Proximal pulmonary arterial and intrapulmonary radiologic features of Eisenmenger syndrome and primary pulmonary hypertension.* Am J Cardiol, 2003. **92**(2): p. 182-7.
73. Ley, S., et al., *Computed tomography and magnetic resonance imaging of pulmonary hypertension: Pulmonary vessels and right ventricle.* J Magn Reson Imaging, 2010. **32**(6): p. 1313-24.
74. Alunni, J.P., et al., *Cardiac MRI in pulmonary artery hypertension: correlations between morphological and functional parameters and invasive measurements.* Eur Radiol, 2010. **20**(5): p. 1149-59.
75. Roeleveld, R.J., et al., *A comparison of noninvasive MRI-based methods of estimating pulmonary artery pressure in pulmonary hypertension.* J Magn Reson Imaging, 2005. **22**(1): p. 67-72.
76. van Wolferen, S.A., et al., *Prognostic value of right ventricular mass, volume, and function in idiopathic pulmonary arterial hypertension.* Eur Heart J, 2007. **28**(10): p. 1250-7.
77. van de Veerdonk, M.C., et al., *Progressive right ventricular dysfunction in patients with pulmonary arterial hypertension responding to therapy.* J Am Coll Cardiol, 2011. **58**(24): p. 2511-9.
78. Hagger, D., et al., *Ventricular mass index correlates with pulmonary artery pressure and predicts survival in suspected systemic sclerosis-associated pulmonary arterial hypertension.* Rheumatology (Oxford), 2009. **48**(9): p. 1137-42.
79. Saba, T.S., et al., *Ventricular mass index using magnetic resonance imaging accurately estimates pulmonary artery pressure.* Eur Respir J, 2002. **20**(6): p. 1519-24.
80. Kind, T., et al., *Right ventricular ejection fraction is better reflected by transverse rather than longitudinal wall motion in pulmonary hypertension.* J Cardiovasc Magn Reson, 2010. **12**: p. 35.
81. Brown, S.B., et al., *Longitudinal shortening accounts for the majority of right ventricular contraction and improves after pulmonary vasodilator therapy in normal subjects and patients with pulmonary arterial hypertension.* Chest, 2011. **140**(1): p. 27-33.
82. Dellegrottaglie, S., et al., *Pulmonary hypertension: accuracy of detection with left ventricular septal-to-free wall curvature ratio measured at cardiac MR.* Radiology, 2007. **243**(1): p. 63-9.
83. Sanz, J., et al., *Prevalence and correlates of septal delayed contrast enhancement in patients with. pulmonary hypertension.* American Journal of Cardiology, 2007. **100**(4): p. 731-735.
84. Freed, B.H., et al., *Late gadolinium enhancement cardiovascular magnetic resonance predicts clinical worsening in patients with pulmonary hypertension.* Journal of Cardiovascular Magnetic Resonance, 2012. **14**.
85. Blyth, K.G., et al., *Contrast enhanced-cardiovascular magnetic resonance imaging in patients with pulmonary hypertension.* European Heart Journal, 2005. **26**(19): p. 1993-1999.

86. McCann, G.P., et al., *Extent of MRI delayed enhancement of myocardial mass is related to right ventricular dysfunction in pulmonary artery hypertension.* American Journal of Roentgenology, 2007. **188**(2): p. 349-355.
87. Sanz, J., et al., *Evaluation of pulmonary artery stiffness in pulmonary hypertension with cardiac magnetic resonance.* JACC Cardiovasc Imaging, 2009. **2**(3): p. 286-95.
88. Helderman, F., et al., *Early Onset of Retrograde Flow in the Main Pulmonary Artery is a Characteristic of Pulmonary Arterial Hypertension.* Journal of Magnetic Resonance Imaging, 2011. **33**(6): p. 1362-1368.
89. Gan, C.T., et al., *Noninvasively assessed pulmonary artery stiffness predicts mortality in pulmonary arterial hypertension.* Chest, 2007. **132**(6): p. 1906-12.
90. Swift, A.J., et al., *Black blood MRI has diagnostic and prognostic value in the assessment of patients with pulmonary hypertension.* Eur Radiol, 2012. **22**(3): p. 695-702.
91. Ley, S., et al., *Value of high spatial and high temporal resolution magnetic resonance angiography for differentiation between idiopathic and thromboembolic pulmonary hypertension: initial results.* Eur Radiol, 2005. **15**(11): p. 2256-63.
92. Kreitner, K.F., et al., *Chronic thromboembolic pulmonary hypertension: pre- and postoperative assessment with breath-hold MR imaging techniques.* Radiology, 2004. **232**(2): p. 535-43.
93. Nikolaou, K., et al., *Pulmonary arterial hypertension: diagnosis with fast perfusion MR imaging and high-spatial-resolution MR angiography--preliminary experience.* Radiology, 2005. **236**(2): p. 694-703.
94. Sergiacomi, G., et al., *Combined pulmonary fibrosis and emphysema: 3D time-resolved MR angiographic evaluation of pulmonary arterial mean transit time and time to peak enhancement.* Radiology, 2010. **254**(2): p. 601-8.
95. Ohno, Y., et al., *Dynamic perfusion MRI: capability for evaluation of disease severity and progression of pulmonary arterial hypertension in patients with connective tissue disease.* J Magn Reson Imaging, 2008. **28**(4): p. 887-99.
96. Ohno, Y., et al., *Time-resolved contrast-enhanced pulmonary MR angiography using sensitivity encoding (SENSE).* J Magn Reson Imaging, 2003. **17**(3): p. 330-6.
97. Skrok, J., et al., *Pulmonary Arterial Hypertension: MR Imaging-derived First-Pass Bolus Kinetic Parameters Are Biomarkers for Pulmonary Hemodynamics, Cardiac Function, and Ventricular Remodeling.* Radiology, 2012. **263**(3): p. 678-687.
98. Swift, A.J., et al., *Pulmonary artery relative area change detects mild elevations in pulmonary vascular resistance and predicts adverse outcome in pulmonary hypertension.* Invest Radiol, 2012. **47**(10): p. 571-7.
99. Moser, K.M., et al., *Do Patients with Primary Pulmonary-Hypertension Develop Extensive Central Thrombi.* Circulation, 1995. **91**(3): p. 741-745.
100. Bergin, C.J., et al., *Accuracy of high-resolution CT in identifying chronic pulmonary thromboembolic disease.* AJR Am J Roentgenol, 1996. **166**(6): p. 1371-7.
101. Virmani, R. and W.C. Roberts, *Pulmonary arteries in congenital heart disease: a structure-function analysis.* Cardiovasc Clin, 1979. **10**(1): p. 455-99.
102. Hoey, E.T., et al., *Cardiac causes of pulmonary arterial hypertension: assessment with multidetector CT.* Eur Radiol, 2009. **19**(11): p. 2557-68.
103. Chung, L., et al., *Characterization of connective tissue disease-associated pulmonary arterial hypertension from REVEAL: identifying systemic sclerosis as a unique phenotype.* Chest, 2010. **138**(6): p. 1383-94.
104. King, M.A., M. Ysrael, and C.J. Bergin, *Chronic thromboembolic pulmonary hypertension: CT findings.* AJR Am J Roentgenol, 1998. **170**(4): p. 955-60.
105. Kauczor, H.U., et al., *Spiral CT of bronchial arteries in chronic thromboembolism.* J Comput Assist Tomogr, 1994. **18**(6): p. 855-61.

106. Ohno, Y., et al., *Primary pulmonary hypertension: 3D dynamic perfusion MRI for quantitative analysis of regional pulmonary perfusion.* AJR Am J Roentgenol, 2007. **188**(1): p. 48-56.
107. Fishman, A.J., K.M. Moser, and P.F. Fedullo, *Perfusion lung scans vs pulmonary angiography in evaluation of suspected primary pulmonary hypertension.* Chest, 1983. **84**(6): p. 679-83.
108. Johnson, T.R., et al., *Material differentiation by dual energy CT: initial experience.* Eur Radiol, 2007. **17**(6): p. 1510-7.
109. Hoey, E.T., et al., *Dual-energy CT angiography for assessment of regional pulmonary perfusion in patients with chronic thromboembolic pulmonary hypertension: initial experience.* AJR Am J Roentgenol, 2011. **196**(3): p. 524-32.
110. Forfia, P.R., et al., *Tricuspid annular displacement predicts survival in pulmonary hypertension.* Am J Respir Crit Care Med, 2006. **174**(9): p. 1034-41.
111. Thenappan, T., et al., *Survival in pulmonary arterial hypertension: a reappraisal of the NIH risk stratification equation.* Eur Respir J, 2010. **35**(5): p. 1079-87.
112. Condliffe, R., et al., *Connective tissue disease-associated pulmonary arterial hypertension in the modern treatment era.* Am J Respir Crit Care Med, 2009. **179**(2): p. 151-7.
113. Lee, W.T., et al., *Predicting survival in pulmonary arterial hypertension in the UK.* Eur Respir J, 2012. **40**(3): p. 604-11.
114. D'Alonzo, G.E., et al., *Survival in patients with primary pulmonary hypertension. Results from a national prospective registry.* Ann Intern Med, 1991. **115**(5): p. 343-9.
115. Mahapatra, S., et al., *Relationship of pulmonary arterial capacitance and mortality in idiopathic pulmonary arterial hypertension.* J Am Coll Cardiol, 2006. **47**(4): p. 799-803.
116. Hurdman, J., et al., *ASPIRE registry: assessing the Spectrum of Pulmonary hypertension Identified at a REferral centre.* Eur Respir J, 2012. **39**(4): p. 945-55.
117. report, A., 2012.
118. van der Meer, R.W., et al., *Right ventricular dysfunction and pulmonary obstruction index at helical CT: prediction of clinical outcome during 3-month follow-up in patients with acute pulmonary embolism.* Radiology, 2005. **235**(3): p. 798-803.
119. Remy-Jardin, M., et al., *Central pulmonary thromboembolism: diagnosis with spiral volumetric CT with the single-breath-hold technique--comparison with pulmonary angiography.* Radiology, 1992. **185**(2): p. 381-7.
120. Engeler, C.E., et al., *Ground-glass opacity of the lung parenchyma: a guide to analysis with high-resolution CT.* AJR Am J Roentgenol, 1993. **160**(2): p. 249-51.
121. Austin, J.H., et al., *Glossary of terms for CT of the lungs: recommendations of the Nomenclature Committee of the Fleischner Society.* Radiology, 1996. **200**(2): p. 327-31.
122. Michaelson, J.E., S.M. Aguayo, and J. Roman, *Idiopathic pulmonary fibrosis: a practical approach for diagnosis and management.* Chest, 2000. **118**(3): p. 788-94.
123. Gay, S.E., et al., *Idiopathic pulmonary fibrosis: predicting response to therapy and survival.* Am J Respir Crit Care Med, 1998. **157**(4 Pt 1): p. 1063-72.
124. Best, A.C., et al., *Idiopathic pulmonary fibrosis: physiologic tests, quantitative CT indexes, and CT visual scores as predictors of mortality.* Radiology, 2008. **246**(3): p. 935-40.
125. Korosec, F.R., et al., *Time-resolved contrast-enhanced 3D MR angiography.* Magn Reson Med, 1996. **36**(3): p. 345-51.
126. Halliburton, S.S., et al., *Estimation and visualization of regional and global pulmonary perfusion with 3D magnetic resonance angiography.* J Magn Reson Imaging, 2001. **14**(6): p. 734-40.
127. Yilmaz, E., et al., *Accuracy and feasibility of dynamic contrast-enhanced 3D MR imaging in the assessment of lung perfusion: comparison with Tc-99 MAA perfusion scintigraphy.* Clin Radiol, 2005. **60**(8): p. 905-13.
128. Nakagawa, T., et al., *Pulmonary ventilation-perfusion MR imaging in clinical patients.* J Magn Reson Imaging, 2001. **14**(4): p. 419-24.

129. Bergin, C.J., et al., *Accuracy of MR angiography compared with radionuclide scanning in identifying the cause of pulmonary arterial hypertension.* AJR Am J Roentgenol, 1997. **168**(6): p. 1549-55.
130. Hurdman, J., et al., *Aspire Registry: assessing the spectrum of pulmonary hypertension identified at a referral centre.* Eur Respir J, 2011.
131. Matsuoka, S., et al., *Detectability of pulmonary perfusion defect and influence of breath holding on contrast-enhanced thick-slice 2D and on 3D MR pulmonary perfusion images.* J Magn Reson Imaging, 2001. **14**(5): p. 580-5.
132. Amundsen, T., et al., *Pulmonary embolism: detection with MR perfusion imaging of lung--a feasibility study.* Radiology, 1997. **203**(1): p. 181-5.
133. Schwickert, H.C., et al., *Pulmonary arteries and lung parenchyma in chronic pulmonary embolism: preoperative and postoperative CT findings.* Radiology, 1994. **191**(2): p. 351-7.
134. Worthy, S.A., et al., *Mosaic attenuation pattern on thin-section CT scans of the lung: differentiation among infiltrative lung, airway, and vascular diseases as a cause.* Radiology, 1997. **205**(2): p. 465-70.
135. Fink, C., et al., *Regional lung perfusion: assessment with partially parallel three-dimensional MR imaging.* Radiology, 2004. **231**(1): p. 175-84.
136. Soler, X., et al., *Pilot study comparing SPECT perfusion scintigraphy with CT pulmonary angiography in chronic thromboembolic pulmonary hypertension.* Respirology, 2012. **17**(1): p. 180-4.
137. *Notes for guidance on the clinical administration of radiopharmaceuticals and use of sealed radioactive sources. Administration of Radioactive Substances Advisory Committee.* Nucl Med Commun, 2000. **21 Suppl**: p. S1-93.
138. Daily, P.O., et al., *Surgical management of chronic pulmonary embolism: surgical treatment and late results.* J Thorac Cardiovasc Surg, 1980. **79**(4): p. 523-31.
139. Jamieson, S.W., et al., *Experience and results with 150 pulmonary thromboendarterectomy operations over a 29-month period.* J Thorac Cardiovasc Surg, 1993. **106**(1): p. 116-26; discussion 126-7.
140. Kreitner, K.F., et al., *Chronic thromboembolic pulmonary hypertension - assessment by magnetic resonance imaging.* Eur Radiol, 2007. **17**(1): p. 11-21.
141. Ley, S., et al., *Bronchopulmonary shunts in patients with chronic thromboembolic pulmonary hypertension: evaluation with helical CT and MR imaging.* AJR Am J Roentgenol, 2002. **179**(5): p. 1209-15.
142. Jahnke, C., et al., *Coronary MR angiography with steady-state free precession: individually adapted breath-hold technique versus free-breathing technique.* Radiology, 2004. **232**(3): p. 669-76.
143. Deshpande, V.S., et al., *3D magnetization-prepared true-FISP: a new technique for imaging coronary arteries.* Magn Reson Med, 2001. **46**(3): p. 494-502.
144. Hui, B.K., et al., *Navigator-gated three-dimensional MR angiography of the pulmonary arteries using steady-state free precession.* J Magn Reson Imaging, 2005. **21**(6): p. 831-5.
145. Bergin, C.J., et al., *Chronic thromboembolism: diagnosis with helical CT and MR imaging with angiographic and surgical correlation.* Radiology, 1997. **204**(3): p. 695-702.
146. Ley, S., et al., *Value of contrast-enhanced MR angiography and helical CT angiography in chronic thromboembolic pulmonary hypertension.* Eur Radiol, 2003. **13**(10): p. 2365-71.
147. Ley, S., et al., *Diagnostic performance of state-of-the-art imaging techniques for morphological assessment of vascular abnormalities in patients with chronic thromboembolic pulmonary hypertension (CTEPH).* Eur Radiol, 2011.
148. Kiely, D.G., et al., *Pulmonary hypertension: diagnosis and management.* BMJ, 2013. **346**: p. f2028.

149. Dellegrottaglie, S., et al., *Serial phase-contrast MRI for prediction of pulmonary hemodynamic changes in patients with pulmonary arterial hypertension.* Int J Cardiol, 2012. **157**(1): p. 140-2.
150. Moua, T., et al., *Frequency of Mediastinal Lymphadenopathy in Patients with Idiopathic Pulmonary Arterial Hypertension.* Chest, 2012.
151. Humbert, M., et al., *Survival in incident and prevalent cohorts of patients with pulmonary arterial hypertension.* Eur Respir J, 2010. **36**(3): p. 549-55.
152. McLaughlin, V.V., et al., *Prognosis of pulmonary arterial hypertension: ACCP evidence-based clinical practice guidelines.* Chest, 2004. **126**(1 Suppl): p. 78S-92S.
153. Dias, C.A., et al., *Reversible pulmonary trunk banding. II. An experimental model for rapid pulmonary ventricular hypertrophy.* J Thorac Cardiovasc Surg, 2002. **124**(5): p. 999-1006.
154. Louie, E.K., et al., *Pressure and volume loading of the right ventricle have opposite effects on left ventricular ejection fraction.* Circulation, 1995. **92**(4): p. 819-24.
155. Voelkel, N.F., et al., *Right ventricular function and failure: report of a National Heart, Lung, and Blood Institute working group on cellular and molecular mechanisms of right heart failure.* Circulation, 2006. **114**(17): p. 1883-91.
156. Mellins, R.B., O.R. Levine, and A.P. Fishman, *Effect of systemic and pulmonary venous hypertension on pleural and pericardial fluid accumulation.* J Appl Physiol, 1970. **29**(5): p. 564-9.
157. Szabo, G. and Z. Magyar, *Effect of increased systemic venous pressure on lymph pressure and flow.* Am J Physiol, 1967. **212**(6): p. 1469-74.
158. Galie, N., et al., *Effects of the oral endothelin-receptor antagonist bosentan on echocardiographic and doppler measures in patients with pulmonary arterial hypertension.* J Am Coll Cardiol, 2003. **41**(8): p. 1380-6.
159. Mugge, A., et al., *Quantification of tricuspid regurgitation by Doppler color flow mapping after cardiac transplantation.* Am J Cardiol, 1990. **66**(10): p. 884-7.
160. Rudski, L.G., et al., *Guidelines for the echocardiographic assessment of the right heart in adults: a report from the American Society of Echocardiography endorsed by the European Association of Echocardiography, a registered branch of the European Society of Cardiology, and the Canadian Society of Echocardiography.* J Am Soc Echocardiogr, 2010. **23**(7): p. 685-713; quiz 786-8.
161. Yeh, B.M., et al., *Clinical relevance of retrograde inferior vena cava or hepatic vein opacification during contrast-enhanced CT.* AJR Am J Roentgenol, 2004. **183**(5): p. 1227-32.
162. Nagueh, S.F., H.A. Kopelen, and W.A. Zoghbi, *Relation of mean right atrial pressure to echocardiographic and Doppler parameters of right atrial and right ventricular function.* Circulation, 1996. **93**(6): p. 1160-9.
163. Kane, G.C., et al., *Integration of clinical and hemodynamic parameters in the prediction of long-term survival in patients with pulmonary arterial hypertension.* Chest, 2011. **139**(6): p. 1285-93.
164. Steen, V.D. and T.A. Medsger, *Changes in causes of death in systemic sclerosis, 1972-2002.* Ann Rheum Dis, 2007. **66**(7): p. 940-4.
165. Wigley, F.M., et al., *The prevalence of undiagnosed pulmonary arterial hypertension in subjects with connective tissue disease at the secondary health care level of community-based rheumatologists (the UNCOVER study).* Arthritis Rheum, 2005. **52**(7): p. 2125-32.
166. Fisher, M.R., et al., *Clinical differences between idiopathic and scleroderma-related pulmonary hypertension.* Arthritis Rheum, 2006. **54**(9): p. 3043-50.
167. Elliot, C. and D.G. Kiely, *Pulmonary hypertension: diagnosis and treatment.* Clin Med, 2004. **4**(3): p. 211-5.
168. Sharp, G.C., et al., *Mixed connective tissue disease--an apparently distinct rheumatic disease syndrome associated with a specific antibody to an extractable nuclear antigen (ENA).* Am J Med, 1972. **52**(2): p. 148-59.

169. Bohan, A. and J.B. Peter, *Polymyositis and dermatomyositis (first of two parts).* N Engl J Med, 1975. **292**(7): p. 344-7.
170. LeRoy, E.C., et al., *Scleroderma (systemic sclerosis): classification, subsets and pathogenesis.* J Rheumatol, 1988. **15**(2): p. 202-5.
171. Bezante, G.P., et al., *Cardiac magnetic resonance imaging detects subclinical right ventricular impairment in systemic sclerosis.* J Rheumatol, 2007. **34**(12): p. 2431-7.
172. Jardim, C., et al., *Pulmonary artery distensibility in pulmonary arterial hypertension: an MRI pilot study.* Eur Respir J, 2007. **29**(3): p. 476-81.
173. Nijveldt, R., et al., *Semi-quantitative assessment of right ventricular function in comparison to a 3D volumetric approach: a cardiovascular magnetic resonance study.* Eur Radiol, 2008. **18**(11): p. 2399-405.
174. Kahan, A. and Y. Allanore, *Primary myocardial involvement in systemic sclerosis.* Rheumatology (Oxford), 2006. **45 Suppl 4**: p. iv14-7.
175. Allanore, Y., et al., *Prevalence and factors associated with left ventricular dysfunction in the EULAR Scleroderma Trial and Research group (EUSTAR) database of patients with systemic sclerosis.* Ann Rheum Dis, 2010. **69**(1): p. 218-21.
176. Kawut, S.M., et al., *Hemodynamics and survival in patients with pulmonary arterial hypertension related to systemic sclerosis.* Chest, 2003. **123**(2): p. 344-50.
177. Condliffe, R., et al., *CT pulmonary angiography combined with echocardiography in suspected systemic sclerosis-associated pulmonary arterial hypertension.* Rheumatology (Oxford), 2011. **50**(8): p. 1480-6.
178. Shehata, M.L., et al., *Myocardial delayed enhancement in pulmonary hypertension: pulmonary hemodynamics, right ventricular function, and remodeling.* AJR Am J Roentgenol, 2011. **196**(1): p. 87-94.
179. Puderbach, M., et al., *MR imaging of the chest: a practical approach at 1.5T.* Eur J Radiol, 2007. **64**(3): p. 345-55.
180. Biederer, J., et al., *Lung morphology: fast MR imaging assessment with a volumetric interpolated breath-hold technique: initial experience with patients.* Radiology, 2003. **226**(1): p. 242-9.
181. Biederer, J., et al., *Simulated pulmonary nodules implanted in a dedicated porcine chest phantom: sensitivity of MR imaging for detection.* Radiology, 2003. **227**(2): p. 475-83.
182. Schroeder, T., et al., *Detection of pulmonary nodules using a 2D HASTE MR sequence: comparison with MDCT.* AJR Am J Roentgenol, 2005. **185**(4): p. 979-84.
183. Hatabu, H., et al., *MR imaging of pulmonary parenchyma with a half-Fourier single-shot turbo spin-echo (HASTE) sequence.* Eur J Radiol, 1999. **29**(2): p. 152-9.
184. Semelka, R.C., et al., *Breath-hold 3D gradient-echo MR imaging of the lung parenchyma: evaluation of reproducibility of image quality in normals and preliminary observations in patients with disease.* J Magn Reson Imaging, 2000. **11**(2): p. 195-200.
185. Karabulut, N., et al., *MR imaging of the chest using a contrast-enhanced breath-hold modified three-dimensional gradient-echo technique: comparison with two-dimensional gradient-echo technique and multidetector CT.* AJR Am J Roentgenol, 2002. **179**(5): p. 1225-33.
186. Koyama, H., et al., *Quantitative and qualitative assessment of non-contrast-enhanced pulmonary MR imaging for management of pulmonary nodules in 161 subjects.* Eur Radiol, 2008. **18**(10): p. 2120-31.
187. Hekimoglu, K., et al., *Fast MRI evaluation of pulmonary progressive massive fibrosis with VIBE and HASTE sequences: comparison with CT.* Diagn Interv Radiol, 2010. **16**(1): p. 30-7.
188. Regier, M., et al., *Detection of small pulmonary nodules in high-field MR at 3 T: evaluation of different pulse sequences using porcine lung explants.* Eur Radiol, 2007. **17**(5): p. 1341-51.

189. Failo, R., et al., *Lung morphology assessment using MRI: a robust ultra-short TR/TE 2D steady state free precession sequence used in cystic fibrosis patients.* Magn Reson Med, 2009. **61**(2): p. 299-306.
190. Fabel, M., et al., *MRI of respiratory dynamics with 2D steady-state free-precession and 2D gradient echo sequences at 1.5 and 3 Tesla: an observer preference study.* Eur Radiol, 2009. **19**(2): p. 391-9.
191. Muller, N.L., J.R. Mayo, and C.V. Zwirewich, *Value of MR imaging in the evaluation of chronic infiltrative lung diseases: comparison with CT.* AJR Am J Roentgenol, 1992. **158**(6): p. 1205-9.
192. Leutner, C.C., et al., *MR imaging of pneumonia in immunocompromised patients: comparison with helical CT.* AJR Am J Roentgenol, 2000. **175**(2): p. 391-7.
193. Iwasawa, T., et al., *Correlation of lung parenchymal MR signal intensity with pulmonary function tests and quantitative computed tomography (CT) evaluation: a pilot study.* J Magn Reson Imaging, 2007. **26**(6): p. 1530-6.
194. Robson, M.D., et al., *Magnetic resonance: an introduction to ultrashort TE (UTE) imaging.* J Comput Assist Tomogr, 2003. **27**(6): p. 825-46.
195. Heidemann, R.M., et al., *Resolution enhancement in lung 1H imaging using parallel imaging methods.* Magn Reson Med, 2003. **49**(2): p. 391-4.
196. Gaeta, M., et al., *Chronic infiltrative lung diseases: value of gadolinium-enhanced MRI in the evaluation of disease activity--early report.* Chest, 2000. **117**(4): p. 1173-8.
197. Lutterbey, G., et al., *Initial experience with lung-MRI at 3.0T: Comparison with CT and clinical data in the evaluation of interstitial lung disease activity.* Eur J Radiol, 2007. **61**(2): p. 256-61.
198. Yi, C.A., et al., *3-T MRI for differentiating inflammation- and fibrosis-predominant lesions of usual and nonspecific interstitial pneumonia: comparison study with pathologic correlation.* AJR Am J Roentgenol, 2008. **190**(4): p. 878-85.
199. Padovani, B., et al., *Chest wall invasion by bronchogenic carcinoma: evaluation with MR imaging.* Radiology, 1993. **187**(1): p. 33-8.
200. Silverstein, M.D., et al., *Trends in the incidence of deep vein thrombosis and pulmonary embolism: a 25-year population-based study.* Arch Intern Med, 1998. **158**(6): p. 585-93.
201. Goldman, L.W., *Principles of CT: multislice CT.* J Nucl Med Technol, 2008. **36**(2): p. 57-68; quiz 75-6.
202. McRobbie, D.W., Moore, E.A., Graves, M.J., and Prince, M.R, *MRI, from Picture to Proton.* (Cambridge, Cambridge University Press), 2007. **Vol 1, 2nd edition**.
203. Chavhan, G.B., et al., *Steady-state MR imaging sequences: physics, classification, and clinical applications.* Radiographics, 2008. **28**(4): p. 1147-60.
204. Srichai, M.B., et al., *Cardiovascular applications of phase-contrast MRI.* AJR Am J Roentgenol, 2009. **192**(3): p. 662-75.
205. Lotz, J., et al., *Cardiovascular flow measurement with phase-contrast MR imaging: basic facts and implementation.* Radiographics, 2002. **22**(3): p. 651-71.
206. Low, R.N., et al., *Dynamic contrast-enhanced breath-hold MR imaging of thoracic malignancy using cardiac compensation.* J Magn Reson Imaging, 1996. **6**(4): p. 625-31.
207. Kauczor, H.U. and K.F. Kreitner, *MRI of the pulmonary parenchyma.* Eur Radiol, 1999. **9**(9): p. 1755-64.
208. Itoh, H., M. Nishino, and H. Hatabu, *Architecture of the lung: morphology and function.* J Thorac Imaging, 2004. **19**(4): p. 221-7.
209. Molinari, F., et al., *Simultaneous cardiac and respiratory synchronization in oxygen-enhanced magnetic resonance imaging of the lung using a pneumotachograph for respiratory monitoring.* Invest Radiol, 2006. **41**(5): p. 476-85.
210. Molinari, F., et al., *Navigator-triggered oxygen-enhanced MRI with simultaneous cardiac and respiratory synchronization for the assessment of interstitial lung disease.* J Magn Reson Imaging, 2007. **26**(6): p. 1523-9.

211. Moseley ME, W.D., Wang SC, Dupon JW, Aicher KP, Brasch RC, *Application of very short TE spin-echo MRI: Imaging of lung.* Proceedings SMRM 1989. **686**.
212. Mayo, J.R., A. MacKay, and N.L. Muller, *MR imaging of the lungs: value of short TE spin-echo pulse sequences.* AJR Am J Roentgenol, 1992. **159**(5): p. 951-6.
213. Muller, N.L., G. Gamsu, and W.R. Webb, *Pulmonary nodules: detection using magnetic resonance and computed tomography.* Radiology, 1985. **155**(3): p. 687-90.
214. Feuerstein, I.M., et al., *Pulmonary metastases: MR imaging with surgical correlation--a prospective study.* Radiology, 1992. **182**(1): p. 123-9.
215. McFadden, R.G., T.J. Carr, and T.E. Wood, *Proton magnetic resonance imaging to stage activity of interstitial lung disease.* Chest, 1987. **92**(1): p. 31-9.
216. Hennig, J., A. Nauerth, and H. Friedburg, *RARE imaging: a fast imaging method for clinical MR.* Magn Reson Med, 1986. **3**(6): p. 823-33.
217. Kersjes, W., et al., *Diagnosis of pulmonary metastases with turbo-SE MR imaging.* Eur Radiol, 1997. **7**(8): p. 1190-4.
218. Ohno, Y., et al., *Single-shot half-Fourier RARE sequence with ultra-short inter-echo spacing for lung imaging.* J Magn Reson Imaging, 2004. **20**(2): p. 336-9.
219. Puderbach, M., et al., *Proton MRI appearance of cystic fibrosis: comparison to CT.* Eur Radiol, 2007. **17**(3): p. 716-24.
220. Hittmair, K., et al., *Evaluation of solitary pulmonary nodules with dynamic contrast-enhanced MR imaging--a promising technique.* Magn Reson Imaging, 1995. **13**(7): p. 923-33.
221. R. C. Semelka, B.M., J. P. Shoenut, R. Kroeker, P. Griffin and M. Lertzman, *Dynamic Gd-DTPA enhanced breath-hold 1.5 t MRI of normal lungs and patients with interstitial lung disease and pulmonary nodules: preliminary results.* Eur Radiol, 1992. **2**(6): p. 576-582.